Regulation of type II interleukin-4 receptor assembly and signaling by ligand binding kinetics and affinities

Dissertation

Presented to the department of Biology/Chemistry, University of Osnabrück
in partial fulfillment of the requirements for the degree of
“Doctor Rerum Naturalium”

David Richter

Osnabrück
March 2017

Table of contents

List of tables and figures .... **IV**

List of abbreviations .... **VII**

Summary **1**

1 Introduction **3**

1.1 Cytokines and their receptors 3

1.2 Yin and yang: cytokines at the interface of health and disease 5

1.3 Cytokine signaling 6

1.3.1 The JAK/STAT pathway 6

1.3.2 Negative regulation and the role of endocytosis 8

1.3.3 Hallmarks of cytokine signaling: pleiotropy, redundancy and specificity 11

1.4 Cytokine receptor assembly in the plasma membrane 12

1.4.1 Receptor dimerization 12

1.4.2 Plasma membrane organization 14

1.5 The type II interleukin-4 receptor: paradigm for functional selectivity 17

1.5.1 IL-4 and IL-13 17

1.5.2 Receptors involved in IL-4 and IL-13 signaling 19

1.5.3 Receptor structures and pathway activation 21

1.5.4 Binding properties and functional selectivity of natural and engineered IL-4/IL-13 variants 23

1.5.5 Receptor endocytosis 24

2 Objectives and strategy **26**

2.1 Objectives 26

2.2 Strategy and techniques 27

2.2.1 Quantification of receptor interaction kinetics 28

2.2.2 Single molecule imaging of receptor subunits and ligands 30

3 Materials and methods ... 35

3.1 Expression, purification and labeling of IL-4/IL-13 variants and IL-4Rα/IL-13Rα1 extracellular domains ... 35

3.2 Quantification of kinetics by simultaneous TIRFS-RIf detection ... 39

3.2.1 Measurement of binary complex (3D) kinetics ... 40

3.2.2 Measurement of ternary complex (2D) kinetics ... 41

3.3 Expression vectors for tagged receptor subunits ... 43

3.4 Cell culture and labeling of receptor subunits in live cells ... 44

3.5 Single molecule fluorescence microscopy and data evaluation ... 45

3.5.1 Total internal reflection fluorescence microscopy (TIRFM) ... 45

3.5.2 Image processing: single molecule localization, tracking and cluster filtering ... 46

3.5.3 Single molecule co-localization/co-tracking and diffusion analysis ... 47

3.5.4 Quantification of receptor dimerization by particle image cross-correlation spectroscopy (PICCS) ... 48

3.5.5 Calculation of effective 2D binding affinities on the cell surface ... 49

3.6 Reconstitution of receptor subunits in polymer-supported membranes (PSM) ... 49

3.7 Ensemble fluorescence microscopy studies ... 52

3.8 Flow cytometry ... 52

3.9 Model simulations ... 53

3.9.1 Diffusion and receptor interaction dynamics simulation (DAIDS) ... 53

3.9.2 STAT6 phosphorylation simulations ... 57

3.10 Protein structure visualization ... 60

3.11 Statistical analysis ... 60

4 Results and discussion ... 61

4.1 Part I: Receptor dimerization and dynamics ... 61

4.1.1 2D affinities determine receptor dimerization in artificial membranes ... 61

4.1.2 Ternary complex lifetimes correlate with 2D affinities ... 69

4.1.3 Signaling complex mobility and STAT6 activation do not depend on 2D affinities ... 72

4.1.4 Randomly distributed IL-4Rα and IL-13Rα1 are dimerized by the ligand in the plasma membrane ... 75

4.1.5 Highly efficient receptor dimerization with minor variations by 2D affinities ... 78

4.1.6 Dynamic complex stabilization by actin-dependent membrane micro-compartmentation ... 81

4.1.7 Spatiotemporal receptor dynamics can be mimicked by a hop diffusion model ... 87

4.2 Part II: Ligand binding affinity and kinetics ... 91

4.2.1 STAT6 activation potencies are in a wide range independent of 3D affinities ... 91

4.2.2 3D association and dissociation rates differentially modulate STAT6 activation and biological potencies ... 95

4.2.3 Decreasing 3D affinity is tolerated by almost two orders of magnitude in terms of receptor dimerization ... 99

4.2.4 Two determinants that play a crucial role in controlling cytokine signaling ... 101

4.2.5 Membrane-proximal signaling events are supported by receptor endocytosis ... 102

4.2.6 A mechanistic model correlating cytokine binding with the functional output ... 104

4.3 Acknowledgments ... 107

5 Conclusions ... 108

6 References ... 119

Acknowledgments ... 133

Declaration ... 135

List of tables and figures

Tables

Table 1 Overview of generated and used IL-4 variants 36
Table 2 Overview of used IL-13 variants 37
Table 3 Tagging and experimental usage of recombinant ligand and receptor proteins 37
Table 4 Conjugates used for protein labeling 38
Table 5 Overview of generated and utilized expression vectors 43
Table 6 Overview of DAIDS parameters 56
Table 7 Common parameters for STAT6 phosphorylation simulations 58
Table 8 Parameters for STAT6 phosphorylation kinetics simulation 58
Table 9 Parameters for pSTAT6 dose response simulation 59
Table 10 Type II IL-4 receptor binary complex kinetics measured in artificial membranes 64
Table 11 Type II IL-4 receptor 2D binding parameters measured in artificial membranes and live cells 71
Table 12 Average diffusion constants obtained from single molecule (co-)tracking data 74
Table 13 Receptor dimerization by IL-4 variants and IL-13 quantified by PICCS 81
Table 14 Distance distributions of IL-4Rα/IL-13Rα1 dimers induced by different ligands 84
Table 15 Receptor dimerization by IL-13 variants quantified by PICCS 101

Figures

Figure 1 Class I and class II cytokine receptors 4
Figure 2 Activation mechanism of cytokine receptor-associated Janus kinases 7
Figure 3 Cytokine signaling via the JAK/STAT pathway and mechanisms of negative regulation 9
Figure 4 Ligand-induced two-step assembly mechanism of dimeric cytokine receptors 13

Figure 5 Organization principles of the plasma membrane and the fence-and-picket model 15

Figure 6 Structure comparison of IL-4 and IL-13 18

Figure 7 IL-4/IL-13 receptor system 20

Figure 8 Scheme of the experimental setup for simultaneous total internal reflection fluorescence spectroscopy reflectance interferometry (TIRFS-RIf) detection 29

Figure 9 Scheme of the experimental setup employed for simultaneous dual-color total internal reflection fluorescence microcopy (TIRFM) of live cells on the single molecule level 32

Figure 10 Orthogonal protein labeling by specialized enzymatic tags 33

Figure 11 Scheme of the single molecule microscopy data acquisition and evaluation sequence 34

Figure 12 Two-step dimerization of the type II IL-4 receptor by different ligands 61

Figure 13 Mutations introduced in IL-4 variants for TIRFS-RIf experiments 62

Figure 14 Receptor interaction properties and functional integrity of IL-4 variants 63

Figure 15 Quantification of binary complex interaction kinetics on SSMs 64

Figure 16 Probing the 2D equilibrium on SSMs 65

Figure 17 Dynamic equilibrium between binary and ternary complexes on SSMs 66

Figure 18 Quantification of 2D association kinetics and equilibrium dissociation constants from ligand dissociation kinetics 67

Figure 19 Quantification of KFR binding affinities at single molecule level with transmembrane receptors reconstituted into PSMs 68

Figure 20 Quantification of 2D dissociation kinetics of ternary complexes induced by IL-4 variants on SSMs 70

Figure 21 Quantification of 2D dissociation kinetics of IL-13 induced ternary complexes on SSMs 71

Figure 22 Binding of IL-4 agonists and IL-13 to endogenous type II IL-4 receptors on Hela cells 73

Figure 23 STAT6 phosphorylation activities of IL-4 agonists and IL-13 in HeLa cells 75

Figure 24 Simultaneous dual color single molecule imaging of the type II IL-4 receptor in the plasma membrane 76

Figure 25 Receptor dimerization in the plasma membrane probed by single molecule co-locomotion analysis 77

Figure 26 Diffusion properties of ^{DY647}IL-4Rα and ^{TMR}IL-13Rα1 in the plasma membrane ... 78

Figure 27 Quantification of receptor dimerization in the plasma membrane ... 80

Figure 28 Analysis of inter-subunit distances in receptor dimers ... 82

Figure 29 Co-trajectory length analysis of RGA- and KFR-induced ternary complexes ... 83

Figure 30 Actin cytoskeleton disruption by Latrunculin B ... 85

Figure 31 Effects of MSK-disruption on receptor mobility and signaling ... 86

Figure 32 Simulation of spatiotemporal receptor dynamics including MSK-like membrane compartmentation and hop diffusion ... 87

Figure 33 Verification of simulated hop diffusion ... 88

Figure 34 Model simulations confirm MSK-mediated dynamic complex stabilization ... 89

Figure 35 Binding affinities and STAT6 activation profiles of IL-13 variants ... 92

Figure 36 Concentration dependency of STAT6 activation for IL-13 variants and IL-13Rα1 ... 94

Figure 37 Biological activities of IL-13 variants ... 96

Figure 38 Correlation of receptor binding kinetics and affinities of IL-13 variants with signaling and bioactivities ... 98

Figure 39 Analysis and quantification of receptor dimerization induced by IL-13 variants ... 100

Figure 40 Dynamics of receptor complexes induced by IL-13 variants ... 101

Figure 41 Investigation of receptor endocytosis and its effect on STAT6 phosphorylation ... 103

Figure 42 A quantitative model of IL-13 signaling reproduces experimental data ... 105

Figure 43 Time-resolved receptor complex assembly simulated with binding parameters of IL-13 variants to mimic STAT6 phosphorylation kinetics ... 106

Figure 44 Mechanistic model for ligand-induced type II IL-4 receptor dimerization sustained by rapid re-association within MSK-dependent plasma membrane microcompartments and accumulation of signaling complexes in endosomes ... 117

List of abbreviations

BG-547	SNAP-Surface® 547
BG-647	SNAP-Surface® 647
cDNA	complementary DNA
CHR	cytokine-binding homology region
CMV	cytomegalovirus
DBSCAN	density-based spatial clustering of applications with noise
DLS	dynamic light scattering
DOL	degree of labeling
DOPC	1,2-dioleoyl-sn-glycero-3-phosphocholine
DOPS	1,2-dioleoyl-sn-glycero-3-phospho-L-serine
DRM	detergent-resistant membrane
ECD	extracellular domain
EC_{50}	half maximal effective concentration
EDTA	ethylenediaminetetraacetic acid
EMCCD	electron multiplying charge coupled device
Epo	erythropoietin
FCCS	fluorescence cross-correlation spectroscopy
FCS	fluorescence correlation spectroscopy
FcεRI/CD23	low-affinity IgE receptor
FERM domain	protein 4.1, ezrin, radixin, moesin domain
FLIM	fluorescence lifetime imaging microscopy
FNIII	fibronectin type-III domain
FPALM	fluorescence photo-activation localization microscopy
FRET	Förster resonance energy transfer
FWHM	full width at half-maximum
G-CSF	granulocyte-colony stimulating factor
GM-CSF	granulocyte macrophage colony-stimulating factor
GR domain	gene regulatory domain
H10	decahistidine tag
HBS	HEPES-buffered saline
HEPES	(4-(2-hydroxyethyl)-1-piperazineethanesulfonic acid
hGHR	human growth hormone receptor
HILO	highly inclined and laminated optical sheet
HTL-TMR	HaloTag® tetramethyl-rhodamine ligand
I4R motif	insulin IL-4 receptor motif
IB	inclusion body
IFN	interferon
IgE	immunoglobulin E
IgG4	immunoglobulin G4
IL	interleukin
IMAC	ion metal affinity chromatography
IRES	internal ribosomal entry site
IRS	insulin receptor substrate
ITC	isothermal titration calorimetry
ITIM	immunoreceptor tyrosine-based inhibitory motif
JAK	Janus kinase
LatB	Latrunculin B
LIF	leukemia inhibitory factor
MBP	maltose-binding protein

MFI	mean fluorescence intensity
MHC II	major histocompatibility complex class II
MSD	mean square displacement
MSK	membrane skeleton
MST	microscale thermophoresis
MTT	multiple-target tracing
NA	numerical aperture
N-WASP	neuronal Wiskott–Aldrich syndrome protein
ORF	open reading frame
PBS	phosphate-buffered saline
PCR	polymerase chain reaction
PDF	probability density function
PI3K	phosphatidylinositol-3-kinase
PIAS	protein inhibitor of activated stats
PICCS	particle image cross-correlation spectroscopy
PLL-PEG	(poly-L-lysine)-(polyethylene glycol)
PM	plasma membrane
PMT	photomultiplier tube
PPT	phosphopantetheinyl transfer
PSF	point spread function
PSM	polymer-supported membrane
PTP	protein tyrosine phosphatase
QCM	quartz crystal microbalance
Rac1	Ras-related C3 botulinum toxin substrate 1
RGD	Arg-Gly-Asp tripeptide
RIf	reflectance interferometry
SEC	size exclusion chromatography
Sf9	*Spodoptera frugiperda*
SH2 domain	SRC-homology 2 domain
SHP	SH2 domain-containing phosphatase
SIM	structured illumination microscopy
SMLM	single-molecule localization microscopy
SOA	stearoyl-octadecylamine
SOCS	suppressor of cytokine signaling
SPR	surface plasmon resonance
SMT	single molecule tracking
STAT	signal transducer and activator of transcription
STED	stimulated emission depletion
STORM	stochastic optical reconstruction microscopy
SUV	small unilamellar vesicle
Tet	Tetracycline
TGF	transforming growth factor
T_H cell	CD4+ T helper cell
TIR	total internal reflection
TIRFM	total internal reflection fluorescence microscopy
TIRFS	total internal reflection fluorescence spectroscopy
TM	transmembrane
TMR	tetramethylrhodamine
TNF	tumor necrosis factor
tris-NTA	tris nitrilotriacetic acid
VCAM-1	vascular adhesion molecule-1
WSXWS motif	Trp-Ser-X-Trp-Ser peptide sequence
γ_c	common gamma-chain

Summary

Cytokines activate cell surface receptors to control and regulate immunity and hematopoiesis. Despite its enormous potential, pharmaceutical use of cytokines is in most cases hampered by their pleiotropic functionality, which renders cytokine-based therapies exceptionally difficult to control. Although there is growing evidence that the functional plasticity of cytokine receptors is largely encoded in the spatiotemporal dynamics of receptor complexes, no mechanistic correlation has hitherto been achieved. Two related aspects, the spatiotemporal organization and the activation mechanism of cytokine receptors in the plasma membrane, have further remained a topic of intensive and controversial debate. To shed to light into the mechanistic principles responsible for functional selectivity, this thesis aimed to quantitatively explore the molecular and cellular determinants governing cytokine receptor assembly and signaling using the type II interleukin-4 (IL-4) receptor as model system. To this end, by taking advantage of IL-4 and interleukin-13 (IL-13) agonists binding the receptor subunits IL-4Rα and IL-13Rα1 with different affinities and rate constants, an *in vitro* kinetic characterization of the receptor system was combined with live cell microscopy on the single molecule level and flow cytometry as well as *in silico* modeling approaches. The quantification of kinetics by a dedicated solid-phase detection method with the extracellular receptor domains tethered onto artificial membranes confirmed that the affinity and stability of the two-dimensional molecular interactions determine receptor dimerization levels and dynamics. Single molecule localization microscopy at physiological cell surface expression levels, however, revealed efficient ligand-induced receptor dimerization, largely independent of the two-dimensional receptor binding affinities, in line with similar STAT6 activation potencies observed for different IL-4 variants. Detailed spatiotemporal analyses and single molecule co-tracking of receptor subunits and ligands in conjunction with spatial-stochastic modeling identified confinement by actin-dependent membrane micro-compartments as an important cellular determinant for sustaining transient receptor dimers. By correlating downstream cellular responses with various three-dimensional binding affinities and kinetics of engineered IL-13 variants, distinct roles of ligand association and dissociation kinetics were uncovered. Whereas the extent of membrane-proximal effector activation is dependent on the association rate by controlling the number of formed receptor complexes in the plasma membrane, the lifetime of receptor complexes determines the potency of a ligand for inducing more distal responses and is, due to accumulation of signaling complexes in endosomes, directly connected to the kinetics of early signaling events.

1 Introduction

1.1 Cytokines and their receptors

The term “cytokine” refers to a large family of small secreted, usually glycosylated proteins including more than 130 members with diverse structures and functions [1]. Cytokines act as messenger molecules in a primarily paracrine or autocrine fashion between various cells, essentially in the context of innate and adaptive immunity as well as hematopoiesis. Their signals are delivered through specific receptors on the surface of particular target cells, triggering complex cellular outcomes that, among others, play crucial roles in cell activation, proliferation, differentiation and recruitment, immunoregulation and the defense against pathogens [2-4].

As the first cytokines were discovered more than half a century ago - far before methods like DNA sequence homology analysis or X-Ray diffraction analysis were employed in broad scale - their nomenclature is more or less inconsistent [1, 5]. Early found cytokines were, for example, named with respect to their cellular sources or targets (e.g. interleukins (ILs)) or the biological activity first attributed to them (e.g. tumor necrosis factor (TNF) or interferon (IFN)). Owing to their multifarious and in many cases overlapping actions (pleiotropy and redundancy, see chapter 1.3.3) as well as the frequently observed various sources and targets of one and the same cytokine, a uniform designation is, however, rather difficult. Today, a widely used classification is based on common structural features of the extracellular cytokine binding domains and shared intracellular signaling mechanisms of the receptors that are engaged [6]. This subdivision defines the two major families of class I and class II cytokine receptors as well as the families of TNF, TGF-β, IL-1/Toll-like, IL-17, tyrosine kinase and chemokine receptors [7-9] that will be not further described here.

The largest part of all hitherto known cytokines utilizes class I cytokine receptors, which are also known as hematopoietin receptors. These either consist of homodimers or heteromeric complexes, whereby the latter are usually assembled from one cytokine specific ligand binding subunit (called α chain) and one or more signal transducing subunits (β-, γ-, or gp130-chain; also called accessory chain). The accessory chains are often being shared between different ligands, giving rise to a further, class-intern subdivision (Figure 1, left). Apart from signaling through homodimers, heterotrimers, tetramers, hexamers and even dodecamers, most class I receptors, however, exert their effects through heterodimerization [7].

The structural linkage between class I cytokine receptors is a common membrane proximal tryptophan-serine-X-tryptophan-serine peptide sequence with X being any amino acid, called “WSXWS” motif, that seems to play an essential role in folding or maintaining the tertiary structure of the protein [7, 10]. Further, class I family members are characterized by two conserved pairs of cysteine residues in the extracellular cytokine binding domains, each forming an interstrand disulfide bond [6, 7]. Also the cytokines recognized by class I cytokine receptors exhibit a strong structural similarity, as they share a common four α-helical bundle fold with a unique “up-up-down-down” configuration but different lengths of the helices [7, 11].

The ligands of class II cytokine receptors are interferons (IFN-α, IFN-β, IFN-γ and IFN-λ) or those that exhibit biological activities commonly attributed to interferons (e.g. IL-10 or IL-22). This group is therefore also known as the interferon receptor family. Class II receptors are structurally related to those of class I by virtue of possessing conserved cysteine residues in the extracellular domains, but the “WSXWS” motif is exclusive for the class I type [6, 12] (Figure 1, right). Additionally, although the primary structural feature of class II cytokines is also a helical bundle topology, the number of the helices varies between different family members [11].

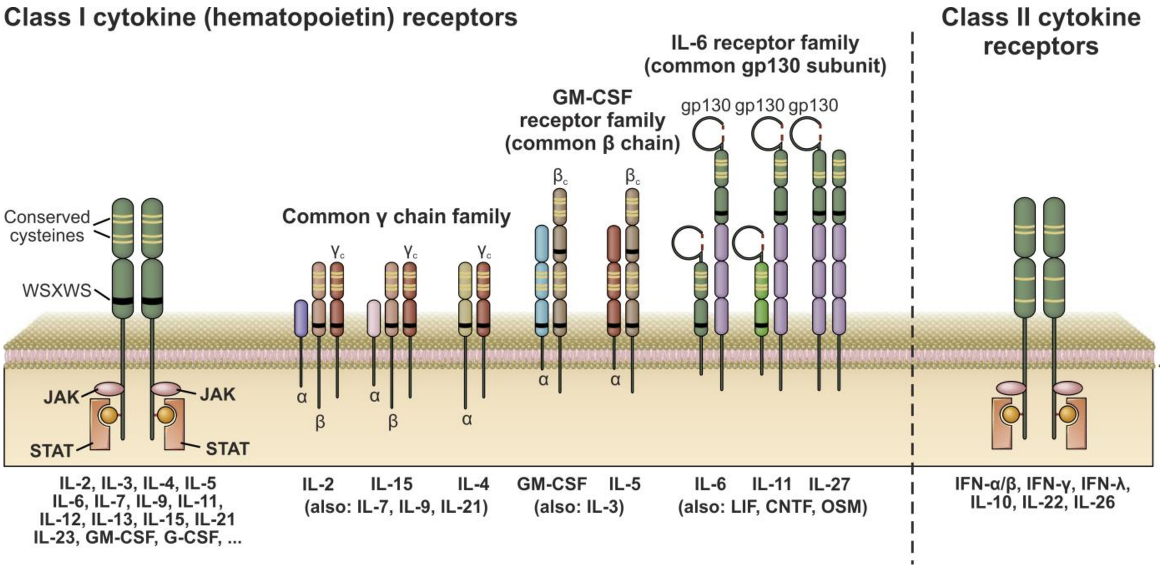

Figure 1. Class I and class II cytokine receptors. Receptors for different cytokines are classified into families on the basis of conserved extracellular domain structures and signaling mechanisms. Representative cytokines or other ligands that bind to each receptor family are listed below the schematic drawings. Groups of cytokine receptors share identical or highly homologous subunit chains. Selected examples of cytokine receptors in each group are shown. Homodimeric class I receptors, such as the growth hormone (GH), erythropoietin (Epo) or thrombopoietin (Tpo) receptor, are omitted for the sake of clarity. WSXWS: tryptophan-serine-X-tryptophan-serine. Modified from [6] with permission from Elsevier.

The extracellular part of both class I and class II cytokine receptors shows a modular architecture, at least consisting of a cytokine-binding homology region (CHR) built up of two interlinked fibronectin type-III (FNIII) domains, which constitutes the classical binding motif for helical cytokines. Depending on the particular receptor additional modules (e.g. Ig-like or further FNIII domains) are found [7].

On the cytoplasmic side cytokine receptors are instead more diverse in length and composition, which is related to the set of intracellular substrates involved in signaling cascades activated by the respective receptor. Accordingly, conserved motifs such as a membrane-proximal “Box1/Box2” region (see chapter 1.3.1) are rare [13].

1.2 Yin and yang: cytokines at the interface of health and disease

Owing to their central role in controlling complex immune responses, maintaining immune system homeostasis and regulating hematopoiesis it is not surprising that in many cases disturbed or unbalanced cytokine functions are at least to some extend related to immunological disorders such as autoimmune (e.g. rheumatoid arthritis, multiple sclerosis or type I diabetes [14]) and atopic diseases (e.g. allergic asthma or atopic dermatitis [15]). Also, the development of various types of cancer and the aggressive biological behavior of many cancerous cells have been linked to abnormal cellular signals mediated by cytokines and their receptors [16, 17]. It was therefore straightforward to develop strategies for interfering with cytokine functions, which already started in the 1970s with pioneering work on the basis of an anti-interferon serum [18]. Since then our knowledge has been massively expanded and techniques evolved rapidly, which today offers the possibility to down-modulate detrimental immune responses by targeting specific cytokines with neutralizing antibodies or soluble receptor molecules [14, 19-21]. A prominent example and within the first cytokine-blocking agents that were developed for medical purposes are tumor necrosis factor (TNF) inhibitors. At present, they are successfully used in the treatment of many autoimmune diseases, most notably of rheumatoid arthritis [19, 20].

From the pharmacological point of view, however, cytokines are not exclusively potent inducers of severe medical conditions that have to be defeated upon degeneration. Instead, several therapies have been established or are currently tested in clinical trials that exploit beneficial immunomodulatory effects of particular cytokines in certain disease conditions [1, 4]. Members of the type I interferon family are, for example, approved therapeutics for the treatment of chronic viral infections (e.g. hepatitis B and C, HIV) and specific types of leukemia, lymphoma or melanoma as well as of multiple sclerosis [1, 4, 22]. Interleukin-2 (IL-2) is one of the most effective agents for the treatment of metastatic melanoma and renal cell carcinoma [23]. Cancer patients who suffered from thrombocytopenia after intensive chemotherapy were successfully medicated with IL-11 [24] and the application of growth factors like G-CSF and GM-CSF were observed to reduce the duration of chemotherapy-induced neutropenia in leukemia patients [25].

A completely different yet highly interesting approach is based on directed tumor cell destruction with engineered cytotoxins. As some cancer cell types show an overexpression pattern of certain cytokine receptors, these cells are amenable to be specifically targeted with a recombinant fusion protein consisting of a cytokine fused to a truncated form of *Pseudomonas* exotoxin. Such cytotoxins exist, for example, on the basis of IL-4 or IL-13 and were shown to be strongly toxic for several human tumor cell lines. Whether they provide a safe and effective therapeutic option for the fight against cancer needs to be examined in the future, but pre-clinical studies already revealed promising results [17, 26, 27].

These examples illustrate the enormous potential of cytokine therapies for the treatment of severe diseases that is still far from being exhausted. The underlying reasons are diverse, but especially the pleiotropic nature of cytokines (see chapter 1.3.3) renders them intrinsically prone to elicit side effects [1, 4]. Interferon-α therapies are frequently accompanied by neuropsychiatric disorders, a development or exacerbation of autoimmune diseases and multiple further adverse effects [1]. The treatment of cancer patients with IL-2, which so far requires high cytokine doses, is likewise impaired by the toxicity profile of IL-2 that is, among several more or less severe side effects, largely associated with a dangerous capillary leak syndrome. Numerous other attempts to gain from particular cytokines in disease conditions are also prone to fail due to comparable drawbacks [1, 22]. Moreover, the enormous complexity and connectivity of the cytokine network constitute a serious obstacle to the targeted treatment of diseases with cytokine-related approaches. Consequently, further detailed knowledge in the field of cytokine biology is needed from the macroscopic to the molecular level to pave the way for new cytokine therapies and to reduce the adverse side effects and frequently observed dose-dependent toxicity of many present ones [1, 4, 22].

1.3 Cytokine signaling

1.3.1 The JAK/STAT pathway

A common feature of class I and class II cytokine receptors is the lack of an intrinsic enzymatic activity as it is found in receptor tyrosine kinases of many growth factors.

Instead, the intracellular domains of these receptors are, unless rare exceptions, constitutively but not covalently associated with tyrosine kinases of the Janus kinase (JAK) family, which comprises four members: JAK1-3 and TYK2 [7, 13]. These are relatively large proteins assembled from more than 1,100 amino acids that fold into a hitherto only partially known three-dimensional structure. However, a molecular organization into four distinct domains was described.

At the N-terminus a “FERM” domain is responsible for receptor association via membrane-proximal “Box1/Box2” regions in the intracellular receptor tails [28, 29]. An adjacent putative “SRC-homology 2” (SH2) domain was reported to be critically involved in receptor binding and hypothesized to play an important role for the conformation of the molecule by acting as a spacer instead of fulfilling a classical SH2 function (i.e. phosphotyrosine binding) [30]. The C-terminal part is made up of two further elements, a catalytically active kinase and an inactive pseudokinase domain, building a tandem structure that constitutes the hallmark of Janus kinases. The former exhibits the properties of a typical tyrosine kinase domain and is responsible for the phosphorylation function of the JAKs. The latter, which has a canonical kinase fold but lacks critical catalytic residues, instead acts in an autoinhibitory fashion by suppressing the activity of the adjoining kinase domain under unstimulated conditions (Figure 2, left) [28, 29].

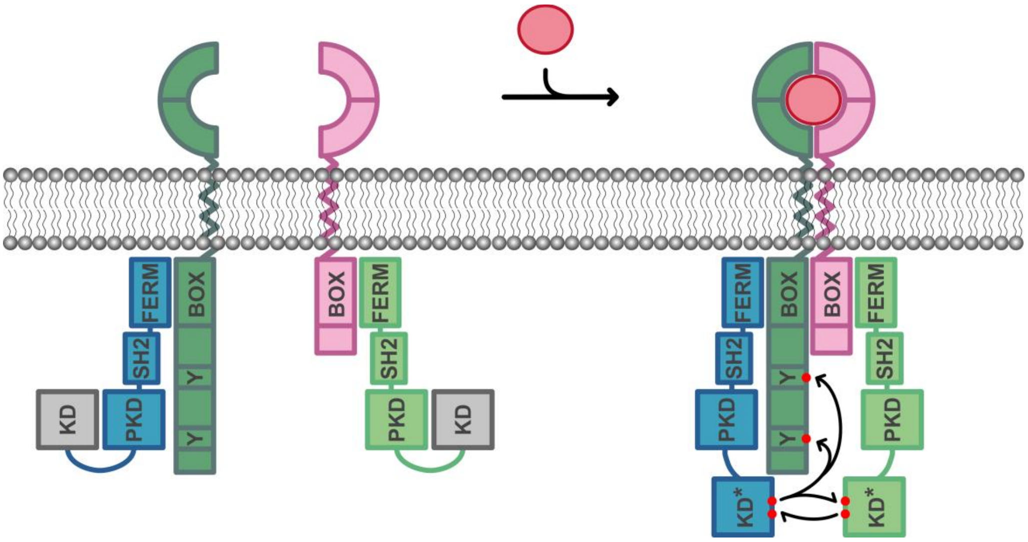

Figure 2. Activation mechanism of cytokine receptor-associated Janus kinases. The fundamental cytokine receptor signaling entity comprises two transmembrane receptor chains, each constitutively associated with a JAK kinase family member. Ligand-mediated receptor dimerization induces the transition of the kinase domain (KD) into an active conformation (KD*) that is further enhanced by mutual cross-phosphorylation of the now juxtaposed JAKs. Fully active JAKs subsequently phosphorylation tyrosine residues (Y) in the receptor chains to create docking sites for intracellular signaling substrates. Inspired by [31].

According to the currently accepted model of cytokine signaling the JAK pseudokinases hold the kinase domains in an inactive state until the transition into an active conformation is stimulated by ligand-mediated receptor dimerization or, as some studies suggest, reorganization of preformed dimers [28, 32]. Regardless of whether the latter exist, in the activated signaling complex two JAKs are brought into close proximity, allowing their mutual full activation by trans-phosphorylation [33]. Subsequently, the activated JAKs phosphorylate intracellular domains of the associated receptors, which in turn serve as docking sites for further signaling substrates (Figure 2, right) [7, 11].

These are primarily transcription factors of the signal transducer and activator of transcription (STAT) family, which contains seven members (STAT1-4, STAT5a, STAT5b and STAT6) [34]. In the inactive state, STATs reside in the cytoplasm as monomers and are recruited to phosphotyrosines of activated cytokine receptors via their SH2 domains, following their activation by JAK-mediated phosphorylation on a conserved C-terminal tyrosine residue. Activated STATs dissociate from the receptor, dimerize by reciprocal SH2 domain-phosphotyrosine interactions and translocate into the nucleus where they bind to specific DNA sequences to modulate the transcription of target genes [13, 33]. This particular sequence that constitutes the most important signaling pathway downstream of cytokine receptors is referred to as “JAK/STAT pathway” (Figure 3, left) [35].

Other pathways that are activated in response to cytokine engagement include the well-known Ras/MAPK and PI3K/Akt signaling cascades [33, 36, 37].

1.3.2 Negative regulation and the role of endocytosis

Cytokine signaling has to be tightly controlled to prevent exaggerated immune responses. Therefore, cells are able to modulate the activation of cytokine receptors and downstream events by several modes of regulation. One of these is based on the activity of negative feedback regulators, of which three major classes exist: SOCS (suppressors of cytokine signaling), PTPs (protein tyrosine phosphatases) and PIAS (protein inhibitors of activated stats) [33]. In a classical negative feedback loop, SOCS proteins that inhibit the kinase activity of JAKs or block phosphorylated tyrosine residues on activated receptors are co-expressed upon cytokine-induced gene transcription [38]. Instead, PTPs like SHP-1, SHP-2 or PTP1B counteract the activity of the JAKs, while PIAS proteins are constitutively expressed transcriptional co-regulators that are able to prevent binding of activated STAT dimers to the DNA (Figure 3, right) [33, 39, 40].

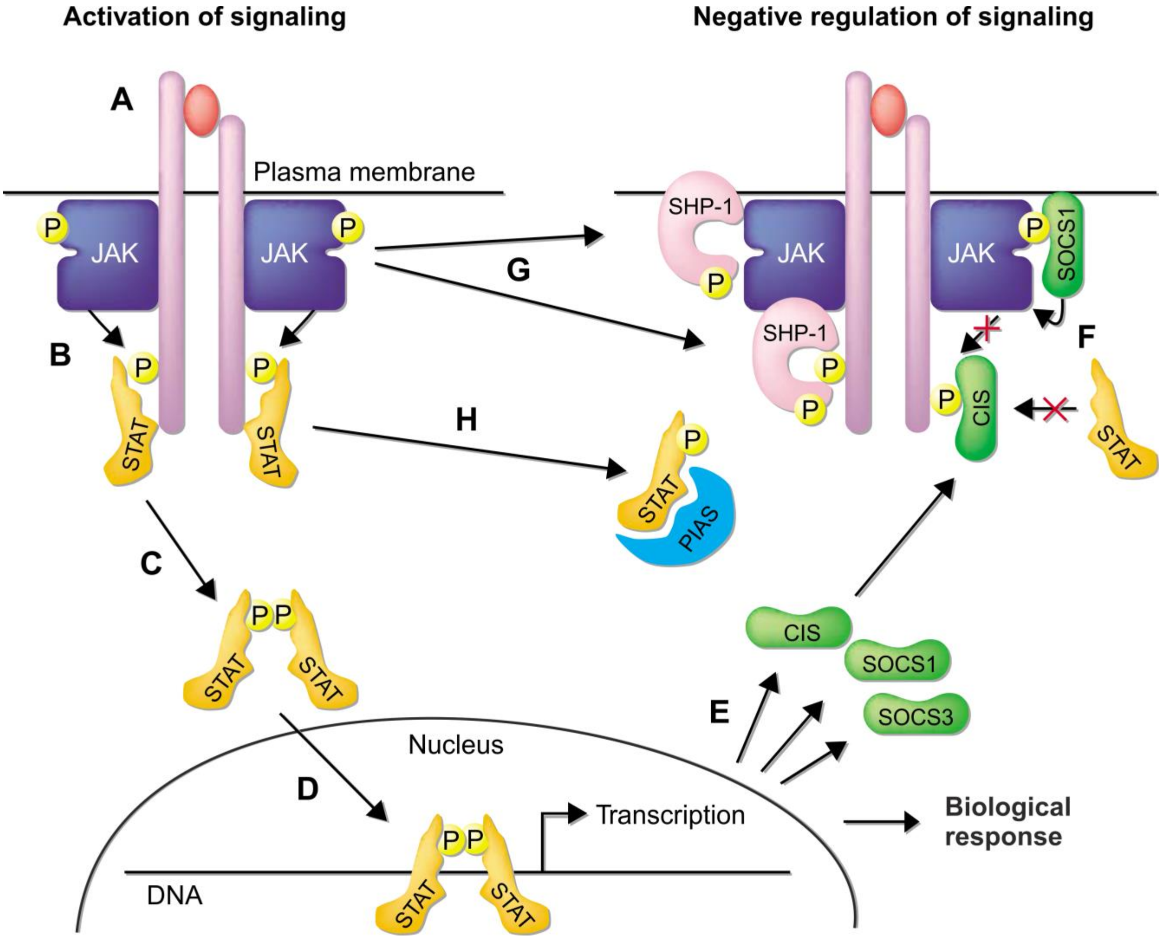

Figure 3. Cytokine signaling via the JAK/STAT pathway and mechanisms of negative regulation. (A) Binding of cytokines to their cognate receptors on the cell surface initiates signaling by receptor dimerization, which results in juxtaposition, cross-phosphorylation (depicted in yellow) and activation of kinases of the Janus family (JAKs). **(B)** Activated JAKs phosphorylate tyrosine residues within intracellular domains of the receptor they are noncovalently bound to, creating docking sites for further signaling substrates, such as members of the signal transducer and activator of transcription (STAT) family. These harbor a SH2 domain for phosphotyrosine binding and are themselves activated by phosphorylation through the JAKs upon receptor engagement. **(C, D)** After their activation STATs dissociate from the receptor and translocate into the nucleus as homo- or heterodimers where they bind to specific DNA sequences to modulate the transcription of target genes. Negative regulation of cytokine signaling is accomplished in several ways: in a classical negative feedback loop **(E)** the expression of suppressors of cytokine signaling (SOCS) family proteins that **(F)** inhibit JAK activity (e.g. SOCS1) or block docking sites on the intracellular receptor domains (e.g. CIS) is enhanced by the STATs. **(G)** Phosphatases like SHP-1 interrupt signaling by JAK and receptor dephosphorylation after being phosphorylated by the JAKs themselves. **(H)** Protein inhibitors of activated stats (PIAS) proteins bind phosphorylated STATs rendering them incapable of binding to the DNA. Modified from [39] with permission from Elsevier.

Another type of regulation depends on secreted receptor variants consisting of extracellular domains only that are either genetically encoded as decoy receptors or can be generated by proteolytic cleavage or alternative splicing [41]. Although these soluble forms can be part of atypical signaling complexes in a process called “trans-signaling” [42], they frequently compete with their membrane-bound counterparts for cytokine binding, thus inhibiting receptor activation in a dose-dependent manner [43].

By transferring receptors into the endosomal pathway for degradation, cells are able to effectively reduce the total amount of receptors available for activation in the plasma membrane within a short time scale. However, although cytokine receptor internalization was originally thought to be a ligand-induced process that aims to attenuate signaling, it is now recognized that endocytosis does not exclusively constitute a negative regulation mechanism. Accumulating evidence rather reveal signal-propagating functions, because signaling from internalized receptors often seems to continue in endosomal compartments or even depend on endosomal uptake [44-46]. In this regard, two aspects are thought to be key to a supporting role of endocytosis: the limited size of endosomes and the lipid composition of their membranes. Owing to the small internal volume the local concentration of ligands and receptors is drastically increased in endosomal structures, which probably allows for efficient ligand re-binding and drives receptor complex assembly, thereby generating potent intracellular signaling hubs. The presence of specific lipids in the endosomal membrane is possibly required for or enhances the recruitment of intermediary substrates like adaptor molecules, respectively, that are critical for efficient pathway activation [44, 47]. Besides, as cellular processing of endosomes is not limited to degradation but also includes recycling pathways, receptor turnover that leads to the regeneration of the receptor pool at the plasma membrane is another aspect that has be taken into account [47].

An example of how multiple facets of endocytosis are closely linked to the particular function of a cytokine receptor can be found in the erythropoietin (Epo) system. On the one hand, ligand-bound Epo receptors are rapidly taken up for down-regulation of signaling and depletion of circulating Epo concentrations [48], but on the other hand continuous receptor turnover at a high rate, which requires a large intracellular receptor pool, compensates the endocytic removal from the cell surface. Importantly, by mathematical modeling of quantitative data and experimental validation, the latter was found to enable a linear translation of extracellular ligand concentration into intracellular receptor activation [49].

Despite ongoing intensive research in this field, such detailed mechanistic studies of the complex interplay between cytokine signaling and endocytosis have, however, been rare. Steadily, new pieces of the puzzle appear instead, which are difficult to put together, because a plethora of different factors have to be considered, while even various existing routes of receptor internalization are not completely understood [47]. Apart from that, the cellular machineries that are involved in endocytosis are frequently pivotal elements of cellular integrity (e.g. actin cytoskeleton, dynamin). Thus, especially methods that aim to interfere with endosomal uptake for investigational purposes are usually difficult to perform, rendering the development of new experimental strategies a desirable task to unravel the intertwined connection of cytokine signaling and endocytosis.

1.3.3 Hallmarks of cytokine signaling: pleiotropy, redundancy and specificity

Most cytokines are characterized by the phenomena of pleiotropy and redundancy, which means that cytokines frequently possess the ability to elicit a multitude of diverse and sometimes opposing functional responses on various different cell types, while these responses are closely overlapping between different cytokines in many cases. The mechanistic origin can be traced back to the promiscuous nature of cytokines and their receptors, as some cytokines are able to engage more than one receptor complex (e.g. IL-4 activates type I and type II IL-4 receptors), different cytokine family subtypes may signal via an identical receptor complex (e.g. type I interferon system), and particular accessory chains are frequently shared between several cytokines (e.g. common beta- and gamma-chain, gp130) [50]. Further, the limited set of available JAK and STAT proteins as well as the widespread distribution of many cytokine receptors (e.g. interferon receptors are found on the surface of virtually every human cell [51]) do not really seem to provide a working framework for the large number of cytokines to control a highly complex immune system, which demands great functional diversity, but in particular specificity.

Indeed, the mechanisms that facilitate the translation of receptor activation by a certain cytokine into a specific biological response, although the pattern of JAK/STAT activation may be similar to the pattern elicited by other cytokines, are largely not understood [50]. The situation becomes even more enigmatic when one and the same receptor complex is activated by different cytokines and yet functional specificity is preserved, examples being the numerous type I interferons [52], the type II IL-4 receptor [53] or the IL-10 receptor [54].

Because the key for a deeper understanding of the basic processes that enable cells to respond specifically to a certain cytokine was not found in early (membrane-proximal) intracellular signaling events (e.g. differential activation of the JAK/STAT pathway or of other signaling routes [50]), the research focus recently shifted towards ligand-receptor complex dynamics. In several cases functional selectivity has been linked to variations in the affinity and stability of ligand interactions with the receptor subunits [52, 53, 55-60] as well as to cell surface receptor densities [61-63]. These factors are associated with the underlying interaction kinetics that essentially determine formation rates of ligand-receptor complexes, their lifetimes and the dynamic equilibrium between the opposed processes of receptor complex assembly and disassembly, suggesting a central role of signaling complex formation dynamics in regulating signaling specificity.

A notable feature of the investigated systems is, however, the poor correlation between receptor binding affinity and signal activation potencies, because large changes in binding affinity are frequently not reflected in early signaling events and are usually not linearly translated into correspondingly altered potencies [50, 52]. Although this phenomenon was highlighted by engineering cytokines with increased receptor binding affinities, specificities, or both [32, 64], the parameters relating cytokine affinity to the functional outcome are still ill-defined. Especially in view of the therapeutic use of cytokines a more granular understanding of the mechanisms governing cytokine potency is strongly desired and calls for further studies with emphasis on the molecular level.

1.4 Cytokine receptor assembly in the plasma membrane

1.4.1 Receptor dimerization

In 1991 a comprehensive study on the human growth hormone receptor (hGHR) proposed for the first time that receptor subunit dimerization at the plasma membrane, which is the prerequisite for cytokine receptor activation, is ligand-induced and occurs in two sequential steps [65]. In the subsequent period, intensive research on the type I interferon receptor [66], the type I IL-4 receptor [67] and other cytokine receptor systems (e.g. LIF [68]) corroborated this model. Receptor dimerization accordingly starts with a bivalent cytokine binding from solution to one receptor subunit, resulting in a binary ligand-receptor complex. This is followed by lateral recruitment of the second receptor subunit within the plasma membrane yielding two possible pathways for ternary receptor-ligand-receptor complex assembly (Figure 4). In homodimeric complexes, as the two involved receptor chains are identical, both binding sequences are equal. This results in self-antagonism at high ligand concentrations and therefore a bell-shaped dose-response relationship due to sequestration of all available receptor chains in 1:1 ligand-receptor complexes [69]. In heterodimeric complexes one pathway is either preferred or exclusive as cytokines commonly exhibit highly asymmetric binding affinities towards their cognate receptor subunits and rapidly bind to a high-affinity α-subunit followed by lateral recruitment of a low-affinity accessory chain [50]. In some cases the binding sequence also includes cooperativity (e.g. hGH or cytokines that utilize the common gamma-chain), when the first binding step results in the presentation of a binding interface with increased affinity of the binary complex towards the accessory chain [32, 70].

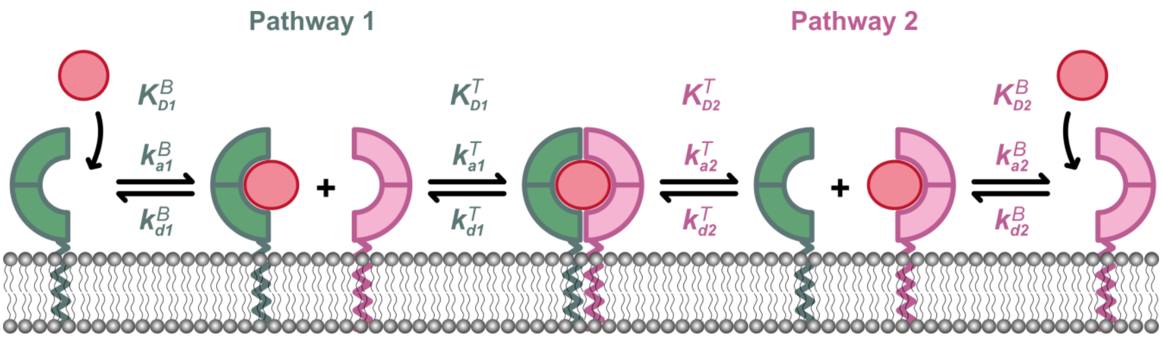

Figure 4. Ligand-induced two-step assembly mechanism of dimeric cytokine receptors. Ligand binding from solution to the receptor is followed by lateral recruitment of a second receptor subunit. Fractions of binary and ternary complexes in equilibrium are determined by three- and two-dimensional dissociation constants K_D^B and K_D^T, and the respective ligand and receptor surface concentrations according to the law of mass action. Mean binary and ternary complex lifetimes correspond to the reciprocal of the dissociation rate constants k_d^B and k_d^T.

Today it is commonly accepted that the majority of class I and class II cytokines exerts its effects through receptor dimers on the cell surface [7]. However, the spatiotemporal organization of cytokine receptors in the plasma membrane and in particular the role of receptor dimerization has remained controversially debated [71, 72]. Because ligand-independent pre-dimerization of the receptor subunits of homodimeric class I cytokine receptors including the GHR was claimed [73-76] and a similar mechanism was reported to hold true for several heterodimeric class I [77-79] and class II [80-83] cytokine receptors, the original model of ligand-induced dimerization of previously separated receptor subunits was severely called into question.

The frequently observed very low affinity of many cytokines towards the accessory chain indeed suggests that its recruitment could be rather inefficient, in particular because many cytokine receptors are expressed at a level of only a few 100 copies per cell [84]. But it has to be taken into consideration that these affinities were in most cases either measured solely in solution with soluble receptor domains or by surface-sensitive techniques with at least one receptor subunit in soluble form. Thus, as the conditions in the membrane environment, where proteins exhibit reduced translational and rotational freedom as well as slower lateral and rotational diffusion, are significantly different from those in solution, such measurements are difficult to translate into lateral (two-dimensional) affinities in the cell membrane [85].

Apart from that, studying receptor assembly in the plasma membrane is prone to experimental bias, as common biophysical techniques for detecting interactions such as Förster resonance energy transfer (FRET) require a combination of strong overexpression of receptors and fusion of fluorescent proteins, which by themselves may promote dimerization or clustering [86]. Biochemical interaction assays such as protein fragment complementation moreover often yield irreversible complex formation and therefore do not provide an accurate picture of dynamic equilibria [87]. To overcome these limitations, recently single molecule imaging techniques were developed on the basis of posttranslational labeling via strictly monomeric tags to visualize and quantify the dimerization of receptors in the plasma membrane of living cells at physiological receptor expression levels [60]. Initial applications of the new techniques to class I (Epo [88]) and class II (type I IFN [60]) cytokine receptors strongly support the original model of ligand-induced dimerization, as pre-dimerization of these receptors could be unequivocally excluded, while receptor dimers were clearly observed upon ligand addition. Importantly, these studies also provided strong evidence against a different mechanism suggested by some reports that is based on enhanced receptor assembly due to ligand-independent co-clustering of receptor subunits, which is thought to be promoted by plasma membrane microdomains [89-92].

1.4.2 Plasma membrane organization

It is commonly known that the fluid mosaic model introduced by Singer and Nicolson in 1972 [93] does not fully reflect the conditions in the plasma membrane, as the latter is evidently structured in domains rather than being an ideal two-dimensional solution [94, 95]. This structural architecture provides a highly complex and flexible framework built by various lipids and proteins that is able to spatiotemporally restrict the movement of membrane-associated and transmembrane proteins. Apart from well-characterized regions with specialized arrangements of lipids and proteins optimized for their individual functions (e.g. adhesion structures, clathrin-coated pits or caveolae), two major principles have emerged that organize the plasma membrane into numerous dynamic sub-microscopic domains: partitioning into lipid microdomains (lipid rafts) and confinement by the membrane skeleton (MSK) [96]. Notably, both principles are not mutually exclusive, but were suggested to coexist in a hierarchical fashion (Figure 5A) [97].

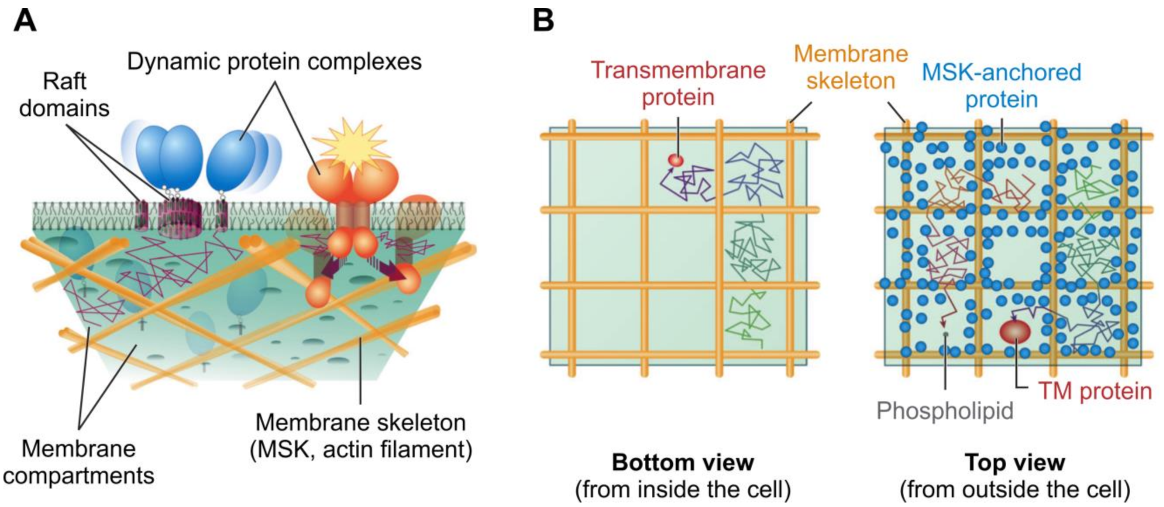

Figure 5. Organization principles of the plasma membrane and the fence-and-picket model. (A) The plasma membrane is believed to be hierarchically structured in domains with different size scales by constitutive compartmentation through the membrane skeleton (MSK, diameter of 40-300 nm), lipid-based partitioning into raft microdomains (2-20 nm) and accumulation of dynamic (transient) protein complexes (3-10 nm). **(B)** Free diffusion of transmembrane proteins is restricted to submicroscopic compartments surrounded by a fence-and-picket-like structure. A cortical meshwork built from actin filaments (MSK) constitutes the fences and membrane-integrated proteins attached to these filaments act as pickets (hidden for clarity in A and in left figure in B). Inter-compartment crossing is unlikely due to physical hindrance by the boundaries and occurs by “hop” movement in dependence of dynamic cytoskeleton remodeling processes, thermal fluctuations and energetic conditions. Adapted from [97].

The lipid raft concept arises from two observations: particular membrane components are insoluble in detergent-containing solvents resulting in detergent-resistant membranes (DRMs) and artificial membranes composed of specific lipid mixtures show spontaneous separation of lipids into lipid-ordered and –disordered phases [98]. It postulates the existence of highly dynamic and heterogeneous microdomains of greater molecular order in the cell membrane, consisting of cholesterol tightly packed with saturated fatty acid chains of specific glycosphingolipids [96, 99]. These domains are believed to constitute platforms for the lateral segregation of proteins. However, the properties and even the existence of lipid rafts in plasma membranes are still controversially discussed, because the conclusions drawn from various studies were strongly dependent on the utilized methods and an unambiguous direct visualization of these nano-sized domains in living cells is lacking so far [96, 100].

Yet lipid rafts were reported to be frequently involved in signal transduction [101, 102], which was in the cytokine context described for the IL-2 as well as the type II interferon (IFN-γ) receptor. But, while two studies of the IFN-γ receptor revealed a consistent critical role of lipid microdomains for signaling and endocytosis [103, 104], the observations made in three different studies of the IL-2 receptor range from receptor partitioning into DRMs that is needed for a specific route of endocytosis [105], over a regulatory role by sequestration of the α-subunit within lipid microdomains [106] to the assembly of supramolecular receptor clusters facilitated by lipid rafts [89]. Thus, our current knowledge of lipid-based domain structures in the plasma membrane and their roles in cytokine signaling are rather fragmentary and there is little consensus about functional consequences.

By contrast, the MSK-dependent organization principle is characterized in significantly more detail. According to a prominent model, which began to emerge in the 1980s and that was continuously refined by Kusumi and colleagues, the plasma membrane is constitutionally compartmentalized into so-called “corrals” with sizes of tens to hundreds of nanometers [95, 107]. The compartment barriers are believed to stem from the actin-based cortical cytoskeleton meshwork acting as fences and transmembrane proteins anchored to and aligned along these MSK fences building pickets. This analogy gave rise to the familiar designation: fence-and-picket model (Figure 5B) [97, 108].

The important consequence that arises from this concept is that the diffusion of membrane-associated and -incorporated proteins (and even lipids) is impaired by collisions with MSK-anchored proteins or with MSK filaments via intracellular parts, respectively. This leads to a temporal confinement of these proteins, as switching between adjacent compartments is a relatively rare event that depends on MSK dynamics (i.e. remodeling or thermal fluctuation-induced transient dissociation of the MSK) and the molecule’s translational momentum [107, 108]. The specific type of molecular motion that proteins and lipids undergo in this scenario is generally referred to as “hop diffusion”. It plausibly explains why macroscopic diffusion coefficients in intact plasma membranes have been observed to be reduced by a factor of up to 50 compared to artificial membranes or liposomes [107] and why protein complex formation further lowers or completely abolishes diffusion (oligomerization-induced trapping) [109]. The fast molecular motion within corrals of various nanometer scales (microscopic diffusion) and the MSK-based hindrance was simply not resolvable for a long time, neither spatially nor temporally [107]. But by now the whole concept is strongly corroborated by various studies [95] including a direct visualization of confined membrane compartments by advanced high-speed single particle-tracking techniques [110], an analytical approach based on the so-called “FCS diffusion law” [96, 111], a morphological investigation by electron tomography [112], and a minimally invasive detection approach using STED-FCS [113].

The functional relevance of this model for cytokine receptors is largely unknown, although several reports hypothesize important implications for signal transduction. For example, a regulative role for receptor distribution was proposed by several studies or a possibility to localize signal sources through oligomerization-induced trapping, which might be important for local or polarized cell responses [97]. Further, based on a computational approach spatiotemporal variations of the bimolecular reaction rate inside the membrane were observed. While the overall rates of dimer and monomer formation and therefore the corresponding equilibrium were not changed upon addition of semipermeable membrane compartments, it was found that these reactions occur in bursts within a confined environment. This mechanism of local reaction enhancement was suggested to be critically involved in signaling, probably by amplifying the activation of intracellular kinases [114]. Indeed, a recent study of the type I IFN receptor combining experimental and computational approaches proposed a key role of MSK-based diffusion barriers in maintaining signaling complexes by supporting the re-association of dissociated receptor subunits [115]. Whether these conclusions can be transferred to other cytokine receptor systems needs to be carefully figured out in the future.

1.5 The type II interleukin-4 receptor: paradigm for functional selectivity

1.5.1 IL-4 and IL-13

IL-4 and IL-13 are functionally closely related, prototypical class I four-helix bundle cytokines with key functions in humoral immune responses [53]. They were discovered in mice in the early (IL-4, first designated as BCGF [116]) and late (IL-13, first designated as P600 [117]) 1980s and have been intensively studied since their human cDNA was successfully cloned a few years later [118, 119]. Although IL-4 and IL-13 share only 20-25% identity in their amino acid sequence [119] and structural data obtained by NMR and X-ray crystallography showed some differences between both cytokines, the overall folding topology is quite similar and there is good agreement in the superposition of shared secondary structure elements (Figure 6) [120].

Both IL-4 and IL-13 are produced and secreted by various cells [121]. The primary sources are, however, a subset of CD4+ T cells, designated T helper type 2 (T_H2) cells, triggered by antigen-mediated T cell receptor engagement. Also mast cells, eosinophils and basophils are in response to immunoglobulin E (IgE)-induced cross-linkage of IgE receptors (FcεRI, also known as CD23) potent producers of IL-4 and IL-13 [122, 123].

The functional bandwidth of IL-4 and IL-13 is, with some pockets of specificity, closely overlapping and, as it is observed for many cytokines, highly diverse [50]. It essentially includes the mediation of proliferation, differentiation and (anti-)apoptotic signals for various hematopoietic and non-hematopoietic cells in the context of type 2 immune responses to provide effective defense against large extracellular parasites (e.g. helminths). The profile of type 2 immunity is, among others, characterized by the presence of T_H2 cells, elevated serum levels of IgE isotype antibodies, the involvement of specific cytokines (IL-4, IL-5, IL-9 and IL-13), eosinophils, mast cells and basophils, and the suppression of type 1 immunity. It targets parasites and foreign substances by inducing their expulsion through mechanisms like increased mucus production, smooth muscle contractility and changes in epithelial tissues [124]. In accordance with their critical role in these rather humoral than cell-driven immune responses, IL-4 and IL-13 equally promote growth, proliferation and survival of B cells [116, 125, 126], their reprogramming to switch to IgE and IgG4 antibody production [127-129] and the upregulation of CD23 on the surface of these cells as well as on mast cells and basophils [129-131]. Further, via the induction of the expression of adhesion molecules (e.g. vascular adhesion molecule-1 (VCAM-1)) and of specific chemokines in endothelial cells, eosinophils and other immune cells are recruited to sites of inflammation [9, 123, 132]. IL-4 and IL-13 are moreover involved in the alternative activation of macrophages, which are critical for the clearance of certain parasitic infections, but also promote tissue repair and the synthesis of anti-inflammatory factors to rebalance the immune system after bacterial or viral infections [64, 133, 134].

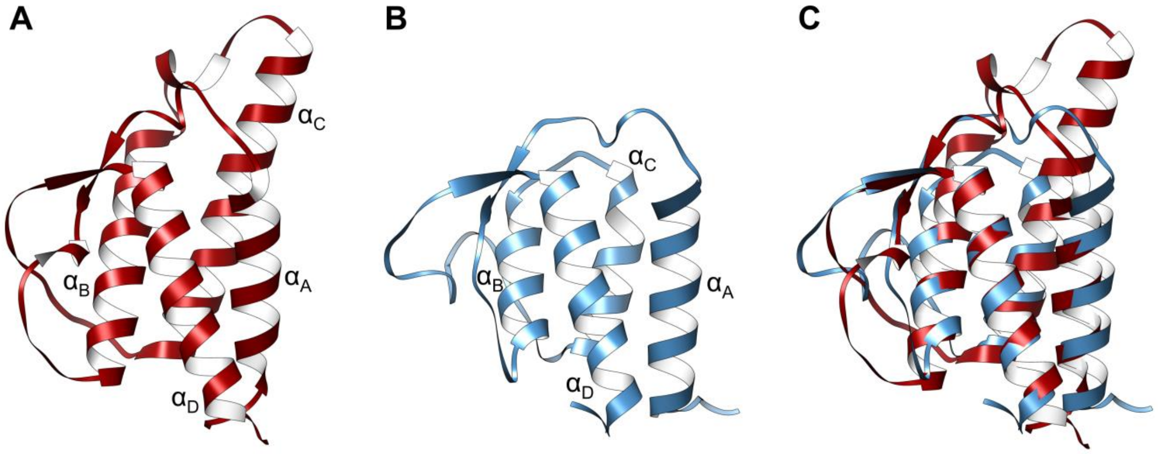

Figure 6. Structure comparison of IL-4 and IL-13. (A) IL-4 and **(B)** IL-13 are folded into a short-chain four α-helical bundle structure with an "up-up-down-down" arrangement including β-sheet structures within the loops connecting helices αA and αB as well as αC and αD. **(C)** Overlay of both structures reveals a quite similar folding topology with a primary difference in the overall molecular size due to shorter αB and αC helices in IL-13 compared to IL-4. Structure data: PDB IDs 2B8U (human IL-4) and 1IJZ (human IL-13).

Despite these and numerous other effects that IL-4 and IL-13 have in common, they exhibit unique and quite different functionalities, which have led to the classification into an effector (IL-13) and a regulatory (IL-4) cytokine [63]. IL-4 is essential for and the only cytokine capable of inducing the differentiation of naïve CD4+ T helper type 0 (T_H0) cells into the T_H2 type. Following differentiation these cells are on the one hand able to secrete canonical type 2 cytokines (see above) that may act as autocrine growth factors and on the other hand inhibit cells of the T_H1 type to progressively develop a type 2 immune response [135, 136]. While the regulatory activity of IL-4 is to a large extent related to B and T cells that are of hematopoietic origin, the effector functions of IL-13 affect primarily non-hematopoietic cells such as fibroblasts and endothelial, smooth muscle and epithelial cells. In this cellular context the effects of IL-13 are apart from helminthic infection control frequently associated with phenotypes of allergic disorders including hyperresponsiveness, inflammation and remodeling of the airway, mucus hypersecretion, goblet cell metaplasia, eosinophilia and fibrosis [64, 134]. Exaggerated type 2 immunity is indeed a key factor for the development of widespread atopic diseases, such as asthma, atopic dermatitis and allergic rhinitis. It may also be involved in uncontrolled microbial or viral infections and promote tumorigenesis and tumor cell growth by suppressing type 1 immune responses [124]. Consequently, the activity of IL-4 and IL-13 is strongly correlated with these and other type 2-related disorders as well as some cancer types rendering the IL-4/IL-13 axes attractive and promising therapeutic targets [17, 137].

1.5.2 Receptors involved in IL-4 and IL-13 signaling

The molecular basis for IL-4 and IL-13 to elicit both overlapping and individual functions was found in the unique composition of the IL-4/IL-13 receptor system. It comprises four canonical class I receptor chains, designated IL-4Rα, IL-13Rα1, common gamma-chain (γ_c) and IL-13Rα2. While IL-4Rα, IL-13Rα1 and γ_c, combine into three distinct heterodimeric signaling complexes, the role of IL-13Rα2 is hitherto ill-defined. The common gamma-chain, which is also shared by other cytokines (IL-2, IL-7, IL-9, IL-15 and IL-21), builds in conjunction with IL-4Rα the exclusively IL-4-responsive type I IL-4 receptor, whereas both IL-4 and IL-13 activate the type II IL-4 receptor that is assembled by IL-4Rα and IL-13Rα1 (Figure 7A) [53, 134]. On the contrary, IL-13Rα2 has generally been considered to act as decoy receptor, because it exhibits only a short cytoplasmic tail without common motifs involved in pathway activation, binds IL-13 with significant higher affinity than IL-13Rα1 and was shown to exist largely as an intracellular molecule in rapidly mobilizable pools [134]. However, signaling of IL-13 through IL-13Rα2 was reported to occur under certain conditions in macrophages [138]. Thus, the precise role of IL-13Rα2 remains questionable.

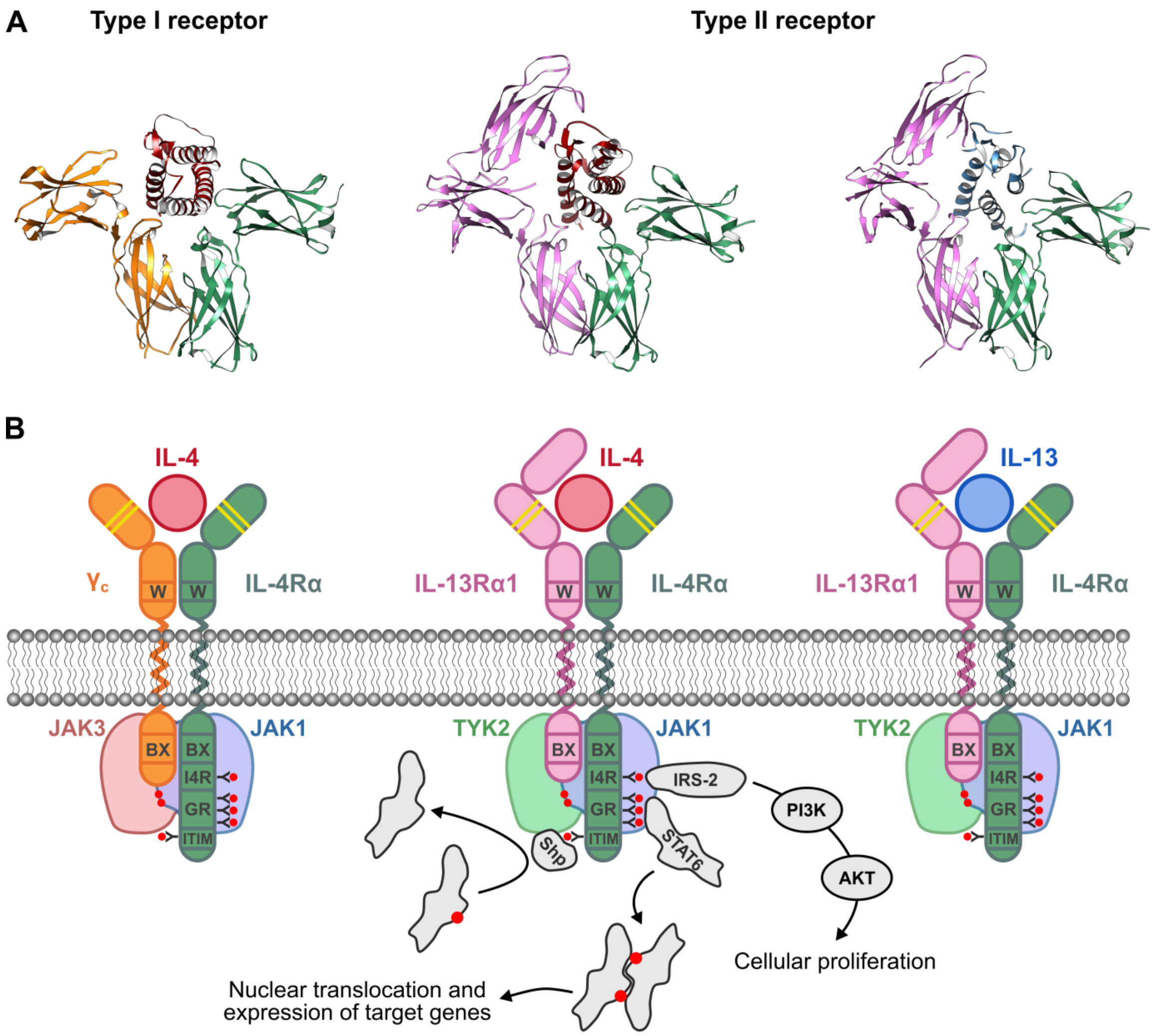

Figure 7. IL-4/IL-13 receptor system. The type I complex is assembled of γ_c and IL-4Rα receptor chains in response to IL-4. The type II complex is formed by IL-4Rα, IL-13Rα1 and either IL-4 or IL-13. Not shown: decoy receptor IL-13Rα2. **(A)** Structure comparison of extracellular parts of type I and type II IL-4 receptor complexes. **(B)** Domain structures and signaling pathways: Common WSXWS motif (W) and conserved pair of disulfide bonds (depicted in yellow) in extracellular receptor parts. Janus kinases (JAK1, JAK3, TYK2) are constitutively associated with the receptors via a “Box-1/Box-2” motif (BX). Activated JAKs phosphorylate (red dots) five tyrosine residues within I4R, “gene regulation” (GR) and ITIM domains. Recruitment of STAT6 to phosphotyrosines in the GR domain and of IRS-2 to the phosphorylated I4R motif, respectively, is followed by pathway activation via JAK-mediated STAT6/IRS-2 phosphorylation. Phosphatases (SHP) associate with the receptor via a phosphotyrosine in the ITIM region and attenuate signaling by STAT6 dephosphorylation and downregulation of JAK1 activity. Structure data in A: PDB IDs 3BPL, 3BPN, 3BPO.

The overlap of the biological effects of IL-4 and IL-13 is to a large degree explained by the shared use of the type II receptor, which is widely expressed on myeloid and non-hematopoietic cells. In contrast, the type I receptor is largely restricted to cells of hematopoietic origin accounting for the potency of IL-4 to operate in a regulatory fashion in the context of type II immunity [53, 139]. The distribution of tasks between IL-4 and IL-13 is further supported by differential spatial expression patterns of these cytokines, as the presence of IL-4 is associated with both active lymph nodes (where priming of T cell precursors takes place [140]) and infected tissue, while IL-13 is produced at sites of infection in far larger amounts than IL-4 [139]. Consequently, the functional segregation into an immunoregulatory cytokine with subordinated effector properties (IL-4) and a primary tissue effector cytokine (IL-13) despite sharing a common receptor complex (type II) is facilitated by the combination of two critical factors: first, by the presence of a second receptor complex (type I) that is exclusively utilized by IL-4 and enables for functional selectivity depending on the target cell. Second, by significant spatial differences in the expression patterns of IL-4 and IL-13.

1.5.3 Receptor structures and pathway activation

The extracellular folding topologies of the type I and type II IL-4 receptor subunits correspond to the classical structure of class I cytokine receptors including an elbow-shaped cytokine-binding homology region (CHR) consisting of tandem FNIII domains, two pairs of conserved cysteines and the WSXWS motif [53]. IL-13Rα1 contains an additional top-mounted Ig-like domain at the N-terminus required for IL-13 signaling [141]. On the intracellular side the receptor chains exhibit a quite different composition with short cytoplasmic tails in case of IL-13Rα1 and γ_c [142]. The comparably larger intracellular domain of IL-4Rα contains five conserved tyrosine residues critically involved in pathway activation and regulation. Each receptor chain moreover possesses a membrane-proximal “Box-1/Box-2” sequence required for the interaction with kinases of the JAK family of which four are linked to the IL-4/IL-13 system: IL-4Rα associates with JAK1, γ_c with JAK3 and IL-13Rα1 either with TYK2 or JAK2 (Figure 7B) [122, 134, 142].

According to the classical model (see chapter 1.3.1), activation of signaling pathways is initiated by IL-4- or IL-13-mediated crosslinking of either type I or type II receptor subunits on the extracellular side, which in turn leads to the activation of the associated JAKs in the cytoplasm by reciprocal phosphorylation. Subsequently, JAK-driven phosphorylation of the conserved tyrosine residues in the intracellular domain of IL-4Rα creates docking sites for signaling intermediates [122, 123].

The first tyrosine (Y497) is part of a so called “insulin IL-4 receptor” (I4R) motif, also found in the insulin receptor. It is necessary for recruitment of proteins of the insulin receptor substrate (IRS) family, especially IRS-2. These are phosphorylated and thereby activated by the JAKs and link the receptor to a signaling pathway particularly involved in cellular proliferation: the PI3K/Akt cascade [123].

The sequence containing the following three tyrosines (Y575, Y603 and Y631) is regarded to constitute a “gene regulation” (GR) domain, as the presence of at least one phosphorylated tyrosine residue within this section is required for the recruitment and activation of members of the family of signal transducers and activators of transcription (STAT), bridging the gap between receptor and gene transcription machinery (see JAK/STAT pathway in chapter 1.3.1) [122, 123]. Although it was shown that IL-4- or IL-13-induced signaling may include STAT1 [143], STAT3 [144] and STAT5 [145], the primary transcription factors for IL-4- and IL-13-responsive genes are STAT6 homodimers [122, 123]. STAT6 is exclusively utilized in the IL-4/IL-13 context and critically involved in numerous responses including the development and differentiation of T_H2 cells, IL-4-stimulated proliferative responses, prevention of apoptosis, immunoglobulin class switching and the expression of several cell surface molecules (e.g. CD23 and MHC II) [146].

The last tyrosine (Y713) is part of a consensus sequence designated “immunoreceptor tyrosine-based inhibitory motif” (ITIM), which is responsible for the regulation of signaling by interacting with SH2 domain-containing phosphatases such as SHP-1, SHP-2 and SHIP [122, 147]. SHP-1 as well as SHP-2 were shown to antagonize STAT6 signaling by promoting STAT6 dephosphorylation [148] or by downregulating JAK1 activity [149], while SHIP was, by contrast, reported to enhance IL-4-induced proliferation [150].

The activation cycle of the IL-4/IL-13 system further includes the expression and action of the negative feedback regulators SOCS-1, SOCS-3 and CIS-1 (see chapter 1.3.2) [151-154]. Additionally, a mechanism allowing for self-amplification of receptor activation by oxidatively inactivating the protein tyrosine phosphatase PTP1B through the generation of reactive oxygen species was described [155].

1.5.4 Binding properties and functional selectivity of natural and engineered IL-4/IL-13 variants

Like most cytokines IL-4 and IL-13 are bivalent ligands harboring a high-affinity and a low-affinity binding site, which suggests a two-step formation of IL-4- and IL-13-induced receptor complexes according to the above-mentioned generic model (see chapter 1.4.1). Sequential complex assembly was indeed confirmed for both type I [67] and type II receptors [53].

The formation of IL-4-dependent type I and type II receptors is initiated by binding of IL-4 to IL-4Rα with high affinity (K_D^B ~ 0.1 nM, [156]) followed by recruitment of either γ_c (type I, K_D^T = 3.3 µM *****) or IL-13Rα1 (type II, K_D^T = 4.2 µM *****) into a ternary complex with relatively low affinity [64]. The unique property of the type II receptor complex is a reversal in the IL-13- versus IL-4-induced assembly sequence, as IL-13 first binds to IL-13Rα1, while IL-4Rα is recruited in the second step (cf. pathway 1 vs. pathway 2 in Figure 4). With an equilibrium dissociation constant (K_D^B) of about 30 nM the affinity of IL-13 for its cognate receptor IL-13Rα1 is, however, rather low compared to the interaction of IL-4 with IL-4Rα. By contrast, the affinity of the IL-13/IL-13Rα1 complex for IL-4Rα is quite high (K_D^T = 20 nM *****) indicating more efficient type II complex formation by IL-13 compared to IL-4.

The respective compositions of these opposing three- and two-dimensional binding affinities were reported to result in similar effective cell surface binding affinities of IL-4 and IL-13 (K_D ranging from 30-400 pM) [53]. In the case of IL-13 the drastic affinity enhancement in presence of both receptor subunits was attributed to a strongly cooperative binding process, while little contribution of the low-affinity subunits to the overall affinity of IL-4 was reported [156]. However, as binding of IL-4 to γ_c or IL-13Rα1 in absence of IL-4Rα is not measurable (I. Moraga, personal communication), complex assembly by IL-4 also seems to include cooperativity analogous to other γ_c cytokines [32].

Although IL-4 and IL-13 activate the same signaling substrates via an identical type II receptor heterodimer and the effective affinity of both cytokines measured on the cell surface is similar, functional selectivity was observed with respect to substantial diverging STAT6 phosphorylation potencies and kinetics [53]. Surprisingly, the activation of STAT6 by IL-4 was found to be more than 10-fold stronger compared to IL-13 [50]. Differing amounts of IL-4Rα and IL-13Rα1 on the cell surface were proposed to provide

---

***** Note that the herein provided equilibrium dissociation constants K_D^T describing two-dimensional affinities are given as volume instead of surface concentrations due to the applied measurement approach.

a rationale for the unexpected strong signaling potency of IL-4. Owing to the very high affinity IL-4/IL-4Rα complex that assembles at low cytokine concentrations, the amount of IL-13Rα1 was identified as the limiting factor in case of IL-4 and a strong IL-4-induced response in presence of abundant IL-13Rα1 was predicted. Estimates in cell lines supported this explanation, as they revealed significantly higher numbers of IL-13Rα1 compared to IL-4Rα. In cells where IL-13Rα1 is limiting IL-13 was accordingly shown to become more potent than IL-4 [53, 63].

Also variations in complex formation kinetics were speculated to play a role in functional selectivity in the IL-4/IL-13 system [50]. Indeed, IL-4 binds to IL-4Rα with an unusual high association rate (> 10^7 M^{-1} s^{-1}) due to a highly charged interface that finds a complementarity counterpart in the CHR of IL-4Rα inducing electrostatic steering during association [157]. Binding of IL-13 to IL-13Rα1 occurs with a considerably lower rate instead [53]. The consequences that arise from these differences are, however, still unknown, because a detailed correlation of kinetics and signaling in the IL-4/IL-13 system (and in most other cytokine receptor systems) is lacking so far.

In a recently initiated research project IL-13 mutants were designed in a targeted manner to gain a library of IL-13 variants binding to IL-13Rα1 with affinities in the range of nearly six orders of magnitude [158]. These, together with IL-4 mutants introduced in another study [64], establish the type II receptor as suitable model system to systematically explore the role of three- and two-dimensional binding affinities in cytokine receptor dynamics and signaling. Two of the IL-4 variants, designated RGA and KFR, were originally engineered as type I and type II receptor-selective agonists, respectively, with the aim to develop more specific IL-4 immunotherapies with reduced side effects. Indeed, these variants were shown to induce the phosphorylation of STAT6 and IRS-1 with potencies that scaled with the expression levels of type I- and type II-related receptor subunits on different cells. Interestingly, although they were reported to exhibit substantially altered affinities towards IL-13Rα1 (RGA: 5-fold decreased, KFR: 440-fold increased) compared to wildtype IL-4, their absolute potencies did not parallel the magnitudes of their differences in second chain affinity in cells with abundant receptor levels, mirroring the apparent mismatch between affinity and potency frequently observed for cytokine receptors (see chapter 1.3.3).

1.5.5 Receptor endocytosis

Both type I and type II receptor subunits are constitutively internalized through a unique clathrin- and caveolin-independent endocytosis route, which was first described for the IL-2 receptor [105, 159-161]. According to a recently proposed working model, this particular type of receptor-mediated endocytosis includes the activity of PI3 kinase (PI3K) to indirectly regulate the Rho GTPase Rac1 via the RhoGEF Vav2. Activation of Rac1 in turn enhances the rate of actin polymerization via the Rac1-Pak1-N-WASP cascade which in conjunction with dynamin facilitates endocytosis [162].

Originally, IL-4 receptor endocytosis was linked to degradative processes, but also to a supporting function by long-term maintenance of intracellular IL-4 levels [161]. A recent study even suggested an essential role of endocytosis for IL-4 receptor-mediated signaling [160]. It originates from the assumption that the lateral affinities between the ligand-bound receptor subunits are too low for efficient dimerization in the plasma membrane at endogenous receptor surface expression levels [163]. Thus, the need of a concentration mechanism was proposed, which was found in a continuous accumulation of signaling complexes in particular endosomes tightly associated with the cell cortex (designated cortical endosomes). This model was, however, developed on the basis of fluorescence cross-correlation spectroscopy (FCCS) and fluorescence lifetime imaging microscopy (FLIM) approaches with substantially increased and therefore un-physiological receptor expression levels. It is further contradictory to the results of an earlier study, in which an elegant antibody-based approach was employed to quantify the amount of endogenous type I IL-4 receptors in a ternary complex on the cell surface revealing a striking dimerization efficiency with about 90% of IL-4-saturated IL-4Rα forming a complex with γ_c [67]. Consequently, the existence of IL-4 receptor dimers in the plasma membrane and the role of receptor endocytosis in the IL-4/IL-13 systems remain unclear.

2 Objectives and strategy

2.1 Objectives

Cytokines are key mediators of the immune system that activate cell surface receptors to control and regulate immunity and hematopoiesis. The pharmaceutical use of cytokines is, despite its enormous potential, in most cases hampered by their pleiotropic functionality, which renders cytokine-based therapies exceptionally difficult to control. There is growing evidence that the functional plasticity of cytokine receptors is largely encoded in the spatiotemporal dynamics of receptor complexes that are governed by ligand receptor binding affinities and kinetics. However, as no mechanistic correlation has hitherto been achieved, a still frequently recurring question is how cells integrate these parameters into similar patterns of early signaling outcomes, while ultimately preserving functional diversity and specificity. Two related aspects, the spatiotemporal organization and the activation mechanism of cytokine receptors in the plasma membrane, have further remained a topic of intensive and controversial debate arguing against the conclusive model of receptor activation by ligand-induced dimerization of previously separated receptor subunits.

To shed light into the mechanistic principles responsible for functional selectivity, this study aimed to establish a comprehensive quantitative correlation of cytokine receptor assembly and trafficking with effector activation and downstream signaling, focusing the link between cytokine binding affinity/kinetics, receptor dimerization efficiency and dynamics, and the functional outcome. For this purpose, the type II IL-4 receptor was taken as a model system, for which a broad spectrum of engineered agonists with varying affinities is available, while the site of receptor assembly and activation is controversially debated. To achieve a quantitative description of receptor complex assembly, a kinetic characterization of all relevant molecular interactions was performed by applying in vitro reconstitution of the receptor into solid-supported membranes. Cellular determinants were explored by probing the spatiotemporal distribution and dynamics of the receptor as well as its dimerization in the plasma membrane. To this end, single molecule localization techniques in conjunction with dedicated correlation approaches were employed and a spatial-stochastic model was implemented to clarify the role of plasma membrane microcompartmentation. Based on linking complex assembly kinetics with downstream signaling and taking endocytic uptake of receptor complexes into account, stringent differential equation-based models quantitatively predicting assembly and signaling for agonists with different binding properties were developed.

2.2 Strategy and techniques

An essential precondition for this study of the type II IL-4 receptor was a recently developed set of IL-13 and IL-4 agonists that exhibit a broad bandwidth of different binding affinities, altering the assembly and stability of either binary (IL-13 variants [158]) or ternary (IL-4 variants [64]) complexes. This library offered the unique possibility to unravel the role of equilibrium binding and interaction kinetics in the context of cytokine signaling using a well-defined and medically relevant model system with suitable intrinsic properties and comparable low complexity. A consistent experimental procedure was designed on the basis of a three-step approach comprising the following key sections that are briefly introduced below: *(i) in vitro* kinetic characterization, *(ii)* quantitative *in vivo* analysis, and *(iii) in silico* modeling.

i. The quantification of ligand-dependent kinetics, equilibrium and stability of the ternary ligand-receptor complex was performed with reconstituted extracellular domains (ECDs) of the receptor subunits on the surface of solid-supported membranes by applying a dedicated surface-sensitive detection technique, namely total internal reflection fluorescence spectroscopy reflectance interferometry (TIRFS-RIf, see chapter 2.2.1 below). For this purpose, decahistidine-tagged receptor ECDs were tethered onto the membrane by means of a lipid analogue functionalized with tris-NTA, ensuring oriented membrane anchoring and two-dimensional mobility. Thus, binding of fluorescently labeled ligands from solution to the receptor as well as and receptor assembly and disassembly in the restricted (two-dimensional) environment of a lipid membrane could be followed in real time.

ii. The spatiotemporal organization, dimerization and dynamics of IL-4Rα and IL-13Rα1 in dependence of three- and two-dimensional binding affinities were explored at physiological expression levels at the surface of HeLa cells by dual-color total internal reflection fluorescence microscopy (TIRFM, see chapter 2.2.2 below) on the single molecule level. To this end, a posttranslational labeling approach was employed, based on fusion constructs of the receptor subunits with one of two enzymatic tags: Halo-tag [164] or SNAPf-tag [165]. These are modified versions of naturally occurring enzymes that were designed to specifically and irreversibly bind their corresponding substrate (haloalkane and benzylguanine derivatives, respectively, that can be attached to an organic fluorophore), rendering them an ideal tool for orthogonal labeling of proteins with fluorescent dyes [60]. A reliable and robust quantification of receptor dimerization was accomplished by analyzing the single molecule data by means of particle image cross-correlation spectroscopy (PICCS [166]). Receptor mobility and dynamics were assessed by single molecule (co-)tracking. For the correlation of signaling outcomes with the kinetics and live cell data, the phosphorylation of STAT6, the proliferation of TF-1 cells and the differentiation of monocytes was quantified by flow cytometry.

iii. Conclusive models including and verifying the obtained and observed results were developed. Their implementation was accomplished on the basis of differential equations and stochastic processes, respectively, with a focus on the lowest achievable complexity.

2.2.1 Quantification of receptor interaction kinetics

While various convenient techniques and devices for monitoring and quantifying protein-protein interactions in solution are available (e.g. isothermal titration calorimetry, ITC; microscale thermophoresis, MST; dynamic light scattering, DLS), measuring the interaction kinetics of membrane-anchored proteins in the constrained two-dimensional environment of a lipid membrane is a challenging task. A few label-free approaches (e.g. surface plasmon resonance, SPR; quartz crystal microbalance, QCM) are established that exploit optical or acoustic phenomena for the detection of mass deposition at a surface in real time, but these have in common that both the discrimination of different molecules is not possible and interactions of molecules are not directly accessible [167]. These limitations can be overcome by combining two surface sensitive detection techniques: total internal reflection fluorescence spectroscopy (TIRFS, [168]) and reflectance interferometry (RIf, [169, 170]). TIRFS offers high sensitivity and the possibility of multicolor detection by selective excitation of fluorophores in close proximity to the surface, while an absolute quantification of surface-bound molecules can be extracted from a RIf signal, thus both techniques mutually compensate the drawbacks of the other. Additionally, by spectrally separating TIRFS and RIf detection, both signals can be acquired simultaneously in real time.

A custom-made experimental setup that was used in this work is described in detail in [167] and schematically depicted in Figure 8A. Its fully automatized syringe pump-driven fluidic system is controlled by self-written software and consists of a flow cell with a small cross-section of 0.1 µm² (volume ~300 nl) that is connected to an autosampler via a multiple valve positioner. A RIf transducer chip on the basis of a coated glass substrate, optimized to give a spectral interference pattern with an inflection point at 800 nm upon perpendicular illumination, is employed to measure the optical thickness of the interference layer (Figure 8B) by detecting the RIf signal intensity at 800 nm [171]. Binding of mass to the transducer surface increases the optical thickness of the interference layer, resulting in a shift of the interference pattern and a change of the RIf signal, which is converted into the absolute surface-bound mass [170, 172]. For TIRF an excitation laser is integrated into the system with an incidence angle suitable to obtain total internal reflection at the transducer surface, allowing evanescent wave excitation of surface-near fluorophores. The signals of fluorescence and RIf are detected simultaneously by photomultiplier tubes after passing appropriate interference filters.

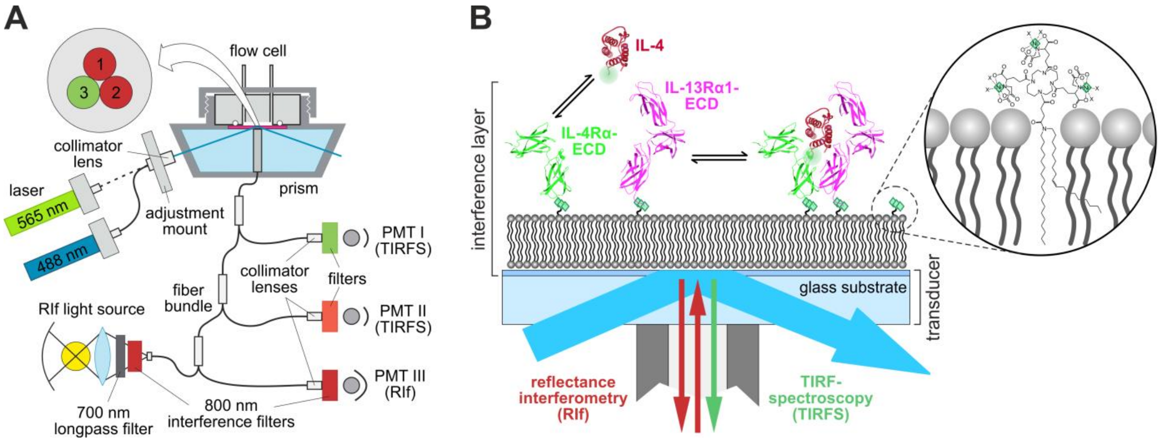

Figure 8. Scheme of the experimental setup for simultaneous total internal reflection fluorescence spectroscopy reflectance interferometry (TIRFS-RIf) detection employed to determine type II IL-4 receptor interaction kinetics. **(A)** A flow cell is mounted onto a glass substrate-based RIf transducer chip. For fluorescence excitation close to the surface one of different lasers (488 nm or 532 nm) is coupled into the system via a prism resulting in total internal reflection at the RIf transducer. Single fibers of a fiber bundle (cross-section depicted in inset) that is coupled to the transducer by running through a central bore of the prism are used for fluorescence detection (3) in the full visible region and for RIf illumination (1) and RIf detection (2) in the near infrared. After passing appropriate filters the fluorescence and RIf intensity is measured with photomultiplier tubes (PMT). Figure adapted from [167]. **(B)** Solid-supported lipid bilayer on a RIf transducer chip (coated glass substrate). The lipid mixture includes a chelator lipid (tris-NTA-SOA, inset) for oriented anchoring of histidine-tagged receptor ECDs with two-dimensional mobility in the plane of the membrane. The RIf signal (dark red) reports on the optical thickness of the interference layer, which is increased by mass binding to the surface, while fluorophores in close proximity to the surface are excited by TIR-illumination (blue arrow).

For the measurement of protein interactions in the plane of a membrane, the RIf transducer additionally serves as solid-support for a lipid bilayer, which is created by injection of small unilamellar vesicles (SUVs) directly on the transducer surface. The lipid mixture of the SUVs includes a lipid-like molecule carrying a multivalent chelator head group (tris-nitrilotriacetic acid fused to stearoyl-octadecylamine, tris-NTA-SOA). This allows for oriented and stable, yet reversible tethering of histidine-tagged proteins (e.g. receptor ectodomains) to the membrane, while two-dimensional mobility of the membrane-anchored proteins is ensured (Figure 8B) [167, 173]. Moreover, it offers an easy way to control the surface concentration of the proteins, which is critical for a reliable determination of kinetic parameters.

Taken together the here described experimental setup constitutes a well-defined model system with a highly sensitive two-way detection concept for kinetic analyses of ligand-receptor and receptor-receptor interactions in the plane of a lipid membrane. By applying suitable ligand chasing experiments and FRET-based approaches with fluorescently labeled ligands and receptor ectodomains, respectively, it allows to specifically determine all intrinsic kinetic rate constants and binding affinities of the examined receptor system (cf. Figure 4). It therefore provided an ideal environment for the characterization of type II IL-4 receptor kinetics and dynamics *in vitro*.

2.2.2 Single molecule imaging of receptor subunits and ligands

As described by Abbe’s well-known equation, the optical resolution in microscopy in the visible spectrum is limited to approximately 200 nm in the lateral dimension by the diffraction of light [174]. However, several recently developed approaches like stimulated emission depletion microscopy (STED, [175]), structured illumination microscopy (SIM, [176]), fluorescence photo-activation localization microscopy (FPALM, [177]) or stochastic optical reconstruction microscopy (STORM, [178]), overcome the so-called diffraction limit with different subtle tricks, yielding a resolution in the range of up to a few nanometers.

FPALM and STORM belong to a class of microscopical techniques termed single-molecule localization microscopy (SMLM). Within this group the resolution enhancement is achieved by an image-processing step, which exploits the typical blurred projection pattern (airy disk) of a point-like fluorescent emitter in wide field microscopy [179]. The intensity distribution of this pattern, called point spread function (PSF), approximately follows a two-dimensional Gaussian function [180]. Thus, the molecule position is determinable by fitting-algorithms with nanometer precision, which is virtually only limited by the background-subtracted intensity of the PSF (i.e. depends on the number of collected photons of the fluorophore) [181]. But, according to the Rayleigh criterion, the minimum distance at which two single molecules can be distinguished, is dictated by the wavelength-dependent dimensions of the airy disk and has to be greater than the full width at half-maximum (FWHM) of the PSF [182, 183]. SMLM therefore strongly depends on the emitter density and their spatial separation. Consequently, the idea behind FPALM and STORM is to reduce the amount of simultaneously emitting fluorophores in a stochastic process [179], which enables for sequential detection of single emitters.

A still frequently used technique has been proven to be exceptionally useful for single molecule imaging of fluorescently labeled probes in the membrane of living cells: total internal reflection fluorescence microscopy (TIRFM, [184]). Owing to evanescent field excitation it enables to selectively excite fluorophores on target molecules in or at the basal plasma membrane of cells grown adherently on a glass cover slip. Thus, the exposure of cells to light at other planes in the sample is minimized, which provides a significant reduction of background fluorescence [185]. Together with the possibility of multicolor excitation and detection, TIRFM is particularly well suited to visualize and study the spatiotemporal organization and dynamics of single receptor molecules with low abundance (less than 1-2 molecules/μm^2) in the plasma membrane, as recently shown for the type I IFN receptor [60]. In combination with a highly photon-sensitive and fast camera, full images can be acquired in milli- or even microseconds, which is key to reduce motion blurring and thus enable the investigation of single molecule motion and dynamics by single molecule tracking (SMT) [186-188]. A qualified experimental setup implementing dual-wavelength fluorescence excitation in TIR-mode and simultaneous two-channel detection was used in this work and is schematically illustrated in Figure 9 (see also materials and methods section for further details).

For effective tracking of single molecules, bright and stable fluorophores with preferably continuous emission are necessary. Recent findings showed that the combination of photostable organic dyes (like tetramethylrhodamine, TMR or cyanine dyes, e.g. Cy5/DY-647) with an orthogonal protein labeling approach by enzymatic tags (like Halo-tag [164] or SNAPf-tag [165], Figure 10) provides ideal prerequisites for localizing and tracking single cytokine receptor subunits in the plasma membrane of living cells [60]. Accordingly, receptor labeling with TMR and DY-647 via the Halo- and the SNAPf-tag, respectively, was applied in this project.

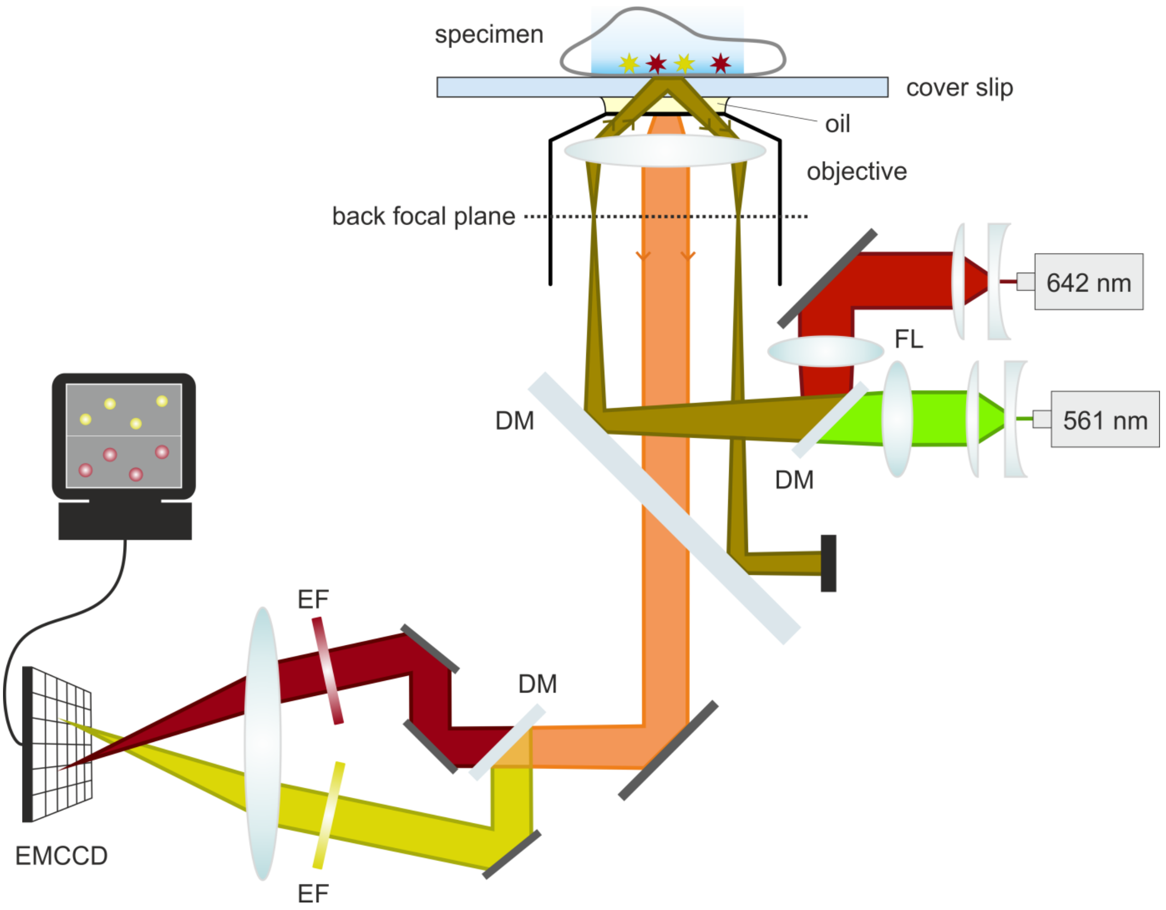

Figure 9. Scheme of the experimental setup employed for simultaneous dual-color total internal reflection fluorescence microcopy (TIRFM) of live cells on the single molecule level. Both a green (λ 561 nm) and a red (λ 642 nm) laser line are focused on the back focal plane of a high numerical aperture objective (NA≥1.45), which collimates the emanating light so that the entire light beam reaches the specimen-holding glass cover slip in the same angle. This angle is adjustable by changing the positions of the laser focusing lenses (FL). Since the light propagates through media with different refractive indices (RI) – the glass cover slip exhibits a higher RI than the water-based solution surrounding the specimen – it is totally internally reflected at the glass/water interface upon reaching the critical angle. In this case, however, a fraction of the light intensity enters the specimen solution as a so-called evanescent wave with a strong distance-dependent exponential intensity decay [184]. Only fluorophores in close proximity to the cover slip are selectively excited. Emitted fluorescence passes a dichroic mirror (DM) that separates excitation from emission light and is spectrally divided by a second DM. Both fluorescence channels are simultaneously imaged by their projection on different regions of an EMCCD camera after passing suitable emission filters (EF) for further improvement of spectral selectivity. Image stacks with a size of 512x512 pixel (0.107 µm/pixel, 512x256 pixel for each channel) are acquired with a frequency of 31.25 Hz or a lag-time of 32 ms, respectively. Figure adapted from [189].

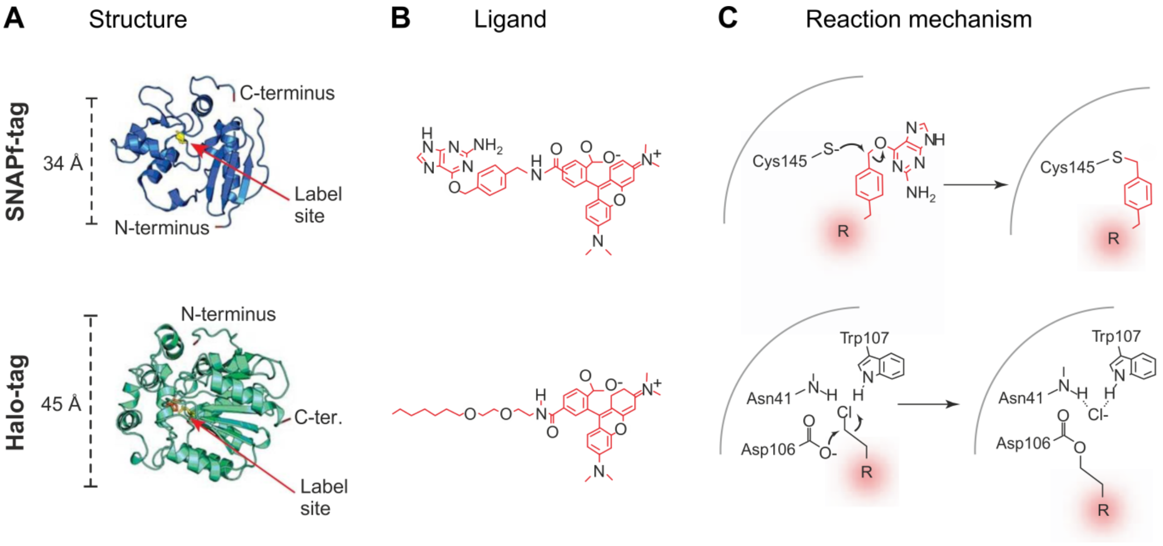

Figure 10. Orthogonal protein labeling by specialized enzymatic tags. (A) Structures and sizes of SNAPf-tag (top) and Halo-tag (bottom), which are modified versions of naturally occurring enzymes that were designed to specifically and irreversibly bind their individual substrate (benzylguanine and haloalkane derivatives, respectively). **(B)** Example structures of appropriate fluorescent ligands: Benzylguanine-linked TMR for SNAPf-tag labeling (top) and haloalkane-linked TMR for Halo-tag labeling (bottom). **(C)** Corresponding molecular reaction mechanisms taking place for covalent ligand attachment. Adapted from [190] with permission from Elsevier.

With this practice and careful data evaluation, diffusing receptor chains labeled with spectrally distinguishable fluorescent dyes can be localized in each image frame (Figure 11A) with an average precision of about 25 nm, like described above. Subsequently their positions are filtered to exclude immobile particles and readily linked over time by smart algorithms [191, 192] to yield a picture of the underlying the movement, called trajectory (Figure 11B). Both the localization and trajectory data contain valuable information, which is extractable by different evaluation methods: apart from building trajectories of the positional data, by cross-correlating the molecule positions in both channels, a robust quantification of the fraction of molecules that are spatiotemporally correlated (e.g. dimerized receptor subunits) can be achieved (Figure 11C). Further, by following the intensity trace of single fluorophores, clustering of molecules can be either excluded or proven, depending on whether irreversible photobleaching of the dyes occurs in one or more steps (Figure 11D). Moreover, filtering for molecules that are co-localized in both channels allowing a maximum fixed inter-particle distance yields a sub-dataset, from which co-locomotion trajectories can be generated (Figure 11B). These in turn, like common trajectories, are the starting point for diffusion analyses by fitting step length distributions or mean-squared displacement (MSD) plots (Figure 11E). A detailed description of the application of these evaluation techniques on single molecule data can be found in the materials and methods section.

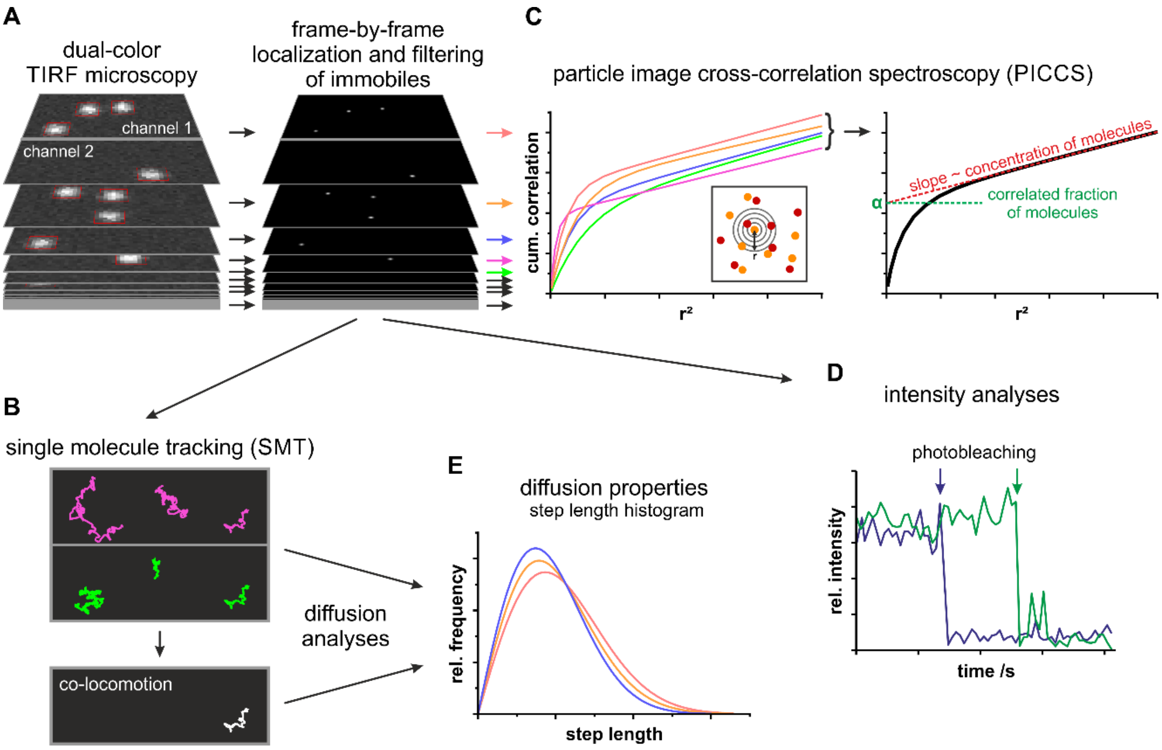

Figure 11. Scheme of the single molecule microscopy data acquisition and evaluation sequence containing dual color imaging, single molecule localization, (co-)tracking, spatial correlation and intensity and diffusion analyses. **(A)** Individual molecules detected in each frame are localized by fitting to a two-dimensional Gaussian function. **(B)** Molecules in each spectral channel are filtered for immobiles, tracked separately (pink and green trajectories) and co-tracked in order to identify receptor heterodimers. **(C)** The amount of ternary complexes is quantified by particle image cross-correlation spectroscopy of the localized particles in both channels. **(D)** Single particle intensity traces are evaluated to identify or exclude (single step bleaching) receptor clustering. **(E)** The mobility of individual receptor subunits and complexes is analyzed by a histogram of the step lengths extracted from the trajectories or by MSD analyses (not shown).

3 Materials and methods

3.1 Expression, purification and labeling of IL-4/IL-13 variants and IL-4Rα/IL-13Rα1 extracellular domains

The IL-4 mutants KFR and RGA and all IL-13 mutants used in this work were originally engineered in the research group of K. Cristopher Garcia (Stanford University School of Medicine) and are described in detail in [64, 158].

For ligand binding studies and TIRFS-RIf experiments, all IL-4 and IL-13 variants were fused to an N-terminal ybbR-tag (sequence: DSLEFIASKLA,) that allows for site-specific labeling by enzymatic phosphopantetheinyl transfer (PPT) [193].

pET-28b expression vectors (Novagen) encoding for ybbR-tagged human IL-4 with H59Y and H59Y K84D mutations, respectively, were provided by Thomas D. Müller (Biocenter University of Würzburg) and taken as template for other IL-4 agonists (Table 1, lower part). Further mutations were introduced by standard PCR with appropriate primers. Expression of the ybbR-tagged IL-4 variants in 2 l cultures of *E. coli* Rosetta grown at 37°C was induced by 1 mM IPTG (Sigma-Aldrich) using standard protocols. Inclusion bodies (IB) were isolated by centrifugation and purified by extensive washing steps after cell lysis via sonification. Unfolded protein was extracted from IBs with Guanidine hydrochlorid/β-Mercaptoethanol (Sigma-Aldrich). Refolding was carried out by dialysis against phosphate-buffered saline (PBS; 120 mM NaCl, 2 mM KCl, 3 mM NaH_2PO_4, 7 mM Na_2HPO_4, pH 7.0) using a volume >200-times greater than the sample volume. Refolded IL-4 variants were purified by cation exchange chromatography utilizing High-Performance SP-Sepharose (HiTrap SP HP 5 ml, GE Healthcare) employing a linear NaCl-gradient from 0 M to 1 M at pH 7.0 (20 mM phosphate buffer). Pooled fractions were further purified by size exclusion chromatography (SEC) on a HiLoad 16/60 Superdex 75 column (GE Healthcare) equilibrated with PBS (pH 7.4).

Coding sequences for all IL-13 variants (tagless and ybbR-tagged, Table 2), and tagless IL-4 wt, IL-4 KFR and IL-4 RGA (Table 3) were cloned into the pAcGP67-A vector (BD Biosciences) in frame with an N-terminal gp67 signal sequence and a C-terminal hexahistidine tag. For protein production the baculovirus expression system was used [194]. Baculovirus stocks were prepared by transfection and amplification in *Spodoptera frugiperda (Sf9)* cells grown in SF900II media (Invitrogen). Protein expression was performed in *Trichoplusia ni* (High Five^{TM}) suspension cells grown in Insect-Xpress media (Lonza). Proteins were captured from High Five^{TM} cell culture medium by nickel-nitrilotriacetic acid (Ni-NTA) agarose (Qiagen) affinity chromatography 60 hours after induction of expression, concentrated and purified by SEC on a Superdex 200 column (GE Healthcare), and equilibrated in 10 mM HEPES (pH 7.2) containing 150 mM NaCl. Proteins were expressed fully glycosylated in High Five$^{\text{TM}}$ cells, as estimated from Coomassie-stained SDS–polyacrylamide gel electrophoresis analysis (data not shown).

Extracellular domains (ECD) of IL-13Rα1 (residues 29-344) and IL-4Rα (residues 27-232) fused to N-terminal ybbR-tags and C-terminal decahistidine tags (ybbR-IL-13Rα1-ECD-H10 and ybbR-IL-4Rα-ECD-H10, respectively) were provided by Thomas D. Müller (Table 3). Cloning, expression in High Five$^{\text{TM}}$ insect cells and purification are described in [195].

Site-specific labeling via the ybbR-tag was carried out by means of Sfp phosphopantetheinyl transferase using self-made coenzyme A (CoA)-DY647, CoA-Alexa Fluor 568, CoA-Atto 488 or CoA-OregonGreen 488 conjugates according to published protocols [196] (required maleimide functionalized dyes were purchased from Dyomics). After labeling, the proteins were purified by SEC on a HiLoad 10/300 Superdex 75 column (GE Healthcare). A degree of labeling (DOL) >90% was obtained as determined by UV/Vis spectroscopy for all ybbR-tagged proteins.

Table 1. Overview of generated and used IL-4 variants. Numbering of mutated amino acids (AA) refers to the mature form without the N-terminal signal sequence. IL-4 variants generated for the present work are marked with an asterisk (*). Sequence data from [64, 197].

Variant/AA		59	84	117	118	121	122	124	125	128	129
IL-4 wt		H	K	K	T	R	E	Y	S	S	S
H59Y		Y									
H59Y K84D		Y	D								
KFR						K		F	R		
RGA				R	V	Q	S	W	F	G	A
H59Y KFR	*	Y				K		F	R		
H59Y RGA	*	Y		R	V	Q	S	W	F	G	A
H59Y DN	*	Y				D		D			
H59Y K84D KFR	*	Y	D			K		F	R		
H59Y K84D RGA	*	Y	D	R	V	Q	S	W	F	G	A
H59Y K84D DN	*	Y	D			D		D			

Table 2. Overview of used IL-13 variants. Numbering of mutated amino acids refers to the mature form without the N-terminal signal sequence. Sequence, kinetics and affinity data from [158].

Var./AA	10	11	12	18	65	86	87	88	89	101	104	105	108	k_{on} ($M^{-1}s^{-1}$)	k_{off} (s^{-1})	K_D (nM)
IL-13 wt	L	R	E	V	R	R	D	T	K	L	K	K	R	$5.21 \cdot 10^6$	0.022	4.4
A11	V			I			S	S		F	R	T		$1.64 \cdot 10^7$	0.0013	0.084
B2				I		T	G	S		Y	R	A		$6.30 \cdot 10^6$	0.0017	0.28
A7	I			I			G	S		H	R	A		$2.90 \cdot 10^6$	0.0034	1.2
A8	I			I			S	S	R	H	R	T		$1.64 \cdot 10^6$	0.0033	2.1
B6	T			I			G	S	K	Y	R	T		$1.40 \cdot 10^6$	0.0082	5.9
B4		S		I		K	G	S	M	Y	R	T		$1.36 \cdot 10^6$	0.024	18
C10	H	L		I		M			R				K	-	-	264
D7	A			F		K	K		R	I	R		K	-	-	4,100
C3	A					T	G	K	R	N	R	A	K	-	-	16,000
C4	V								R	N		E	T	-	-	36,000
DN	V		A	I	D		S	S		F	R	T		$1.64 \cdot 10^7$	0.0013	0.084

Table 3. Tagging and experimental usage of recombinant ligand and receptor proteins. Categorization: A) ligand binding experiments (TIRFM), B) receptor dimerization experiments (TIRFM), C) *in vitro* kinetic studies (TIRFS-RIf), D) flow cytometry.

Variant	Designation	Experimental usage	Expressed in
ybbR-tagged			
IL-13 wt	IL-13	A, C	*High Five™*
IL-13 D7	D7	A	*High Five™*
IL-4 H59Y	IL-4	A, C	*E. coli*
IL-4 H59Y KFR	KFR	A, C	*E. coli*
IL-4 H59Y RGA	RGA	A, C	*E. coli*
IL-4 H59Y DN	DN4	A, B	*E. coli*
IL-4 H59Y K84D	IL-4$_D$	C	*E. coli*
IL-4 H59Y K84D KFR	KFR$_D$	C	*E. coli*
IL-4 H59Y K84D RGA	RGA$_D$	C	*E. coli*

Variant	Designation	Experimental usage	Expressed in
ybbR-tagged			
IL-4 H59Y K84D DN	DN4$_D$	C	*E. coli*
IL-13Rα1-ECD-H10	IL-13Rα1-ECD	C	*High Five*^{TM}
IL-4Rα-ECD-H10	IL-4Rα-ECD	C	*High Five*^{TM}
tagless			
IL-13 wt	IL-13	B, D	*High Five*^{TM}
IL-13 A11	A11	B, D	*High Five*^{TM}
IL-13 B2	B2	B, D	*High Five*^{TM}
IL-13 A7	A7	B, D	*High Five*^{TM}
IL-13 A8	A8	B, D	*High Five*^{TM}
IL-13 B6	B6	B, D	*High Five*^{TM}
IL-13 B4	B4	B, D	*High Five*^{TM}
IL-13 C10	C10	B, D	*High Five*^{TM}
IL-13 D7	D7	B, D	*High Five*^{TM}
IL-13 C3	C3	B, D	*High Five*^{TM}
IL-13 C4	C4	B, D	*High Five*^{TM}
IL-13 DN	DN13	B, D	*High Five*^{TM}
IL-4 wt	IL-4	B, D	*High Five*^{TM}
IL-4 KFR	KFR	B, D	*High Five*^{TM}
IL-4 RGA	RGA	B, D	*High Five*^{TM}

Table 4. Conjugates used for protein labeling.

Variant	Dye	Designation
ybbR-IL-13 wt	CoA-DY647	^{DY647}IL-13
ybbR-IL-13 wt	CoA-OregonGreen 488	^{OG488}IL-13
ybbR-IL-13 D7	CoA-DY647	^{DY647}D7
ybbR-IL-4 H59Y	CoA-DY647	^{DY647}IL-4
ybbR-IL-4 H59Y KFR	CoA-DY647	^{DY647}KFR

Variant	Dye	Designation
ybbR-IL-4 H59Y RGA	CoA-DY647	^{DY647}RGA
ybbR-IL-4 H59Y DN	CoA-DY647	^{DY647}DN4
ybbR-IL-4 H59Y K84D	CoA-Atto 488	^{AT488}IL-4$_D$
ybbR-IL-4 H59Y K84D KFR	CoA-Atto 488	^{AT488}KFR$_D$
ybbR-IL-4 H59Y K84D RGA	CoA-Atto 488	^{AT488}RGA$_D$
ybbR-IL-4 H59Y K84D DN	CoA-Atto 488	^{AT488}DN4$_D$
ybbR-IL-13Rα1-ECD-H10	CoA-Alexa Fluor 568	^{AF568}IL-13Rα1-ECD

3.2 Quantification of kinetics by simultaneous TIRFS-RIf detection

The binary and ternary complex interaction kinetics of the IL-4 variants and IL-13 with IL-4Rα and IL-13Rα1 were determined by simultaneous total internal reflection fluorescence spectroscopy (TIRFS) and reflectance interference (RIf) detection in a home-built setup including a flow system (cf. chapter 2.2.1), as described in detail in [167, 171]. All experiments were performed at 25°C using HEPES-buffered saline (HBS: 20 mM HEPES, 150 mM NaCl, pH 7.5), which was complemented with 30 mM Imidazole to minimize unspecific binding of ligands to free chelator lipids. After mounting a freshly plasma-cleaned RIf transducer into the flow cell, a solid supported membrane (SSM) was generated by injection of small unilamellar vesicles (SUV), which were prepared by sonication of 250 µM 1,2-dioleoyl-sn-glycero-3-phosphocholine (DOPC, Avanti Polar Lipids) containing 1 mol% tris-nitrilotriacetic acid-stearoyl-octadecylamin (tris-NTA-SOA, [173]). The SSM was then sequentially washed with 500 mM Imidazole in HBS and 250 mM EDTA in HBS. Finally, 10 mM $NiCl_2$ in Imidazole-free HBS was injected to load the tris-NTA head groups with Ni^{2+}, creating membrane associated binding sites for decahistidine-tagged receptor ectodomains.

The following steps were dependent on the rate constant to be measured and are described in the corresponding section. After each experiment, all attached proteins were removed by injecting 500 mM Imidazole in HBS to recover the membrane for the next measurement and to check the integrity of the bilayer.

Please note that because IL-4 wt carries a histidine residue at position 59 that promotes non-specific binding to the membrane via the complexed Ni(II)-ions, all IL-4 variants used in this assay exhibit a H59Y mutation. This mutation has no effect on interaction kinetics or activity and is for clarity reasons not explicitly indicated in the following. Additionally, the mutation K84D (indicated by the subscript D) was introduced in order to increase the dissociation rate constant of the IL-4/IL-4Rα complex to a similar level as of the IL-13/IL-13Rα1 complex and to decrease the association rate constant to eliminate mass transport-limited association and strong rebinding during dissociation that was observed for IL-4 wt, thus ensuring unbiased analyses of ligand dissociation curves. The interaction with IL-13Rα1 is not affected by this mutation as the corresponding binding interface is unaltered, making this mutant suitable for probing the K_D^T of IL-13Rα1 recruitment into the ternary complex.

Data were analyzed using Origin 9.1 (OriginLab Corp.), Biaevaluation 3.1 (Biacore) or Berkeley Madonna 8.3 (UCB, Berkeley, CA).

3.2.1 Measurement of binary complex (3D) kinetics

The decahistidine-tagged ectodomain of IL-4Rα (IL-4Rα-ECD) or IL-13Rα1 (IL-13Rα1-ECD) was injected for binding to the solid-supported membrane and to obtain surface concentrations of 1-1.5 fmol/mm². Then, decahistidine-tagged Maltose-binding protein (MBP) [173] was injected to block free chelator lipids. After loading the receptors and MBP to the membrane, 50-100 nM of the respective ^{AT488}IL-4$_D$ variant or ^{OG488}IL-13 was injected. Subsequently, the dissociation of the fluorescently labeled ligand from the surface was monitored during rinsing for 600 s with HBS at a flow rate of 10 µl/s.

Binding of IL-4$_D$ variants to IL-4Rα and of IL-13 to IL-13Rα1, respectively, was fitted with Biaevaluation using a standard pseudo first order kinetic model [198]:

Association: $$R(t) = R_{eq}\left(1 - e^{-(k_a^B \cdot c + k_d^B)\cdot(t - t_0)}\right) \qquad \textbf{Eqn. 1}$$

Dissociation: $$R(t) = R_0 \cdot e^{-k_d^B \cdot (t - t_0)} \qquad \textbf{Eqn. 2}$$

$R(t)$ is the signal at time t, R_{eq} is the equilibrium signal, R_0 is the signal at $t = t_0$, k_a^B and k_d^B are the binary complex association and dissociation rate constants, respectively, and c is the ligand concentration.

The binary complex equilibrium dissociation constant K_D^B (3D binding affinity) was determined from the binary complex association and dissociation rate constants of the interaction according to the familiar equation:

$$K_D = \frac{k_d}{k_a} \qquad \textbf{Eqn. 3}$$

3.2.2 Measurement of ternary complex (2D) kinetics

A. Ternary complex dissociation rate constant: k_d^T

In order to determine the ternary complex dissociation rate constant k_d^T re-association of the binary complex IL-13Rα1-ECD/IL-13 with IL-4Rα-ECD or IL-4Rα-ECD/IL-4 with IL-13Rα1-ECD (corresponding to k_a^T), respectively, was suppressed [85]. This was achieved by ligand displacement (chasing) using non-labeled IL-4 that binds to IL-4Rα with sub-nanomolar affinity and requires an IL-4Rα-ECD to IL-13Rα1-ECD surface concentration ratio of at least 5-10:1. Free IL-4Rα-ECD produced upon ternary complex dissociation is bound by IL-4 and therefore unavailable to re-associate into a ternary complex with a labeled ligand that as a result dissociates from the surface.

A-1. IL-13 (ligand displacement assay)

IL-4Rα-ECD and IL-13Rα1-ECD were injected for binding to the solid-supported membrane and to obtain surface concentrations with a 10:1 ratio of IL-4Rα-ECD and IL-13Rα1-ECD. Following ternary complex formation with 75 nM ^{OG488}IL-13, injection of 1 µM IL-4 was used to suppress the re-association of ^{OG488}IL-13 into ternary complexes and the dissociation of the fluorescently labeled ligand from the surface was monitored during rinsing for 600 s with HBS at a flow rate of 10 µl/s.

During chasing the rate of ^{OG488}IL-13 dissociation is dependent on k_d^T and k_d^B alone. Since the dissociation of the ternary complex is the rate limiting step in case of IL-13, fitting a single exponential decay to the dissociation curve measured during IL-4 injection allowed the direct determination of k_d^T.

A-2. IL-4 mutants (ligand displacement & FRET assay)

As IL-4 dissociates with a remarkably slow rate from binary complexes and the ternary complex dissociation is rather fast in case of IL-4, the ligand displacement assay had to be extended by a Förster resonance energy transfer (FRET) approach to directly visualize the ternary complex dissociation via decreasing FRET between labeled ligands and IL-13Rα1-ECDs.

IL-4Rα-ECD and ^{AF568}IL-13Rα1-ECD were injected for binding to the solid-supported membrane and to obtain surface concentrations with a 1:1 ratio of both receptors. Then, 50-100 nM of the respective ^{DY647}IL-4 variant was injected resulting in FRET between Alexa568 (donor) and DY647 (acceptor). Additional tethering of excess IL-4Rα-ECD was performed to offer binding sites for the subsequent ligand displacement by injection of 1 µM unlabeled IL-4. Rapid exchange of ligands in ternary complexes leads to a loss in FRET and therefore a donor fluorescence recovery whose rate correlates with the ternary complex dissociation rate. The donor fluorescence recovery curve was fitted to a single exponential decay to obtain k_d^T and was compared to the corresponding RIf-signal to check whether chasing was limited by mass transport/association kinetics.

B. Ternary complex association rate constant k_a^T and equilibrium dissociation const. K_D^T

IL-4Rα-ECD and IL-13Rα1-ECD were injected for binding to the solid-supported membrane and to obtain surface concentrations of 1-1.5 fmol/mm^2 with a 1:1 ratio of both receptors. Then, decahistidine-tagged MBP was injected to block free chelator lipids. After loading the receptors and MBP to the membrane, 50-100 nM of the respective ^{A488}IL-4$_D$ variant or ^{OG488}IL-13 was injected. Subsequently, the dissociation of the fluorescently labeled ligand from the surface was monitored during rinsing for 900 s with HBS at a flow rate of 10 µl/s.

The ternary complex association rate constant k_a^T was determined from the ligand dissociation kinetics, which reports on the equilibrium between binary and ternary complexes as detailed in [171]. To this end, the ligand dissociation curves were fitted numerically with Berkeley Madonna using the following set of differential equations based on a two-step assembly/disassembly model:

$$\frac{d[T]}{dt} = k_a^T \cdot [B] \cdot ([R] - [T]) - k_d^T \cdot [T] \qquad \textbf{Eqn. 4}$$

$$\frac{d[B]}{dt} = k_d^T \cdot [T] - k_a^T \cdot [B] \cdot ([R] - [T]) - k_d^B \cdot [B] \qquad \textbf{Eqn. 5}$$

$$[S] = [T] + [B] \text{ with } [T]_{t=0} = [R] \text{ and } [B]_{t=0} = [0] \qquad \textbf{Eqn. 6}$$

$[S]$ is the total surface concentration of labeled ligand measured in a time-resolved manner by the TIRFS signal and converted into an absolute concentration via calibration with RIf. $[T]$ and $[B]$ are the ternary and binary complex surface concentrations, respectively. $[R]$ is the IL-13Rα1-ECD (for IL-4 experiments) or IL-4Rα-ECD (for IL-13 experiments) surface concentration, measured by RIf. k_a^T and k_d^T are the ternary complex association and dissociation rate constants, respectively, and k_d^B is the binary complex dissociation rate constant. The curves were fitted keeping k_d^T and k_d^B fixed at the experimentally determined values before. Then, the ternary complex equilibrium dissociation constant K_D^T (2D binding affinity) was determined from the association and dissociation rate constants of the interaction according to equation 3.

Since k_d^T could not be measured for KFR and RGA with the FRET assay, K_D^T of KFR$_D$ and RGA$_D$ was estimated by fitting the ligand dissociation curves keeping k_a^T fixed at the value determined for IL-4$_D$.

3.3 Expression vectors for tagged receptor subunits

For the expression of tagged receptor subunits in HeLa cells, a modified version of the mammalian expression vector pSEMS1-26m (NEB, former Covalys Biosciences) was used. It contains the human cytomegalovirus (CMV) promotor and a Neomycin or Puromycin resistance cassette, respectively, that is linked to the open reading frame (ORF) via an internal ribosomal entry site (IRES), thus enabling a robust transient and stable expression of inserted genes.

A pDisplay vector (Invitrogen) including an ORF that consists of an N-terminal murine Ig κ-chain leader sequence followed by a HaloTag [164] sequence and the gene of full length human IL-13Rα1 without its native N-terminal signal sequence was generated and provided by Ignacio Moraga. The leader sequence targets the protein to the secretory pathway [199] displaying the tagged receptor efficiently on the cell surface. The complete ORF was transferred into the pSEMS1-26m Neomycin vector yielding the plasmid construct pSEMS-neo HaloTag::IL-13Rα1 used for most single molecule experiments.

The gene of full length human IL-4Rα lacking its native N-terminal signal sequence was cloned from a self-made HeLa cell cDNA library and inserted into a pDisplay vector at the C-terminus of a Ig κ-chain leader sequence followed by a SNAPf-tag [165, 200, 201] sequence (NEB). The resulting ORF was transferred into the pSEMS1-26m Puromycin vector yielding the plasmid construct pSEMS-puro SNAPf::IL-4Rα that was used for most single molecule experiments.

Table 5. Overview of generated and utilized expression vectors.

Vector	Promoter	Features & tags	Resistances
pSEMS-neo HaloTag::IL-13Rα1	CMV	Ig κ-chain leader sequence HaloTag	Neo^r Amp^r
pSEMS-puro SNAPf::IL-4Rα	CMV	Ig κ-chain leader sequence SNAPf-tag	$Puro^r$ Amp^r
pSEMS-neo His10::SNAPf::IL-13Rα1	CMV	Ig κ-chain leader sequence SNAPf-tag & His10-tag	Neo^r Amp^r
pSEMS-neo His10::SNAPf::IL-4Rα	CMV	Ig κ-chain leader sequence SNAPf-tag & His10-tag	Neo^r Amp^r
pWHE655-neo TREtight HaloTag::IL-13Rα1	TREtight	Ig κ-chain leader sequence HaloTag	Neo^r Amp^r
pWHE644	EF1α	Tet transsilencer tTS^D-PP Tet transactivator $rtTA2^S$-M2	$Puro^r$ Amp^r

A Tetracycline (Tet)-regulated inducible gene expression system was kindly provided by Christian Berens and adapted to this project. It comprises a regulatory vector, pWHE644, and a vector to incorporate the target gene, pWHE655, containing a Neomycin resistance and a multiple cloning side whose expression is controlled by the TREtight promoter [202]. The regulatory element of pWHE644-puro consists of a tricistronic transregulator cassette for the simultaneous expression of the Tet trans-silencer tTS^{D}-PP and the reverse Tet transactivator rtTA2^{S}-M2, linked to a Puromycin resistance. In the absence of Doxycycline tTS^{D}-PP effectively suppresses expression by binding to the TREtight promoter, whereas addition of the Tetracyline derivative leads to the release of tTS^{D}-PP and the association of rtTA2^{S}-M2 that induces moderate target gene expression.

The ORF of pSEMS-neo HaloTag::IL-13Rα1 was transferred into the pWHE655-neo vector as inducible target gene to yield the plasmid construct pWHE655-neo TREtight HaloTag::IL-13Rα1 that was used for those single molecule experiments in which explicitly low surface concentrations of tagged IL-13Rα1 were needed.

For the expression of transmembrane-only receptor subunits in HEK 293T cells, DNA constructs of receptors truncated after their transmembrane domains, IL-13Rα1Δ369-427 (IL-13Rα1-TM) and IL-4RαΔ258-825 (IL-4Rα-TM), were generated from full-length receptor constructs and individually inserted into the pSEMS-neo His10::fSnap::IFNAR2 vector [203] to finally obtain pSEMS-neo His10::SNAPf::IL-13Rα1-TM and pSEMS-neo His10::SNAPf::IL-4Rα-TM, respectively.

All plasmid constructs (summarized in Table 5) were generated using standard cloning protocols and verified by sequencing.

3.4 Cell culture and labeling of receptor subunits in live cells

HeLa cells were cultivated at 37°C and 5% CO_2 in MEM with Earle’s salts, stable glutamine and phenol red (Biochrom AG) supplemented with 10% fetal bovine serum (FBS, Biochrom AG), 1% non-essential amino acids (PAA laboratories GmbH) and 1% 2(4-(2-hydroxyethyl)-1-piperazineethanesulfonic acid (HEPES, PAA laboratories GmbH) buffer without addition of antibiotics.

For microscopy experiments, 20 mm glass coverslips (VWR) were coated with a poly-L-lysine-graft-(polyethylene glycol) (PLL-PEG) copolymer functionalized with RGD [204] [19] to minimize the fluorescent background arising from non-specifically adsorbed dye molecules. Cells were plated on the coverslips in 35 mm cell-culture dishes (Greiner

Labortechnik) to a density of ca. 50% confluence and treated with a Penicillin-Streptomycin mixture.

Typically, the seeded cells were used after 3-4 days for ligand binding experiments or, after one day, were transfected with plasmids coding for HaloTag::IL-13Rα1 (pSEMS-neo HaloTag::IL-13Rα1 vector) and SNAPf::IL-4Rα (pSEMS-puro SNAPf::IL-4Rα vector) using calcium phosphate precipitation according to [205]. 12 hours after transfection, the cells were washed twice with pre-warmed phosphate-buffered saline (PBS, PAA laboratories GmbH) and fresh medium was added. Transiently transfected cells were typically used for co-tracking and ternary complex quantification experiments 3-4 days after transfection, when the receptor density was close to the endogenous level.

Alternatively, low level gene expression of HaloTag::IL-13Rα1 was achieved by treating HeLa-TET cells (stably transfected with regulator plasmid pWHE644-puro) that were transiently transfected with the reporter plasmid pWHE655-neo TREtight HaloTag::IL-13Rα1 with 10-25 ng/ml Doxycycline for 24 hours.

The HaloTag and SNAPf-tag carrying receptor molecules were simultaneously labeled with 30 nM HaloTag® tetramethylrhodamine (TMR) ligand (HTL-TMR, Promega) and 80 nM SNAP-Surface® 647 (BG-647, New England Biolabs) in culture medium at 37°C for 15 min. After labeling, the cells were washed 5 times with pre-warmed PBS to remove unreacted dye. Labeling, washing and subsequent imaging was accomplished in custom-made incubation chambers with a volume of 500 µl. Labeled receptors are denoted as $^{\text{TMR}}$IL-13Rα1 and $^{\text{DY647}}$IL-4Rα henceforth.

The actin polymerization was for some experiments moderately inhibited by treating the cells with 10 µM Latrunculin B (Sigma-Aldrich) for 20 minutes after labeling.

3.5 Single molecule fluorescence microscopy and data evaluation

3.5.1 Total internal reflection fluorescence microscopy (TIRFM)

All single molecule imaging experiments were carried out by total internal reflection fluorescence (TIRF) microscopy with an inverted microscope (Olympus IX71) equipped with a triple-line total internal reflection (TIR) illumination condenser (Olympus) and a back-illuminated electron multiplying charge coupled device (EMCCD) camera (Ixon DU897D, 512×512 pixel, Andor Technology). A 150× magnification objective with a numerical aperture of 1.45 (UAPO 150×/1.45 TIRFM, Olympus) was employed for TIR illumination of the sample.

During ligand binding experiments, DY647-labeled ligands were excited by a 642 nm laser diode (LuxX® 642-140, Omicron) at 0.65 mW (power output after passage of the objective). Stacks of 1000-2000 frames were recorded with a time resolution of 32 ms/frame (31.25 Hz).

Upon dual-color acquisition, $^{\mathrm{TMR}}$IL-13Rα1 was excited by a 561 nm diode-pumped solid state laser (CL-561-200, CrystaLaser) at 0.95 mW and $^{\mathrm{DY647}}$IL-4Rα or DY647-labeled ligands, respectively, were excited by a 642 nm laser diode (LuxX® 642-140, Omicron) at 0.65 mW. Fluorescence was detected using a spectral image splitter (DualView, Optical Insight) that was prepared with a 640 DCXR dichroic beam splitter (Chroma) in combination with bandpass filters for detection of TMR (585/40, Semrock) and of DY647 (690/70, Chroma), projecting each channel onto 512x256 pixels (Figure 9). Stacks of 300-500 images were acquired at 31.25 Hz (32 ms/frame).

Microscopy was performed at room temperature in phenol red-free medium supplemented with an oxygen scavenger and a redox-active photoprotectant consisting of 0.5 mg/ml glucose oxidase (Roche Applied Science), 0.04 mg/ml catalase, 4.5 mg/ml glucose, 1 mM ascorbic acid and 1 mM methyl viologene (all Sigma-Aldrich) to prevent blinking of the DY647 fluorophore and to minimize photobleaching of both dyes [206].

For ligand binding studies, the respective DY647-labeled ligand was added to a final concentration of 2 nM for at least 5 min. After 5 washing steps with PBS, microscopy medium was added and imaging was started rapidly.

Receptor dimerization was probed before and after incubating with the respective ligand at a concentration of 20 nM for at least 5 min if not otherwise stated. Images of the same coverslip were acquired up to 30 min after stimulation only to reduce artifacts that may arise from cellular feedback mechanisms such as receptor endocytosis or stress responses.

3.5.2 Image processing: single molecule localization, tracking and cluster filtering

The processing of recorded image stacks in order to localize and track single molecules was realized by employing a lab-intern software solution written in MATLAB (The MathWorks) that uses the “multiple-target tracing” (MTT) algorithm [191] as described in detail in [207]. Some settings were modified to optimize the localization and tracking fidelity for the current project: A detection box of 9x9 pixels was applied and 5 deflation loops were performed to ensure the identification of all particles. A maximum of 3 nearest neighbors was analyzed for recovering particle trajectories and a detection gap between successive frames of 3 missing points was closed. The local diffusion coefficient was calculated from the past 10 frames to model the PDF for observed displacements and the expected diffusion coefficient was set to an empirically optimized value between 0.09 and 0.15 µm²/s (local and expected diffusion equally weighted). With the applied parameter set a sub-micrometer localization precision (Ø 25 nm) of single molecules was achieved.

Before the image stacks were subjected to the localization and tracking process, the channels of dual color images were aligned by performing a spatial transformation on the basis of a calibration measurement with multicolor fluorescent beads (TetraSpeck microspheres 0.1 µm, Invitrogen) that are visible in both spectral channels. To this end, the “cp2tform” function of MATLAB’s “Image Processing Toolbox” was utilized to calculate a transformation matrix that enabled the correction of the channel alignment with sub-pixel precision (5-10 nm, [115]). Additionally, in each single and dual color image stack, immobile molecules (unspecific immobilized dyes and endocytosed labeled receptors and ligands) were identified by the “density-based spatial clustering of applications with noise” (DBSCAN) algorithm [208] as described in [209] and removed from the data set.

3.5.3 Single molecule co-localization/co-tracking and diffusion analysis

For single molecule co-localization analysis, individual molecules detected in both spectral channels were regarded as co-localized, if the co-particle was found contemporaneously within a distance threshold of 2 pixels or 214 nm, respectively. In a consecutive step, co-localized particles were subjected to tracking by the MTT algorithm to generate co-locomotion trajectories. For the receptor distance analysis, only trajectories with a minimum length of 30 frames (~960 ms) were considered.

The diffusion characteristics were analyzed by fitting of step-length histograms (increment 32 ms or 1 frame, respectively) that were obtained from a collection of single molecule trajectories of the labeled ligands with a minimum length of 150 frames (4.8 s). The utilized model is based on unhindered Brownian motion and is described by a two-component two-dimensional Gaussian probability distribution function

$$P(r,t) = f \cdot \frac{1}{4\pi D_1 t} e^{-\frac{r^2}{4D_1 t} \cdot 2\pi r} + (1-f) \frac{1}{4\pi D_2 t} e^{-\frac{r^2}{4D_2 t} \cdot 2\pi r} \qquad \textbf{Eqn. 7}$$

where P is the probability of finding a molecule with diffusion constants D_1 and D_2 (in µm²/s) and their corresponding fractions f and $(1-f)$, respectively, in a distance r (in µm) from its origin at time point $t_0 = 0$ after time t (in s). After fitting the distributions for all examined ligands one component was fixed set to the mean values for parameters D_2 (0.037±0.003 µm²/s) and f (0.83±0.03) and all distributions were fitted again to obtain D_1.

3.5.4 Quantification of receptor dimerization by particle image cross-correlation spectroscopy (PICCS)

The fraction of receptors in a ternary complex was determined by “particle image cross-correlation spectroscopy” (PICCS), as described in [166]. To this end, a self-written MATLAB script was used to calculate the mean correlated fraction of localized particles in channel 1 ($^{\mathrm{TMR}}$IL-13Rα1) with respect to channel 2 ($^{\mathrm{DY647}}$IL-4Rα or DY647-labeled ligand) in a 20-25 µm² region of interest (ROI). Only the first 20 frames of each image stack were evaluated, as the reduction of cross-correlation due to photobleaching was negligible during this short time interval [210]. The script proceeds in three steps as described below:

1. Calculation of the mean correlation function $C_{cum}(r)$ from the particle coordinates of the first 20 frames of the selected image stack with interval Δr = 0.03 µm and r_{max} = 0.7 µm (r_{max}^2 = 0.49 µm²)
2. Fitting of the linear part of C_{cum} in the range of 0.1 µm $> r \geq$ 0.7 µm to equation 8 to obtain α and ρ
3. Fitting of full range C_{cum} to equation 9 with fixed values for α and ρ (determined in step 2) to obtain σ

$$C_{cum}^{lin.}(r) = \rho \cdot \pi r^2 + \alpha \qquad \textbf{Eqn. 8}$$

$$C_{cum}(r) = \alpha \cdot \left(1 - e^{-\frac{r^2}{2\sigma^2}}\right) + \rho \cdot \pi r^2 \qquad \textbf{Eqn. 9}$$

Here, α is the fraction of $^{\mathrm{TMR}}$IL-13Rα1 particles spatiotemporally correlated with $^{\mathrm{DY647}}$IL-4Rα (or DY647-labeled ligand) particles, ρ is the two-dimensional surface concentration of $^{\mathrm{DY647}}$IL-4Rα (or DY647-labeled ligand) and σ is the correlation length.

Typically, due to the lower labeling efficiency achieved with HTL-TMR (see below), a moderate excess of $^{\mathrm{DY647}}$IL-4Rα was observed in the transiently transfected cells. Consequently $^{\mathrm{TMR}}$IL-13Rα1 was regarded as the limiting partner and taken as reference for the correlation analysis. Cells with $^{\mathrm{DY647}}$IL-4Rα and $^{\mathrm{TMR}}$IL-13Rα1 receptor numbers that differed more than 30% from each other were discarded from the analysis to exclude artifacts that may arise from distinctly varying expression levels.

The degree of labeling (DOL) of the tagged receptor chains was determined by PICCS evaluation of dual-color images of HeLa cells expressing a HaloTag/SNAPf-tag double construct (HaloTag::SNAPf::IFNAR2c, [60]) fused to the type I interferon receptor 2 chain that was labeled with HTL-TMR and BG-647 according to the same protocol that was used for labeling the receptor chains. Here, the DOL of HaloTag/HTL-TMR corresponds to the correlated fraction when running a correlation analysis of HTL-TMR-labeled particles (channel 1) with respect to BG-647-labeled particles (channel 2). Switching channels yields a correlated fraction that corresponds to the DOL of SNAPf/BG-647. For HaloTag/HTL-TMR a mean DOL of 32% and for SNAPf/BG-647 of 42% was determined. The double construct was also used as positive control for single molecule co-localization.

3.5.5 Calculation of effective 2D binding affinities on the cell surface

The molecular two-dimensional binding affinity K_D^T of IL-13Rα1 for ligand-bound IL-4Rα and of IL-4Rα for IL-13-bound IL-13Rα1 in the plasma membrane of HeLa cells was calculated according to the law of mass action:

$$K_D^T = \frac{([IL-4R\alpha]-\alpha\cdot[IL-13R\alpha 1])\cdot([IL-13R\alpha 1]-\alpha\cdot[IL-13R\alpha 1])}{\alpha\cdot[IL-13R\alpha 1]} \qquad \textbf{Eqn. 10}$$

The respective cell surface concentrations of IL-4Rα and IL-13Rα1 were taken from the PICCS analyses (ρ, see above) and corrected for the determined DOLs. The correlated fraction α was corrected for the basal α of unstimulated cells (caused by random co-localizations and fitting fidelity) and normalized to the maximum dimerization level (62%) that was obtained by setting the fractions of $^{\text{DY647}}$IL-4/$^{\text{TMR}}$IL-13Rα1 (~18%) and $^{\text{DY647}}$IL-4/$^{\text{TMR}}$IL-4Rα (~28%) interactions in relation. The error of the calculated K_D^T values depends on deviations of the degree of labeling, receptor concentrations and uncertainty in PICCS evaluation and was estimated at ±50%.

3.6 Reconstitution of receptor subunits in polymer-supported membranes (PSM)

To quantify the KFR-induced ternary complex formation by a PSM-based single molecule dimerization assay [203], fluorescently labeled transmembrane-only mutants of the receptor chains were reconstituted in polymer-supported membranes and imaged with by TIRF-microscopy as described above. Therefore His10::SNAPf::IL-13Rα1-TM and His10::SNAPf::IL-4Rα-TM were expressed in HEK293T cells that were transiently transfected with the respective constructs (pSEMS-neo His10::SNAPf::IL-13Rα1 or pSEMS-neo His10::SNAPf::IL-4Rα) at 40% confluency. A 10 cm dish grown to full confluency for each construct was pelleted after a short incubation with 50 mM EDTA and after two washing steps with PBS, the cells were homogenized in 500 µl of lysis buffer (25 mM HEPES pH 7.4, 0.5 µl Benzonase, 10 µl protease inhibitors and 20 mM of Triton-X100). After cell lysis, 800 nM of SNAP-Surface® 647 (BG-647) or SNAP-Surface® 547 (BG-547, both New England Biolabs) was added to the lysis mixture of His10::SNAPf::IL-13Rα1-TM or His10::SNAPf::IL-4Rα-TM, respectively, and the labeling mixture was incubated for 30 minutes at room temperature. The lysate was then cleared by ultra-centrifugation (55.000 x g, 45 min, 4°C), followed by an ion metal affinity chromatography (IMAC) with the supernatant. For this purpose, 50 µl of Ni-NTA agarose and the supernatant was given into a small spin column, incubated for 5 min and then washed twice with buffer A (25 mM HEPES pH 7.4, 300 mM NaCl, 10 mM Imidazole, 0.6 mM Triton-X100). Elution was performed by the use of 60 µl buffer B (25 mM HEPES, 300 mM NaCl, 500 mM Imidazole, 0.6 mM Triton-X100). The labeled receptors are denoted as ^{DY647}IL-13Rα1-TM and ^{DY547}IL-4Rα-TM henceforth for all experiments on PSM.

Microscopy coverslips modified with poly(ethylene glycol) and terminal palmitic acid were produced as described in [211]. Palmitic acid functionalized surfaces were washed in chloroform and could be stored at 4°C until use.

Proteoliposomes were formed by mixing 5 mM of 1,2-dioleoyl-sn-glycero-3-phosphocholine (DOPC, Avanti Polar Lipids) supplemented with 2 mol% 1,2-dioleoyl-sn-glycero-3-phospho-L-serine (DOPS, Avanti Polar Lipids) in HBS containing 20 mM Triton-X100 with 0.5-1 µl of the eluted protein solution, followed by a detergent extraction by addition of an twofold excess of ß-cyclodextrin over the detergent and incubation for 5 minutes [212]. After dilution to a final lipid concentration of 250 µM in HBS, the formed proteoliposomes were incubated with the surface for 30 minutes, followed by induced vesicle rupture by addition of 10% (w/v) PEG8000 solved in HBS. 15 minutes later, the formed PSM was washed extensively with buffer to remove excess lipid material.

Ternary complex formation of reconstituted receptors induced by KFR was investigated with increasing ligand concentrations. After addition of higher concentrations of ligand, a previously unbleached area of the surface was imaged.

For the determination of the DOL of ^{DY647}IL-13Rα1-TM and ^{DY547}IL-4Rα-TM, ^{DY547}IL-4Rα-TM reconstituted in a PSM was incubated with ^{DY647}KFR (DOL = 0.95). The fraction of occupied receptors at a given concentration of the ligand in equilibrium is given by:

$$f_{binary} = \frac{c}{c + K_D} \qquad \textbf{Eqn. 11},$$

where c is the concentration of the ligand in solution and K_D the affinity of KFR for IL-4Rα. The DOL was then calculated according to

$$DOL_{IL-4R\alpha} = \frac{N_{IL-4R\alpha}}{N_{IL-4R\alpha}^{total}} = \frac{N_{IL-4R\alpha}}{\left(\frac{N_{KFR}}{DOL_{KFR} \cdot f_{binary}}\right)} \qquad \textbf{Eqn. 12},$$

where $N_{IL-4R\alpha}^{total}$ is the total number of labeled and unlabeled IL-4Rα-TM, $N_{IL-4R\alpha}$ is the number of localizations of ^{DY547}IL-4Rα-TM and N_{KFR} the number of localizations of ^{DY647}KFR in a given ROI in the first frame to minimize photobleaching of both dyes. The fraction of IL-4Rα-TM in ternary complexes is then given by:

$$f_{ternary} = \frac{\frac{N_{co-loc}}{N_{IL-4R\alpha}}}{DOL_{IL-13R\alpha 1}} = \frac{\frac{N_{co-loc}}{N_{IL-4R\alpha}}}{DOL_{IL-4R\alpha}} \qquad \textbf{Eqn. 13}$$

Here, N_{co-loc} is the number of co-localizations of ^{DY647}IL-13Rα1-TM and ^{DY547}IL-4Rα-TM, $N_{IL-4R\alpha}$ is the number of localizations of ^{DY547}IL-4Rα-TM and since both receptor subunits are labeled via the same tag, $DOL_{IL-13R\alpha 1}$ is assumed to equal $DOL_{IL-4R\alpha}$.

The resulting fraction of ternary complexes was corrected for false-positive random co-localizations in absence of any ligand and plotted against the ligand concentration, yielding a bell-shaped concentration-dimerization relationship. The data was fitted with a two-step dimerization model containing two pathways for receptor binding and ternary complex assembly and including four equilibrium dissociation constants K_1, K_2, K_3, K_4 as well as receptor and ligand concentrations (cf. [203] for further details). K_1 (KFR + IL-4Rα ↔ KFR/IL-4Rα) and K_4 (KFR + IL-13Rα1 ↔ KFR/IL-13Rα1) are volume binding constants associated with the corresponding binary complex (3D) equilibrium. K_2 (IL-13Rα1 + KFR/IL-4Rα ↔ IL-13Rα1/KFR/IL-4Rα; equivalent to K_D^T in this script) and K_3 (IL-4Rα + KFR/IL-13Rα1 ↔ IL-4Rα/KFR/IL-13Rα1) are surface binding constants related to the corresponding ternary complex (2D) equilibrium.

3.7 Ensemble fluorescence microscopy studies

To roughly estimate endocytosed ligands, HeLa cells were grown on PLL-PEG-RGD-coated glass coverslips as described above and incubated with 2 nM ^{DY647}IL-13 or ^{DY647}IL-13 D7. After an incubation time of 15 min at 37°C followed by 5 washing steps, endosomes containing large amounts of labeled ligand were imaged in a highly inclined and laminated optical sheet (HILO) mode [213] with the TIRF microscopy setup described above. In some experiments endocytosis was diminished by pre-incubating the cells with 100 µM EHT1864 (Santa Cruz Biotechnology) for 1 hour. The integral fluorescence intensity was extracted after background subtraction with a customized version of the known "rolling ball" algorithm to quantify the relative amount of endocytosed ligands.

3.8 Flow cytometry

The levels of phosphorylated STAT6 (pSTAT6) in HeLa and A549 cells were quantified by phospho-flow cytometry. Therefore intracellular pSTAT6 was stained with antibodies coupled to Alexa Fluor 488 (1:50 dilution, BD Biosciences cat: 612600) after cell permeabilization with ice-cold methanol (100% v/v) and the fluorescence was measured using an Accuri^{TM} C6 flow cytometer (BD Biosciences). The mean fluorescence intensity (MFI) was then calculated by subtracting the mean fluorescence signal of the stimulated samples from that of an unstimulated sample.

For the determination of STAT6 phosphorylation kinetics a ligand concentration of 1 µM was used. Dose-response data was acquired 15 minutes after induction and the normalized values were plotted against the respective cytokine concentration. The yielded dose-response curves were fitted with Prism (GraphPad Software) using a common model to obtain EC_{50} (half maximal effective concentration) values.

In order to quantify receptor levels in the plasma membrane, HeLa cells were stained at 4°C with Fluorescein-5-isothiocyanate (FITC) or Phycoerythrin (PE) labeled antibodies against IL-13Rα1 (1:100, R&D cat: FAB1462F), IL-4Rα (1:100, BD Biosciences cat: 552178) and γ_c (1:100, Biolegend cat: 338605) for 1 hr. The cells were then washed, the levels of surface receptors were measured by flow cytometry as described above and the MFI was compared to that of an isotype control.

The EC_{50} values for TF-1 cell (human cell line of immature erythroid origin that has been derived from a patient with erythroleukemia [214]) proliferation were obtained as described in [158]. Briefly, TF-1 cells were stimulated for 96 hours with different concentrations of the respective IL-13 variant and the cell number was determined by flow cytometry-based counting. The number of cells obtained for each agonist was plotted against the cytokine concentration to obtain sigmoidal dose-response curves, from which the EC_{50} values were extracted.

The differentiation of monocytes into dendritic cells was analyzed as described in [158]. Briefly, $CD14^+$ monocytes were stimulated for 6-7 days with different concentrations of the respective IL-13 agonist. Then, the differentiation into dendritic cells was assessed by measuring the surface abundance of the classical dendritic cell markers CD86 and CD209. Therefore the cells were stained with appropriate fluorescently labeled antibodies and the MFI was determined by flow cytometry with a BD^{TM} LSR II flow cytometer (BD Biosciences) as described above.

3.9 Model simulations

3.9.1 Diffusion and receptor interaction dynamics simulation (DAIDS)

Simulation algorithm

A simple spatial-stochastic diffusion-reaction model including a two-dimensional interaction space, confined by a sub-microscopic, semipermeable meshwork, was implemented in MATLAB (Version R2015a) to verify the proposed critical role of the MSK in stabilizing transient receptor dimers *in silico*.

The simulation with time-resolution Δt_{sim} consists of two massless molecular species (1: binary complex of ligand and high affinity ligand-binding receptor subunit, 2: accessory receptor subunit) with the corresponding particle surface concentrations N_1 and N_2. The particles are diffusing with diffusion constant D according to a simple isotropic random walk model [215] in a two-dimensional space (plasma membrane), having the dimensions 8.99 x 8.99 µm (80.78 µm²) or 84 x 84 pixel (pixel-size 0.107 µm, taken from experimental setup), respectively. The membrane is divided into triangular compartments with cathetus side lengths of 74.9 nm (0.7 pixel) that are arranged in an alternating order. Particles are allowed to switch between neighbouring compartments with probability p_{hop}. If each of a molecule of species 1 and 2 are getting closer together than a defined association threshold d_a, a ternary complex is formed with probability p_a. The dissociation of existing ternary complexes occurs with probability p_d.

At the beginning of a simulation all particles are randomly distributed on the surface and, depending on the corresponding degree of labelling (DOL_1 and DOL_2), marked as visible or invisible by chance, followed by the execution of the main loop in which 6 steps are consecutively computed until the simulation time exceeds a predefined duration (t_{end}):

1. A possible dissociation of each existing ternary complex is probed by comparing a random value between 0 and 1 to the dissociation probability p_d.

2. For each particle of species 1 a new position is calculated on the basis of an independent displacement in x- and y-direction that depends on the common equation 14 multiplied by a value that is randomly drawn from a normal distribution. If the new position is located outside the current compartment, a random value between 0 and 1 is compared to the hopping probability p_{hop} to check whether compartment switching is allowed. If hopping is forbidden, a new position is calculated as long as it is located in the current compartment. If a particle leaves the simulation space at a border, it re-enters immediately at the opposite side to mimic a spherical surface and to avoid boundary effects.

   $$\Delta x = \Delta y = \sqrt{2 \cdot D \cdot \Delta t_{sim}} \qquad \textbf{Eqn. 14}$$

   Here, D is the diffusion constant and Δx and Δy are the mean displacements in the corresponding directions of the particle. Δt_{sim} is the time-resolution of the simulation. Additionally, possible bleaching of each visible particle is calculated during this step by comparing a random value between 0 and 1 to the bleaching probability p_{bleach}. Each bleached particle gets marked as invisible and is not further considered for image generation.

3. A new position for each particle of species 2 is calculated in the same way, excluding particles that belong to a ternary complex. Those are assigned a new position in step 5.

4. For each particle of species 1 a list of species 2 particles located in the same compartment, is generated. If the inter-particle distance of a particle-pair in the list is lower than or equal to the association threshold d_a, a random value between 0 and 1 is compared to the association probability p_a to check for the assembly of a ternary complex.

5. Particles of species 2 that belong to a ternary complex are randomly placed around the position of the corresponding species 1 particle keeping a ternary complex inter-receptor distance d_c.

6. To emulate motion blurring of a single molecule experimental setup that arises from the finite acquisition time of an EMCCD camera, all particle positions are saved until a virtual lag-time Δt_{lag} has expired. In this case an image of the current frame is

generated by *(i)* merging all positions from all time-points since the frame has started, *(ii)* blurring with a 2-D Gaussian smoothing kernel[1] to simulate diffraction at an objective aperture and *(iii)* adding Gaussian noise[2] to mimic different noise sources an EMCCD camera is subjected to.

Parameter estimation (summarized in Table 6)

The diffusion constant D (1.25 µm²/s) that represents the molecule's free diffusion constant in a barrier-free membrane was determined experimentally by single molecule tracking of diffusing ^{DY547}IL-4Rα-TM in polymer-supported membranes.

The hopping probability p_{hop} (0.02) was obtained empirically by varying its value until step-length distributions (molecule displacements at 32 ms intervals = 1 frame) acquired from simulations resembled experimentally derived distributions for IL-4Rα. Analogically an additional factor was estimated (0.75) to decrease the diffusion constant and the hopping probability for ternary complexes since their movement was experimentally observed to be slower.

The ternary complex dissociation probability p_d was calculated as follows:

$$p_d = 1 - e^{-k_d \cdot \Delta t_{sim}}$$ **Eqn. 15** [216]

where k_d is the experimentally determined ternary complex dissociation rate and Δt_{sim} is the time-resolution of the simulation.

The probability p_a (0.06) of forming a ternary complex upon two molecules of different species getting closer than the association threshold was estimated to yield a fraction of about 50-60% of all species 1 particles being part of a ternary complex when running the simulation with IL-4 wt k_d. The association threshold d_a (8 nm) was set simultaneously to fulfil the former criterion and for simplicity the same value was assigned to the ternary complex inter-receptor distance d_c (8 nm), which is consistent with structural data of the receptor chains [53].

The average one-dimensional displacement of all particles determines the spatial resolution of the simulation and is, according to equation 14, dependent on the diffusion constant as well as on the time-resolution of the simulation. The latter (8 µs) was chosen as short as possible to achieve a spatial resolution (4.5 nm) significantly below the ternary complex association threshold on the one hand, and as large as feasible to minimize the needed computation time for a simulation run.

---

[1] MATLAB function: "imgaussfilt"
[2] MATLAB function: "imnoise"

Image creation was started only after a distinct number (f_{img}) of initial frames that was determined to be 300 (9.6 s) to ensure an established dynamic equilibrium between binary and ternary complexes.

Table 6. Overview of DAIDS parameters.

Parameter	Value	Source
Δt_{sim}	8 µs	calculated
Δt_{lag}	32 ms	experimental setup
t_{end}	70 s	manually set
f_{img}	300 frames (9.6 s)	empirically determined
p_a	0.06	empirically determined
d_a, d_c	8 nm	estimated from structural data [53]
p_d	$3.68 \cdot 10^{-5}$ (RGA) $1.84 \cdot 10^{-6}$ (wt)	estimated for RGA from experimentally determined rate constants, calculated for wt
p_{hop}	0.02 / 0.015	empirically determined (particles/complexes)
D	1.25 / 0.94 µm²/s	experimentally determined (particles/complexes)
p_{bleach}	$1 \cdot 10^{-7}$	experimentally determined
Compartment size	74.9 nm	empirically determined and [110]
N_1	A: 0.5 molecules/µm² B: 0.65 molecules/µm²	manually set experimentally determined
N_2	A: 0.5 molecules/µm² B: 0.77 molecules/µm²	manually set experimentally determined
DOL_1	A: 100% B: 42%	manually set experimentally determined
DOL_2	A: 100% B: 32%	manually set experimentally determined

A/B: Simulation runs that were evaluated to obtain inter-receptor distances and correlation lengths were performed with parameter-set B (experimentally determined), while for all others parameter-set A (manually set for simplicity reasons) was used.

The corresponding parameters of the used MATLAB functions for image manipulation (blurring, noise addition) were optimized to finally generate images that resemble their experimentally obtained counterparts (i.e. single molecule evaluation leads to a comparable localization precision of simulated and experimentally derived images).

3.9.2 STAT6 phosphorylation simulations

Two MATLAB scripts simulating STAT6 phosphorylation kinetics and pSTAT6 dose response experiments on the basis of differential equations were developed to verify the proposed endocytosis-including steady-state model *in silico*. The simulations are premised on the following assumptions and the parameters summarized in Table 7:

1. The receptor (*R*) comprising the IL-13Rα1 and the IL-4Rα subunits is treated as a single entity at a volume concentration of 1 pM. Thus, a realistic excess of ligand over cell surface receptor is ensured.
2. Ligand (*L*) binding to the cell surface receptor is reversible and determined by ligand-dependent k_a (association of ligand and receptor) and k_d (dissociation of ligand and receptor) rate constants.
3. The dissociation rate constant k_d determined for the binary IL-13/IL-13Rα1 complex is decreased by a factor of 100 due to the simultaneous interaction with IL-4Rα on the cell surface.
4. Ligand-receptor complexes (*RL*) are taken up irreversibly into endosomes with a rate constant k_{endo} and are further sorted into degradation and recycling pathways with rate constants k_{deg} and k_{rec}, respectively.
5. New synthesis of receptors is negligible during the time course of the simulation.
6. The amount of pSTAT6 is proportional to the number of signaling complexes (i.e. ligand-receptor complexes) at the plasma membrane (PM) and in endosomes.

Common differential equations for both simulations:

$$\frac{d(c_{RL}^{PM})}{dt} = k_a \cdot c_R \cdot c_L - k_{off} \cdot c_{RL}^{PM} - k_{endo} \cdot c_{RL}^{PM} \qquad \textbf{Eqn. 16}$$

$$\frac{d(c_R)}{dt} = k_d \cdot c_{RL}^{PM} - k_a \cdot c_R \cdot c_L + k_{rec} \cdot c_{RL}^{endo} \qquad \textbf{Eqn. 17}$$

$$\frac{d(c_{RL}^{endo})}{dt} = k_{endo} \cdot c_{RL}^{PM} - k_{deg} \cdot c_{RL}^{endo} - k_{rec} \cdot c_{RL}^{endo} \qquad \textbf{Eqn. 18}$$

Table 7. Common parameters for STAT6 phosphorylation simulations.

Name	Value	Description
Δt_{sim}	1 ms	time resolution of simulation
k_{endo}	$3 \cdot 10^{-3}$ s^{-1}	estimated endocytosis rate
k_{deg}	$6 \cdot 10^{-5}$ s^{-1}	estimated degradation rate
k_{rec}	$6.5 \cdot 10^{-4}$ s^{-1}	estimated recycling rate
c_R	1 pM at t=0	receptor concentration
c_{RL}^{PM}	0 at t=0	PM ligand-receptor complex concentration at t
c_{RL}^{endo}	0 at t=0	endosomal ligand-receptor complex conc. at t

STAT6 phosphorylation kinetics simulation

The simulations were performed for IL-13 and A11, C10, D7 and C4 agonists. Since no rate constants for C10, D7 and C4 were available, the dissociation rates were calculated based on IL-13 k_d and measured K_D values. k_a was set to a common reasonable value ($1 \cdot 10^6$ $M^{-1}s^{-1}$). For modeling treatment with endocytosis-blocking agents, the endocytosis rate was decreased by 75%. The ligand concentration (200 nM) was kept constant due to pseudo first order reaction conditions. All parameters are summarized in Table 8.

Table 8. Parameters for STAT6 phosphorylation kinetics simulation.

Name	Value	Description
k_d^{A11}	$4 \cdot 10^{-4}$ s^{-1}	A11 dissociation rate
k_d^{WT}	$2 \cdot 10^{-2}$ s^{-1}	IL-13 dissociation rate
k_d^{C10}	1 s^{-1}	C10 dissociation rate
k_d^{D7}	20 s^{-1}	D7 dissociation rate
k_d^{C4}	150 s^{-1}	C4 dissociation rate
k_a	$1 \cdot 10^6$ $M^{-1}s^{-1}$	common association rate
t_{end}	14400 s	simulation end time, 3 h
c_L	200 nM	ligand concentration, constant

The simulation main result was plotted as relative concentration of ligand-associated receptors (sum of ligand-receptor complexes at the plasma membrane and in endosomes divided by the initial receptor concentration) over time, which is supposed to correlate with the level of pSTAT6.

pSTAT6 dose response simulation

The simulations of STAT6 dose response curves are based on the phosphorylation kinetics simulation described above with the following changes: Curves were modeled for IL-13 and A11, A7 and B4 agonists. In each run the relative concentration of ligand-associated receptors (PM and endosomes) at $t = 15$ min was calculated with an increasing initial ligand concentration in the range between 10^{-13} and 10^{-7} mol/l and plotted against the applied ligand concentration. All parameters are summarized in Table 9. Since no pseudo first order reaction conditions were present for low concentrations, the change in the ligand concentration during each run was calculated according to an additional differential equation:

$$\frac{d(c_L)}{dt} = k_d \cdot c_{RL}^{PM} - k_a \cdot c_R \cdot c_L \qquad \textbf{Eqn. 18}$$

Table 9. Parameters for pSTAT6 dose response simulation.

Name	**Value**	**Description**
$\boldsymbol{k_d^{A11}}$	$1.3 \cdot 10^{-3}$ s^{-1}	A11 dissociation rate constant
$\boldsymbol{k_d^{A7}}$	$3.4 \cdot 10^{-3}$ s^{-1}	A7 dissociation rate constant
$\boldsymbol{k_d^{WT}}$	$2.2 \cdot 10^{-2}$ s^{-1}	IL-13 dissociation rate constant
$\boldsymbol{k_d^{B4}}$	$2.4 \cdot 10^{-2}$ s^{-1}	B4 dissociation rate constant
$\boldsymbol{k_a^{A11}}$	$1.64 \cdot 10^{7}$ $M^{-1}s^{-1}$	A11 association rate constant
$\boldsymbol{k_a^{A7}}$	$2.90 \cdot 10^{6}$ $M^{-1}s^{-1}$	A7 association rate constant
$\boldsymbol{k_a^{WT}}$	$5.21 \cdot 10^{6}$ $M^{-1}s^{-1}$	IL-13 wt association rate constant
$\boldsymbol{k_a^{B4}}$	$1.36 \cdot 10^{6}$ $M^{-1}s^{-1}$	B4 association rate constant
$\boldsymbol{t_{end}}$	900 s	simulation end time, 15 min
$\boldsymbol{c_L^{range}}$	10^{-13} to 10^{-7} M	IL-13 concentration range

3.10 Protein structure visualization

Protein structures were visualized with the UCSF Chimera package [217] (Figure 6 and 7A) or the Swiss-PdbViewer [218] (Figure 12).

3.11 Statistical analysis

If not otherwise stated, the experiments were repeated three times and all data are expressed as means ± SD. Statistical differences between two groups were determined by Student’s t-test or the Kolmogorov-Smirnov test.

4 Results and discussion

4.1 Part I: Receptor dimerization and dynamics

The first part of this study aimed to identify molecular and cellular determinants that govern cytokine receptor assembly. The main focus was thereby placed on the two-dimensional binding affinity (K_D^T) that dictates the equilibrium between binary and ternary receptor complexes in the plasma membrane according to the generic two-step assembly model (Figure 12). The role of K_D^T in receptor dimerization and dynamics was investigated *in vitro* and *in vivo* on the basis of the type II IL-4 receptor.

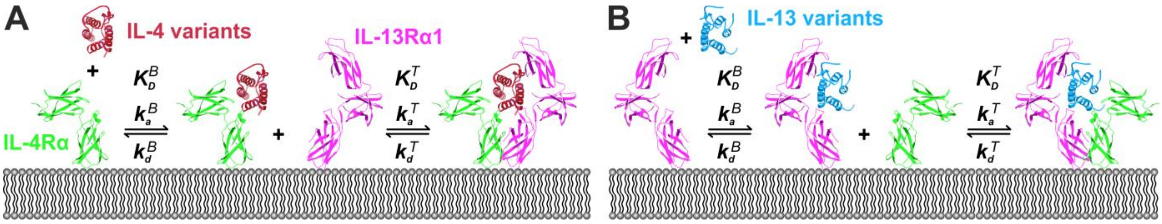

Figure 12. Two-step dimerization of the type II IL-4 receptor by different ligands. (A) Binding of IL-4 to IL-4Rα followed by recruitment of IL-13Rα1 at the membrane. For IL-4 mutants with altered affinities to IL-13Rα1, changes in the equilibrium between binary and ternary complexes (K_D^T) are expected. **(B)** Binding of IL-13 to IL-13Rα1 followed by recruitment of IL-4Rα.

4.1.1 2D affinities determine receptor dimerization in artificial membranes

To begin with, the molecular features of the assembly of the type II IL-4 receptor were carefully characterized under well-defined conditions *in vitro* using a solid-supported membrane (SSM)-based model system [171]. For this purpose, the ectodomains of IL-4Rα and IL-13Rα1 fused to a C-terminal decahistidine tag (IL-4Rα-ECD and IL-13Rα1-ECD, respectively) were tethered onto solid-supported membranes by means of a lipid analogue functionalized with tris-NTA [173]. Thus, oriented membrane anchoring and two-dimensional mobility of the receptor subunits in the plane of the membrane was ensured. The receptor assembly was monitored by simultaneous total internal reflection spectroscopy and reflectance interference (TIRFS-RIf) detection [167, 171].

For ligand binding assays, IL-4 variants and IL-13 were site-specifically labeled through an N-terminal ybbR-tag. The short ybbR-sequence (11 AA) thereby enables for covalent fusion of Coenzyme A-conjugated fluorescent dyes with the proteins by enzymatic phosphopantetheinyl-transfer (PPT) using the PPTase Sfp [193].

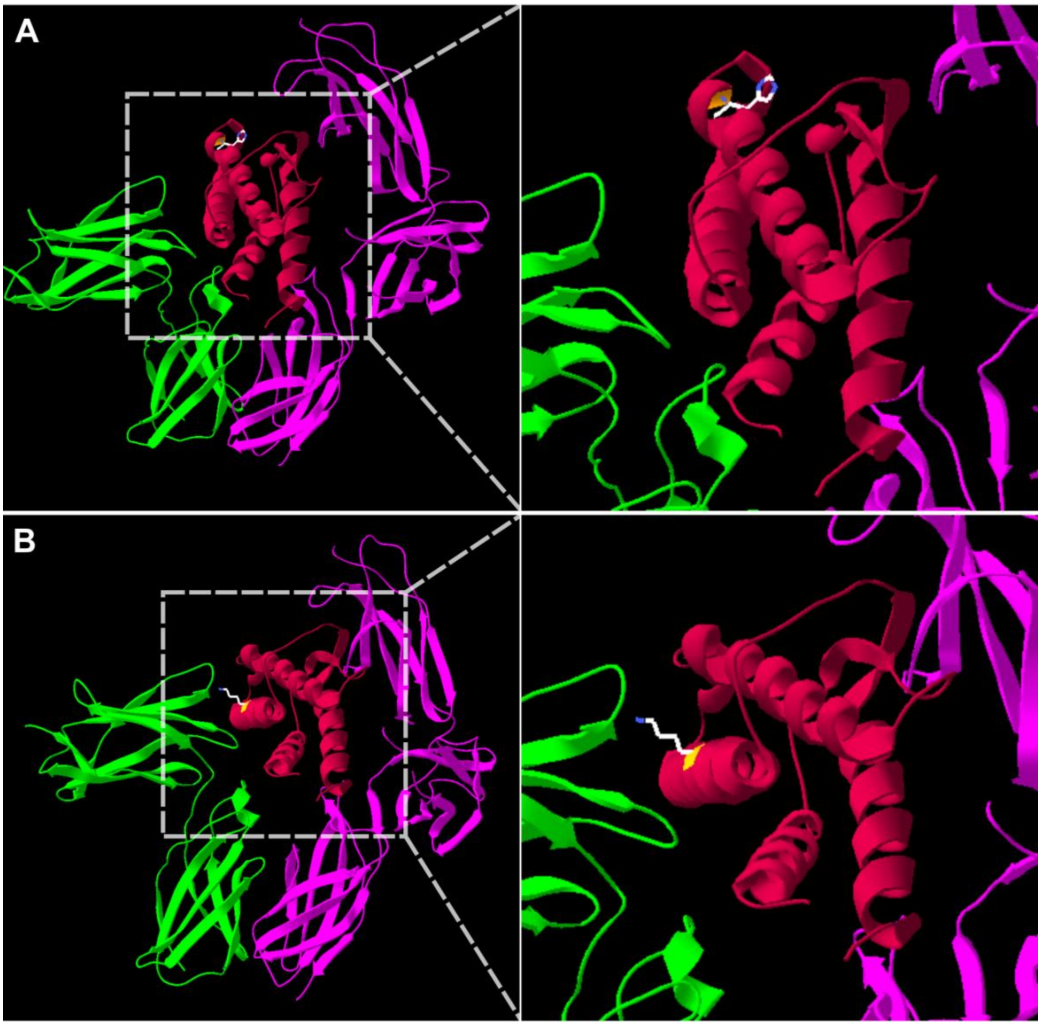

Figure 13. Mutations introduced in IL-4 variants for TIRFS-RIf experiments. (A) H59Y: Change of Histidine residue at position 59 into Tyrosine to eliminate non-specific binding to complexed Ni(II) ions. The mutated amino acid side-chain is oriented to the protein core. **(B)** K84D: Lysine residue at position 84 is replaced by Aspartate. This mutation only changes the binding interface of the interaction with IL-4Rα while the IL-13Rα1 binding interface is unaltered.

In order to eliminate non-specific binding of IL-4 to complexed Ni(II) ions, the mutation H59Y was introduced (Figure 13A). Neither the ybbR-tag nor the H59Y mutation affected receptor binding properties or activity of IL-4 and therefore these modifications will not be explicitly declared in the following (Figure 14A, B). Moreover, the mutation K84D (indicated by the subscript D in the following; Figure 13B) was introduced in order to increase the dissociation rate constant of the IL-4/IL-4Rα complex to a similar level as of the IL-13/IL-13Rα1 complex. This mutation also eliminated mass transport-limited association and strong rebinding during dissociation observed for IL-4, as the association rate constant of the IL-4/IL-4Rα interaction was ~10-fold reduced (from $1.3\pm0.3\cdot10^{7}$ $M^{-1}s^{-1}$ to $1.7\pm0.4\cdot10^{6}$ $M^{-1}s^{-1}$, [156]), thus ensuring unbiased analyses of ligand dissociation curves.

Importantly, the interaction with IL-13Rα1 is not affected by this mutation as the corresponding binding interface is unaltered (Figure 14C). Therefore, the receptor assembly mechanism depicted in Figure 12A can still be assumed valid making this mutant suitable for probing the K_D^T of IL-13Rα1 recruitment into the ternary complex.

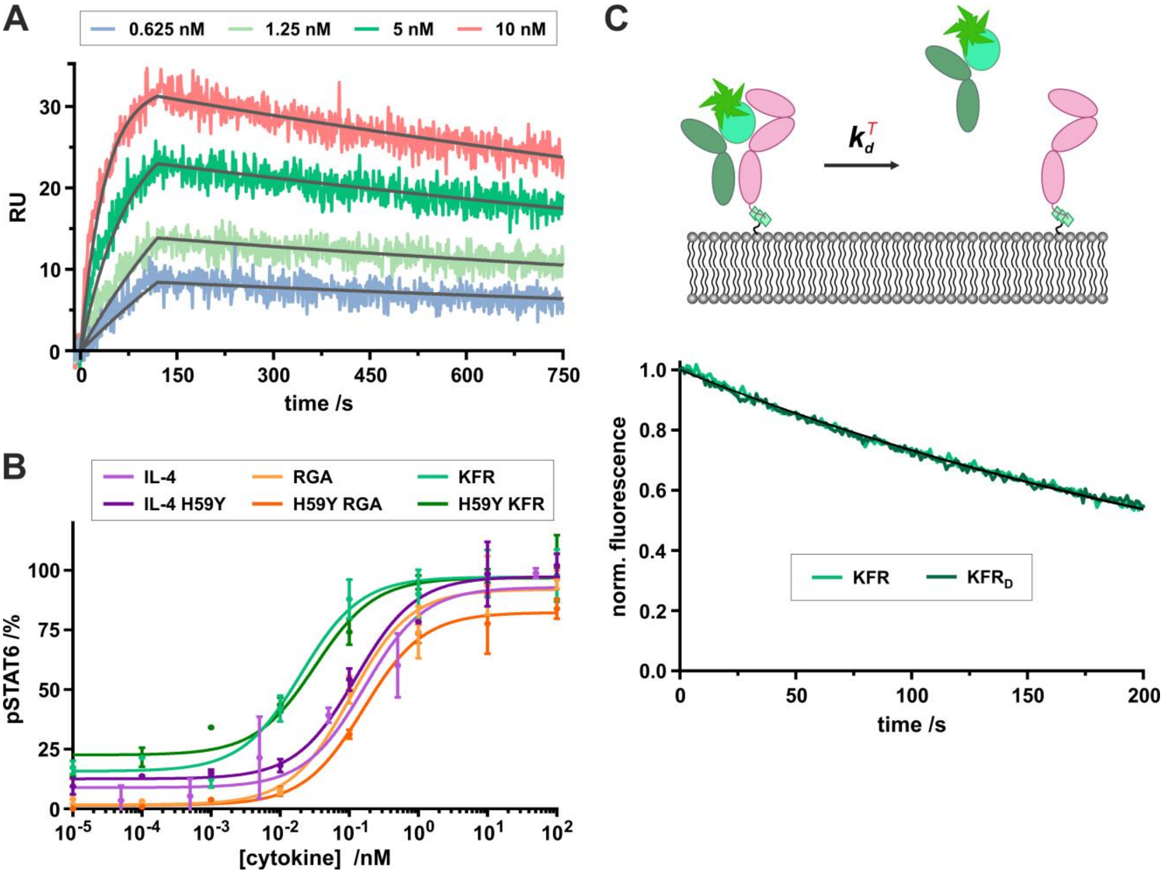

Figure 14. Receptor interaction properties and functional integrity of IL-4 variants. (A) SPR measurements of soluble IL-4Rα ectodomain binding at different concentrations to IL-4 H59Y immobilized on a Neutravidin chip via a biotinylated N-terminal ybbR tag. Kinetic rate constants obtained by these measurements are similar to those of the interaction with IL-4 wt (see Table 10). **(B)** Similar activity of IL-4 variants with and without H59Y mutation as revealed by pSTAT6 dose-response analysis. **(C)** Normalized dissociation of KFR and KFR_D variants (100 nM) in complex with soluble tagless IL-4Rα-ECD (1 µM) from surface-tethered IL-13Rα1-ECD (5 fmol/mm^2). Overlapping curves confirm unaffected interaction with IL-13Rα1 by the K84D mutation.

The rate constants of the fluorescently labeled IL-4 variants and IL-13 interacting with the individual receptor subunits were quantified by TIRFS detection. Thereby similar results for all ligands were obtained, resulting in calculated three-dimensional binding affinities K_D^B between ~17 nM (IL-4_D) and ~61 nM (RGA_D) (Figure 15 and Table 10).

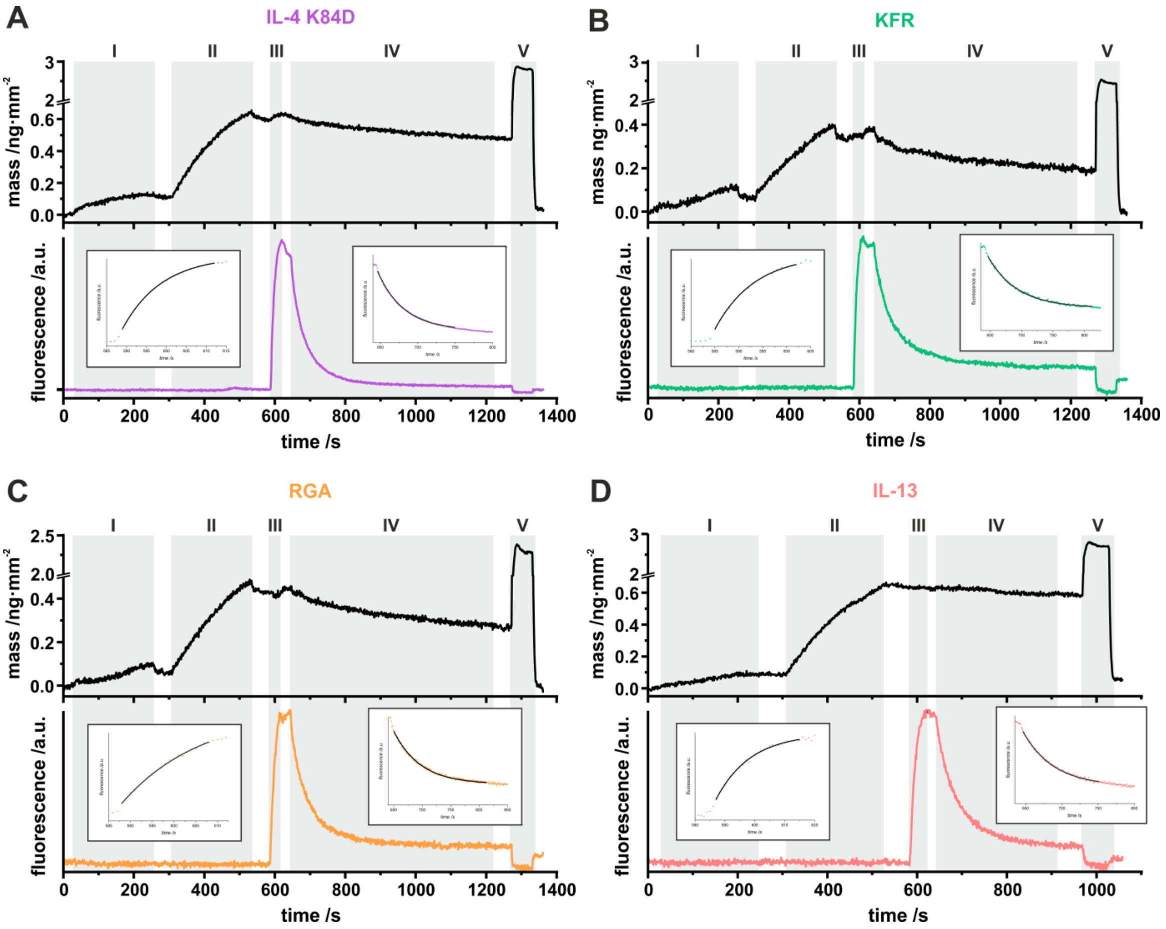

Figure 15. Quantification of binary complex interaction kinetics on SSMs of **(A)** ^{AT488}IL-4$_D$, **(B)** ^{AT488}KFR$_D$, **(C)** ^{AT488}RGA$_D$ binding to IL-4Rα-ECD and of **(D)** ^{OG488}IL-13 binding to IL-13Rα1-ECD by simultaneous TIRFS-RIf detection. Insets show corresponding fits of association and dissociation phases. Experimental procedure on solid-supported membranes doped with tris-NTA lipids: *(I)* Tethering of IL-4Rα-ECD (75 nM) or IL-13Rα1-ECD (75 nM), respectively, and *(II)* MBP-H10 (2 µM) for blocking of excess chelator lipids, *(III)* followed by injection of the respective ligand (100 nM), *(IV)* a 600 s dissociation phase and *(V)* a final Imidazole wash. Depicted curves show representative single experiments.

Table 10. Type II IL-4 receptor binary complex kinetics measured in artificial membranes.

Interacting entities	k_a^B **[M^{-1}s^{-1}]**	k_d^B **[s^{-1}]**	K_D^B **[nM]**
IL-4$_D$ ↔ IL-4Rα	(1.7±0.4)·10^6	0.029±0.002	17.1±4.5
IL-13 ↔ IL-13Rα1	(0.8±0.1)·10^6	0.024±0.001	30.1±4.9
KFR$_D$ ↔ IL-4Rα	(1.0±0.1)·10^6	0.021±0.001	22.3±2.9
RGA$_D$ ↔ IL-4Rα	(0.4±0.1)·10^6	0.022±0.002	60.7±21.7
DN4$_D$ ↔ IL-4Rα	(0.3±0.1)·10^6	0.024±0.004	83.7±42.0

Interacting entities	k_a^B **[M^{-1}s^{-1}]**	k_d^B **[s^{-1}]**	K_D^B **[nM]**
IL-4 ↔ IL-4Rα	$(1.3\pm0.3)\cdot10^{7}$	0.0013±0.0002	0.10±0.02[a]
IL-4 H59Y ↔ IL-4Rα	$(3.8\pm0.4)\cdot10^{7}$	0.0019±0.0003	0.05±0.01
DN4 ↔ IL-4Rα	-	-	0.10±0.01[b]
IL-4 ↔ IL-13Rα1	-	-	2500[a]
IL-13 ↔ IL-4Rα	n.b.[c]	n.b.[c]	n.b.[c]

[a] from reference [156], [b] from reference [197], [c] no interaction detectable [156]

Subsequently, receptor dimerization was probed with both subunits at surface concentrations of ~5 fmol/mm^2 (~3000 molecules/µm^2). Owing to the formation of ternary complexes, the dissociation of ^{AT488}IL-4$_D$ was substantially slower compared to experiments with IL-4Rα-ECD only (Figure 16). The change in dissociation kinetics was used for quantifying the equilibrium between binary and ternary complexes and the corresponding association rates by fitting a kinetic model schematically depicted in the inset in Figure 16 [171].

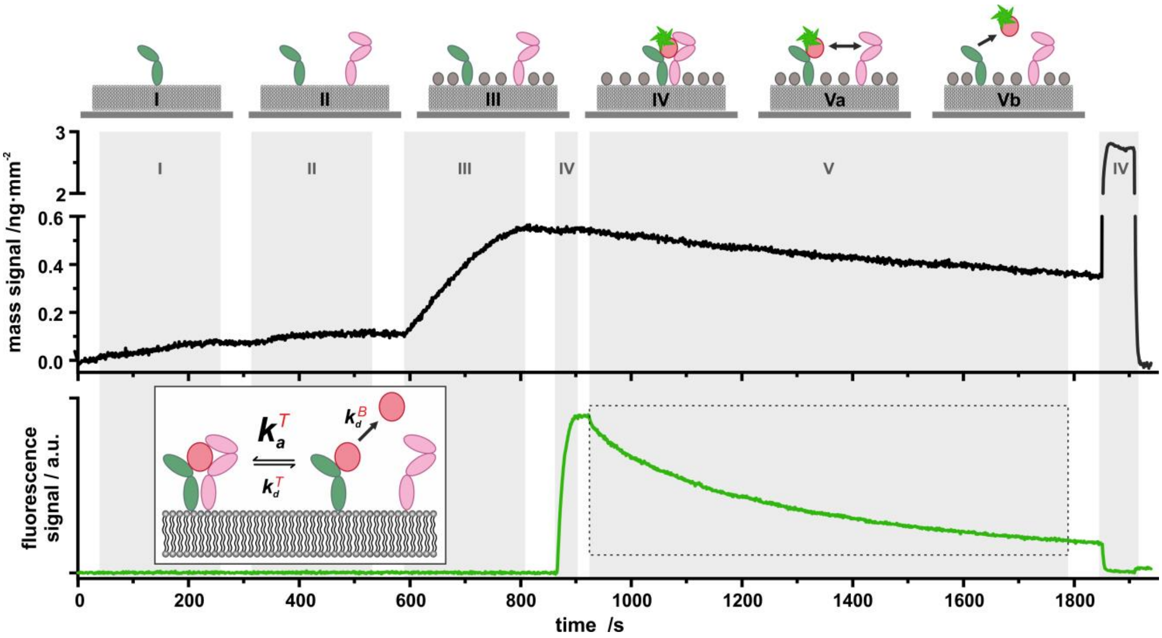

Figure 16. Probing the 2D equilibrium on SSMs by monitoring the dissociation of fluorescently labeled IL-4 variants and IL-13 (dashed rectangle) using simultaneous TIRFS-RIf detection. Top: Carton of the assay. Bottom: Typical assay including sequential tethering of *(I)* IL-4Rα-ECD (75 nM) and *(II)* IL-13Rα1-ECD (100 nM) onto a SSM and *(III)* blocking free chelator lipids with MBP-H10 (2 µM), followed by injection of *(IV)* ^{AT488}IL-4$_D$ (100 nM) and *(V)* rinsing for 900 s. *(VI)* Final Imidazole wash for surface regeneration. Depicted curves show a representative single experiment.

Control experiments at elevated IL-13Rα1-ECD surface concentrations revealed significantly further reduced dissociation kinetics (Figure 17A), which can be explained by a shift of the two-dimensional equilibrium towards ternary complex formation. Moreover, strongly enhanced dissociation of $^{\mathrm{AT488}}$IL-4$_{\mathrm{D}}$ was observed upon blocking vacant IL-13Rα1-ECD on the SSM by a fast injection of IL-13 A11 (Figure 17B, C). These results corroborate the formation of a dynamic equilibrium between binary and ternary complexes, which is quantitatively probed by the ligand dissociation kinetics and confirms that the utilized model is applicable for the IL-4Rα/IL-13Rα1 receptor system.

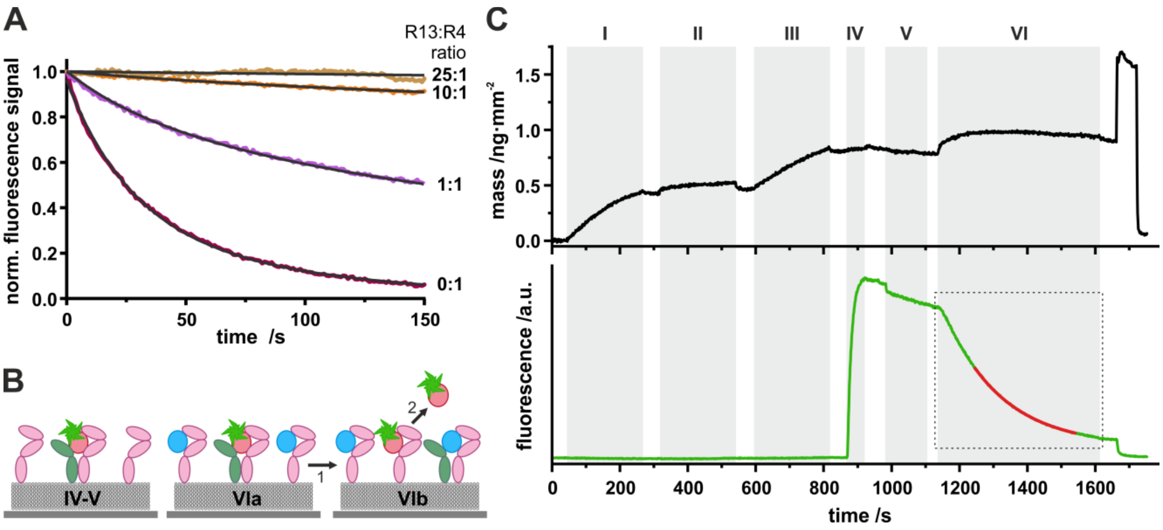

Figure 17. Dynamic equilibrium between binary and ternary complexes on SSMs. (A) Surface concentration-dependent dimerization of IL-4Rα and IL-13Rα1: $^{\mathrm{AT488}}$IL-4$_{\mathrm{D}}$ dissociation kinetics were probed at different ratios of membrane-tethered IL-13Rα1-ECD and IL-4Rα-ECD (const. at 1.3 fmol/mm^2). **(B, C)** Ligand chasing with high affinity IL-13 mutant A11. Carton in B depicts chasing mechanism: IL-13Rα1-ECD/IL-13 A11 competes with IL-13Rα1-ECD/$^{\mathrm{AT488}}$IL-4$_{\mathrm{D}}$ (*step 1*), followed by rapid IL-13Rα1-ECD/$^{\mathrm{AT488}}$IL-4$_{\mathrm{D}}$ dissociation (*step 2*) and exchange by IL-13 A11 (not shown). As step 1 is rate-limiting, dissociation of IL-13Rα1-ECD/$^{\mathrm{AT488}}$IL-4$_{\mathrm{D}}$ with IL-4Rα-ECD is probed, which was quantified by an exponential fit (red curve in dashed rectangle, rate constant $6.1 \pm 0.1 \cdot 10^{-3}$ s^{-1}). Experimental procedure on SSMs: *(I)* Tethering of excess IL-13Rα1-ECD (300 nM), *(II)* IL-4Rα-ECD (20 nM) and *(III)* MBP-H10 (1 µM), *(IV)* followed by an injection of $^{\mathrm{AT488}}$IL-4$_{\mathrm{D}}$ under conditions saturating IL-4Rα-ECD (100 nM), *(V)* 150 s rinsing and *(VI)* chasing by IL-13 A11 injection (0.5 µM). Depicted curves show representative single experiments.

From the fit of the ligand dissociation kinetics (Figure 18A), a ternary complex dissociation constant (2D binding affinity) K_D^T of (36±15) molecules/µm^2 was obtained for the interaction of IL-4Rα-ECD/IL-4$_{\mathrm{D}}$ with IL-13Rα1-ECD. The assay was further employed to compare the receptor dimerization by the IL-4 mutants with altered binding affinities towards IL-13Rα1, namely RGA (~5-fold increased K_D) and KFR (~440-fold decreased K_D) [64] as well as DN4 with no measurable affinity for IL-13Rα1 [197]. These mutants were combined with the H59Y and K84D mutations for probing the recruitment of IL-13Rα1-ECD. The expected shift in the equilibrium between binary and ternary complexes compared to ^{AT488}IL-4$_D$ was clearly confirmed (Figure 18B): for ^{AT488}RGA$_D$, a nearly 10-fold increase in the K_D^T compared to ^{AT488}IL-4$_D$ was observed; by contrast, more than 30-fold more efficient ternary complex formation compared to ^{AT488}IL-4$_D$ was found for ^{AT488}KFR$_D$.

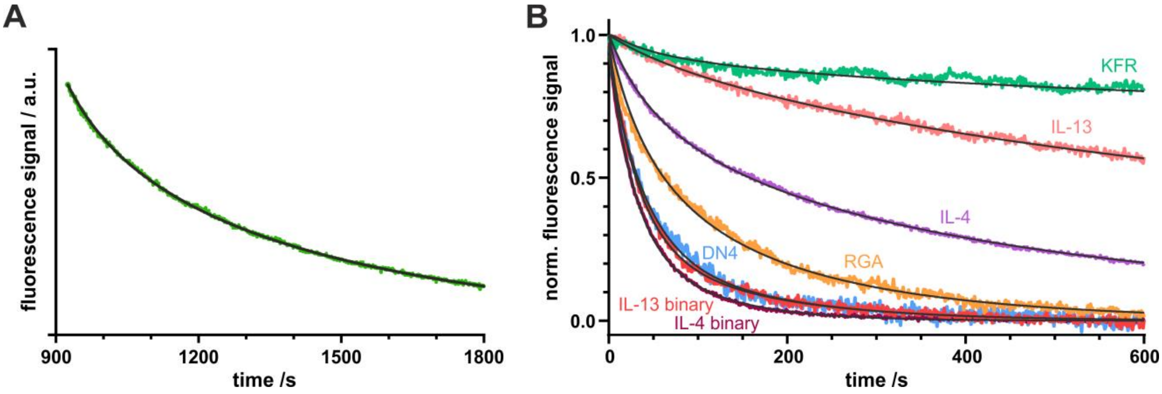

Figure 18. Quantification of 2D association kinetics and equilibrium dissociation constants from ligand dissociation kinetics by **(A)** fitting the dissociation curve of ^{AT488}IL-4$_D$ (dashed rectangle in Fig. 16) with a two-step disassembly model (cartoon in Fig. 16) to obtain k_a^T and K_D^T. **(B)** Comparison of ^{AT488}KFR$_D$ (green), ^{OG488}IL-13 (light red), ^{AT488}IL-4$_D$ (violet), ^{AT488}RGA$_D$ (orange) and ^{AT488}DN4$_D$ (blue) dissociation kinetics from ternary complexes and of ^{AT488}IL-4$_D$ (dark rose) and ^{OG488}IL-13 (red) from binary complexes. Depicted curves show representative single experiments.

In case of KFR$_D$, the determination of K_D^T by this technique was obstructed because the ligand dissociation kinetics was too slow to be reliably analyzed. Therefore, a single molecule assay was employed by reconstituting transmembrane IL-4Rα and IL-13Rα1, which were produced in HEK 293T cells and labeled with BG-547 and BG-647 via an N-terminal SNAPf-tag (^{DY547}IL-4Rα-TM and ^{DY647}IL-13Rα1-TM, respectively), into polymer-supported membranes as described previously [203]. At the much lower surface concentrations employed in this assay, ligand concentration-dependent receptor dimerization in presence of KFR could be directly quantified by co-localization (Figure 19A) yielding a bell-shaped concentration-dimerization relationship. By fitting the data to a two-pathway receptor assembly model including four equilibria (Figure 19B, C; [203]) a K_D^T of (0.3±0.1) molecules/µm^2 was obtained, which is in very good agreement with the ~440-fold increased binding affinity of KFR vs. IL-4 for IL-13Rα1 [64] and with an roughly estimated K_D^T of ~0.1 molecules/µm^2 from the TIRFS-RIf data.

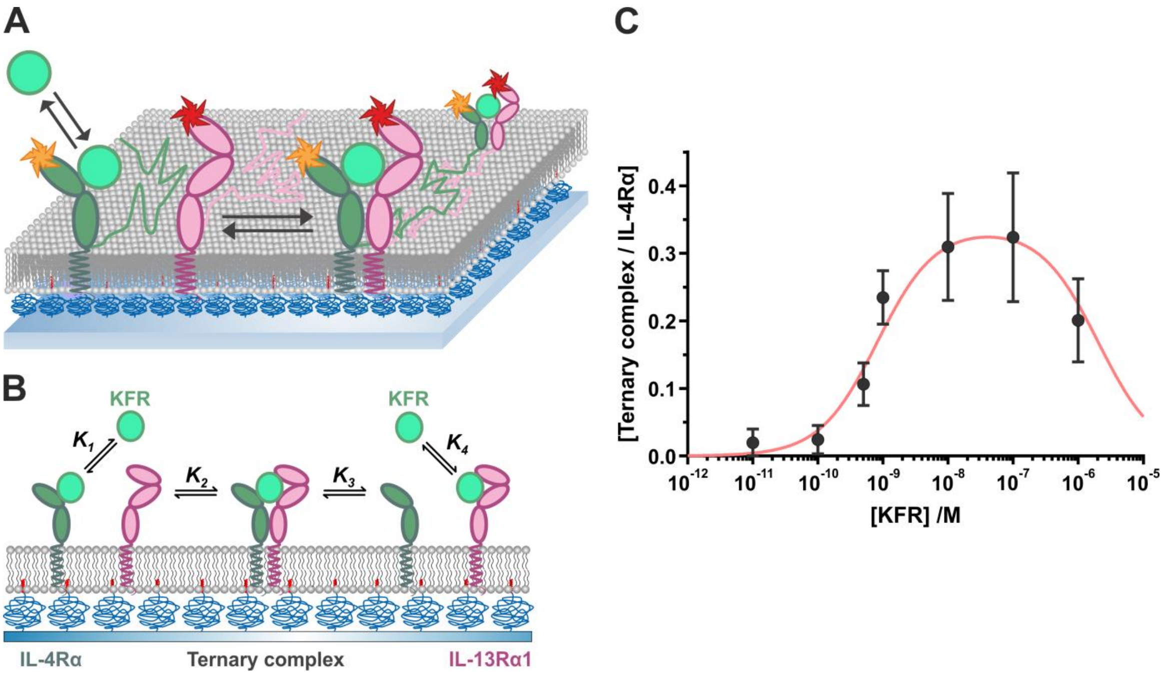

Figure 19. Quantification of KFR binding affinities at single molecule level with transmembrane receptors reconstituted into PSMs. SNAPf-IL-4Rα-TM and SNAPf-IL-13Rα1-TM were expressed in HEK 293T cells and labeled with BG-547 and BG-647, respectively. **(A)** After affinity purification, receptors were reconstituted into 98/2 mol% DOPC/DOPS polymer-supported membranes and their dimerization was quantified by single molecule co-localization. **(B)** KFR-induced dimerization of IL-4Rα and IL-13Rα1 is determined by four equilibria. K_1 and K_4 are volume dissociation constants associated with the binary complex equilibria (unit: [mol/l]). The constants K_2 (corresponding to K_D^T in Fig. 12) and K_3 are surface dissociation constants related to the ternary complex equilibria (unit: [molecules/µm²]). **(C)** Dimerization of ^{DY547}IL-4Rα-TM and ^{DY647}IL-13Rα1-TM as a function of KFR concentration, fitted with a model that is defined by the four equilibrium dissociation constants depicted in B as well as the receptor and ligand concentrations as described in detail in [203]. Obtained dissociation constants: K_1=1.7±1.1 nM, K_2=0.32±0.09 µm^{-2}, K_3=(0.54±1.0) 10^{-3} µm^{-2}, K_4=1.0±1.9 µM.

Analogous TIRFS-RIf experiments were carried out using ^{AT488}DN4$_D$ and ^{OG488}IL-13. No significant receptor dimerization was detectable for ^{AT488}DN4$_D$ (Figure 18B), in line with its heavily reduced IL-13Rα1 binding affinity. With ^{OG488}IL-13, for which the opposite sequence of subunit binding is assumed (Figure 12B), a K_D^T of (13±11) molecules/µm^2 was obtained for the interaction of IL-13Rα1-ECD/IL-13 with IL-4Rα-ECD, suggesting a somewhat more efficient ternary complex formation as for IL-4$_D$ (Figure 18B).

4.1.2 Ternary complex lifetimes correlate with 2D affinities

Different binding affinities towards the receptor subunits are accompanied by changes in the interaction kinetics, which has important implications for the formation and the lifetime of individual complexes. Thus, chasing experiments in combination with Förster resonance energy transfer (FRET) were employed to quantify the two-dimensional dissociation kinetics of receptor dimers in the plane of a membrane [85, 219].

For this purpose, IL-13Rα1-ECD site-specifically labeled with a donor fluorophore via an N-terminal ybbR-tag (^{AF568}IL-13Rα1-ECD) and IL-4 carrying an acceptor fluorophore (^{DY647}IL-4) were used to monitor the dissociation of IL-13Rα1 from IL-4/IL-4Rα in the ternary complex as depicted in the carton in Figure 20A. For these experiments, the K84D mutation of IL-4 was not required as dissociation in plane of the membrane was probed and therefore ligand dissociation from IL-4Rα was not necessary. Chasing with unlabeled IL-4 ensured very rapid and tight binding to IL-4Rα-ECD, allowing for maximum contrast and time resolution of this assay. Under these conditions, the two-dimensional dissociation of ^{DY647}IL-4/IL-4Rα-ECD from ^{AF568}IL-13Rα1-ECD was monitored by a decay in FRET, as observed in both the donor and the acceptor channel (Figure 20A, dashed rectangle).

Comparison of the mass signal for ^{DY647}IL-4 binding to the surface and the recovery of the donor fluorescence confirmed that the dissociation of the ternary complex could be quantified by this method (Figure 20B), yielding a two-dimensional dissociation rate constant k_d^T of (0.23±0.04) s^{-1}. In case of ^{DY647}RGA, a significantly faster dissociation was observed, which could not be temporally resolved by this assay (Figure 20C). Moreover, only negligible ternary complex dissociation prevented the accurate measurement of k_d^T for ^{DY647}KFR. However, a more than tenfold decreased k_d^T (<0.002 s^{-1}) could be estimated for the latter IL-4 agonist (Figure 20D), in line with its increased IL-13Rα1 binding affinity.

By quantifying the stability of the IL-13Rα1-ECD/IL-13 interaction with IL-4Rα-ECD, the interaction predicted to determine the lifetime of ternary complexes formed by IL-13 was also investigated. Since IL-13 exhibits a tenfold faster dissociation from binary than from ternary complexes, the dissociation rate constant k_d^T could be determined without a FRET approach by fitting the ligand dissociation kinetics of an appropriate ligand chasing experiment (Figure 21) [85]. Interestingly, with a k_d^T of (0.0023±0.0007) s^{-1} a similar complex stability was observed for this interaction (IL-13Rα1-ECD/IL-13/IL-4Rα-ECD) as for the IL-4Rα-ECD/KFR/IL-13Rα1-ECD complex (~100-fold higher than for IL-4), while the ternary complex association rate constant was more than 30-fold lower compared to IL-4.

The results of this chapter are summarized in Table 11.

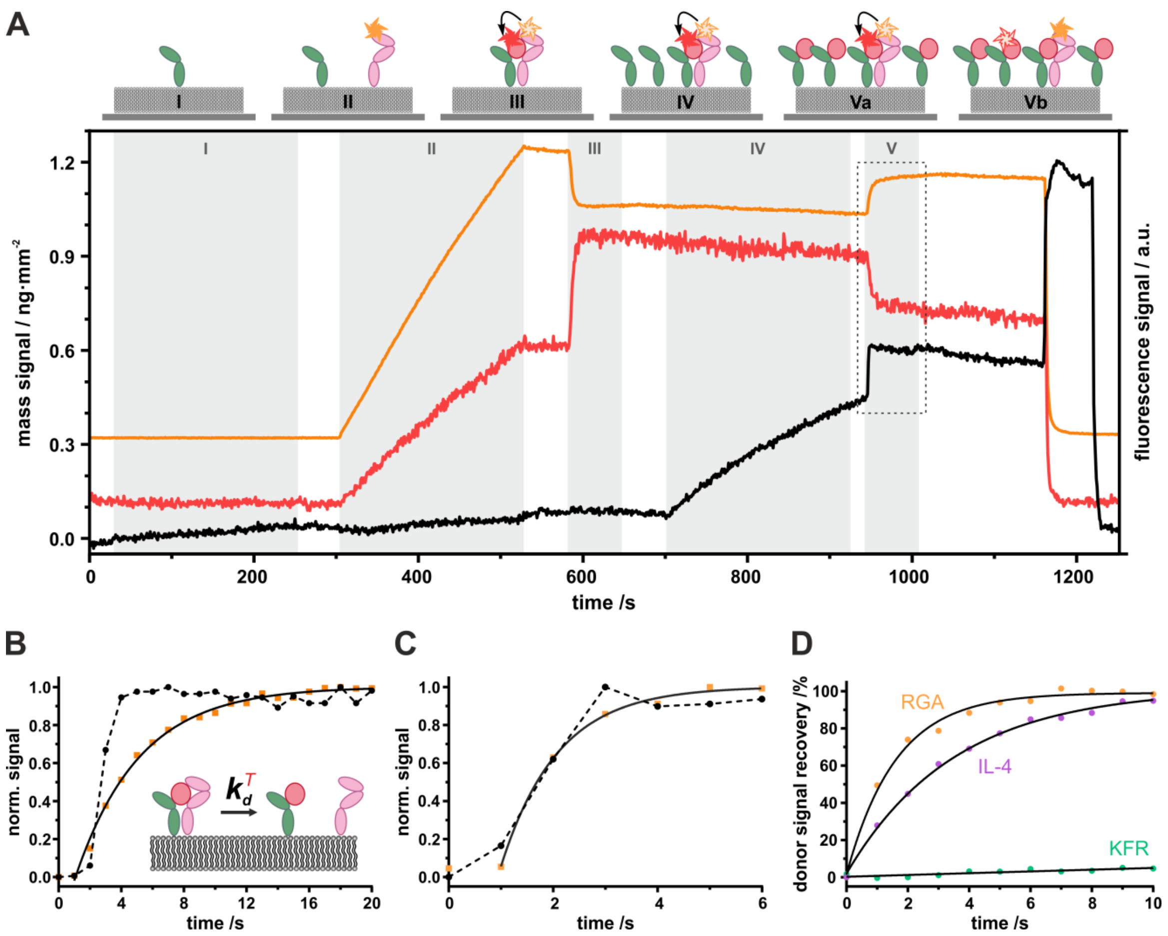

Figure 20. Quantification of 2D dissociation kinetics of ternary complexes induced by IL-4 variants on SSMs by simultaneous TIRFS-RIf detection and FRET. **(A)** Typical assay (cartoon depicted at the top): after sequentially tethering *(I)* IL-4Rα-EC (100 nM) and *(II)* ^{AF568}IL-13Rα1-EC (150 nM, FRET donor) onto a SSM, *(III)* ^{DY647}IL-4 (100 nM, FRET acceptor) was injected to form a ternary complex in an approximate 1:1:1 stoichiometry. AF568 fluorescence (orange curve) decreases during ^{DY647}IL-4 binding due to FRET from ^{AF568}IL-13Rα1-EC upon ternary complex formation, while in turn the DY647 fluorescence (red curve) increases (dotted rectangle). After washing out unbound ligand, *(IV)* excess IL-4Rα-EC (1 µM) is tethered onto the membrane prior to *(V)* fast chasing with unlabeled IL-4 (1 µM) that rapidly occupies all free IL-4Rα-EC. Thus, a 2D exchange of ^{DY647}IL-4/IL-4Rα-EC bound to ^{AF568}IL-13Rα1-EC by IL-4/IL-4Rα-EC is initiated, which is accompanied by recovery of the donor fluorescence with a rate constant corresponding to k_d^T. RIf signal is shown in black. **(B)** Fitting an exponential function (black line) to the donor fluorescence signal (orange points) in the time window of chasing (cf. dashed rectangle in A) yielded k_d^T for IL-4-induced ternary complexes (cf. inset). Comparison of fluorescence and the corresponding mass signal (black points and dashed line) indicates the time resolution of this assay and excludes a limitation by chasing velocity. **(C)** Overlapping fluorescence and mass signals for RGA-induced complexes due to limited association kinetics of the chasing ligand. **(D)** Comparison of donor fluorescence recovery (i.e. dissociation kinetics) obtained for ^{DY647}RGA (orange), ^{DY647}IL-4 (violet) and ^{DY647}KFR (green). Depicted curves show representative single experiments.

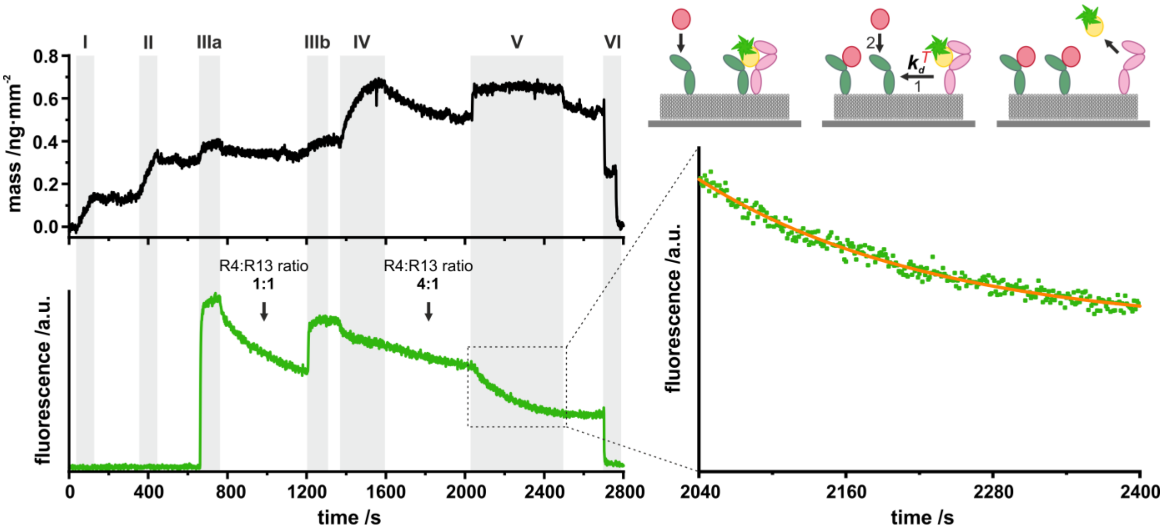

Figure 21. Quantification of 2D dissociation kinetics of IL-13 induced ternary complexes on SSMs by simultaneous TIRFS-RIf detection**.** Cartoon depicts chasing mechanism. During chasing IL-4Rα-ECD dissociating from a ternary complex *(step 1)* readily binds IL-4 *(step 2)* with sub-nanomolar affinity and is not available for ternary complex re-assembly. ^{OG488}IL-13/IL-13Rα1-ECD dissociates faster than ternary complexes, whose dissociation rate k_d^T is the limiting step in this experiment and is obtained by fitting the decreasing fluorescence signal (left, dashed rectangle) with an exponential function (right). Note that in the depicted representative experiment ligand dissociation at increased surface concentration of the second receptor chain IL-4Rα-ECD (4:1 ratio) is significantly lower (second dissociation phase) compared to the dissociation at stoichiometrically equal amounts of receptors (first dissociation phase, cf. Fig. 17A). Experimental procedure on SSM: *(I)* Tethering of IL-13Rα1-ECD and *(II)* IL-4Rα-ECD, *(IIIa and IIIb)* followed by two injections of ^{OG488}IL-13 and *(IV)* additional tethering of excess IL-4Rα-ECD. *(V)* Chasing by injection of 1 µM IL-4. *(VI)* Final Imidazole wash for surface regeneration.

Table 11. Type II IL-4 receptor 2D binding parameters measured in artificial membranes and live cells.

Interacting moieties	k_a^T **[mol^{-1}mm^{2}s^{-1}]^a**	k_d^T **[s^{-1}]^a**	K_D^T **[µm^{-2}]^a**	K_D^T **[µm^{-2}]^b**
IL-4/IL-4Rα ↔ IL-13Rα1	$(3.8\pm1.0)\cdot10^{15}$	0.23±0.04	36±15	0.1±0.1
IL-13/IL-13Rα1 ↔ IL-4Rα	$(1.1\pm0.6)\cdot10^{14}$	0.0023±0.0007	13±11	0.4±0.2
KFR/IL-4Rα ↔ IL-13Rα1	-	<0.002	0.3±0.1	0.4±0.2
RGA/IL-4Rα ↔ IL-13Rα1	-	-	296±104	1.2±0.6

[a] Molecular interactions determined in artificial membranes, K_D^T in [molecules/µm^2]

[b] Effective K_D^T [molecules/µm^2] estimated from single molecule dimerization assays in the plasma membrane of living cells (see chapter 4.1.5)

4.1.3 Signaling complex mobility and STAT6 activation do not depend on 2D affinities

The comprehensive quantitative picture of the molecular properties governing receptor assembly confirmed a broad spectrum of two-dimensional binding affinities and rate constants (Table 11) suitable for a systematic correlation with receptor assembly and activation in living cells.

At first, the interaction of IL-4 variants and IL-13 site-specifically labeled with DY647 (^{DY647}IL-4 and ^{DY647}IL-13) with the endogenous cell surface receptor was investigated by single molecule imaging techniques in order to explore the spatiotemporal organization of type II IL-4 signaling complexes in the plasma membrane under physiological conditions. Using PEGylated glass coverslips [60], ligand binding to the surface of HeLa cells, which were confirmed to express IL-4Rα and IL-13Rα1, but not γ_c (Figure 22A), was observed by total internal reflection fluorescence microscopy (TIRFM) at single molecule level (Figure 22B). Individual ligands diffusing in the plasma membrane could be discerned as confirmed by single step photobleaching at elevated laser power (Figure 22C). Under saturating ligand concentrations (2 nM), similar densities of receptor complexes (0.06 – 0.08/µm²) were observed for ^{DY647}IL-4 and its variants ^{DY647}KFR, ^{DY647}RGA and ^{DY647}DN4 as well as for ^{DY647}IL-13 (Figure 22D). A control experiment proved highly specific ligand binding to endogenous IL-4Rα, as the total amount of bound ^{DY647}IL-4 was drastically reduced after blocking the receptor with unlabeled KFR (Figure 22D). No tendency of clustering was observed, but a stochastic receptor distribution in the plasma membrane.

Under these conditions, individual ligands could be readily tracked with high fidelity (Figure 22B) and their diffusion properties could be quantified by evaluating the trajectories. Mean square displacement (MSD) analysis confirmed random diffusion of ligand-bound receptors in the plasma membrane (see next chapter). Typically, ~25% of the tracked molecules were immobile, which can in part be ascribed to non-specific adsorption to the coverslip surface as well as to complexes involved in endocytosis. For this reason, the immobile fraction was removed from the dataset prior to further analyses to ensure that only ligands bound to the cell surface were covered. Diffusion constants, obtained by fitting step-length histograms (Figure 22E) to a two-component model including a fixed slow and variable fast mobile fraction, revealed a significantly reduced mobility of ^{DY647}KFR (0.086±0.001 µm²/s) compared to ^{DY647}DN4 (0.113±0.002 µm²/s). Since DN4 is supposed to interact with IL-4Rα only, these results suggest that a loss in receptor mobility is caused by the ligand-induced receptor dimerization. Similar changes in the diffusion properties upon ligand-induced complex assembly have been observed for the type I interferon receptor. Notably, comparable slowed mobility as for KFR was observed for all IL-4 variants (except DN) and IL-13 (Table 12), indicating a similar ability to form signaling complexes in the plasma membrane.

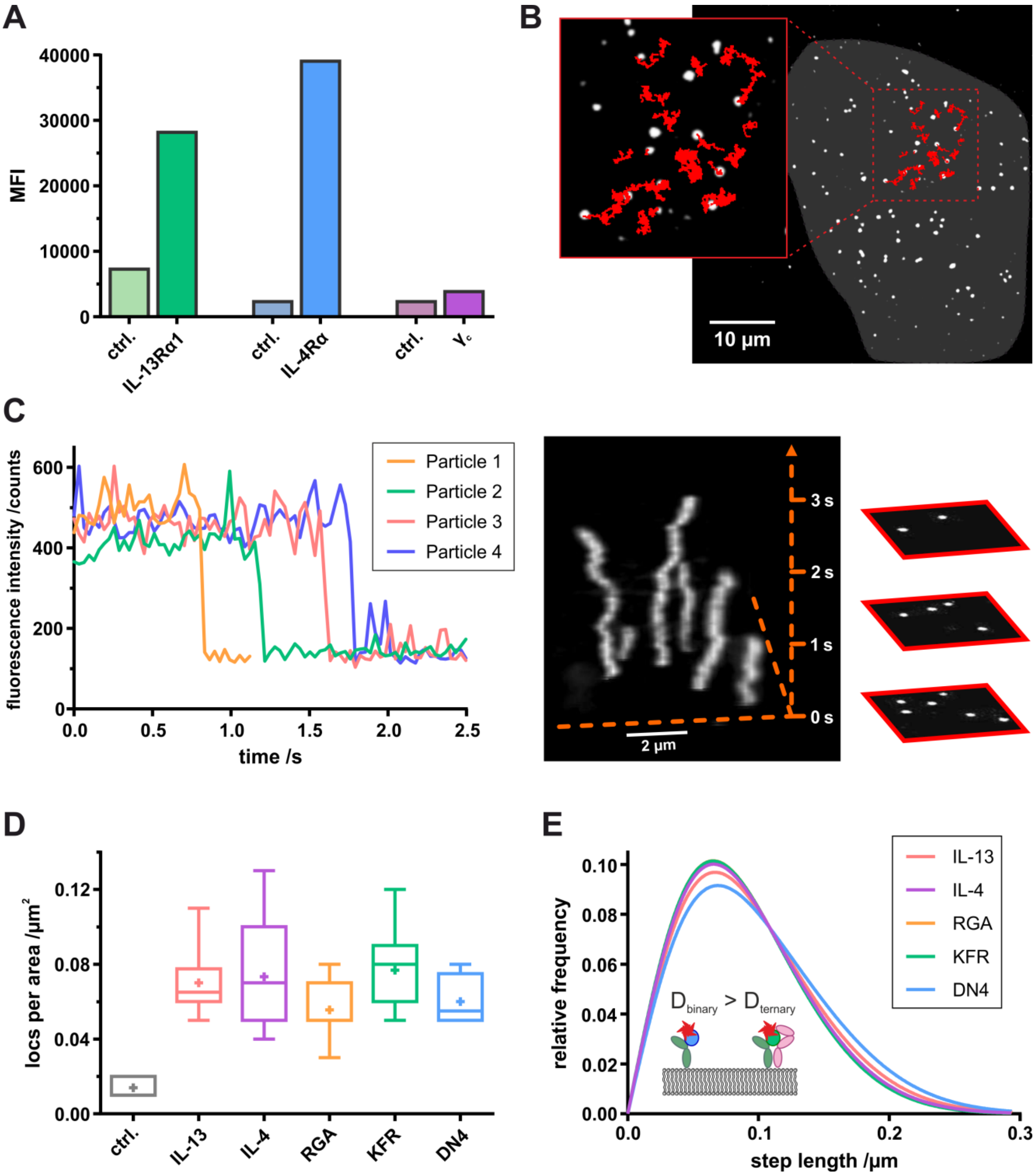

Figure 22. Binding of IL-4 agonists and IL-13 to endogenous type II IL-4 receptors on Hela cells. (A) Expression of type I and type II IL-4 receptor chains on the surface of HeLa cells. Cells were stained with fluorescently labeled antibodies against IL-13Rα1, IL-4Rα and γ_c. Expression levels were assessed by flow cytometry. Appropriate isotype controls served as negative control. **(B)** Live-cell single molecule localization and tracking of ^{DY647}KFR binding to endogenous IL-4Rα and IL-13Rα1 on the surface of a HeLa cell (indicated by grey background). Red lines depict

single molecule trajectories. **(C)** Single-step photobleaching of ^{DY647}A11. **(D)** Quantification of surface-bound IL-4 variants and IL-13 on single molecule level. As control for specific binding, IL-4Rα receptors were blocked with 20 nM unlabeled KFR before ^{DY647}IL-4 binding. Data from n≥10 cells (n=5 cells for DN4 and ctrl.). **(E)** Comparison of the step length distributions for ^{DY647}IL-13, ^{DY647}IL-4, ^{DY647}RGA, ^{DY647}KFR and ^{DY647}DN4, fitted by considering two components corresponding to a slow and a fast mobile fraction. Fitted curves are based on data from n>350 single-molecule trajectories (n=200 for DN4) with minimum length of 150 frames. Individual step lengths were determined for a time lapse of 32 ms (1 frame) and histogramed.

Table 12. Average diffusion constants obtained from single molecule (co-)tracking data.

Ligand	**D [µm²/s]**
DN4 *(primarily binary complex)*	0.113±0.002[a]
KFR *(primarily ternary complex)*	0.086±0.001[a]
IL-4	0.091±0.001[a]
RGA	0.088±0.001[a]
IL-13	0.099±0.001[a]
IL-4Rα (w/o ligand)	0.119±0.010[b]
IL-4Rα (w/ KFR)	0.107±0.002[b]
IL-13Rα1 (w/o ligand)	0.140±0.012[b]
IL-13Rα1 (w/ KFR)	0.108±0.001[b]
IL-4Rα/IL-13Rα1 dimers (ligand-induced)	0.087±0.003[c]

[a] Obtained with DY647-labeled ligands bound to the endogenous receptor

[b] Mean values determined in cells co-expressing IL-4Rα and IL-13Rα1 w/o and w/ addition of KFR

[c] Mean values from ^{DY647}IL-4Rα/^{TMR}IL-13Rα1 co-trajectories in presence of IL-4, IL-13 or KFR

In line with these experiments, ligand-induced STAT6 phosphorylation probed by phospho-flow cytometry showed largely overlapping potencies (Figure 23A) and similar kinetics (Figure 23B) of STAT6 activation for all IL-4 variants, with only a minor increase in potency observed for KFR. In contrast, significantly lower potency of IL-13 and slower signaling kinetics compared to the IL-4 variants were observed, which could be related to the substantially lower association rate (cf. chapter 4.2.2).

In conclusion, these results suggest efficient receptor assembly by the examined IL-4 variants irrespective of the large differences in IL-13Rα1 binding affinity, hinting towards a spatiotemporal organization of IL-4Rα and IL-13Rα1 in the cellular context.

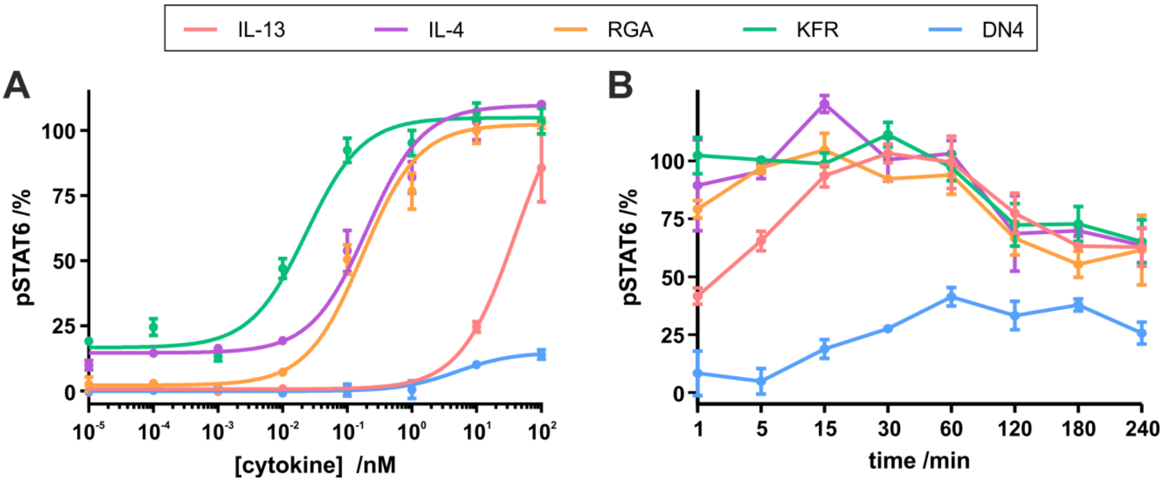

Figure 23. STAT6 phosphorylation activities of IL-4 agonists and IL-13 in HeLa cells analyzed by phospho-flow cytometry. **(A)** Fitted dose-response curves of STAT6 phosphorylation observed after stimulation for 15 min and **(B)** kinetics of STAT6 phosphorylation after stimulation with 1 µM of the indicated agonist. Compared to IL-4 and its variants, the potency and the rate of STAT6 activation is lower for IL-13. Quantification of the total amount of phosphorylated STAT6 was achieved by labeling with pSTAT6-specific antibodies coupled to fluorescent dyes.

4.1.4 Randomly distributed IL-4Rα and IL-13Rα1 are dimerized by the ligand in the plasma membrane

To identify the cellular determinants governing receptor dimerization, the receptor subunits were visualized in the plasma membrane by simultaneous dual color single molecule fluorescence imaging. For this purpose, IL-4Rα fused to the SNAPf-tag and IL-13Rα1 fused to the HaloTag were co-expressed in HeLa cells, labeled with BG-DY647 (^{DY647}IL-4Rα) and HTL-TMR (^{TMR}IL-13Rα1), respectively (Figure 24A), and imaged by TIRF microscopy.

Individual ^{DY647}IL-4Rα and ^{TMR}IL-13Rα1 could be discerned at a surface concentration 0.1-0.5 molecules/µm², representing nearly physiological conditions with only minor elevated density compared to the endogenous receptor (~5-10-fold, cf. Figure 22D). The integrity of the cloned receptor constructs with respect to ligand recognition and ligand-receptor complex stability was confirmed by chasing experiments. To this end, the dissociation of ^{DY647}IL-13 or ^{DY647}IL-4 bound to cells transiently overexpressing either HaloTag::IL-13Rα1 or SNAPf::IL-4Rα was probed by addition of an unlabeled competitor. As predicted by the *in vitro* measurements, dissociation of IL-13 was substantially faster compared to IL-4 under chasing conditions (Figure 24B), verifying intact ligand-receptor interactions of the generated constructs.

Single molecule tracking enabled to follow individual receptors for extended periods and trajectory analyses yielding MSD-plots and diffusion constants confirmed random diffusion of both receptor subunits (Figure 24C) with similar diffusion properties as observed for DN4 bound to the endogenous receptor (Table 12). Likewise, an equivalent level of typically 25% immobile molecules was observed, which were excluded from further analyses.

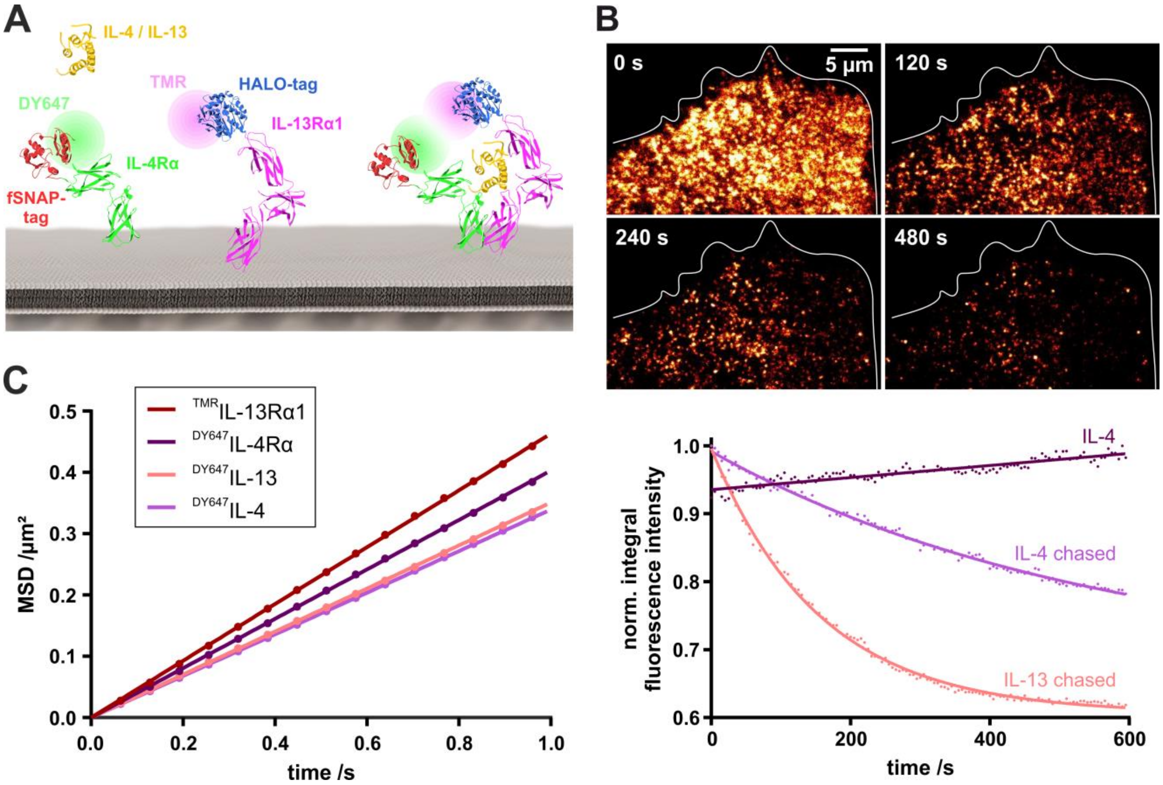

Figure 24. Simultaneous dual color single molecule imaging of the type II IL-4 receptor in the plasma membrane of HeLa cells. **(A)** Schematic representation of the receptor chains labeled for microscopy studies. IL-4Rα (green) was fused to the SNAPf-tag and labeled with BG-DY647. IL-13Rα1 (magenta) was fused to the HaloTag and labeled with HTL-TMR. **(B)** Time-lapse TIRF microscopy imaging of DY647-labeled ligands bound to HeLa cells, transiently over-expressing the corresponding receptor chain, after addition of an unlabeled competitor. Images show chasing of ^{DY647}IL-13 bound to HaloTag-IL-13Rα1 with IL-13. Quantification of the relative integral fluorescence over time yields ligand dissociation curves, as exemplary depicted for ^{DY647}IL-13 and ^{DY647}IL-4, respectively. As a control for photobleaching, fluorescence of ^{DY647}IL-4 without competitor is shown (the slight increase is caused by endocytosis of ^{DY647}IL-4 during the experiment, since endosomes close to the plasma membrane contribute to the integral fluorescence). **(C)** Diffusion properties depicted as mean square displacement (MSD) plots of ^{TMR}IL-13Rα1 (w/o ligand, dark rose), ^{DY647}IL-4Rα (w/o ligand, violet), ^{DY647}IL-13 (pink) and ^{DY647}IL-4 (purple). Data are based on trajectories with min. length of 150 frames, pooled from experiments of at least 10 cells.

The receptor dimerization was analyzed by single molecule co-localization and subsequent co-tracking of ^{DY647}IL-4Rα and ^{TMR}IL-13Rα1. Thereby, no indication of receptor pre-dimerization was found (Figure 25A). Upon ligand addition, however, individual receptor dimers diffusing in the plasma membrane could be clearly identified and tracked for several seconds (exemplary depicted for IL-4 in Figure 25A, B), even in case of RGA. Analysis of time-dependent inter-subunit distances extracted from co-trajectories verified the highly correlated motion in a quantitative manner, as the observed distances were well below the applied distance threshold of ~200 nm (Figure 25C).

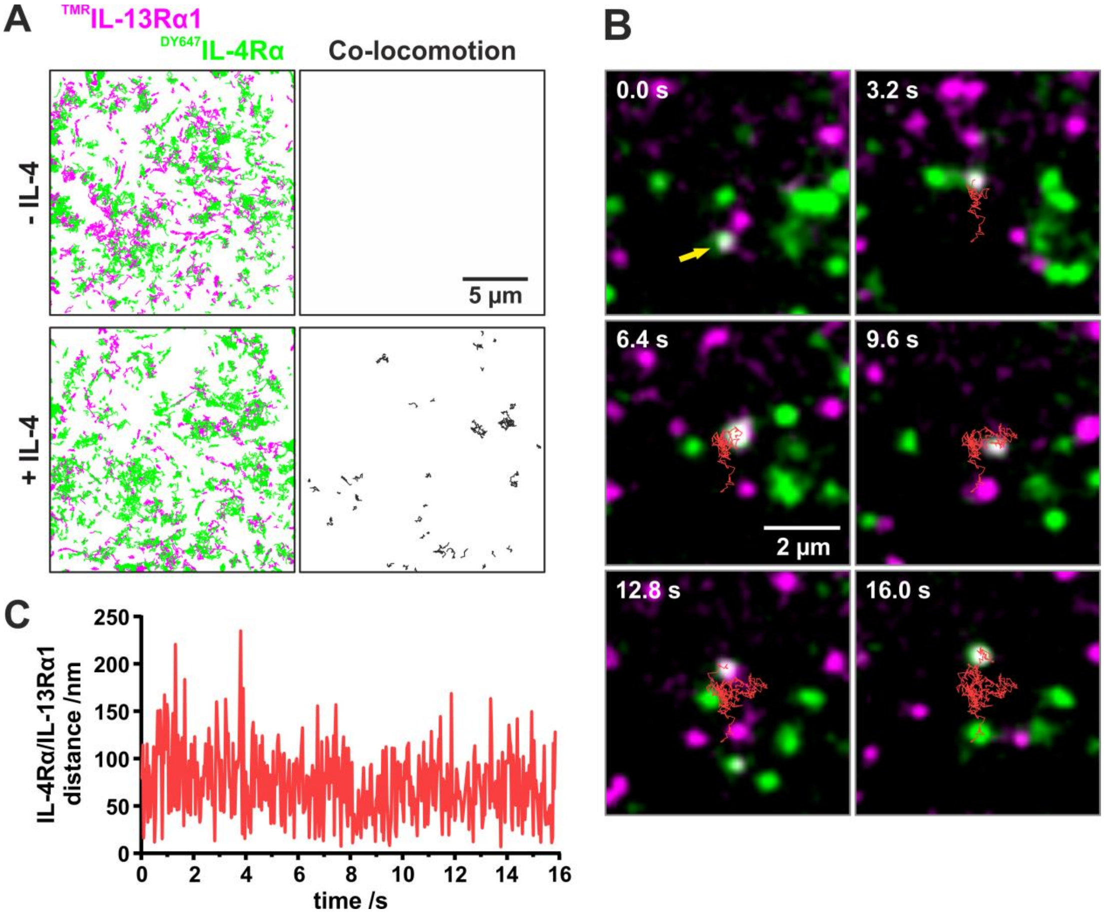

Figure 25. Receptor dimerization in the plasma membrane probed by single molecule co-locomotion analysis in HeLa cells of **(A)** ^{DY647}IL-4Rα and ^{TMR}IL-13Rα1 in the absence and in the presence of 20 nM IL-4. Only trajectories with a minimum length of 10 frames are shown. **(B)** Images show an individual ^{DY647}IL-4Rα/^{TMR}IL-13Rα1 dimer in presence of 20 nM IL-4 co-tracked over 500 frames (16 s). The corresponding trajectory is depicted as a red line. **(C)** Distance between the two molecules depicted in B in each frame.

Dimerized receptors subunits exhibited similar diffusion properties independent of the added ligand. Importantly, a small, but significant (verified by Student's t-test, $p < 0.0001$)

reduction in mobility of ^{DY647}IL-4Rα and ^{TMR}IL-13Rα1 from 0.119±0.010 µm^2/s and 0.140±0.012 µm^2/s, respectively, to 0.087±0.003 µm^2/s upon ligand-induced dimerization was noticed (Figure 26). Thus, the diffusion constant of receptor dimers matches the diffusion constant obtained for ^{DY647}KFR bound to the endogenous receptor (0.086±0.001 µm^2/s, Table 12).

These results clearly confirm the hypothesis of ligand-induced receptor dimerization in the plasma membrane and suggest unexpectedly high dimerization efficiency for all ligands.

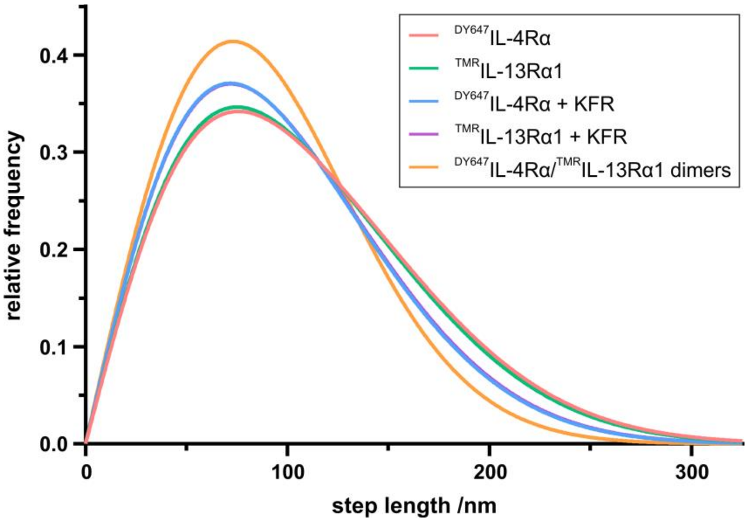

Figure 26. Diffusion properties of ^{DY647}IL-4Rα and ^{TMR}IL-13Rα1 in the plasma membrane of HeLa cells before and after stimulation with 200 nM KFR as well as of ligand-induced ^{DY647}IL-4Rα/^{TMR}IL-13Rα1 dimers presented as fitted step-length distributions (time lapse 32 ms, 1 frame), based on two components corresponding to a fixed slow and a variable fast mobile fraction. Depicted curves are based on data of a representative single cell experiment comprising n>400 trajectories (n=24 for dimers) with min. length of 10 frames.

4.1.5 Highly efficient receptor dimerization with minor variations by 2D affinities

In order to quantify the dimerization and spatial organization of the receptor in the plasma membrane more precisely, the single molecule localization data was analyzed by particle image cross-correlation spectroscopy (PICCS) [166]. This evaluation technique allows for a robust quantification of the fraction of two spectrally separated molecule species that are spatiotemporally correlated by fitting a cross-correlation function calculated from the molecule positions in an ensemble approach.

^{DY647}IL-4Rα and ^{TMR}IL-13Rα1 did not show any significant spatial cross-correlation in absence of ligand (Figure 27A, left), confirming that the receptor subunits are neither pre-dimerized nor pre-organized in the plasma membrane. Instead, the shape of the cumulative correlation function indicates a random/uniform receptor distribution, as the section after the curvature shows an invariably linear dependency from the squared search radius. In presence of IL-4 at a concentration saturating all IL-4Rα subunits (20 nM), however, dimerization could clearly be identified as an increase of the labeling degree-limited correlated fraction (α) to about 11 % (Figure 27A, right and Figure 27B). An observed basal α of not more than 2% was attributed to the goodness of the fitted parameters defining the correlation function and to random co-localizations (Figure 27B).

For an absolute quantification of receptor dimerization, a reliable determination of the degree of labeling achieved in these assays is required, which was obstructed by the substantial receptor turnover after cell surface labeling [160, 161]. Therefore, by taking advantage of the highly asymmetric binding affinities of IL-4 towards the receptor subunits, labeled IL-4 was used to quantify the fraction of IL-4-bound IL-4Rα forming a ternary complex with IL-13Rα1. For this purpose, the interaction of ^{DY647}IL-4 with ^{TMR}IL-4Rα and with ^{TMR}IL-13Rα1, respectively, was quantified by PICCS in separate experiments. A cross-correlated fraction of ~18 % was observed for the interaction of ^{DY647}IL-4 (in complex with unlabeled IL-4Rα) and ^{TMR}IL-13Rα1 compared to ~28 % for the ^{DY647}IL-4/^{TMR}IL-4Rα complex (Figure 27C). These results implicate that more than 60% of IL-4Rα bound to IL-4 on the cell surface forms a ternary complex with IL-13Rα1.

Taking into account the average cell surface concentrations of ^{DY647}IL-4Rα (0.65/µm^2) and ^{TMR}IL-13Rα1 (0.77/µm^2) quantified by single molecule localization and corrected for the degree of labeling (assessed by an independent calibration measurement with a Halo-tag/SNAPf-tag double construct), an effective K_D^T of ~0.1 molecules/µm² was estimated for IL-13Rα1 interacting with the IL-4Rα/IL-4 complex. Thus, receptor recruitment in the plasma membrane is 200- to 300-fold more efficient compared to the K_D^T measured with receptor ectodomains tethered onto artificial membranes (Table 11).

Furthermore, only minor differences in the dimerization efficiencies were observed for the IL-4 mutants as well as for IL-13 (Figure 27B and Table 13), despite the very large differences observed *in vitro*. Thus, the increase in IL-13Rα1 binding affinity of the KFR mutant did not yield any increase in dimerization efficiency (α ~8.5%, K_D^T ~0.4/µm^2). It rather had a slightly weakening effect on the complex assembly, maybe caused by the increased affinity of KFR towards IL-13Rα1, which possibly leads to a reduced amount of free IL-13Rα1 available for dimerization (cf. bell-shaped dimerization in PSM-experiment; Figure 19C). A small, yet significant drop in dimerization efficiency was, however, observed for RGA (α ~5.2%, K_D^T ~1.2/µm^2), resulting in an approximately 10-fold higher

K_D^T compared to IL-4. Although excluded by the *in vitro* experiments, even for the variant DN4 with immeasurable binding affinity for IL-13Rα1, receptor dimerization in the plasma membrane above the background could be detected (α ~2.8%), in line with its residual STAT6 phosphorylation activity (Figure 23). Interestingly, the dimerization efficiency of IL-13 (α ~7.4%, K_D^T ~0.4/µm^2) turned out to be lower compared to IL-4, despite the overall higher K_D^T of IL-4 observed *in vitro*, which may be explained by the ~20% excess of IL-13Rα1 in all experiments.

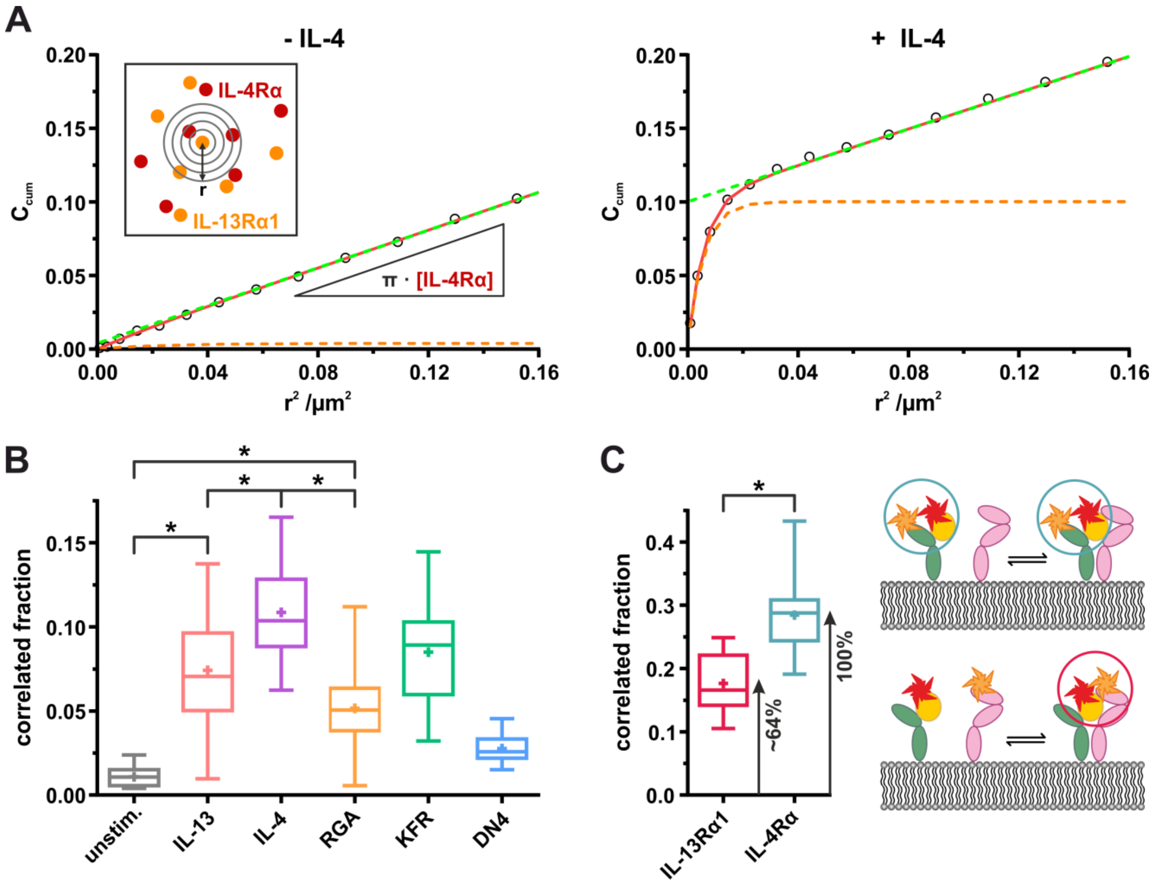

Figure 27. Quantification of receptor dimerization in the plasma membrane of HeLa cells. **(A)** Spatial correlation of ^{TMR}IL-13Rα1 and ^{DY647}IL-4Rα molecules for a representative single cell in absence (left) and presence (right) of IL-4, analyzed by PICCS. Black circles: cumulative correlation function (C_{cum}) obtained from single molecule localizations, averaged over frames 1-20. Dashed green line: linear contribution of C_{cum}. Orange dashed line: C_{cum} after linear term subtracttion (red curve). **(B)** Correlated fraction of ^{TMR}IL-13Rα1 and ^{DY647}IL-4Rα for the examined ligands. Depicted data are pooled from at least two independent experiments with n>20 cells (unstim.: n=9 cells, DN4: n=6 cells). **(C)** Absolute quantification of IL-4-induced receptor dimerization by comparison of the apparent fraction of ^{DY647}IL-4 bound to either ^{TMR}IL-13Rα1 (red, DOL-limited fraction of ligand in a ternary complex) or ^{TMR}IL-4Rα (blue, maximum achievable, DOL-limited correlated fraction), determined by PICCS. Data are based on n=16 cells (IL-13Rα1 + IL-4) and n=9 cells (IL-4Rα + IL-4). Statistical analysis by a two-sample Kolmogorov-Smirnov test (*, $p < 0.05$).

Table 13. Receptor dimerization by IL-4 variants and IL-13 quantified by PICCS.

Ligand	α [%]	σ [μm]	ρ [μm^{-2}]	Norm. α [%][a]
unstimulated	1.1±0.6	0.14±0.08	0.24±0.09	-
DN4	2.8±1.0	0.11±0.05	0.23±0.07	11±10
RGA	5.2±2.1	0.14±0.05	0.26±0.09	26±18
IL-13	7.4±3.2	0.07±0.03	0.24±0.10	40±25
KFR	8.5±2.7	0.09±0.03	0.30±0.11	47±22
IL-4	10.9±2.7	0.07±0.02	0.28±0.12	62±22
IL-4Rα + IL-4	28.4±5.5	0.07±0.01	0.40±0.10	-
IL-13Rα1 + IL-4	17.6±4.7	0.13±0.01	0.31±0.10	-
positive control	38.2±4.0	0.06±0.01	0.57±0.26	-

[a] Cross-correlated fraction corrected for the basal α and normalized to the maximum dimerization level, obtained from setting the spatial correlation of IL-4 with IL-4Rα and with IL-13Rα1 in relation

These observations substantiate that the dimerization of IL-4Rα and IL-13Rα1 in the plasma membrane is not exclusively controlled by the molecular two-dimensional binding affinities, suggesting a supporting role of the membrane, potentially facilitated by its organization in microscale compartments [110].

4.1.6 Dynamic complex stabilization by actin-dependent membrane micro-compartmentation

Since any pre-organization of the receptor subunits in the absence of ligand was excluded by the PICCS analysis and the observed dimerization efficiencies turned out to be surprisingly high for all variants, the spatiotemporal dynamics of receptor dimers after ligand stimulation were explored in more detail. For this purpose, the correlation length obtained from the PICCS analysis were compared for the different ligands as a measure for the average distance of receptor subunits within assembled dimers. As the correlated fraction is interpreted as ^{TMR}IL-13Rα1 and ^{DY647}IL-4Rα dimers in a ternary complex, which would correspond to an estimated correlation length of 5-10 nm based on the crystal structure [53], the correlation lengths of 50-100 nm experimentally observed upon dimerization by IL-4, KFR and IL-13 can be ascribed to the limited overall single molecule co-localization precision (Figure 28A).

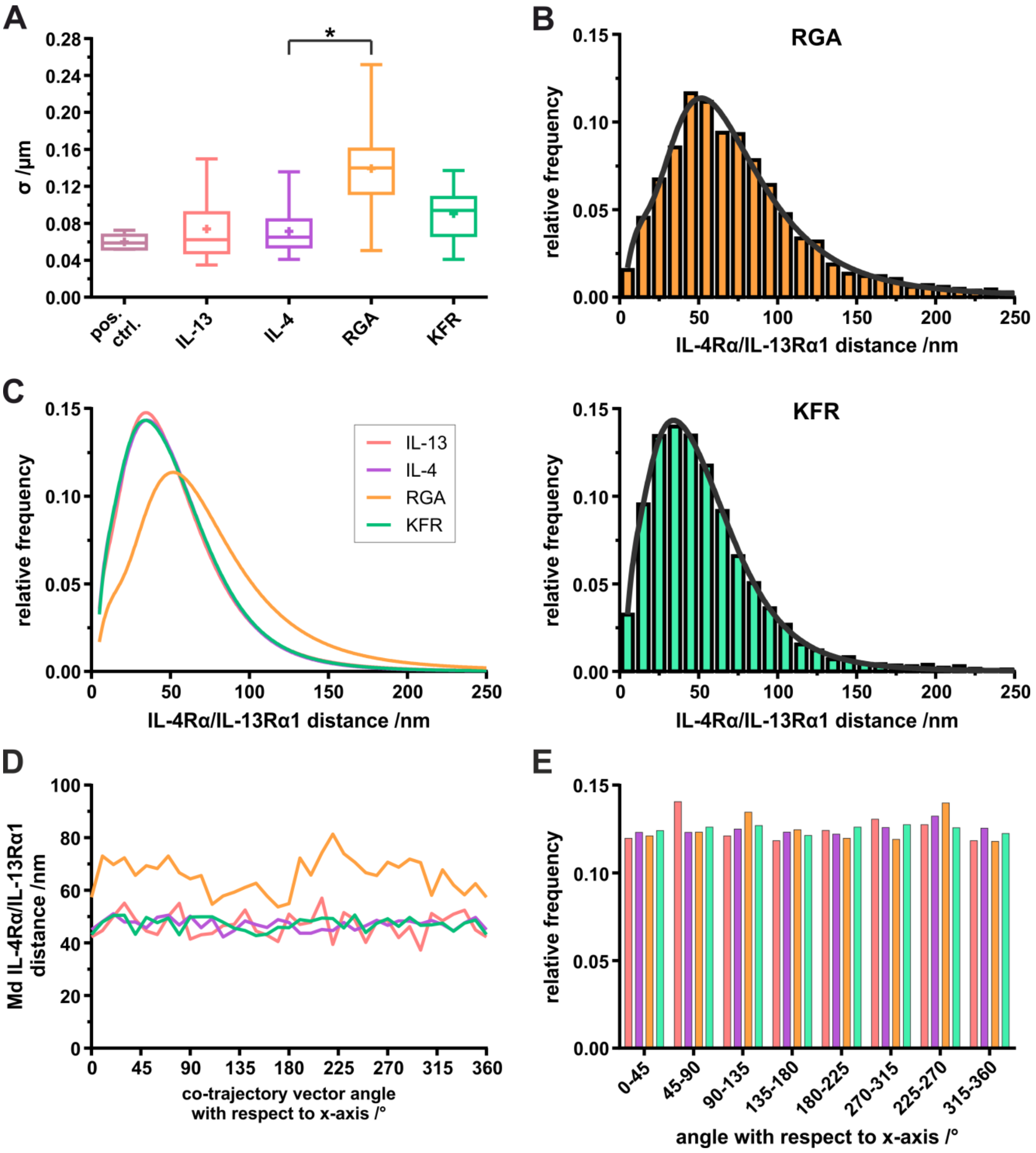

Figure 28. Analysis of inter-subunit distances in receptor dimers. **(A)** Comparison of the correlation length (σ) of ligand-induced ^{DY647}IL-4Rα/^{TMR}IL-13Rα1 dimers obtained by PICCS. Depicted data are pooled from at least two independent experiments with n>20 cells (n=6 cells for pos. ctrl.). **(B, C)** Fitted receptor distance distributions extracted from ligand-induced ^{DY647}IL-4Rα/^{TMR}IL-13Rα1 co-locomotion trajectories. Histogramed data was fitted with a three-component log-normal function as exemplary shown for RGA and KFR in B. Depicted curves are based on data from different cells comprising n>50 trajectories with min. length of 30 frames. **(D)** The median inter-receptor distance is independent of the direction of movement, while the **(E)** distribution of movement directions is equal for all ligands. Statistical analysis by a two-sample Kolmogorov-Smirnov test (*, $p < 0.05$).

Interestingly though, a significantly increased correlation length was found for spatial correlated ^{DY647}IL-4Rα and ^{TMR}IL-13Rα1 receptors upon stimulation with RGA (Figure 28A). Therefore the inter-subunit distances in ^{DY647}IL-4Rα/^{TMR}IL-13Rα1 dimers, identified by dual color single molecule co-tracking analysis, were directly quantified, confirming a significantly increased distance in ternary complexes formed by RGA compared to all other ligands (Figure 28B, C). Importantly, a possible bias by a misalignment of the experimental setup could be excluded, as the distribution of the distances (Figure 28D) and the receptor movement (Figure 28E) were verified to be isotropic in vectorial terms.

The increased inter-subunit distance observed for the mutant most transiently interacting with IL-13Rα1 was hypothesized to be caused by trapping of receptor dimers within submicroscopic membrane compartments, which are spatially not resolvable by the utilized experimental setup. Consequently, the stability of individual complexes was explored by directly probing the low-affinity interaction of IL-4Rα/IL-4 with IL-13Rα1 via dual color single molecule co-tracking. To this end, HaloTag::IL-13Rα1 was expressed at physiological levels in HeLa cells by means of an inducible promotor [202]. After labeling of HaloTag::IL-13Rα1 with HTL-TMR, ^{DY647}KFR or ^{DY647}RGA was added at a concentration sufficient to rapidly bind and saturate endogenous IL-4Rα (2 nM). Because *in vitro* labeling of IL-4 is achieved with a yield > 90%, dimerized receptor subunits could be well detected at these low concentrations, while co-tracking of ^{DY647}KFR or ^{DY647}RGA and ^{TMR}IL-13Rα1 was possible with high fidelity.

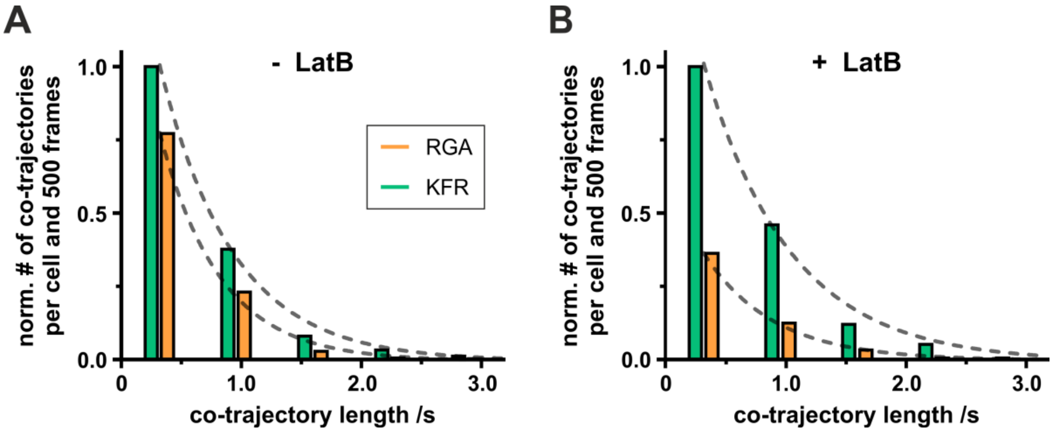

Figure 29. Co-trajectory length analysis of RGA- and KFR-induced ternary complexes (A) without and **(B)** with treatment of HeLa cells with 10 µM Latrunculin B (LatB). Data are based on n>60 (-LatB) and n>17 (+LatB) cells. Co-trajectories shorter than 30 frames were not considered.

The distribution of co-trajectory lengths was taken as a semi-quantitative measure for the complex stability. Very similar patterns were obtained for KFR and RGA (Figure

29A), despite the more than 100-fold faster dissociation of RGA from IL-13Rα1 observed on artificial membranes. While the experimental trajectory length is strongly limited by photobleaching and tracing fidelity, a significant lower complex stability (< 1 s) of receptor dimers induced by RGA was expected from the molecular dissociation kinetics. Thus, confinement of receptors by the cortical membrane skeleton (MSK) [97, 114] was speculated to be responsible for a dynamic stabilization of ternary complexes by ensuring rapid re-association of separated dimers.

The MSK of HeLa cells has been reported to have an average mesh size of ~70 nm [110], in good agreement with the increased mean inter-receptor distance observed for RGA (Table 14). Therefore, the dimerization of receptors was probed in the presence of Latrunculin B (LatB), a compound that partially inhibits actin polymerization by binding to monomeric G-actin [220], thus reducing receptor confinement. For a minimum bias of other cellular functions, a concentration of LatB was applied (10 µM), which resulted in a rapid dissipation of the actin fine structure (< 2 min) while only slightly affecting cell morphology, as confirmed by confocal imaging of HeLa cells stably expressing a fluorescent F-actin marker [221, 222] (Figure 30). Under these conditions, the diffusion constants of IL-4Rα and IL-13Rα1 increased (Figure 31A), as expected for MSK-limited hop diffusion in the plasma membrane [95, 223]. Despite this relatively minor alteration of receptor confinement by LatB treatment, the length of co-trajectories was substantially reduced for RGA, but not for KFR (Figure 29B), which was verified to be not caused by differentially enhanced mobilities (data not shown). The importance of receptor confinement by MSK-dependent membrane microcompartments was further supported by the differences in mobility observed for IL-4 and mutants in presence of LatB: the largest increase was observed for RGA, in line with its higher propensity to exist bound to IL-4Rα only.

Table 14. Distance distributions of IL-4Rα/IL-13Rα1 dimers induced by different ligands.

Component distance	**Component fractions [%]**			
	IL-4	**KFR**	**RGA**	**IL-13**
30 nm	35±2	34±2	**0±2**	30±2
50 nm	54±3	55±3	**34±4**	65±3
70 nm	11±5	10±5	**66±6**	5±5

Data were obtained by fitting inter-subunit distance distributions from co-trajectories of ligand-induced dimers with a three-component log-normal function to adapt the component fractions with its corresponding distances fixed set to 30, 50 and 70 nm. The latter were determined previously by fitting of the distributions with variable fractions and distances.

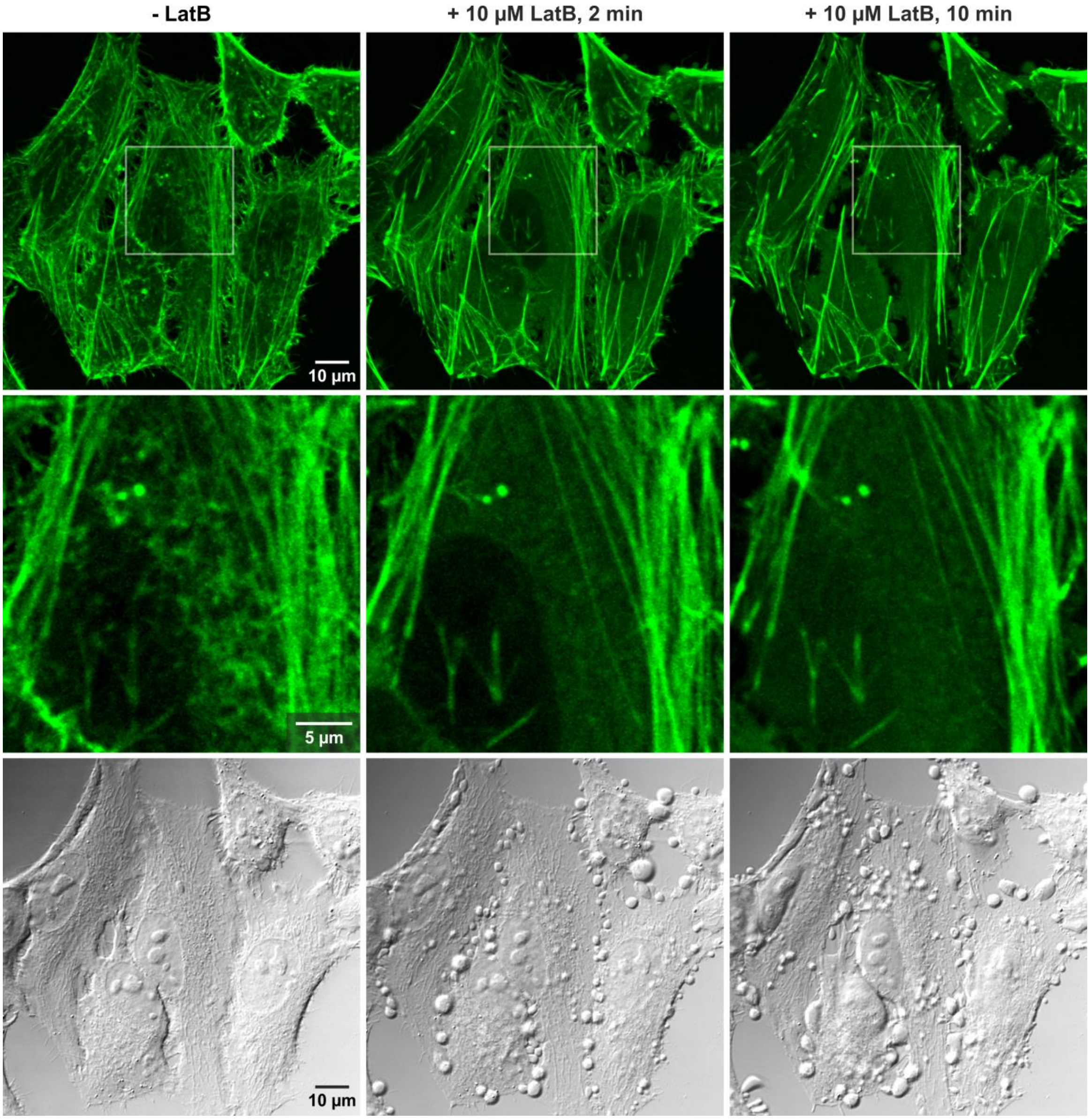

Figure 30. Actin cytoskeleton disruption by Latrunculin B. HeLa cells stably expressing LifeAct-EGFP [221], a small peptide fused to EGFP that binds to F-actin structures, were imaged using an inverted confocal laser scanning microscope (FV1000, Olympus) equipped with a 60x water objective (NA 1.2, Olympus) and an Argon multiline laser (GLG3135, Showa Optronics) before and after addition of 10 µM Latrunculin B (LatB). Fluorescence images (top, middle: enlarged regions) prove actin fine structure loss and DIC images (bottom) confirm detachment of the actin-based cortical membrane skeleton (MSK) from the cell membrane by showing the appearance of membrane blebs and slow shrinking of cells after LatB treatment.

To additionally investigate the relevance of efficient complex re-association by MSK confinement, its effect on membrane-proximal downstream signaling events was investigated by quantifying the maximum level of STAT6 phosphorylation in presence of LatB using phospho-flow cytometry. Strikingly, a substantial decrease in activity was only observed for RGA, consistent with the lower stability of signaling complexes induced by this mutant (Figure 31B), since such a complex destabilization gains influence upon disturbing the actin cytoskeleton and thereby weakening the apparent supportive features of membrane microcompartmentation.

Combined, these results highlight a critical role of the MSK in stabilizing transient receptor dimers, probably by ensuring efficient re-association of dissociated complexes. For some trajectories, re-association events of receptor subunits could even be followed with the spatiotemporal resolution of the utilized experimental setup (Figure 31C), corroborating the relevance of this process under physiological conditions.

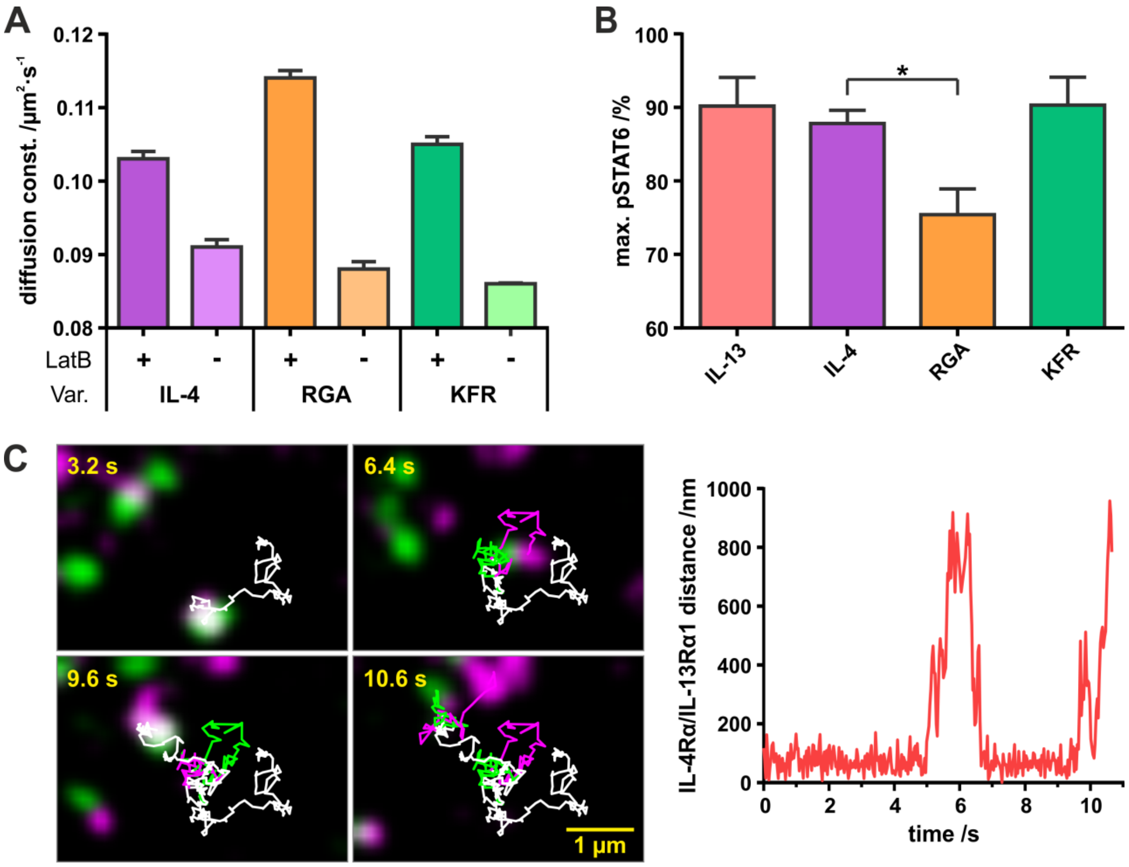

Figure 31. Effects of MSK-disruption on receptor mobility and signaling. (A) Diffusion constants of fluorescent ligand-bound IL-4Rα receptors in absence and in presence of LatB. **(B)** Ligand-dependent maximum relative pSTAT6 level in presence of LatB. HeLa cells were treated with 10 µm LatB, stimulated for 15 min with saturating doses of the respective ligand and relative levels of pSTAT6 compared to untreated cells were analyzed by phospho-flow cytometry using anti-pSTAT6 specific antibodies coupled to fluorescent dyes. Statistical analysis by Student's t-test (*, $p < 0.05$). **(C)** ^{DY647}IL-4Rα (green) and ^{TMR}IL-13Rα1 (magenta) complex re-association at single molecule level in presence of RGA. Images showing the complex at different time points in a 10.6 s time window including its corresponding co-trajectory (white). Right: distance between the two molecules in each frame.

4.1.7 Spatiotemporal receptor dynamics can be mimicked by a hop diffusion model

To validate the hitherto drawn conclusions, a simple spatial-stochastic diffusion-reaction model including two interacting molecular species was established. As proposed by the MSK concept [95], the applied model (described in Figure 32 and in materials and methods section) implemented a submicroscopic, semi-permeable meshwork constraining the diffusion in a two-dimensional interaction space.

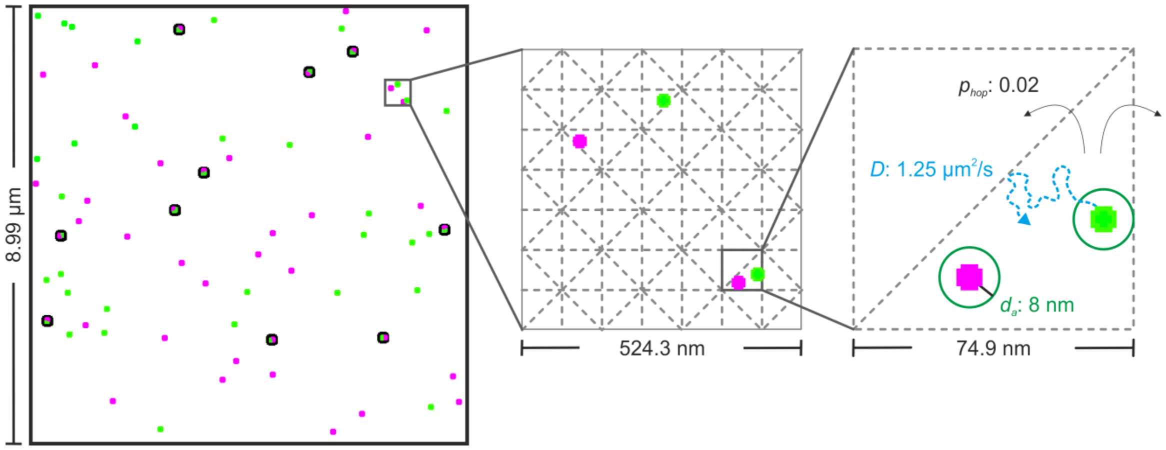

Figure 32. Simulation of spatiotemporal receptor dynamics including MSK-like membrane compartmentation and hop diffusion. Illustration of a representative state during a simulation run. Dots indicate binary complexes of ligand and high affinity ligand-binding receptor subunit (green), and accessory receptor subunits (magenta). Black circles mark ternary complexes. Receptor molecules are diffusing (D = 1.25 µm^2/s) inside membrane compartments (triangles with 74.9 nm edge length) and can pass boundaries (dashed grey lines) with possibility p_{hop} (0.02 s^{-1}). Interactions may occur if two molecules come into closer proximity than an association distance threshold d_a (8 nm). Association and dissociation events take place in dependence of fixed possibilities estimated from spatial correlation analyses in living cells (p_a) or calculated from molecular kinetic rate constants measured *in vitro* (p_d).

To run simulations under preferably realistic conditions, molecular dissociation probabilities and local diffusion properties were parameterized as quantified *in vitro*. Further, by adjusting the hopping and association probabilities, the diffusion properties of the receptor subunits and the ternary complex (Figure 33) as well as total receptor levels in complex (Figure 34A) could be closely adapted to the experimentally obtained data.

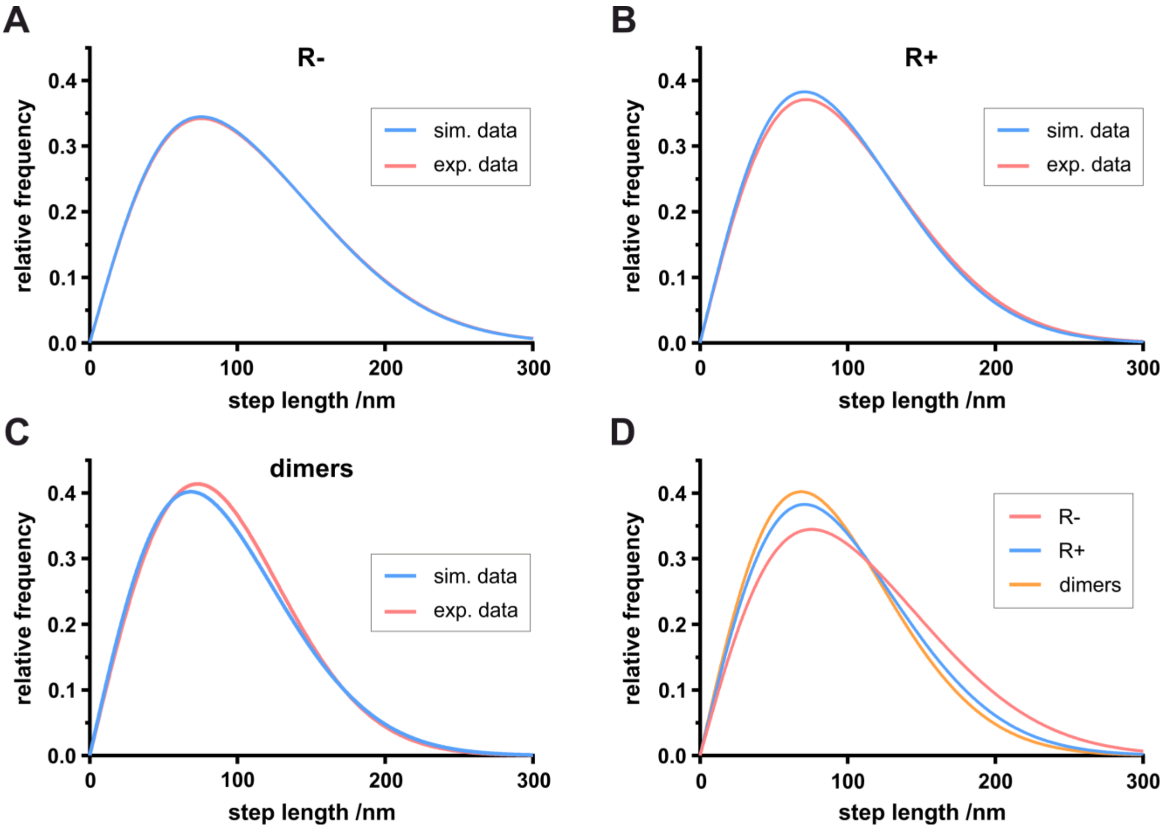

Figure 33. Verification of simulated hop diffusion. Experimentally obtained (^{DY647}IL-4Rα in A+B, ^{DY647}IL-4Rα/^{TMR}IL-13Rα1 in C) and simulation-derived step-length distributions perfectly match for **(A)** unstimulated receptors. High degree of similarity for **(B)** ligand exposed receptors and **(C)** for receptors in ternary complexes. **(D)** Comparison of diffusion properties of simulated receptors with (blue, wt k_d^T) and without (red) ligand as well as in ternary complexes (orange, cf. Fig. 26). Step-length distributions were obtained by fitting histogramed step-length data (time lapse 32 ms, 1 frame) with a two-component diffusion model including a slow and a fast mobile fraction. Data from 5 independent simulation runs (parameter-set A).

Under these conditions, a slightly increased probability (+10%) for molecule collisions compared to a fully homogenous diffusion scenario was observed (data not shown), which is caused by the meshwork constraints. The number of re-associations after dissociation of receptor dimers, however, is in this scenario increased by 125% due to the membrane confinement and the re-association frequency is, as expected, explicitly higher (~4-fold) for less stable complexes (Figure 34B).

Importantly, the receptor distance distributions of co-trajectories as well as the corresponding correlation lengths, extracted from simulation runs with different ternary complex dissociation constants, are comparable to the experimentally derived data and reproduce a shift to longer distances/correlation lengths for a low-affinity ligand (like RGA) (Figure 34C, D), as experimentally observed (Figure 28A, C).

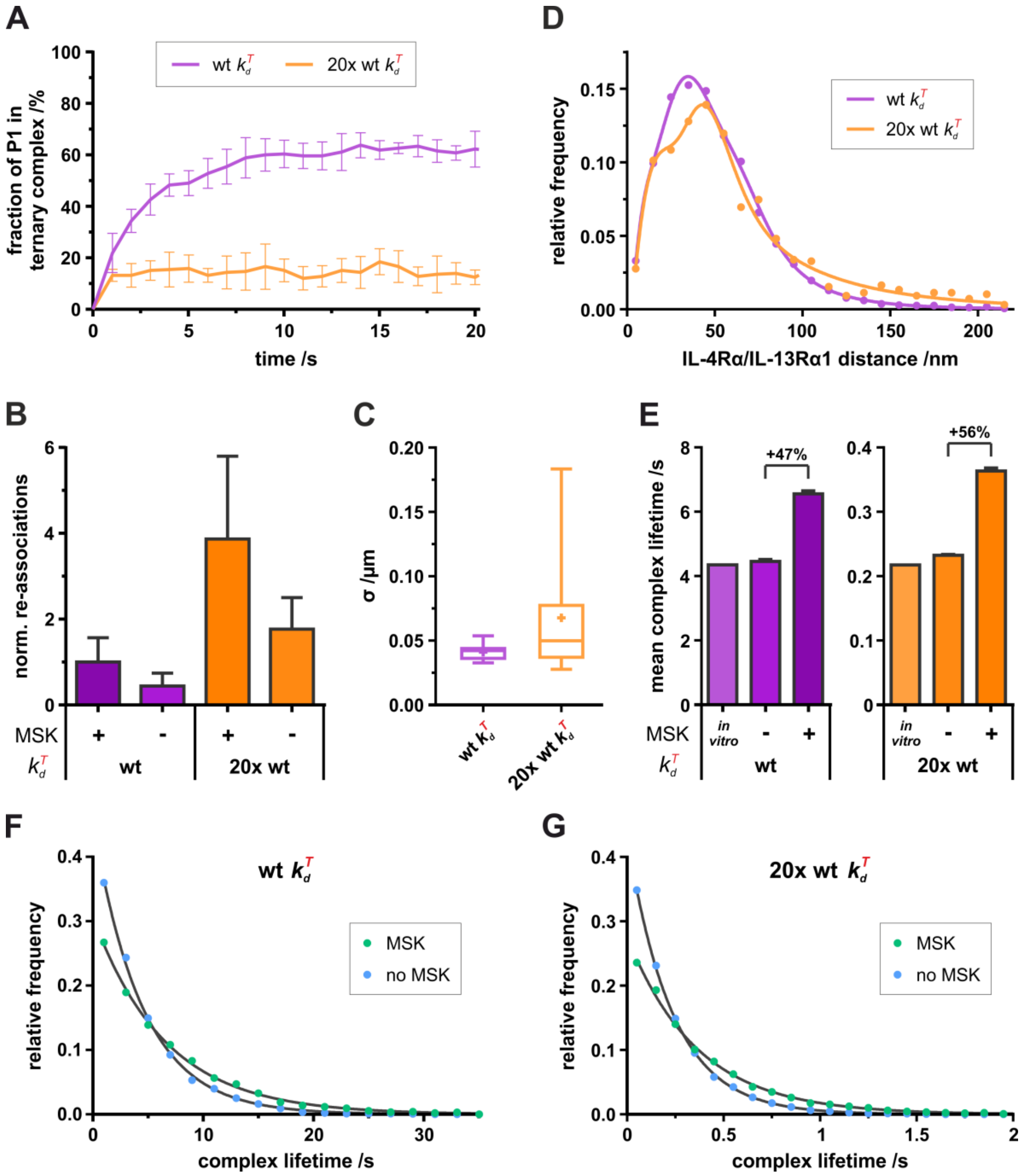

Figure 34. Model simulations confirm MSK-mediated dynamic complex stabilization. (A) A dynamic binary/ternary complex equilibrium is established in less than 2 (20x wt k_d^T) to 10 (wt k_d^T) seconds with up to 60% of receptors in a ternary complex (wt k_d^T). **(B)** Without membrane confinement, the number of contemporary re-associations per particle and time is reduced by more than 50% and the amount of re-associations increases with the ternary complex dissociation probability (i.e. increases with higher k_d^T). **(C)** Correlation lengths and **(D)** receptor distance distributions of co-trajectories simulated with two different ternary complex dissociation constants. **(E)** Mean ternary complex lifetime is increased by ~50% in simulation runs including confinement, as obtained by fitting **(F, G)** frequency distributions of ternary complex lifetimes (measured as the time both receptor subunits reside in the same compartment after undergoing at least one association event) with an exponential function: wt k_d^T: t=4460±60 ms / t=6560±88 ms (-/+ MSK). 20x wt k_d^T: t=233±1 ms / t=363±5 ms (-/+ MSK). Data in A-C from 5 independent simulation runs (parameter-set A) and in D-G from 10 independent simulation runs for each ligand scenario (parameter-set B).

Similar to the negative effect of LatB on the length of RGA-induced co-trajectories (Figure 29B), the model simulations revealed a ~50% increased mean ternary complex lifetime (measured as the time both receptor subunits reside in the same compartment after undergoing at least one association event) when comparing simulations with and without constrained diffusion by the MSK (Figure 34E-G).

Taken together, these results strongly support the hypothesis that plasma membrane compartmentation by the MSK contributes to a robust ligand-induced receptor dimerization by enhancing the complex re-association probability. Additionally, these findings offer an explanation for the missing connection between the ligand-dependent two-dimensional binding affinities and the overall similar apparent receptor dimerization efficiencies.

4.2 Part II: Ligand binding affinity and kinetics

The detailed investigation of the spatiotemporal receptor dynamics revealed efficient receptor dimerization in the plasma membrane, which was found to be hardly dependent on the two-dimensional binding affinities. Membrane-proximal signaling with respect to STAT6 activation was confirmed to be almost independent from lateral affinities as well. Consequently, in the second part of this study the three-dimensional interaction between the ligand and the high-affinity receptor chain was examined carefully to explore the role of ligand binding affinity and ligand-receptor complex stability with regard to cytokine receptor signaling and function.

4.2.1 STAT6 activation potencies are in a wide range independent of 3D affinities

To systematically analyze the relevance of the ligand binding affinity, an engineered series of IL-13 variants with binding affinities (K_D^B) ranging from ~50-fold more (A11) to ~8,200-fold less (C4) than that of IL-13 for IL-13Rα1 [158] (Figure 35A) was characterized in terms of STAT6 activation, biological activities and receptor dimerization. Importantly, the variations in the binding affinity of these mutants primarily depend on altered dissociation rates (k_d^B) (Table 2), hence by changing the lifetime of the ligand-receptor complex, whereas the association rate constants (k_a^B) are relatively similar between the different IL-13 variants. Further, although kinetic rate constants for the IL-13 variants with binding affinities in the higher nanomolar to micromolar range were not available, it was assumed that their k_d^B values were further increased proportionally to the change in K_D^B.

As the first and most prominent response upon type II IL-4 receptor activation is the phosphorylation of STAT6, the concentration-dependent generation of pSTAT6 was measured for the IL-13 variants in the IL-13-responsive cell line A549 by phospho-flow cytometry 15 minutes after ligand addition. Fitting of the thereby obtained dose-response data with a common model yielded the half maximal effective concentration (EC_{50}) for STAT6 phosphorylation for each agonist. Strikingly, two groups of IL-13 variants were observed that differed in their abilities to activate STAT6 (Figure 35B). One group (D7, C3 and C4) exhibited a substantially lower phosphorylation of STAT6 after 15 minutes, compared to IL-13. The other group (A11, B2, A7, A8, C10, B6 and B4) activated STAT6 with very similar potencies to each other and to IL-13. These observations were confirmed by Western blotting analysis (data not shown). The range of IL-13Rα1 binding affinities among the second group of agonists varies from 84 pM (A11) to 264 nM (C10), while about a 1000-fold increase in K_D^B compared to that of IL-13 is required for an IL-13 mutant (D7) to induce the generation of considerably decreased amounts of pSTAT6. These findings suggested the existence of a large “buffering region” that enables A549 cells to respond very similarly to IL-13 agonists with large differences in K_D^B. Indeed, such a region was readily observed by plotting of the binding affinities of the IL-13 variants for IL-13Rα1 against their respective STAT6 activation potencies (i.e. EC_{50} values, Figure 35C).

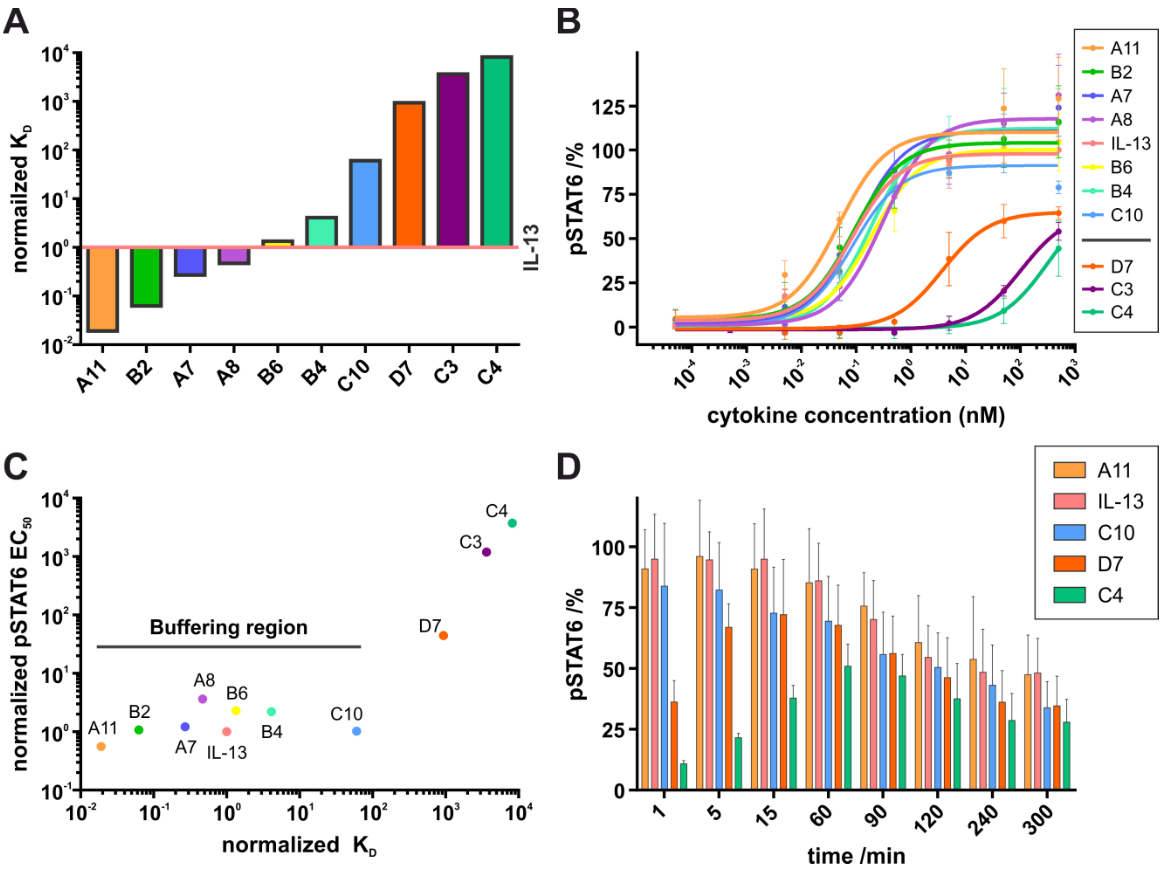

Figure 35. Binding affinities and STAT6 activation profiles of IL-13 variants. (A) Overview of normalized binding affinities (K_D^B) of the examined recombinant IL-13 variants. **(B)** Dose-response curves of STAT6 phosphorylation. A549 cells were stimulated with the indicated concentrations of IL-13 or its variants, and the abundance of pSTAT6 was analyzed after 15 min by flow cytometry with pSTAT6-specific antibodies coupled to fluorescent dyes. Sigmoidal curves were fitted using a common dose-response relationship, yielding two distinguishable groups. **(C)** Plotting of normalized EC_{50} values against the normalized binding affinities of the corresponding IL-13 variant uncovers a “buffering region”, as variants with a K_D^B within 100-fold of that of IL-13 in either direction exhibit similar profiles of STAT6 activation. **(D)** Kinetics of STAT6 phosphorylation in A549 cells after stimulation with 200 nM of the indicated agonist, analyzed by flow cytometry. Normalizations were performed with regard to IL-13 (wt).

To complete the analysis of the STAT6 activation profiles for some representative variants of the examined ligands, the phosphorylation kinetics were studied by measuring the levels of pSTAT6 in a time-dependent manner in A549 cells. While after stimulation with IL-13 as well as with A11 and C10 very similar phosphorylation kinetics with a pSTAT6-level of nearly 100% after only one minute were observed, the agonists D7 and C4, which bind to IL-13Rα1 even more weakly than C10, showed a delay in STAT6 activation (Figure 35D). For C4, which binds to IL-13Rα1 more than 8000-times weaker than does IL-13, the level of pSTAT6 after one hour of stimulation was only half of that of IL-13. And after stimulation with D7, the amount of phosphorylated STAT6 only almost reached the IL-13-induced level and only after 15 minutes.

Interestingly, this delayed kinetics of STAT6 activation exhibited by the very low-affinity mutants D7 and C4 were also observed for IL-13, A11 and C10 when sub-saturating doses of the ligand were used (Figure 36A). However, the number of STAT6 molecules activated per unit of time, measured as the quotient of the area under the phosphorylation kinetics curves and the time frame of the measurement, was only minimally altered for the tested IL-13 variants, despite the different activation kinetics or decreased ligand concentrations (data now shown). Combined, these results indicate that cells may have evolved to activate a finite number of STAT molecules by an amplification mechanism that is largely independent of the ligand binding affinity and concentration, and therefore does not depend on the saturation of receptors at the cell surface.

In the case of the interferon system, the surface receptor density contributes to the potency of signal activation [61]. Thus, the influence of reduced IL-13Rα1 surface densities on the activation of STAT6 was also explored. To this end, the STAT6 activation potencies of three IL-13 variants (A11, IL-13 and B4) were determined in cells in which the abundance of IL-13Rα1 was decreased by short inhibitory RNA (siRNA) (Figure 36B). Minimal differences in pSTAT6 EC_{50} values between the three agonists were observed in cells treated with control siRNA. However, when the IL-13Rα1 abundance was reduced to 40% of that in control cells, the B4 variant, which binds more weakly than IL-13 to IL-13Rα1, activated STAT6 less potently than did IL-13 and A11. This gap was further increased when the IL-13Rα1 abundance was reduced to 20% of that in control cells, suggesting a close correlation between ligand binding affinity, cell-surface receptor abundance and signaling potency.

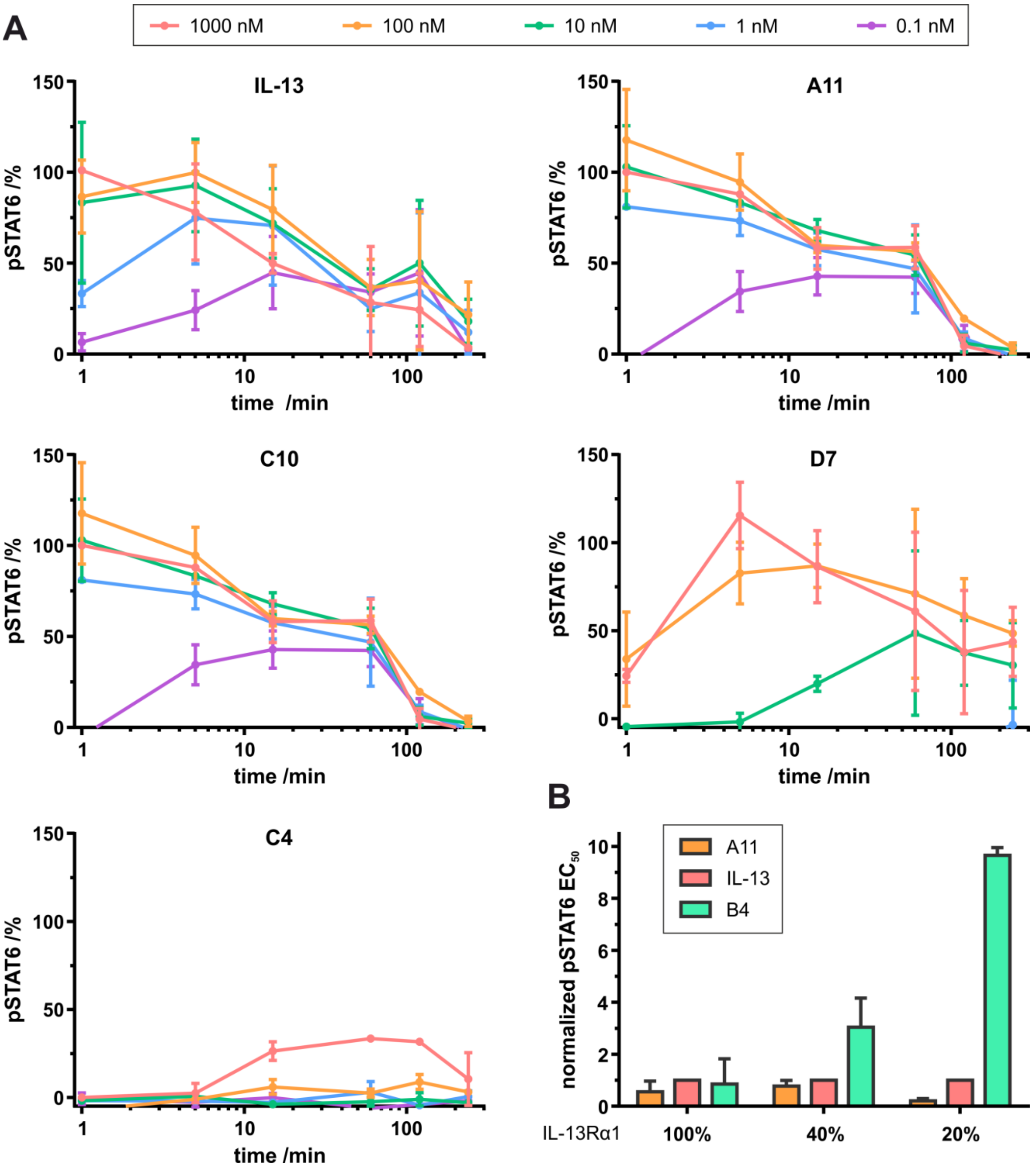

Figure 36. Concentration dependency of STAT6 activation for IL-13 variants and IL-13Rα1. (A) STAT6 phosphorylation kinetics in response to stimulation of A549 cells with different concentrations of the indicated IL-13 variants, as measured by flow cytometry. STAT6 activation rate and total pSTAT6 are strongly reduced at ligand concentrations below 100 nM (D7). At concentrations below 1 µM (C4) nearly no STAT6 phosphorylation occurs. IL-13, A11 and C10 exhibit delayed kinetics of STAT6 phosphorylation when sub-saturating ligand-doses are used. **(B)** The STAT6 activation potency in terms of EC_{50} values correlates with the ligand binding affinity upon reducing receptor levels. A549 cells were transfected with different amounts of IL-13Rα1-specific or control siRNA to reduce the IL-13Rα1 abundance to 40% and 20% compared to control cells. Cells were then stimulated with the indicated IL-13 variants and the total amount of pSTAT6 was quantified by flow cytometry. Normalization was performed with regard to IL-13 (wt).

4.2.2 3D association and dissociation rates differentially modulate STAT6 activation and biological potencies

Because the huge differences in the IL-13Rα1 binding affinity of the examined IL-13 variants turned out to have only minor effects on the final STAT6 activation potency, its role in inducing IL-13-related biological activities was additionally investigated.

First, the proliferation of TF-1 cells in response to the IL-13 variants was examined. The TF-1 cell system is commonly used to assess the potency of a large number of cytokines. Upon stimulation with IL-13, these cells proliferate in a concentration-dependent manner, which readily enabled the evaluation of the potency of the IL-13 variants [224]. Thus, TF-1 cells were stimulated with different agonist concentrations for 96 hours, then the cell number was determined by flow cytometry-based counting and EC_{50} values were obtained by fitting the thereby yielded dose-response curves. A broad range of proliferation potencies was observed (Figure 37A), which partially contrasted with the similar STAT6 activation profiles of the different IL-13 variants. Whereas the strong-binding agonist A11, for example, was virtually identical to IL-13 in its ability to activate STAT6 (Figure 35B), it was the more potent inducer (~30-fold) of TF-1 cell proliferation. On the contrary, the low-affinity variant D7 exhibited a significantly lower potency (~20-fold) to induce TF-1 cell proliferation compared to IL-13, although the total levels of phosphorylated STAT6 were similar after 15 minutes of stimulation with this agonist in A549 cells (Figure 35D). However, the different extents of cell proliferation induced by the IL-13 variants matched their binding affinities more closely than their respective abilities to activate STAT6 only for those agonists with extremely high or low affinity, while those in between showed a mostly diffuse distribution of potencies.

To broaden the evaluation of the biological activities of the IL-13 variants, the *in vitro* differentiation of monocytes into dendritic cells was analyzed. To this end, monocytes were stimulated with IL-13 or the engineered variants for seven days and then the cell-surface abundance of two classical dendritic markers, CD86 and CD209, was quantified by flow cytometry. The dose-response curves that were obtained by this approach were mostly consistent with the findings for the proliferation response of TF-1 cells (Figure 37B). However, the potency of the different IL-13 variants to stimulate dendritic cell generation correlated significantly stronger with their binding affinities (Figure 37C, D). As before, A11 turned out to be more potent than IL-13 in inducing membrane-distal responses, that is, the generation of dendritic cells, despite eliciting very similar profiles of STAT6 activation. Likewise, for low-affinity variants like D7 and C4, the opposite was observed, as these ligands were much less potent in their ability to induce monocyte differentiation.

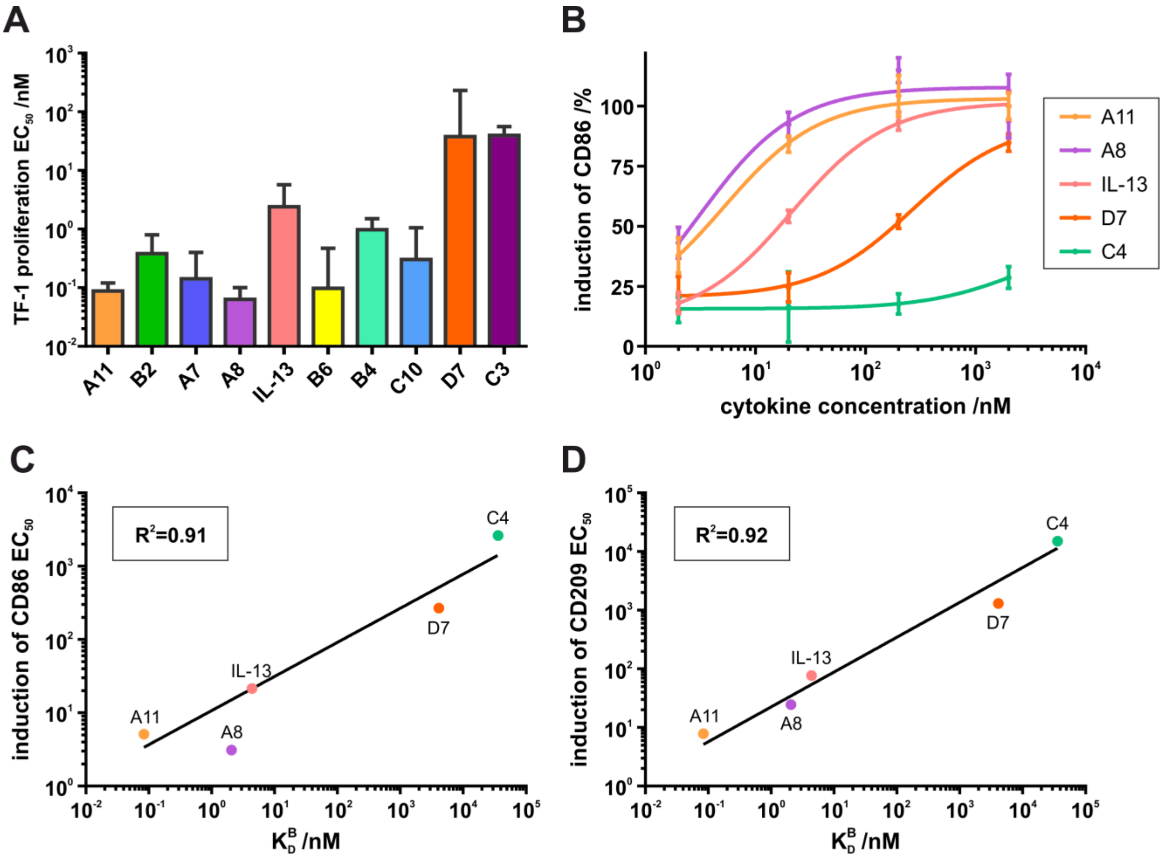

Figure 37. Biological activities of IL-13 variants. (A) Mean effective concentration (EC$_{50}$) values for the *in vitro* induction of TF-1 cell proliferation by different IL-13 variants. For agonists with extremely high and low affinity the proliferation potency more closely matches their binding affinity compared to their potency of STAT6 activation. TF-1 cells were stimulated with different agonist concentrations for 96 hours. Then, cell numbers were measured by flow cytometry and dose-response curves were fitted to obtain EC$_{50}$ values. **(B)** *In vitro* analysis of the potency of IL-13 variants to induce the differentiation of monocytes into dendritic cells by probing the cell surface abundance of CD86. Compared to TF-1 cell proliferation, a significantly stronger affinity-activity correlation is observed for dendritic cell differentiation. Monocytes were stimulated for 7 days with the indicated agonist concentrations, stained with fluorescently labeled antibodies against CD86 and fluorescence was measured by flow cytometry. Curves were fitted with a common sigmoidal dose-response model. **(C, D)** The potency to induce the differentiation of monocytes into dendritic cells is strongly correlated with the agonist binding affinity, as can be seen from the relationship of the agonist K_D^B with the EC$_{50}$ values for induction of **(C)** dendritic cells markers CD86 and **(D)** CD209 on monocytes.

Owing to the fact that these contrasting results could not be explained by correlating the membrane-proximal and -distal responses just with the ligand-receptor binding affinity, further correlation approaches were performed with the two kinetic parameters from which the K_D^B of the ligand-receptor interaction is derived: the rate at which the ligand binds to its cognate receptor (k_a^B) and the rate at which the binary complex dissociates (k_d^B), while the latter is inversely proportional to the complex lifetime (cf. Figure 12B). For both components, their roles in activating early signaling events (i.e. STAT6 activation) as well as in inducing IL-13-related bioactivities (i.e. TF-1 cell proliferation) were unraveled. Therefore, a series of linear correlation plots was generated in which the EC_{50} values of the different IL-13 variants for the generation of pSTAT6 and the induction of TF-1 cell proliferation were plotted against the respective k_a^B , k_d^B or K_D^B values of these agonists. The potency of STAT6 activation of the IL-13 variants correlates reasonably well with their k_a^B values and poorly with their k_d^B values (Figure 38A). In contrast, the potency of induction of TF-1 cell proliferation by the different IL-13 agonists correlates more closely with their k_d^B values, but virtually no correlation is obtained with their k_a^B values (Figure 38B). In both cases, the correlation with K_D^B is weak.

These findings hint towards a mechanism that differentially controls the activation of STAT6 and the final biological outcome at least partly on the basis of the kinetic parameters that determine the ligand-receptor interaction. Thus, in terms of STAT6 activation potency, agonists like A11 do not benefit from an overall increased ligand binding affinity as long as the k_a^B values are not significantly changed. Likewise, lower-affinity agonists like C10 are still able to potently induce the generation of pSTAT6, if their k_a^B values are only marginally altered. Consequently, the here employed IL-13 variants showed similar STAT6 activation profiles over a broad range of ligand binding affinities. In contrast, as the induction of TF-1 cell proliferation (and most likely also the induction of monocyte differentiation) is primarily dependent on the ligand-receptor dissociation rate k_d^B, agonists like A11 that form complexes with longer lifetimes exhibit an increased potency to induce such distal effects. The opposite is the case for agonists like D7 and C4 that form considerably more short-lived complexes.

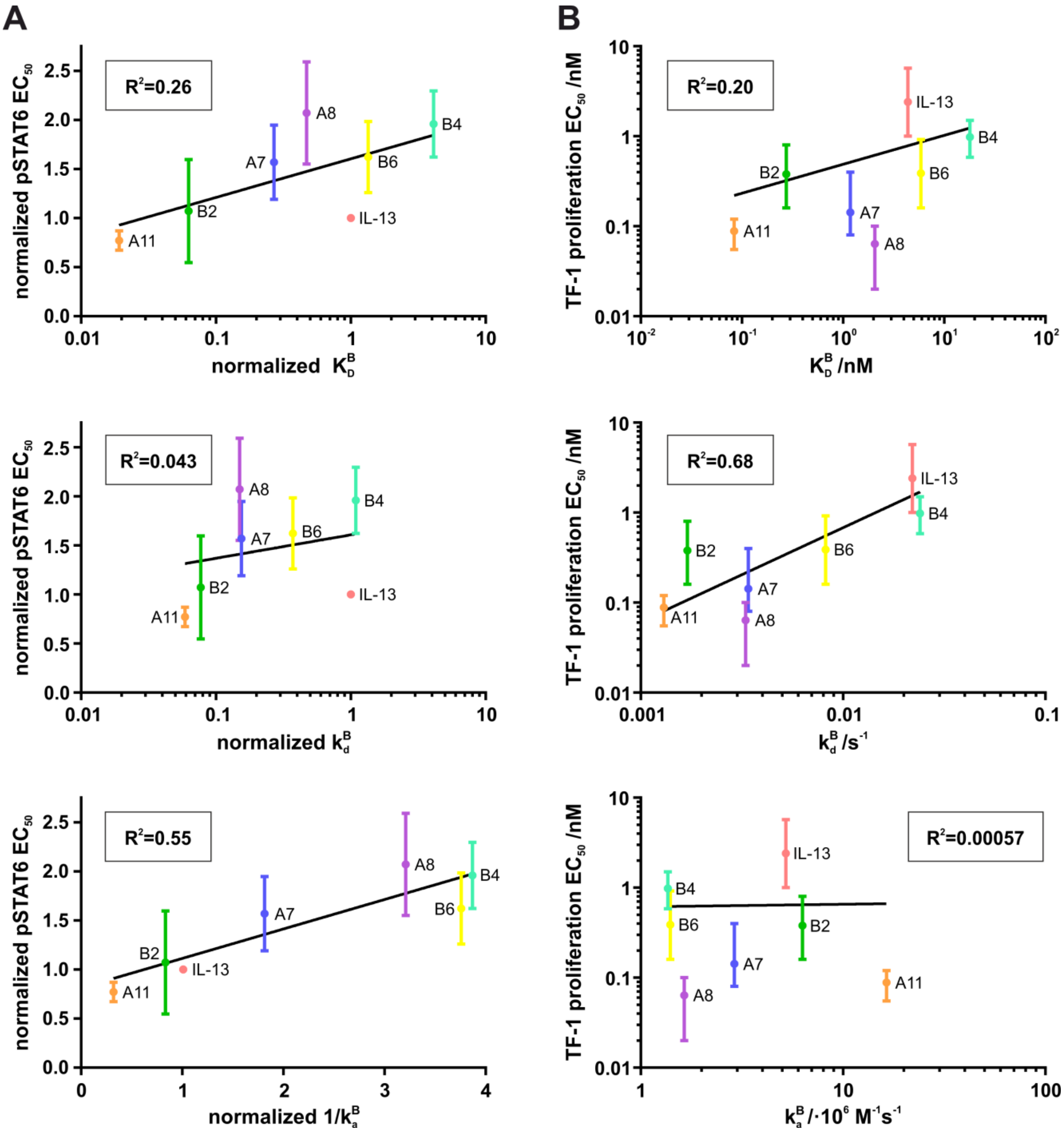

Figure 38. Correlation of receptor binding kinetics and affinities of IL-13 variants with signaling and bioactivities. (A) Normalized STAT6 phosphorylation EC$_{50}$ values of the indicated IL-13 variants plotted against their normalized binding parameters. Correlation is weak with the binding affinity (K_D^B, top), non-existent with the dissociation rate (k_d^B, middle) and strong with the inverse association rate ($1/k_a^B$, bottom). **(B)** EC$_{50}$ values for the induction of TF-1 cell proliferation of the indicated IL-13 variants plotted against their binding parameters. Correlation is weak with the binding affinity (K_D^B, top), strong with the dissociation rate (k_d^B, middle) and non-existent with the association rate (k_a^B, bottom). Normalizations were performed with regard to IL-13 (wt).

4.2.3 Decreasing 3D affinity is tolerated by almost two orders of magnitude in terms of receptor dimerization

The biochemical analysis of the effects induced by the examined IL-13 variants provided striking insights into the differential roles of the kinetic parameters that govern ligand-receptor interactions. To deepen the understanding of these results also at the molecular level, the role of the ligand binding affinity regarding the spatiotemporal dynamics of IL-13 signaling complexes was probed by the same receptor dimerization assay based on single-molecule fluorescence imaging that was employed for the IL-4 variants (cf. chapter 4.1.4). As before, ^{DY647}IL-4Rα and ^{TMR}IL-13Rα1 were imaged at physiological relevant expression levels in HeLa cells by TIRF microscopy and the receptor dimerization was analyzed and quantified by single molecule co-localization/co-tracking of ^{DY647}IL-4Rα and ^{TMR}IL-13Rα1 as well as by PICCS [166]. Instead of using a ligand concentration of 20 nM, cells were, however, stimulated with 200 nM of the respective ligand to partially compensate for the lower affinity of the IL-13 variants towards their cognate receptor subunit.

Again, dimerized receptors could only be discerned after ligand addition, verifying a two-step mechanism of ternary complex assembly. For all IL-13 variants that were subjected to these studies, even for the very low-affinity agonists D7 and C4, substantial ligand-induced receptor subunit co-locomotion was readily observable. A deconvolution of the co-trajectory step-length distribution yielded for the receptor subunits after binding of IL-13 corroborated the previous finding that 40-50% of the available IL-13Rα1 forms a ternary complex at saturating concentrations of IL-13 (Figure 39A). In contrast, no co-locomotion of IL-13Rα1 and IL-4Rα was detectable in the presence of a dominant-negative IL-13 mutant (DN13, [158]), which binds to IL-13Rα1 with high affinity, but does not bind to IL-4Rα (Figure 39B).

A similar receptor dimerization efficiency of the IL-13 variants compared to the IL-4 variants was obtained by cross-correlation analysis (Figure 39C, D and Table 15). Moreover, the fraction of correlated ^{TMR}IL-13Rα1 and ^{DY647}IL-4Rα molecules neither changed for the binary complex-stabilizing A11 variant (α ~8.9%) nor for the moderately destabilizing C10 (α ~9.2%) variant with respect to IL-13 (α ~8.1%). However, the correlated fraction was significantly decreased for the very low-affinity agonists D7 (α ~6.8%) and C4 (α ~2.8%), probably because saturated receptor occupancy was not achieved. Notably, even for the DN13 mutant the fraction of correlated subunits was above the background (α ~2.8%) and comparable to the level of C4.

These results underscore the previous conclusion that the recruitment of IL-13Rα1 and IL-4Rα by its respective ligand in the plasma membrane is very robust across a wide range of binding affinities, tolerating an increase of the two-dimensional affinity K_D^T by a factor of ten and of the three-dimensional affinity K_D^B by almost two orders of magnitude.

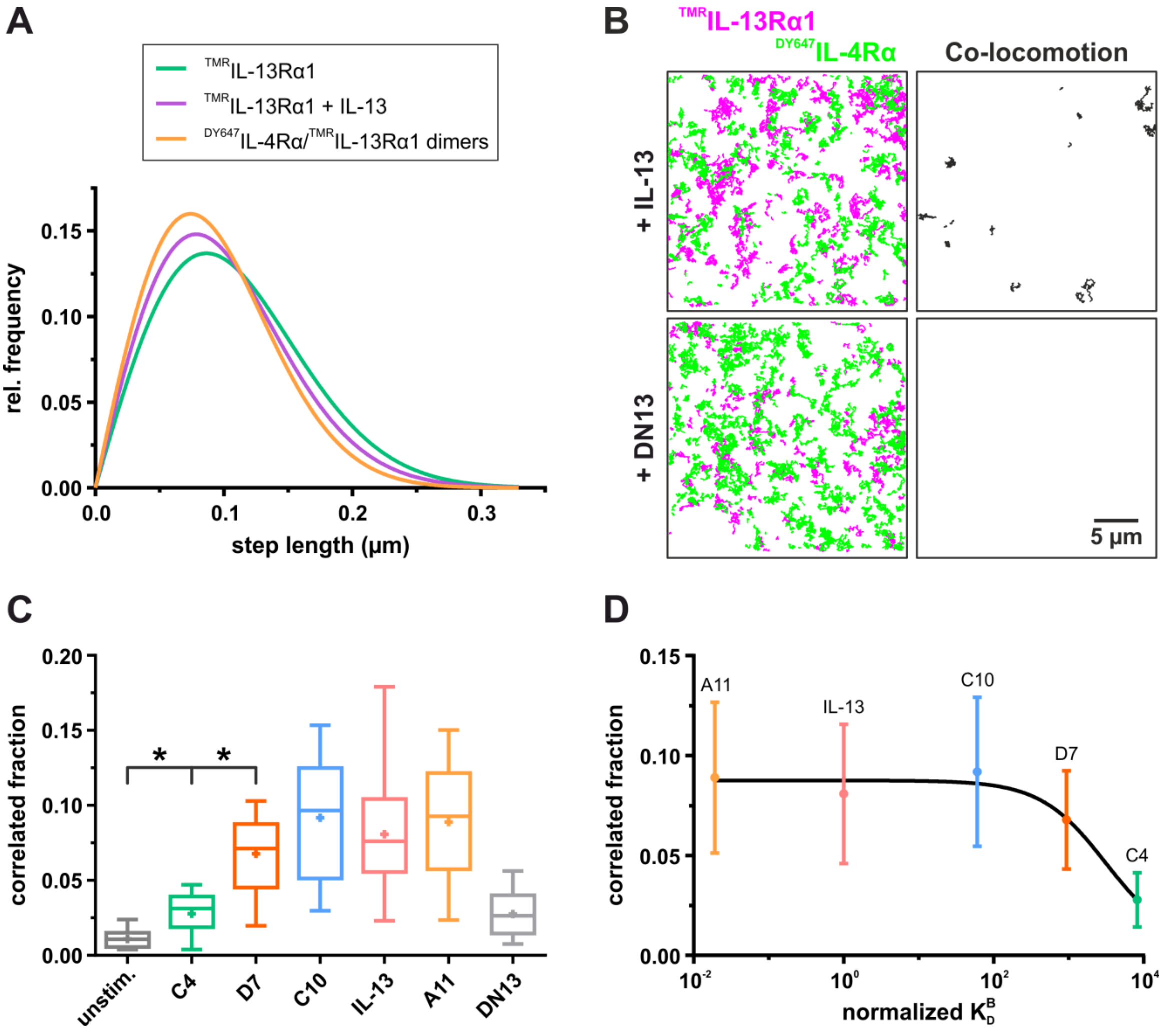

Figure 39. Analysis and quantification of receptor dimerization induced by IL-13 variants. (A) Diffusion properties of ^{TMR}IL-13Rα1 before (green) and after (purple) stimulation with 200 nM IL-13 as well as of ligand-induced ^{DY647}IL-4Rα/^{TMR}IL-13Rα1 dimers (yellow), presented as fitted step-length distributions (time lapse 32 ms, 1 frame), based on two components corresponding to a fixed slow and a variable fast mobile fraction. Data from >2500 trajectories. **(B)** Co-locomotion analysis of ^{DY647}IL-4Rα and ^{TMR}IL-13Rα1 in presence of 200 nM IL-13 or DN13 (antagonist incapable of binding to IL-4Rα). Only trajectories with a minimum length of 10 frames are shown. **(C)** Correlated fraction of ^{TMR}IL-13Rα1 and ^{DY647}IL-4Rα subunits for the examined ligands, quantified by PICCS. **(D)** Mean correlated fraction values as function of IL-13 variant binding affinity.

Table 15. Receptor dimerization by IL-13 variants quantified by PICCS.

Ligand	α [%]	σ [μm]	ρ [μm^{-2}]
DN13	2.8±1.5	0.12±0.04	0.35±0.15
C4	2.8±1.4	0.10±0.06	0.21±0.06
D7	6.8±2.5	0.07±0.03	0.18±0.06
C10	9.2±3.7	0.12±0.02	0.13±0.05
IL-13	8.1±3.5	0.06±0.03	0.24±0.12
A11	8.9±3.8	0.07±0.03	0.16±0.05

4.2.4 Two determinants that play a crucial role in controlling cytokine signaling

Because the engineered IL-13 agonists bind to IL-13Rα1 with markedly altered stabilities, the individual complex lifetime, a property that has been conjectured to play a critical role in the functional plasticity of other cytokine receptors [56, 60, 64, 225], was also investigated. Indeed, like for RGA (Figure 31C), the formation and dissociation of individual complexes was observed (Figure 40A), which is consistent with reversible ligand-binding to the cell surface receptor as well as with reversible receptor dimerization in the plasma membrane.

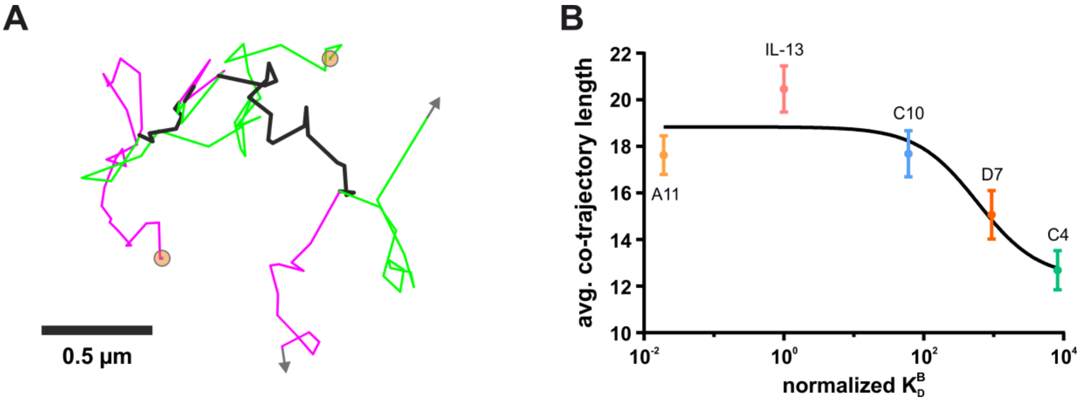

Figure 40. Dynamics of receptor complexes induced by IL-13 variants. (A) Assembly and dissociation of an individual dimer of ^{TMR}IL-13Rα1 and ^{DY647}IL-4Rα in presence of D7. Overlaying co-locomotion trajectories are colored in black. **(B)** Average co-trajectory length of receptor dimers as a function of agonist binding affinity. Mean values and SDs were obtained from fitting exponential functions to lifetime histograms built from >400 trajectories for each variant, pooled from at least two independent experiments with n>10 cells. Normalizations were performed with regard to IL-13 (wt).

Even though the lengths of the co-trajectories are strongly limited by photobleaching and tracing fidelity as already mentioned above, substantial decreased complex lifetimes were observed for the very low-affinity agonists D7 and C4 (Figure 40B). The mean complex lifetimes paralleled the increased dissociation kinetics of these IL-13 variants, corroborating the relevance of reversible ligand binding for the spatiotemporal dynamics of ternary complexes.

Combined, the collected data highlight the potential to control the signal delivered to a responsive cell by two distinct mechanisms: First, by regulating the maximum number of complexes formed by a given cytokine, which is largely determined by the receptor density on the cell surface. Second, by adjusting the lifetime of individual complexes, which heavily relies on the dissociation rate (k_d^B) of the ligand.

4.2.5 Membrane-proximal signaling events are supported by receptor endocytosis

Although the single-molecule data provided further insights into the complex interplay between ligand binding affinity, ternary complex dynamics and signaling of the type II IL-4 receptor system, it still remained an open question why the very-low affinity agonists like D7 and C4 stimulated the phosphorylation of STAT6 with a clear delay. Since endocytosis was proposed to play an important role in IL-4 signaling [160, 163], the unexpectedly high activity of very low-affinity agonists was hypothesized to be caused by endocytosis of functional signaling complexes, which would lead to their accumulation over time. In order to confirm this hypothesis, first, the endosomal uptake of both ^{DY647}IL-13 and ^{DY647}D7 bound to endogenous receptors in HeLa cells was visually verified by image acquisition in HILO mode with the same microscopy setup used before (Figure 41A, top). Then, the possibility of blocking type II IL-4 receptor endocytosis by EHT 1864, an inhibitor of Rho family guanosine triphosphatases [226, 227], which have been implicated in the endocytosis of IL-2Rs [105] and the IL-4 receptor [160], was tested.

Indeed, the uptake of both IL-13 and D7 was substantially reduced upon addition of the inhibitor (Figure 41A, bottom). In cells treated with the highest concentration of EHT 1864 that could be applied without causing loss of cell surface receptors (100 µM), an approximately twofold reduction in endocytosis was found, as quantified from the intensity of endosomes containing captured fluorescently labeled ligand (Figure 41B) and from the amount of ^{DY647}IL-13 bound to the cell surface (Figure 41C). The quantity of cell surface bound ^{DY647}D7, however, was only marginally, but not significantly increased after EHT 1864 treatment.

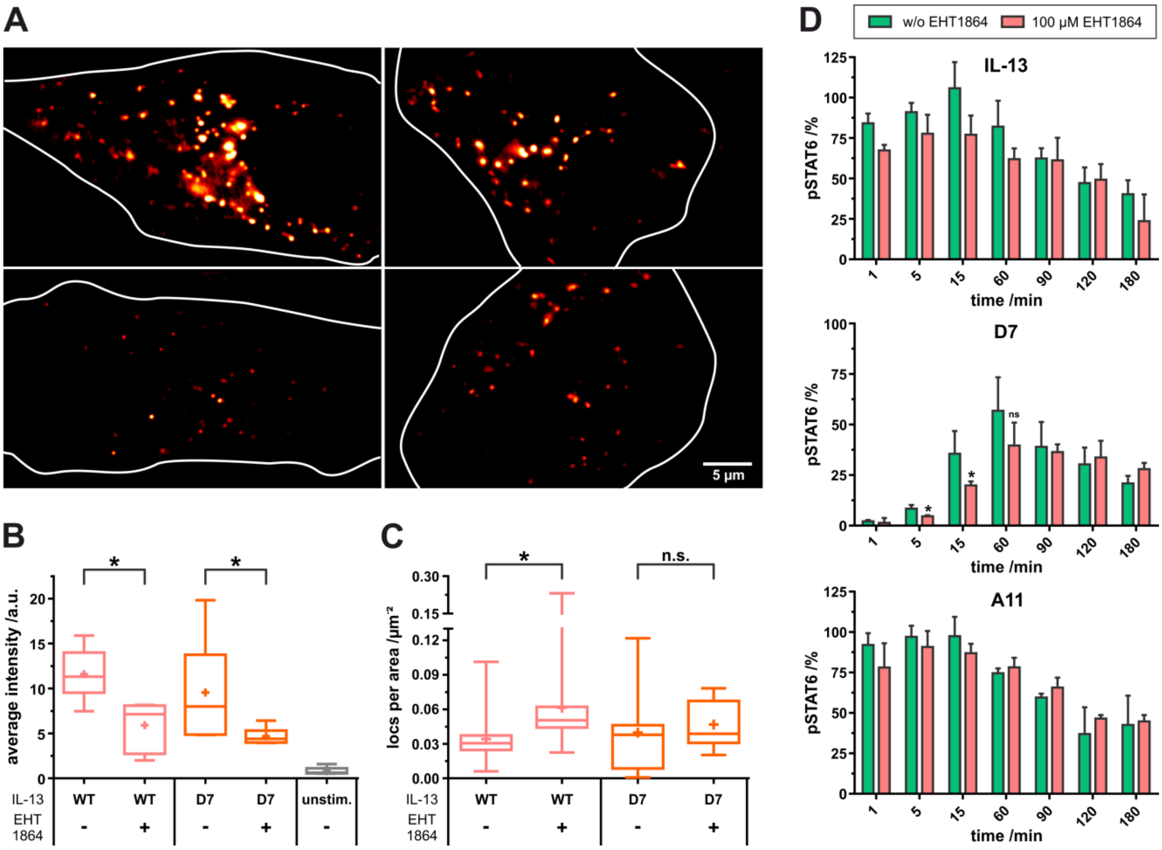

Figure 41. Investigation of receptor endocytosis and its effect on STAT6 phosphorylation. (A) Epifluorescence images showing decreased endocytosis of ^{DY647}IL-13 (left) and ^{DY647}D7 (right) bound to IL-13Rα1 in HeLa cells after treatment with 100 µM EHT 1864 (bottom) compared to untreated cells (top). **(B)** Quantification of the amount of ^{DY647}IL-13 (left) and ^{DY647}D7 (right) in endosomal compartments and **(C)** at the plasma membrane in absence and in presence of EHT 1864. **(D)** Kinetics of STAT6 phosphorylation in HeLa cells treated with IL-13 (top), D7 (middle) or A11 (bottom) with and without blocking of endocytosis by EHT 1864, measured by flow cytometry. Data in B and C are based on n>5 cells and data in D represent mean ± SD from three independent experiments.

The functional role of endocytosis was investigated by flow cytometry-based time-lapse STAT6 phosphorylation assays in the absence or presence of the blocking agent. Thereby, a correlation between the agonist binding affinity and the role of endocytosis was noticed. Whereas no statistically significant reduction in pSTAT6 generation kinetics was observed for the high-affinity variant A11 in presence of the inhibitor, STAT6 phosphorylation in response to the very low-affinity agonist D7 was further slowed in EHT 1864-treated cells (Figure 41D). Importantly, EHT 1864 did not affect the EC_{50}

values for STAT6 activation of any of the three IL-13 variants (data now shown), pointing towards an indirect effect of the inhibitor on the phosphorylation of STAT6, namely by weakening the proposed amplification mechanism that depends on the accumulation of functional signaling complexes via endocytosis.

4.2.6 A mechanistic model correlating cytokine binding with the functional output

These results strongly suggested that endocytosis is a key determinant for STAT6 phosphorylation. To further support this conclusion, an *in silico* modelling approach in line with the previous outcomes was carried out. To this end, a simple steady-state model for receptor activation was conceived (inspired by [228]), consisting of reversible ligand binding to the cell surface, followed by irreversible uptake of functional signaling complexes into endosomes and their subsequent sorting into degradative and recycling pathways (Figure 42A). As a consequence of endocytosis, the captured ligand is considered to remain bound to the receptor most of the time because of comparable high local concentration of individual ligand molecules in the exceedingly small volume of the endosome [45]. The model further assumes that signaling complexes retain their ability to induce the phosphorylation of STAT6 in endosomes until they are processed, and in particular that the concentration profile of pSTAT6 is proportional to the total number of active signaling complexes in the plasma membrane and in endosomes.

On the basis of differential equations describing this model (Figure 42B), the kinetics of pSTAT6 formation in response to different representative IL-13 variants was computed. Using the respective binding parameters of the IL-13 variants, global realistic rate constants of endocytosis, recycling and degradation (Table 7) were obtained by fitting the experimental data to the model equations. With the thus derived entire parameter-set the observed pattern of STAT6 phosphorylation kinetics as well as the selective effect of inhibited endocytosis on the activity of low-affinity agonists (D7 and C4) was remarkably well reproduced by this relatively simple model (Figure 42C, cf. Figure 35D and Figure 41D).

The simulations furthermore confirmed the strong correlation between the potency of STAT6 activation (EC_{50}) of an IL-13 variant and its association rate (k_a^B), while the respective correlations with its binding affinity (K_D^B) and its dissociation rate (k_d^B) were somewhat more pronounced compared to the experimentally derived data. (Figure 42D, cf. Figure 38A).

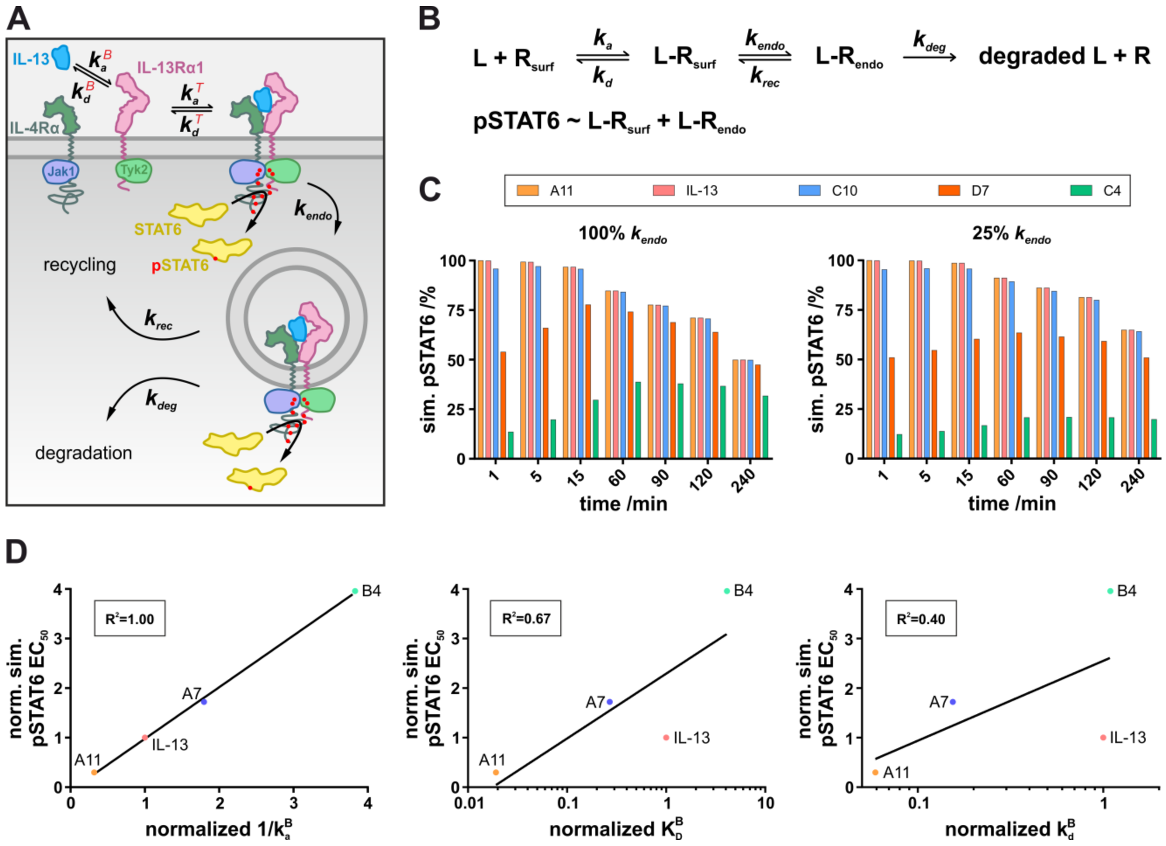

$$L + R_{surf} \underset{k_d}{\overset{k_a}{\rightleftharpoons}} L\text{-}R_{surf} \underset{k_{rec}}{\overset{k_{endo}}{\rightleftharpoons}} L\text{-}R_{endo} \xrightarrow{k_{deg}} \text{degraded } L + R$$

$$pSTAT6 \sim L\text{-}R_{surf} + L\text{-}R_{endo}$$

Figure 42. A quantitative model of IL-13 signaling reproduces experimental data. (A) Schematic illustration of a simple steady-state model established for simulations of STAT6 phosphorylation kinetics and dose-response curves. Ligand binding and receptor dimerization is followed by uptake of ternary complexes into early endosomes. During endocytic trafficking, the fate of endocytosed complexes is determined by entering either recycling or degradation pathways. **(B)** Reaction equation of the developed model. The originally two-step receptor assembly and disassembly is simplified by a single-step in which a ligand (*L*) binds to and dissociations from the receptor on the surface (R_{surf}) according to experimentally determined rate constants. Endocytosis of ligand-receptor complexes ($L\text{-}R_{surf}$) as well as recycling and degradation of endocytosed complexes ($L\text{-}R_{endo}$) occur with estimated rates. The level of pSTAT6 is assumed to be correlated with the total receptor complex concentration on the surface and in endosomes. **(C)** Simulated STAT6 phosphorylation kinetics in absence (left) and in presence (right) of an endocytosis inhibitor (75% reduced endocytosis rate). **(D)** Normalized pSTAT6 EC_{50} values, derived from simulated dose-response curves, plotted against the corresponding normalized IL-13 agonist binding parameters. Correlation is perfect with the inverse association rate ($1/k_a^B$, left), strong with the binding affinity (K_D^B, middle) and moderate with the dissociation rate (k_d^B, right). Normalizations were performed with regard to IL-13 (wt).

The characteristic changes in the STAT6 phosphorylation kinetics at decreased ligand concentrations were also observed in the model-derived data (Figure 43A, cf. Figure 36A). For completeness, detailed time courses of the relative concentrations of all entities involved in the simulation of the STAT6 phosphorylation kinetics curves shown in Figure 42C are depicted in Figure 43B.

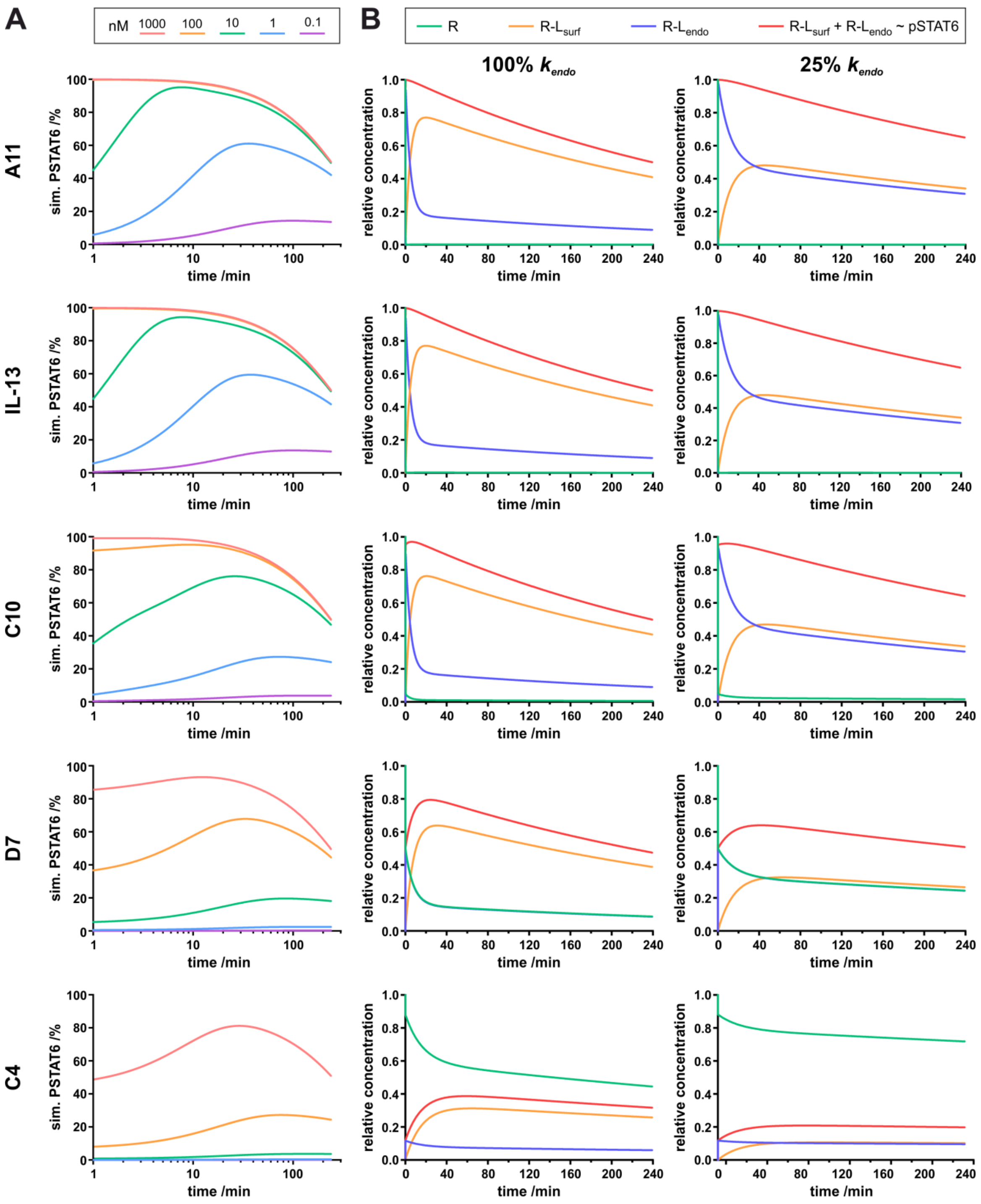

Figure 43. Time-resolved receptor complex assembly simulated with binding parameters of IL-13 variants to mimic STAT6 phosphorylation kinetics. (A) Temporal changes in the total number of ligand-receptor complexes (~pSTAT6) simulated for IL-13 variants at various nanomolar ligand concentrations (cf. Fig. 36A). **(B)** Temporal changes in the sum of the relative concentrations of ligand-receptor complexes at the surface and in early endosomes (red, cf. Fig.

42C). For comparison, the relative concentrations of free receptor (green) as well as of ligand-receptor complexes at the surface (yellow) and in endosomes (blue), respectively, are shown. Curves were simulated for different IL-13 variants and with two different rates of endocytosis, which correspond to untreated (left) and EHT 1864-treated (right) cells. Owing to pseudo first-order conditions the ligand concentration was kept constant in simulations depicted in B. STAT6 phosphorylation was assumed to change directly proportionally to the total number of ligand-receptor complexes (all curves in A, red curves in B).

Altogether, these findings provide clear evidence that the membrane-proximal signaling events induced by IL-13 and its variants are primarily regulated by the interplay of ligand binding and receptor endocytosis kinetics.

4.3 Acknowledgments

I would like to thank Ignacio Moraga for performing flow cytometry experiments (pSTAT6 EC_{50} and kinetics, quantification of receptor levels, TF 1 cell proliferation studies) and for expression and purification of IL-13 variants and tagless IL-4 variants. Hella Kenneweg kindly took over the entire protein labeling work and expressed and purified ybbR-tagged IL-13 variants. Oliver Beutel was of great help in every sense, especially with TIRFS-RIf studies. Hauke Winkelmann adapted and implemented the Tet-regulated inducible gene expression system, performed ensemble and single molecule fluorescence measurements and helped with data evaluation. Stephan Wilmes assisted a lot with microscopy and data evaluation. The clone-work was greatly supported by Gabriele Hikade. Also, I would like to thank Christian P. Richter for providing the single molecule localization and tracking software, Philipp Selenschik for the collaboration on implementing PICCS, Oliver Birkholz for performing PSM experiments and Megan M. Suhoski for realizing the dendritic cell studies.

5 Conclusions

Despite intensive scientific research regarding the central role of cytokines in controlling the immune system, some fundamental questions remained hitherto unanswered. Thus, for example, the spatiotemporal organization of cytokine receptors was not clarified and details concerning receptor assembly were missing, because controversial models from different studies were positioned opposite each other [71, 72, 229]: While one side claimed that the receptors were pre-dimerized [73-83, 230, 231] and/or organized in clusters [89-92] independent of the ligand, the other presumed a non-clustered distribution [60] and excluded any dimerization in absence of the ligand [60, 65, 68, 232]. Also, the site of receptor activation was not clearly defined, because in contrast to the common concept of subunit dimerization at the cell membrane [60, 65, 67, 68, 232, 233], recent studies proposed that receptor endocytosis is critical for efficient complex assembly [163] and that signaling occurs exclusively at a particular type of early endosomes [160]. The role of ligand receptor binding affinities that determine the equilibrium state was likewise not systematically explored, although recent findings of the type I interferon (IFN) receptor suggested a correlation between functional selectivity and affinity-dependent recruitment of the second receptor chain into the complex, sub-sequent to ligand binding to the high-affinity chain [60].

Owing to the immense diversity in the large family of cytokines with receptors formed from homodimers (e.g. GHR [65]) up to higher order oligomers (e.g. GM-CSF receptor [234]), differences regarding the above mentioned aspects are quite possible and likely exist. Nevertheless, an attempt to gain a comprehensive mechanistic picture of the molecular and cellular determinants that govern cytokine receptor assembly and signaling was still missing, which gave rise to a systematical analysis of an appropriate receptor model system encompassing the quantification of the affinity-dependent dimerization efficiency, complex stability and interaction dynamics as well as the correlation of these results with the induced cellular responses. This was carried out in the present study using the type II IL-4 receptor, for which a large library of engineered ligands with a broad bandwidth of two- and three-dimensional binding affinities was available, rendering it an ideal basis for this project. With its critical implications in allergy [124, 137], asthma [21, 137, 235-237] and cancer [17, 137, 237], the type II IL-4 receptor is also an important and desirable drug target. Therefore, the insights obtained in this work might have direct pharmaceutical relevance and could probably contribute to further IL-4/IL-13-related medication development.

The first part of this work focused on the two-dimensional dimerization and spatiotemporal dynamics of receptor subunits in the plasma membrane. Using *in vitro* assays with the receptor subunits tethered onto solid-supported membranes, the K_D^T values and complex lifetimes that limit receptor dimerization were determined. The binding constants in the two-dimensional environment of an artificial membrane were scaling with the volume binding affinities of the different agonists and predicted inefficient receptor dimerization at physiological receptor cell surface concentrations, which were found to be 100-fold lower than the K_D^T values observed *in vitro*. The quantification of the ligand-induced receptor dimerization on the cell surface by analyzing dual color single molecule data of fluorescently labeled full-length IL-4Rα and IL-13Rα1, however, yielded a surprisingly high efficiency (>60% for IL-4 and ~40% for IL-13) with only little dependence on two-dimensional binding affinities. This striking observation was corroborated by the analysis of the receptor mobility, as IL-4Rα/IL-13Rα1 dimers exhibited significantly slowed diffusion in relation to the single subunits alone, which was found for all ligands in a comparable manner and may be explained by increased friction upon dimer assembly. Consequently, substantially lower effective K_D^T values (200- to 300-fold) as compared to the *in vitro* data were obtained from these experiments.

This relatively high degree of ligand-induced receptor dimerization on the cell surface is in good agreement with a previous study of the related type I IL-4 receptor on the basis of competitive antibody binding experiments, wherein 90% of the IL-4Rα chain was estimated to be in complex with the common gamma chain [67]. Similar dimerization efficiencies in the plasma membrane were also observed for the type I IFN receptor using single molecule assays akin to those of the present study [60]. By contrast, recent live cell fluorescence cross-correlation spectroscopy studies claimed that the dimerization of the type II IL-4 receptor is entirely inefficient at the plasma membrane under physiological conditions and presumed even higher K_D^T values (5 times for IL-4 and 40 times for IL-13) than those that were obtained in this work with reconstituted receptors *in vitro* [163]. But, importantly, exceptionally high receptor densities were required for these measurements (>1000-fold above the endogenous cell surface expression level), which were achieved by massive transient overexpression and very likely account for these fundamental differences.

The results obtained in the present work indicated an important role of the cellular context for ensuring efficient receptor assembly, e.g. by enhancing the local subunit concentrations due to partitioning into membrane microdomains or by receptor pre-dimerization. The investigation of the spatial organization of the receptor subunits at naturally occurring expression levels in the plasma membrane of living cells by particle image cross correlation spectroscopy analysis, however, revealed a random and uncorrelated distribution of IL-4Rα and IL-13Rα1. Thus, any co-organization or co-clustering as well as ligand-independent dimerization could be unambiguously excluded.

Receptor dimers also did not exhibit any tendency of partitioning at the plasma membrane. Instead, free diffusion within the experimentally limited time window (lag-time 32 ms) was observed for both single receptor subunits and dimers. These findings clearly support the model of ligand-induced subunit dimerization at the cell surface, which was shown to occur with sufficient efficiency at physiological conditions and is very likely the key event for the activation of cytokine receptors.

Enhanced dimerization observed for the receptor at the cell surface compared to the *in vitro* data, despite the absence of both local subunit concentration enrichment by partitioning effects and IL-4Rα/IL-13Rα1 pre-dimerization, suggested contributions of other cellular determinants, with actin-based plasma membrane microcompartmentation constituting a possible candidate. The cortical membrane skeleton (MSK) meshwork in combination with associated membrane proteins is believed to form a “picket fence”, which transiently confines the diffusion of receptors within submicroscopic zones [95, 107, 238]. These transient confinement zones, in turn, have been predicted to enhance signaling by promoting receptor activation bursts [97, 114].

Here, detailed studies of the spatiotemporal dynamics of receptor dimers actually revealed a critical role of the MSK in dynamically stabilizing receptor complexes. In particular highly transient interactions like those induced by the RGA variant were observed to gain from spatial confinement, as the disruption of the actin cytoskeleton strongly decreased the periods of correlated motion of IL-4Rα and IL-13Rα1 in presence of RGA. In contrast, the complex stability of KFR-induced dimers was not affected by the reduction of receptor confinement. The transient nature of RGA-induced complexes was also indirectly observed by an increased average inter-subunit distance in MSK-intact cells, because the high interaction frequency was speculated to be spatiotemporal not resolvable by the utilized experimental setup, resulting in a blurred intermediate picture. The corresponding shift of the IL-4Rα/IL-13Rα1 distance distribution towards a high 70 nm fraction in case of RGA additionally supported the proposed dynamical stabilization by receptor confinement, because the average MSK-dependent compartment size in HeLa cells was previously determined to be in the same range (~68 nm, [110]).

Based on these findings, the experimentally parameterized ternary complex interaction kinetics and the diffusion properties of the receptor in the plasma membrane, a simple spatial-stochastic model simulation was developed, which reproduced essential features of the observed spatiotemporal dynamics of the receptor on the cell surface. For this straightforward model, only two interacting molecular species are needed that undergo probability-dependent hop-diffusion in a homogeneously compartmentalized two-dimensional space, while interacting according to appropriate association and dissociation probabilities. After addition of a virtual image acquisition step (exposure time

32 ms) including experimentally not avoidable motion blurring, the evaluation of simulation-derived single molecule images confirmed the characteristic inter-receptor distance shift of transient dimers. Moreover, a positive effect on the complex lifetime by restricting the diffusional freedom could be demonstrated by means of simulated data. This model therefore clearly corroborates the hypothesis that membrane compartmentation by the MSK is an important determinant for dynamically stabilizing cytokine receptors by ensuring rapid re-association of transient receptor dimers.

These results, however, imply that for highly transient complexes the dimerization efficiency of the receptor, expressed in terms of the correlated faction of IL-4Rα and IL-13Rα1, is overestimated by the used experimental approach, because temporally dissociated dimers within submicroscopic membrane compartments are continuously detected as assembled complexes. Thus, the calculated effective two-dimensional binding affinities on the cell surface have to be regarded as apparent K_D^T values, particularly in the case of RGA and DN4. Importantly, similar re-association in transient confinement zones can also be expected for the other ligands, but, due to the substantially higher molecular complex stability, over substantially longer time-scales that are beyond the time-scale of the single molecule co-tracking experiments performed in the present study. Interestingly though, these transient dissociation events do not seem to compromise signaling as the potency of STAT6 activation by RGA is similar compared to the other ligands. These results suggest that downstream signaling may be maintained during transient dissociation events as schematically depicted in Figure 44, which can be rationalized by the very short lifetime of the dissociated state.

Irrespective of the applied ligand the IL-4Rα/IL-13Rα1 dimers overall appeared to be remarkably stable on the higher milliseconds-to-seconds timescale. Indeed, with the completely minimalistic model developed in this work a >50% increase in the mean lifetime of RGA-induced complexes was already verified. Interestingly, a combined experimental and computational investigation of the type I IFN receptor just recently identified a secondary confinement within ~300 nm-sized compartments. Within this study, hierarchical, two-tiered plasma membrane compartmentation by the MSK was found to essentially promote the maintenance of IFN-induced signaling complexes on the cell surface [115]. It seems very likely that the same holds true for other cytokine receptors including the IL-4/IL-13 system, which could explain the residual discrepancies between experimental and minimal model simulation data. Nevertheless, it has to be considered that other types of plasma membrane microcompartmentation (e.g. lipid-based segregation) might also contribute to the stabilization of receptor dimers [103, 105, 239, 240], although such mechanisms could not be verified or excluded by the present study.

Importantly, the cellular basis to support effective receptor dimerization is not limited to properties of the plasma membrane. In case of the type I IFN receptor for instance, an improvement of the inter-subunit affinity by intracellular, endogenous proteins like RACK-1 and Jak1 was proposed [80]. Indeed, a gain in affinity due to intracellular interactions with the constitutively associated Janus kinases (JAKs) was recently verified by a quantitative single molecule approach [60]. Preliminary, unpublished results of the type II IL-4 receptor using the same technique also indicate a slight complex stabilizing effect via the associated JAKs. Additional ways of dimerization enhancement would on any account explain why even in case of RGA almost no complete IL-4Rα/IL-13Rα1 complex dissociation events were detectable, despite the comparable fast dissociation of the IL-13Rα1 subunit observed *in vitro*.

Considering the physiological environment, mechanisms for keeping activated receptor dimers together beyond their molecular lifetimes would be particularly beneficial at the low ligand concentrations available, where only a minor fraction of receptors is occupied. Moreover, as shown in this work and by others, ligand binding is followed by uptake into endosomes [160, 161, 163], which plays an important role for the signaling potency (see below). Taking into account the very low physiological receptor expression levels of only a few hundred copies per cell [84, 241, 242], re-association of activated receptor dimers could ensure the uptake of intact signaling complexes at low receptor occupancies, allowing to maintain signaling activity in endosomes. According to that, the presence of IL-4 receptor signaling complexes in endosomes was reported previously [160].

So far, plasma membrane microcompartmentation has been mostly associated with receptor pre-organization to promote the formation of dimers or oligomers [243-245]. The results of the present study, however, highlight an important role in stabilizing signaling complexes once they are formed by exploiting transient confinement zones, while any superordinate organizational structure (e.g. receptor clustering) evidently does not exist. In combination with other cellular aspects like the above mentioned gain in complex stability by intracellular associated proteins (e.g. JAKs), the receptor dimerization efficiency in the plasma membrane is consequently not determined by the molecular two-dimensional affinities to such an extent as predicted by *in vitro* measurements. In the cellular environment the apparent K_D^T instead lies in the range of endogenous receptor levels. This in turn offers a possible explanation for the frequently observed phenomenon that early signal events (e.g. STAT6 phosphorylation) are hardly affected by changes of the two-dimensional affinity between receptor subunits [56, 225], as it was previously shown [64] and verified in this work for the RGA and KFR variants.

Further plausible explanations for the seeming disconnect between cytokine receptor complex stability and early signal activation were derived from the second part of this study, in which the role of the three-dimensional ligand-receptor dynamics with respect to receptor dimerization and signaling was systematically explored. By employing a library of IL-13 variants, which covers ligand binding affinities of nearly six orders of magnitude, striking observations were made that support a model in which the fine-tuning of initial receptor binding kinetics enables cytokines to exhibit robust signal activation at a wide range of binding affinities and yet preserve differential responses. The ligand-dependent association and dissociation rates k_a^B and k_d^B are thereby connected to distinct functions in determining the signaling output of a given cytokine: k_a^B correlates with the amount of pSTAT that is generated by controlling the number of ligand-receptor complexes formed in the plasma membrane, whereas k_d^B is directly connected to the kinetics of STAT activation through modulation of the lifetime of ligand-receptor complexes as a function of endocytosis.

An observation that emerges from the STAT6 phosphorylation data is the presence of a region in the receptor binding affinity space, herein referred as the “buffering region”, in which the extent of STAT6 activation appears to be unaffected by large three-dimensional affinity changes. Agonists with 100-fold increased (A11) and 100-fold decreased (C10) binding affinities for the IL-13Rα1 subunit compared to that of wild-type IL-13 elicited STAT6 activation to similar extents. Congruent results have been obtained in other systems in which affinity maturation of the cognate ligands did not yield stronger signal activation [56, 64, 246, 247]. Importantly, the >100,000-fold difference in the three-dimensional binding affinities of the IL-13 variants result from changes in their k_d^B values, while all variants exhibit comparable k_a^B values. Thus, it was suggested that the activation of STAT remains largely unaffected by changes in k_d^B above a certain threshold. Moreover, all IL-13 variants yielded cell surface complex formation to similar extends, arguing in favor of k_a^B, but not k_d^B, as the main factor that determines the number of complexes formed by a given cytokine, generating the experimentally observed “buffering region”. Notably, such distinct roles of the ligand association and dissociation kinetics are also able to explain the frequently observed phenomenon that IL-4 is superior to IL-13 in inducing the phosphorylation of STAT6 [53]. Because IL-4 exhibits a tenfold higher rate of binding to its cognate receptor subunit IL-4Rα and a twentyfold higher binary complex lifetime compared to the interaction of IL-13 and IL-13Rα1, it induces a faster and more potent activation of STAT6, as was confirmed in this work. Since RGA and KFR bind to IL-4Rα with k_a^B and k_d^B values similar to IL-4 (data from personal communication with I. Moraga), the observation of an STAT6 activation pattern almost identical to IL-4 further supports the proposed interrelationships.

A caveat to this interpretation is that because the examined IL-13 variants bind with rather similar association rates, it was not possible to systematically test the effect that large changes in k_a^B could have in cytokine receptor complex formation and signal activation. More directed engineering of ligand association rates by manipulating the electrostatic potential [248] will be required to explore whether a further gain in STAT activation potency could be achieved by substantially increasing the speed of binary ligand-receptor complex assembly. Collectively, the here discussed data suggest that cytokines are able to effectively signal given a sufficient association rate, largely independent of their affinity. In nature, cytokine signaling would benefit from loose affinity constraints by enabling cells to sense and respond to a wide range of binding affinities and complex stabilities.

How cells translate virtually identical STAT activation profiles into different extents of cell proliferation and differentiation remains, however, unclear. But the present study demonstrates that IL-13 agonists with slower dissociation rates persist longer as receptor complexes, promote faster kinetics of STAT activation and induce more potent effector functions (i.e., increased proliferative responses and enhanced monocyte differentiation) than do low-affinity ligands. Thus, cytokines apparently fine-tune their distal responses by controlling the lifetime of their complexes and the kinetics of downstream signaling. Consistent with this notion, it could be shown that the total amounts of STAT6 molecules activated by a cytokine-receptor complex remained unaltered through a wide range of binary complex stabilities and ligand concentrations. Although short-lived complexes and reduced ligand concentrations resulted in delayed kinetics of pSTAT6 generation, the absolute number of molecules activated after a certain time did not change substantially. These observations are in line with previous studies of the IL-4 variants RGA and KFR [64] and with the STAT6 phosphorylation data obtained in this work. Despite there being a more than 2,000-fold difference in the two-dimensional receptor binding affinities of these mutants, they activate STAT6 to roughly similar extents and with almost identical kinetics. The potencies of their distal responses correlate, however, with the stabilities of the respective receptor dimers.

The collected data suggested that the cell surface abundance of cytokine receptors constitutes a pivotal determinant in “titrating” high- and low-affinity ligands with respect to signaling and function. In accordance with previous studies of the IL-4 receptor system [53, 64], cells with increased amounts of cytokine receptors were speculated to be relatively insensitive to differences in ligand affinity with respect to the membrane-proximal activation of STATs. Conversely, in cells that are equipped with a low cytokine receptor density, high-affinity ligands would gain a functional advantage. Indeed, siRNA-mediated reduction of the cell surface abundance of IL-13Rα1 resulted in a spread of the

STAT6 activation potencies of different IL-13 variants: low-affinity agonists induced substantially weaker signaling than high-affinity ones. Similarly, the cell surface receptor density determined the differential antiproliferative responses exhibited by low- and high-affinity IFN subtypes [61, 62].

But, although a clear correlation between k_d^B values, receptor complex lifetimes, signaling kinetics and the potency of membrane-distal signaling was observed in the present study, a full understanding of how all of these parameters interconnect together and translate into more potent and diverse responses has not yet been reached. Moreover, the effect of negative feedback mechanisms in signal activation remains largely unexplored. In fact, a recently proposed model states that the plasticity of the type I IFN receptor is regulated on the level of receptor dimerization by a specific negative feedback regulator, which interferes with the recruitment of the second receptor subunit into the ternary complex [60]. In line with this conclusive mechanism, low-affinity IFN subtypes were shown to be more sensitive to this form of regulation than were high-affinity IFN variants [249]. It is therefore tempting to speculate that high-affinity cytokines are in general able to withstand the negative regulation of comparable feedback mechanism by forming more stable complexes, thus eliciting more potent or more diverse distal signaling responses. The presence of such mechanisms in other cytokine receptor systems remains, however, to be shown.

The here obtained new insights challenge the equilibrium model for cytokine-mediated signal activation. In that model, cytokines recruit their receptor subunits through a two-step mechanism, reaching a dynamic equilibrium between binary and ternary complexes on the plasma membrane [52, 69, 250]. A modulation of the association and dissociation rates for any of the two receptor chains is predicted to produce a parallel alteration in the number of complexes formed by a given cytokine and in its signaling potency. However, it could be shown that 10,000-fold differences in the three-dimensional binding affinity, which were primarily attributed to changes in k_d^B, only marginally altered the STAT activation. This is not a unique feature of IL-13, as it is also found for other cytokines, such as those of the type I IFN family, of which there are more than 15 members that share the same cell surface receptor, but bind with very different affinities and still activate STAT with very similar potencies [251].

In the present study, by extending the equilibrium ligand binding model into a steady-state model including endocytic trafficking, the kinetics and the potencies of STAT phosphorylation by IL-13 variants that exhibit a large range of k_d^B values were reproduced with high fidelity. Indeed, the entangled interplay of cytokine-receptor complex stability and receptor trafficking has been appreciated for explaining the potencies of cytokines and other hormones [252, 253]. Thus, a minimal model comprising reversible ligand binding to the cell surface receptor followed by irreversible uptake of intact signaling complexes into endosomes and further sorting into degradative and recycling pathways was applied on the basis of differential equations. In this model, increasing the binding affinity of the ligand by increasing the stability of the complex (that is, by decreasing ligand dissociation from the surface) enhances signaling only until the dissociation rate is exceeded by the rate of endocytosis (k_{endo}). Once k_{endo} dominates over k_d^B, the final number of signaling complexes is determined by the k_a^B rate of the ligand, and any further increase in affinity by changes in k_d^B will not have an effect on membrane-proximal signal activation. Consequently, this model explains the existence of a buffering region in which agonists with similar k_a^B and $k_d^B < k_{endo}$ will promote early signaling outcomes to comparable extents. Moreover, it readily offers an explanation for the delayed kinetics of signal activation that was observed for low-affinity IL-13 variants: assuming that downstream signaling is maintained in early endosomes, the number of active signaling complexes increases with ongoing endocytosis, because they are constantly and irreversible removed from the equilibrium at the cell surface.

Considering these findings and the results from the dimerization assays that were performed with full-length receptors at physiologically relevant amounts, the critical role for receptor endocytosis in efficient receptor dimerization and signaling exclusively from endosomes that was proposed by recent studies [160, 163] was not verified. Instead, the present study revealed that endocytosis is critical for controlling ligand binding to the receptor by accumulation of ligand-bound receptors, thus buffering signaling activity over a large range of ligand binding affinities.

To sum up, it could be shown in this study that signaling via the type II IL-4 receptor is primarily governed by at least four molecular and cellular key determinants that were combined in a conclusive mechanistic model (Figure 44). While an intricate interplay of *(i)* molecular interactions and *(ii)* receptor confinement in plasma membrane micro-compartments controls the spatiotemporal dynamics of the receptor complex, the accumulation of active signaling complexes by *(iii)* endocytosis significantly extends the functional range of ligand binding affinities, which is in turn limited by the *(iv)* surface expression level of the receptor subunits. Consequently, the dimerization of the type II IL-4 receptor is unequivocally ligand-induced and occurs on the cell surface with sufficient efficiency, but is sustained by endosomal uptake of active signaling complexes. Considering recent studies of the type I IFN receptor that yielded similar findings [60], it is tempting to speculate that these parameters in general determine cytokine receptor signaling, at least in the case of heterodimeric class I and class II cytokine receptors.

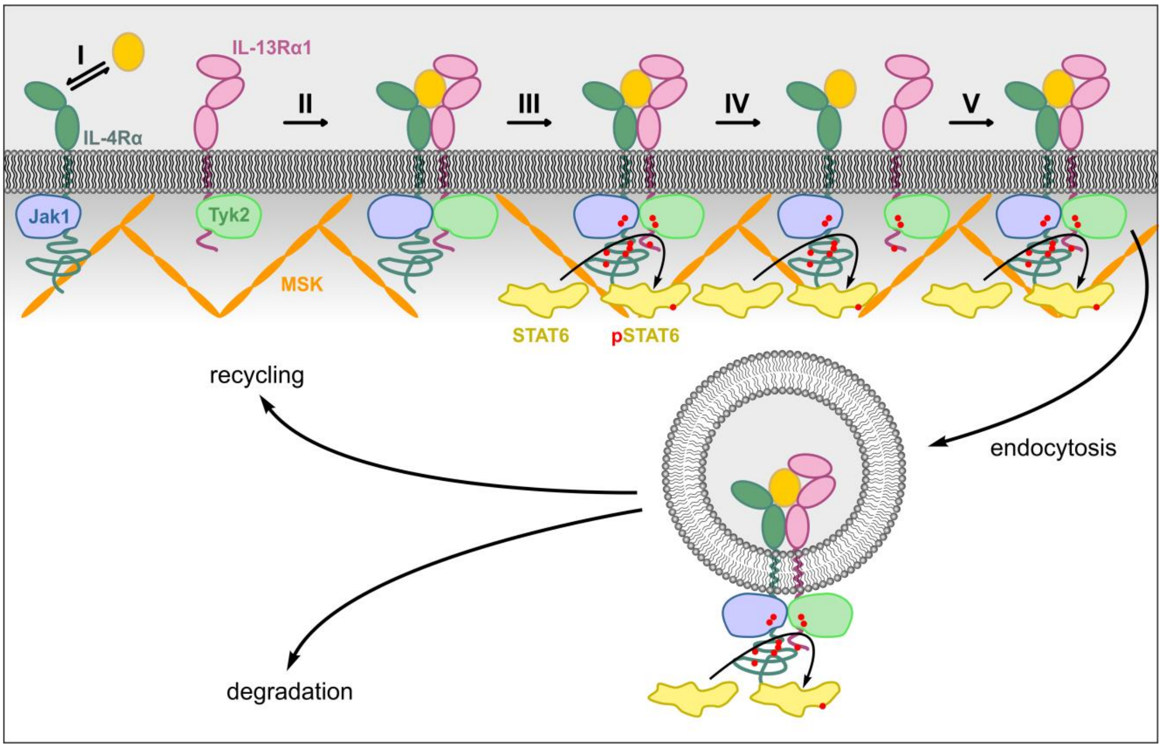

Figure 44. Mechanistic model for ligand-induced type II IL-4 receptor dimerization sustained by rapid re-association within MSK-dependent plasma membrane microcompartments and accumulation of signaling complexes in endosomes. After reversible ligand binding to the cell surface receptor *(I)* and ternary complex assembly by lateral second chain recruitment *(II)*, downstream signaling is initiated *(III)* that is maintained during transient dissociation events within MSK-dependent confinement zones *(IV and V)* until receptor uptake by endocytosis. Ongoing endocytosis slowly increases the number of signalling complexes with time by irreversibly removing them from the equilibrium at the cell surface.

There is also growing evidence that the affinity and dynamics of signaling complexes play a key role for the differential activity and pleiotropy of cytokines [32, 50, 52-54, 56, 59, 64, 246, 254, 255]. This hypothesis was supported by the present study, although large changes in the two- and three-dimensional binding affinities resulted only in minor alterations of receptor dimerization levels and the total amount of membrane-proximal signaling. But, distinct roles of ligand binding kinetics were found that enable cells to respond with unique membrane-proximal signaling patterns when the receptor assembly is induced by ligands with significantly different affinities. Moreover, although dynamic complex stabilization by MSK-based plasma membrane microcompartmentation was identified, the ligand-dependent complex stability was confirmed to constitute the key factor that determines the potency of a given cytokine to elicit membrane-distal signaling outcomes, as previously proposed by other studies [56, 60, 64, 225].

How the initial signaling pattern, the complex stability and the potency to induce complex biological outcomes (e.g. cell proliferation and differentiation) are intertwined, remains, however, an open question. Since feedback mechanisms interfering at the level of receptor dimerization have recently been reported [60], a better understanding of this complex interplay may be obtained by focusing further investigations onto the regulation of cytokine receptor signaling. In this regard, also the MSK-based dynamic stabilization of receptors dimers has to be taken into account, because due to the fact that the size and permeability of the MSK meshwork varies in different cells types and also depends on the cell cycle and cellular environment [110], it may have important implications for the regulation of cellular responses.

Considering consequences for future drug development, there now appears to be a mechanistic rationale for purposeful modulation of ligand-receptor association and dissociation rates by protein engineering to design cytokine variants that preserve efficacy, yet are less toxic therapeutics. Low-dose IL-2 is showing great promise as a medication for cancer, diabetes and other autoimmune diseases [256-258]. Thus, it appears likely that similar low-dose approaches with other cytokines or higher-dose treatments with affinity-impaired, rather than affinity-enhanced cytokines could rescue cytokine therapies, which were previously limited by dose-dependent toxicity.

6 References

1. Baldo, B.A., *Side effects of cytokines approved for therapy.* Drug Saf, 2014. **37**(11): p. 921-43.
2. Borish, L.C. and J.W. Steinke, *2. Cytokines and chemokines.* J Allergy Clin Immunol, 2003. **111**(2 Suppl): p. S460-75.
3. O'Shea, J.J., S.M. Holland, and L.M. Staudt, *JAKs and STATs in immunity, immunodeficiency, and cancer.* N Engl J Med, 2013. **368**(2): p. 161-70.
4. Vacchelli, E., et al., *Trial Watch: Immunostimulatory cytokines.* Oncoimmunology, 2012. **1**(4): p. 493-506.
5. Davies, D.R. and A. Wlodawer, *Cytokines and their receptor complexes.* FASEB J, 1995. **9**(1): p. 50-6.
6. Abbas, A.K., Lichtman, A.H. and S. Pillai, *Cellular and Molecular Immunology*. Eighth Edition 2015, Philadelphia, PA, USA: Saunders, an imprint of Elsevier Inc.
7. Wang, X., et al., *Structural biology of shared cytokine receptors.* Annu Rev Immunol, 2009. **27**: p. 29-60.
8. Gaffen, S.L., *Structure and signalling in the IL-17 receptor family.* Nat Rev Immunol, 2009. **9**(8): p. 556-67.
9. Fitzgerald, K., et al., *The Cytokine Factsbook*. Second Edition 2001, London, UK: Academic Press.
10. Yawata, H., et al., *Structure-function analysis of human IL-6 receptor: dissociation of amino acid residues required for IL-6-binding and for IL-6 signal transduction through gp130.* EMBO J, 1993. **12**(4): p. 1705-12.
11. Leonard, W.J., *Cytokines and immunodeficiency diseases.* Nat Rev Immunol, 2001. **1**(3): p. 200-8.
12. Richard Coico, G.S., *Immunology: A Short Course*. Seventh Edition ed. 2015, Chichester, West Sussex, UK: John Wiley & Sons, Ltd.
13. Ihle, J.N., et al., *Signaling through the hematopoietic cytokine receptors.* Annu Rev Immunol, 1995. **13**: p. 369-98.
14. Kunz, M. and S.M. Ibrahim, *Cytokines and cytokine profiles in human autoimmune diseases and animal models of autoimmunity.* Mediators Inflamm, 2009. **2009**: p. 979258.
15. Williams, C.M., et al., *Cytokine pathways in allergic disease.* Toxicol Pathol, 2012. **40**(2): p. 205-15.
16. Lin, W.W. and M. Karin, *A cytokine-mediated link between innate immunity, inflammation, and cancer.* J Clin Invest, 2007. **117**(5): p. 1175-83.
17. Suzuki, A., et al., *Targeting of IL-4 and IL-13 receptors for cancer therapy.* Cytokine, 2015. **75**(1): p. 79-88.
18. Skurkovich, S.V., et al., *Immunosuppressive effect of an anti-interferon serum.* Nature, 1974. **247**(5442): p. 551-2.
19. Chatenoud, L., *Immune therapies of autoimmune diseases: are we approaching a real cure?* Curr Opin Immunol, 2006. **18**(6): p. 710-7.
20. Astrakhantseva, I.V., et al., *Modern anti-cytokine therapy of autoimmune diseases.* Biochemistry (Mosc), 2014. **79**(12): p. 1308-21.
21. Chung, K.F., *Targeting the interleukin pathway in the treatment of asthma.* Lancet, 2015. **386**(9998): p. 1086-96.
22. Lee, S. and K. Margolin, *Cytokines in cancer immunotherapy.* Cancers (Basel), 2011. **3**(4): p. 3856-93.

23. Dutcher, J., *Current status of interleukin-2 therapy for metastatic renal cell carcinoma and metastatic melanoma.* Oncology (Williston Park), 2002. **16**(11 Suppl 13): p. 4-10.
24. Isaacs, C., et al., *Randomized placebo-controlled study of recombinant human interleukin-11 to prevent chemotherapy-induced thrombocytopenia in patients with breast cancer receiving dose-intensive cyclophosphamide and doxorubicin.* J Clin Oncol, 1997. **15**(11): p. 3368-77.
25. Ravandi, F., *Role of cytokines in the treatment of acute leukemias: a review.* Leukemia, 2006. **20**(4): p. 563-71.
26. Puri, R.K., et al., *Targeting of interleukin-13 receptor on human renal cell carcinoma cells by a recombinant chimeric protein composed of interleukin-13 and a truncated form of Pseudomonas exotoxin A (PE38QQR).* Blood, 1996. **87**(10): p. 4333-9.
27. Kawakami, M., K. Kawakami, and R.K. Puri, *Interleukin-4-Pseudomonas exotoxin chimeric fusion protein for malignant glioma therapy.* J Neurooncol, 2003. **65**(1): p. 15-25.
28. Lupardus, P.J., et al., *Structure of the pseudokinase-kinase domains from protein kinase TYK2 reveals a mechanism for Janus kinase (JAK) autoinhibition.* Proc Natl Acad Sci U S A, 2014. **111**(22): p. 8025-30.
29. Yamaoka, K., et al., *The Janus kinases (Jaks).* Genome Biol, 2004. **5**(12): p. 253.
30. Radtke, S., et al., *The Jak1 SH2 domain does not fulfill a classical SH2 function in Jak/STAT signaling but plays a structural role for receptor interaction and up-regulation of receptor surface expression.* J Biol Chem, 2005. **280**(27): p. 25760-8.
31. Silvennoinen, O., et al., *New insights into the structure and function of the pseudokinase domain in JAK2.* Biochem Soc Trans, 2013. **41**(4): p. 1002-7.
32. Spangler, J.B., et al., *Insights into cytokine-receptor interactions from cytokine engineering.* Annu Rev Immunol, 2015. **33**: p. 139-67.
33. Rawlings, J.S., K.M. Rosler, and D.A. Harrison, *The JAK/STAT signaling pathway.* J Cell Sci, 2004. **117**(Pt 8): p. 1281-3.
34. Ihle, J.N., *The Stat family in cytokine signaling.* Curr Opin Cell Biol, 2001. **13**(2): p. 211-7.
35. Imada, K. and W.J. Leonard, *The Jak-STAT pathway.* Mol Immunol, 2000. **37**(1-2): p. 1-11.
36. Leonard, W.J. and J.X. Lin, *Cytokine receptor signaling pathways.* J Allergy Clin Immunol, 2000. **105**(5): p. 877-88.
37. Baker, S.J., S.G. Rane, and E.P. Reddy, *Hematopoietic cytokine receptor signaling.* Oncogene, 2007. **26**(47): p. 6724-37.
38. Alexander, W.S., *Suppressors of cytokine signalling (SOCS) in the immune system.* Nat Rev Immunol, 2002. **2**(6): p. 410-6.
39. Gadina, M., et al., *Signaling by type I and II cytokine receptors: ten years after.* Curr Opin Immunol, 2001. **13**(3): p. 363-73.
40. Sharrocks, A.D., *PIAS proteins and transcriptional regulation--more than just SUMO E3 ligases?* Genes Dev, 2006. **20**(7): p. 754-8.
41. Levine, S.J., *Molecular mechanisms of soluble cytokine receptor generation.* J Biol Chem, 2008. **283**(21): p. 14177-81.
42. Rose-John, S., *IL-6 trans-signaling via the soluble IL-6 receptor: importance for the pro-inflammatory activities of IL-6.* Int J Biol Sci, 2012. **8**(9): p. 1237-47.
43. Mantovani, A., et al., *Decoy receptors: a strategy to regulate inflammatory cytokines and chemokines.* Trends Immunol, 2001. **22**(6): p. 328-36.

44. Platta, H.W. and H. Stenmark, *Endocytosis and signaling.* Curr Opin Cell Biol, 2011. **23**(4): p. 393-403.
45. Sorkin, A. and M. von Zastrow, *Endocytosis and signalling: intertwining molecular networks.* Nat Rev Mol Cell Biol, 2009. **10**(9): p. 609-22.
46. Sadowski, L., I. Pilecka, and M. Miaczynska, *Signaling from endosomes: location makes a difference.* Exp Cell Res, 2009. **315**(9): p. 1601-9.
47. Cendrowski, J., A. Maminska, and M. Miaczynska, *Endocytic regulation of cytokine receptor signaling.* Cytokine Growth Factor Rev, 2016.
48. Sulahian, R., O. Cleaver, and L.J. Huang, *Ligand-induced EpoR internalization is mediated by JAK2 and p85 and is impaired by mutations responsible for primary familial and congenital polycythemia.* Blood, 2009. **113**(21): p. 5287-97.
49. Becker, V., et al., *Covering a broad dynamic range: information processing at the erythropoietin receptor.* Science, 2010. **328**(5984): p. 1404-8.
50. Moraga, I., et al., *Multifarious determinants of cytokine receptor signaling specificity.* Adv Immunol, 2014. **121**: p. 1-39.
51. de Weerd, N.A. and T. Nguyen, *The interferons and their receptors--distribution and regulation.* Immunol Cell Biol, 2012. **90**(5): p. 483-91.
52. Piehler, J., et al., *Structural and dynamic determinants of type I interferon receptor assembly and their functional interpretation.* Immunol Rev, 2012. **250**(1): p. 317-34.
53. LaPorte, S.L., et al., *Molecular and structural basis of cytokine receptor pleiotropy in the interleukin-4/13 system.* Cell, 2008. **132**(2): p. 259-72.
54. Yoon, S.I., et al., *Same structure, different function crystal structure of the Epstein-Barr virus IL-10 bound to the soluble IL-10R1 chain.* Structure, 2005. **13**(4): p. 551-64.
55. Subramaniam, P.S., et al., *Differential recognition of the type I interferon receptor by interferons tau and alpha is responsible for their disparate cytotoxicities.* Proc Natl Acad Sci U S A, 1995. **92**(26): p. 12270-4.
56. Jaitin, D.A., et al., *Inquiring into the differential action of interferons (IFNs): an IFN-alpha2 mutant with enhanced affinity to IFNAR1 is functionally similar to IFN-beta.* Mol Cell Biol, 2006. **26**(5): p. 1888-97.
57. Rao, B.M., et al., *Interleukin 2 (IL-2) variants engineered for increased IL-2 receptor alpha-subunit affinity exhibit increased potency arising from a cell surface ligand reservoir effect.* Mol Pharmacol, 2004. **66**(4): p. 864-9.
58. Rao, B.M., et al., *High-affinity CD25-binding IL-2 mutants potently stimulate persistent T cell growth.* Biochemistry, 2005. **44**(31): p. 10696-701.
59. Yoon, S.I., et al., *Epstein-Barr virus IL-10 engages IL-10R1 by a two-step mechanism leading to altered signaling properties.* J Biol Chem, 2012. **287**(32): p. 26586-95.
60. Wilmes, S., et al., *Receptor dimerization dynamics as a regulatory valve for plasticity of type I interferon signaling.* J Cell Biol, 2015. **209**(4): p. 579-93.
61. Moraga, I., et al., *Receptor density is key to the alpha2/beta interferon differential activities.* Mol Cell Biol, 2009. **29**(17): p. 4778-87.
62. Levin, D., D. Harari, and G. Schreiber, *Stochastic receptor expression determines cell fate upon interferon treatment.* Mol Cell Biol, 2011. **31**(16): p. 3252-66.
63. Junttila, I.S., et al., *Tuning sensitivity to IL-4 and IL-13: differential expression of IL-4Ralpha, IL-13Ralpha1, and gammac regulates relative cytokine sensitivity.* J Exp Med, 2008. **205**(11): p. 2595-608.
64. Junttila, I.S., et al., *Redirecting cell-type specific cytokine responses with engineered interleukin-4 superkines.* Nat Chem Biol, 2012. **8**(12): p. 990-8.

65. Cunningham, B.C., et al., *Dimerization of the extracellular domain of the human growth hormone receptor by a single hormone molecule.* Science, 1991. **254**(5033): p. 821-5.
66. Cohen, B., et al., *Ligand-induced association of the type I interferon receptor components.* Mol Cell Biol, 1995. **15**(8): p. 4208-14.
67. Whitty, A., et al., *Interaction affinity between cytokine receptor components on the cell surface.* Proc Natl Acad Sci U S A, 1998. **95**(22): p. 13165-70.
68. Giese, B., et al., *Dimerization of the cytokine receptors gp130 and LIFR analysed in single cells.* J Cell Sci, 2005. **118**(Pt 21): p. 5129-40.
69. Whitty, A. and C.W. Borysenko, *Small molecule cytokine mimetics.* Chem Biol, 1999. **6**(4): p. R107-18.
70. Lopez, A.F., et al., *Molecular basis of cytokine receptor activation.* IUBMB Life, 2010. **62**(7): p. 509-18.
71. Stroud, R.M. and J.A. Wells, *Mechanistic diversity of cytokine receptor signaling across cell membranes.* Sci STKE, 2004. **2004**(231): p. re7.
72. Atanasova, M. and A. Whitty, *Understanding cytokine and growth factor receptor activation mechanisms.* Crit Rev Biochem Mol Biol, 2012. **47**(6): p. 502-30.
73. Remy, I., I.A. Wilson, and S.W. Michnick, *Erythropoietin receptor activation by a ligand-induced conformation change.* Science, 1999. **283**(5404): p. 990-3.
74. Constantinescu, S.N., et al., *Ligand-independent oligomerization of cell-surface erythropoietin receptor is mediated by the transmembrane domain.* Proc Natl Acad Sci U S A, 2001. **98**(8): p. 4379-84.
75. Brown, R.J., et al., *Model for growth hormone receptor activation based on subunit rotation within a receptor dimer.* Nat Struct Mol Biol, 2005. **12**(9): p. 814-21.
76. Yang, N., et al., *Role of the growth hormone (GH) receptor transmembrane domain in receptor predimerization and GH-induced activation.* Mol Endocrinol, 2007. **21**(7): p. 1642-55.
77. Damjanovich, S., et al., *Preassembly of interleukin 2 (IL-2) receptor subunits on resting Kit 225 K6 T cells and their modulation by IL-2, IL-7, and IL-15: a fluorescence resonance energy transfer study.* Proc Natl Acad Sci U S A, 1997. **94**(24): p. 13134-9.
78. Tenhumberg, S., et al., *gp130 dimerization in the absence of ligand: preformed cytokine receptor complexes.* Biochem Biophys Res Commun, 2006. **346**(3): p. 649-57.
79. Zaks-Zilberman, M., et al., *Interleukin-5 receptor subunit oligomerization and rearrangement revealed by fluorescence resonance energy transfer imaging.* J Biol Chem, 2008. **283**(19): p. 13398-406.
80. Krause, C.D., et al., *Ligand-independent interaction of the type I interferon receptor complex is necessary to observe its biological activity.* Cytokine, 2013. **64**(1): p. 286-97.
81. Krause, C.D., et al., *Preassembly and ligand-induced restructuring of the chains of the IFN-gamma receptor complex: the roles of Jak kinases, Stat1 and the receptor chains.* Cell Res, 2006. **16**(1): p. 55-69.
82. Krause, C.D., et al., *Interactions among the components of the interleukin-10 receptor complex.* Biochem Biophys Res Commun, 2006. **340**(2): p. 377-85.
83. Krause, C.D., et al., *Seeing the light: preassembly and ligand-induced changes of the interferon gamma receptor complex in cells.* Mol Cell Proteomics, 2002. **1**(10): p. 805-15.

84. McKinstry, W.J., et al., *Cytokine receptor expression on hematopoietic stem and progenitor cells.* Blood, 1997. **89**(1): p. 65-71.

85. Gavutis, M., et al., *Determination of the two-dimensional interaction rate constants of a cytokine receptor complex.* Biophys J, 2006. **90**(9): p. 3345-55.

86. Cranfill, P.J., et al., *Quantitative assessment of fluorescent proteins.* Nat Methods, 2016. **13**(7): p. 557-62.

87. Piehler, J., *New methodologies for measuring protein interactions in vivo and in vitro.* Curr Opin Struct Biol, 2005. **15**(1): p. 4-14.

88. Moraga, I., et al., *Tuning cytokine receptor signaling by re-orienting dimer geometry with surrogate ligands.* Cell, 2015. **160**(6): p. 1196-208.

89. Vamosi, G., et al., *IL-2 and IL-15 receptor alpha-subunits are coexpressed in a supramolecular receptor cluster in lipid rafts of T cells.* Proc Natl Acad Sci U S A, 2004. **101**(30): p. 11082-7.

90. de Bakker, B.I., et al., *Nanometer-scale organization of the alpha subunits of the receptors for IL2 and IL15 in human T lymphoma cells.* J Cell Sci, 2008. **121**(Pt 5): p. 627-33.

91. Jenei, A., et al., *Non-random distribution of interleukin receptors on the cell surface.* Chemphyschem, 2009. **10**(9-10): p. 1577-85.

92. Kramer, J.M., et al., *Evidence for ligand-independent multimerization of the IL-17 receptor.* J Immunol, 2006. **176**(2): p. 711-5.

93. Singer, S.J. and G.L. Nicolson, *The fluid mosaic model of the structure of cell membranes.* Science, 1972. **175**(4023): p. 720-31.

94. Cambi, A. and D.S. Lidke, *Nanoscale membrane organization: where biochemistry meets advanced microscopy.* ACS Chem Biol, 2012. **7**(1): p. 139-49.

95. Marguet, D., et al., *Dynamics in the plasma membrane: how to combine fluidity and order.* EMBO J, 2006. **25**(15): p. 3446-57.

96. Lenne, P.F., et al., *Dynamic molecular confinement in the plasma membrane by microdomains and the cytoskeleton meshwork.* EMBO J, 2006. **25**(14): p. 3245-56.

97. Kusumi, A., et al., *Dynamic organizing principles of the plasma membrane that regulate signal transduction: commemorating the fortieth anniversary of Singer and Nicolson's fluid-mosaic model.* Annu Rev Cell Dev Biol, 2012. **28**: p. 215-50.

98. Mayor, S. and M. Rao, *Rafts: scale-dependent, active lipid organization at the cell surface.* Traffic, 2004. **5**(4): p. 231-40.

99. Pike, L.J., *The challenge of lipid rafts.* J Lipid Res, 2009. **50 Suppl**: p. S323-8.

100. Munro, S., *Lipid rafts: elusive or illusive?* Cell, 2003. **115**(4): p. 377-88.

101. Dykstra, M., et al., *Location is everything: lipid rafts and immune cell signaling.* Annu Rev Immunol, 2003. **21**: p. 457-81.

102. Simons, K. and D. Toomre, *Lipid rafts and signal transduction.* Nat Rev Mol Cell Biol, 2000. **1**(1): p. 31-9.

103. Marchetti, M., et al., *Stat-mediated signaling induced by type I and type II interferons (IFNs) is differentially controlled through lipid microdomain association and clathrin-dependent endocytosis of IFN receptors.* Mol Biol Cell, 2006. **17**(7): p. 2896-909.

104. Subramaniam, P.S. and H.M. Johnson, *Lipid microdomains are required sites for the selective endocytosis and nuclear translocation of IFN-gamma, its receptor chain IFN-gamma receptor-1, and the phosphorylation and nuclear translocation of STAT1alpha.* J Immunol, 2002. **169**(4): p. 1959-69.

105. Lamaze, C., et al., *Interleukin 2 receptors and detergent-resistant membrane domains define a clathrin-independent endocytic pathway.* Mol Cell, 2001. **7**(3): p. 661-71.
106. Marmor, M.D. and M. Julius, *Role for lipid rafts in regulating interleukin-2 receptor signaling.* Blood, 2001. **98**(5): p. 1489-97.
107. Kusumi, A., et al., *Paradigm shift of the plasma membrane concept from the two-dimensional continuum fluid to the partitioned fluid: high-speed single-molecule tracking of membrane molecules.* Annu Rev Biophys Biomol Struct, 2005. **34**: p. 351-78.
108. Kapus, A. and P. Janmey, *Plasma membrane--cortical cytoskeleton interactions: a cell biology approach with biophysical considerations.* Compr Physiol, 2013. **3**(3): p. 1231-81.
109. Lino, R., I. Koyama, and A. Kusumi, *Single molecule imaging of green fluorescent proteins in living cells: E-cadherin forms oligomers on the free cell surface.* Biophys J, 2001. **80**(6): p. 2667-77.
110. Murase, K., et al., *Ultrafine membrane compartments for molecular diffusion as revealed by single molecule techniques.* Biophys J, 2004. **86**(6): p. 4075-93.
111. Wawrezinieck, L., et al., *Fluorescence correlation spectroscopy diffusion laws to probe the submicron cell membrane organization.* Biophys J, 2005. **89**(6): p. 4029-42.
112. Morone, N., et al., *Three-dimensional reconstruction of the membrane skeleton at the plasma membrane interface by electron tomography.* J Cell Biol, 2006. **174**(6): p. 851-62.
113. Andrade, D.M., et al., *Cortical actin networks induce spatio-temporal confinement of phospholipids in the plasma membrane--a minimally invasive investigation by STED-FCS.* Sci Rep, 2015. **5**: p. 11454.
114. Kalay, Z., T.K. Fujiwara, and A. Kusumi, *Confining domains lead to reaction bursts: reaction kinetics in the plasma membrane.* PLoS One, 2012. **7**(3): p. e32948.
115. You, C., et al., *Receptor dimer stabilization by hierarchical plasma membrane microcompartments regulates cytokine signaling.* Sci Adv, 2016. **2**(12): p. e1600452.
116. Howard, M., et al., *Identification of a T cell-derived b cell growth factor distinct from interleukin 2.* J Exp Med, 1982. **155**(3): p. 914-23.
117. Brown, K.D., et al., *A family of small inducible proteins secreted by leukocytes are members of a new superfamily that includes leukocyte and fibroblast-derived inflammatory agents, growth factors, and indicators of various activation processes.* J Immunol, 1989. **142**(2): p. 679-87.
118. Yokota, T., et al., *Isolation and characterization of a human interleukin cDNA clone, homologous to mouse B-cell stimulatory factor 1, that expresses B-cell- and T-cell-stimulating activities.* Proc Natl Acad Sci U S A, 1986. **83**(16): p. 5894-8.
119. Minty, A., et al., *Interleukin-13 is a new human lymphokine regulating inflammatory and immune responses.* Nature, 1993. **362**(6417): p. 248-50.
120. Moy, F.J., et al., *Solution structure of human IL-13 and implication for receptor binding.* J Mol Biol, 2001. **310**(1): p. 219-30.
121. Okada, H.B., J.; Lotze, M.T., *Interleukin-4. In: The Cytokine Handbook. Edited by: Thomson, A.W. and Lotze, M.T.* 2003, Elsevier Science: London. p. 227-262.
122. Kelly-Welch, A.E., et al., *Interleukin-4 and interleukin-13 signaling connections maps.* Science, 2003. **300**(5625): p. 1527-8.

123. Nelms, K., et al., *The IL-4 receptor: signaling mechanisms and biologic functions.* Annu Rev Immunol, 1999. **17**: p. 701-38.

124. Wynn, T.A., *Type 2 cytokines: mechanisms and therapeutic strategies.* Nat Rev Immunol, 2015. **15**(5): p. 271-82.

125. Tadmori, W., et al., *Human B cell proliferation in response to IL-4 is associated with enhanced production of B cell-derived growth factors.* J Immunol, 1989. **142**(3): p. 826-32.

126. Cocks, B.G., et al., *IL-13 induces proliferation and differentiation of human B cells activated by the CD40 ligand.* Int Immunol, 1993. **5**(6): p. 657-63.

127. Bacharier, L.B. and R.S. Geha, *Molecular mechanisms of IgE regulation.* J Allergy Clin Immunol, 2000. **105**(2 Pt 2): p. S547-58.

128. Gascan, H., et al., *Human B cell clones can be induced to proliferate and to switch to IgE and IgG4 synthesis by interleukin 4 and a signal provided by activated CD4+ T cell clones.* J Exp Med, 1991. **173**(3): p. 747-50.

129. Punnonen, J., et al., *Interleukin 13 induces interleukin 4-independent IgG4 and IgE synthesis and CD23 expression by human B cells.* Proc Natl Acad Sci U S A, 1993. **90**(8): p. 3730-4.

130. Defrance, T., et al., *Human recombinant interleukin 4 induces Fc epsilon receptors (CD23) on normal human B lymphocytes.* J Exp Med, 1987. **165**(6): p. 1459-67.

131. Pawankar, R., et al., *Nasal mast cells in perennial allergic rhinitics exhibit increased expression of the Fc epsilonRI, CD40L, IL-4, and IL-13, and can induce IgE synthesis in B cells.* J Clin Invest, 1997. **99**(7): p. 1492-9.

132. Moore, P.E., et al., *IL-13 and IL-4 cause eotaxin release in human airway smooth muscle cells: a role for ERK.* Am J Physiol Lung Cell Mol Physiol, 2002. **282**(4): p. L847-53.

133. Van Dyken, S.J. and R.M. Locksley, *Interleukin-4- and interleukin-13-mediated alternatively activated macrophages: roles in homeostasis and disease.* Annu Rev Immunol, 2013. **31**: p. 317-43.

134. Hershey, G.K., *IL-13 receptors and signaling pathways: an evolving web.* J Allergy Clin Immunol, 2003. **111**(4): p. 677-90; quiz 691.

135. Steinke, J.W. and L. Borish, *Th2 cytokines and asthma. Interleukin-4: its role in the pathogenesis of asthma, and targeting it for asthma treatment with interleukin-4 receptor antagonists.* Respir Res, 2001. **2**(2): p. 66-70.

136. Abbas, A.K., K.M. Murphy, and A. Sher, *Functional diversity of helper T lymphocytes.* Nature, 1996. **383**(6603): p. 787-93.

137. May, R.D. and M. Fung, *Strategies targeting the IL-4/IL-13 axes in disease.* Cytokine, 2015. **75**(1): p. 89-116.

138. Fichtner-Feigl, S., et al., *IL-13 signaling through the IL-13alpha2 receptor is involved in induction of TGF-beta1 production and fibrosis.* Nat Med, 2006. **12**(1): p. 99-106.

139. Redpath, S.A., G. Heieis, and G. Perona-Wright, *Spatial regulation of IL-4 signalling in vivo.* Cytokine, 2015. **75**(1): p. 51-6.

140. Janeway, C.A., Jr., *The priming of helper T cells.* Semin Immunol, 1989. **1**(1): p. 13-20.

141. Arima, K., et al., *Characterization of the interaction between interleukin-13 and interleukin-13 receptors.* J Biol Chem, 2005. **280**(26): p. 24915-22.

142. Chomarat, P. and J. Banchereau, *Interleukin-4 and Interleukin-13: Commonalities and Differences. In: Cytokines and Cytokine Receptors Physiology and Pathological Disorders. Edited by: Bona, C.A. and Revillard, J.-P.* 2000, Overseas Publishers Association (OPA): Amsterdam. p. 53-82.

143. Wang, I.M., et al., *STAT-1 is activated by IL-4 and IL-13 in multiple cell types.* Mol Immunol, 2004. **41**(9): p. 873-84.

144. Umeshita-Suyama, R., et al., *Characterization of IL-4 and IL-13 signals dependent on the human IL-13 receptor alpha chain 1: redundancy of requirement of tyrosine residue for STAT3 activation.* Int Immunol, 2000. **12**(11): p. 1499-509.

145. Lischke, A., et al., *The interleukin-4 receptor activates STAT5 by a mechanism that relies upon common gamma-chain.* J Biol Chem, 1998. **273**(47): p. 31222-9.

146. Goenka, S. and M.H. Kaplan, *Transcriptional regulation by STAT6.* Immunol Res, 2011. **50**(1): p. 87-96.

147. Kashiwada, M., et al., *Immunoreceptor tyrosine-based inhibitory motif of the IL-4 receptor associates with SH2-containing phosphatases and regulates IL-4-induced proliferation.* J Immunol, 2001. **167**(11): p. 6382-7.

148. Johnson, D.J., et al., *Shp1 regulates T cell homeostasis by limiting IL-4 signals.* J Exp Med, 2013. **210**(7): p. 1419-31.

149. Tao, B., et al., *Myeloid-specific disruption of tyrosine phosphatase Shp2 promotes alternative activation of macrophages and predisposes mice to pulmonary fibrosis.* J Immunol, 2014. **193**(6): p. 2801-11.

150. Giallourakis, C., et al., *Positive regulation of interleukin-4-mediated proliferation by the SH2-containing inositol-5'-phosphatase.* J Biol Chem, 2000. **275**(38): p. 29275-82.

151. Losman, J.A., et al., *Cutting edge: SOCS-1 is a potent inhibitor of IL-4 signal transduction.* J Immunol, 1999. **162**(7): p. 3770-4.

152. Hebenstreit, D., et al., *IL-4 and IL-13 induce SOCS-1 gene expression in A549 cells by three functional STAT6-binding motifs located upstream of the transcription initiation site.* J Immunol, 2003. **171**(11): p. 5901-7.

153. Hebenstreit, D., et al., *SOCS-1 and SOCS-3 inhibit IL-4 and IL-13 induced activation of Eotaxin-3/CCL26 gene expression in HEK293 cells.* Mol Immunol, 2005. **42**(3): p. 295-303.

154. Yang, X.O., et al., *The signaling suppressor CIS controls proallergic T cell development and allergic airway inflammation.* Nat Immunol, 2013. **14**(7): p. 732-40.

155. Sharma, P., et al., *Redox regulation of interleukin-4 signaling.* Immunity, 2008. **29**(4): p. 551-64.

156. Kraich, M., et al., *A modular interface of IL-4 allows for scalable affinity without affecting specificity for the IL-4 receptor.* BMC Biol, 2006. **4**: p. 13.

157. Mueller, T.D., et al., *Structure, binding, and antagonists in the IL-4/IL-13 receptor system.* Biochim Biophys Acta, 2002. **1592**(3): p. 237-50.

158. Moraga, I., et al., *Instructive roles for cytokine-receptor binding parameters in determining signaling and functional potency.* Sci Signal, 2015. **8**(402): p. ra114.

159. Sauvonnet, N., A. Dujeancourt, and A. Dautry-Varsat, *Cortactin and dynamin are required for the clathrin-independent endocytosis of gammac cytokine receptor.* J Cell Biol, 2005. **168**(1): p. 155-63.

160. Kurgonaite, K., et al., *Essential role of endocytosis for interleukin-4-receptor-mediated JAK/STAT signalling.* J Cell Sci, 2015. **128**(20): p. 3781-95.

161. Friedrich, K., et al., *The two subunits of the interleukin-4 receptor mediate independent and distinct patterns of ligand endocytosis.* Eur J Biochem, 1999. **265**(1): p. 457-65.
162. Basquin, C., et al., *The signalling factor PI3K is a specific regulator of the clathrin-independent dynamin-dependent endocytosis of IL-2 receptors.* J Cell Sci, 2013. **126**(Pt 5): p. 1099-108.
163. Gandhi, H., et al., *Dynamics and interaction of interleukin-4 receptor subunits in living cells.* Biophys J, 2014. **107**(11): p. 2515-27.
164. Los, G.V., et al., *HaloTag: a novel protein labeling technology for cell imaging and protein analysis.* ACS Chem Biol, 2008. **3**(6): p. 373-82.
165. Cole, N.B., *Site-specific protein labeling with SNAP-tags.* Curr Protoc Protein Sci, 2013. **73**: p. Unit 30 1.
166. Semrau, S., et al., *Quantification of biological interactions with particle image cross-correlation spectroscopy (PICCS).* Biophys J, 2011. **100**(7): p. 1810-8.
167. Gavutis, M., S. Lata, and J. Piehler, *Probing 2-dimensional protein-protein interactions on model membranes.* Nat Protoc, 2006. **1**(4): p. 2091-103.
168. Axelrod, D., T.P. Burghardt, and N.L. Thompson, *Total internal reflection fluorescence.* Annu Rev Biophys Bioeng, 1984. **13**: p. 247-68.
169. Gauglitz, G., et al., *Chemical and biochemical sensors based on interferometry at thin (multi-) layers.* Sensor Actuator, 1993. **11**(1-3): p. 21-27.
170. Piehler, J., A. Brecht, and G. Gauglitz, *Affinity detection of low molecular weight analytes.* Anal Chem, 1996. **68**(1): p. 139-43.
171. Gavutis, M., et al., *Lateral ligand-receptor interactions on membranes probed by simultaneous fluorescence-interference detection.* Biophys J, 2005. **88**(6): p. 4289-302.
172. Brecht, A. and G. Gauglitz, *Recent developments in optical transducers for chemical or biochemical applications.* Sensor Actuator, 1997. **38**(1-3): p. 1-7.
173. Beutel, O., et al., *High-fidelity protein targeting into membrane lipid microdomains in living cells.* Angew Chem Int Ed Engl, 2014. **53**(5): p. 1311-5.
174. Abbe, E., *Theorie des Mikroskops und der mikroskopischen Wahrnehmung.* Arch Mikrosk Anat, 1873. **9**: p. 413–468.
175. Hell, S.W. and J. Wichmann, *Breaking the diffraction resolution limit by stimulated emission: stimulated-emission-depletion fluorescence microscopy.* Opt Lett, 1994. **19**(11): p. 780-2.
176. Gustafsson, M.G., *Surpassing the lateral resolution limit by a factor of two using structured illumination microscopy.* J Microsc, 2000. **198**(Pt 2): p. 82-7.
177. Hess, S.T., T.P. Girirajan, and M.D. Mason, *Ultra-high resolution imaging by fluorescence photoactivation localization microscopy.* Biophys J, 2006. **91**(11): p. 4258-72.
178. Rust, M.J., M. Bates, and X. Zhuang, *Sub-diffraction-limit imaging by stochastic optical reconstruction microscopy (STORM).* Nat Methods, 2006. **3**(10): p. 793-5.
179. Patterson, G., et al., *Superresolution imaging using single-molecule localization.* Annu Rev Phys Chem, 2010. **61**: p. 345-67.
180. Schmidt, T., et al., *Imaging of single molecule diffusion.* Proc Natl Acad Sci U S A, 1996. **93**(7): p. 2926-9.
181. Thompson, R.E., D.R. Larson, and W.W. Webb, *Precise nanometer localization analysis for individual fluorescent probes.* Biophys J, 2002. **82**(5): p. 2775-83.
182. Rayleigh, L., *On the theory of optical images, with special reference to the microscope.* J R Microsc Soc, 1903. **23**: p. 474–482.

183. Fenz, S.F., A. Pezzarossa, and T. Schmidt, *The Basics and Potential of Single-Molecule Tracking in Cellular Biophysics. In: Comprehensive Biophysics - Volume 2: Biophysical Techniques for Characterization of Cells. Edited by: Egelman, E.H.* 2012, Academic Press: London. p. 260-272.
184. Axelrod, D., *Cell-substrate contacts illuminated by total internal reflection fluorescence.* J Cell Biol, 1981. **89**(1): p. 141-5.
185. Axelrod, D., *Total internal reflection fluorescence microscopy in cell biology.* Traffic, 2001. **2**(11): p. 764-74.
186. Deschout, H., et al., *Precisely and accurately localizing single emitters in fluorescence microscopy.* Nat Methods, 2014. **11**(3): p. 253-66.
187. Semrau, S., A. Pezzarossa, and T. Schmidt, *Microsecond single-molecule tracking (musSMT).* Biophys J, 2011. **100**(4): p. L19-21.
188. Fujiwara, T., et al., *Phospholipids undergo hop diffusion in compartmentalized cell membrane.* J Cell Biol, 2002. **157**(6): p. 1071-81.
189. Roder, F., *Polymer-Supported Membranes for Quantitative Analysis of Membrane Receptor Interactions in a Controlled Lipid Environment*, PhD thesis, FB5 - Department of Biology / Division of Biophysics. 2014, University of Osnabrueck.
190. Crivat, G. and J.W. Taraska, *Imaging proteins inside cells with fluorescent tags.* Trends Biotechnol, 2012. **30**(1): p. 8-16.
191. Serge, A., et al., *Dynamic multiple-target tracing to probe spatiotemporal cartography of cell membranes.* Nat Methods, 2008. **5**(8): p. 687-94.
192. Meijering, E., O. Dzyubachyk, and I. Smal, *Methods for cell and particle tracking.* Methods Enzymol, 2012. **504**: p. 183-200.
193. Yin, J., et al., *Genetically encoded short peptide tag for versatile protein labeling by Sfp phosphopantetheinyl transferase.* Proc Natl Acad Sci U S A, 2005. **102**(44): p. 15815-20.
194. Jarvis, D.L., *Baculovirus-insect cell expression systems.* Methods Enzymol, 2009. **463**: p. 191-222.
195. Kraich, M., *Strukturelle und funktionelle Untersuchungen der Interaktion zwischen Ligand und Rezeptor im Interleukin-4- und Interleukin-13-System*. PhD thesis, 2008, University of Wuerzburg.
196. Yin, J., et al., *Site-specific protein labeling by Sfp phosphopantetheinyl transferase.* Nat Protoc, 2006. **1**(1): p. 280-5.
197. Tony, H.P., et al., *Design of human interleukin-4 antagonists inhibiting interleukin-4-dependent and interleukin-13-dependent responses in T-cells and B-cells with high efficiency.* Eur J Biochem, 1994. **225**(2): p. 659-65.
198. Eddowes, M.J., *Direct immunochemical sensing: basic chemical principles and fundamental limitations.* Biosensors, 1987. **3**(1): p. 1-15.
199. Coloma, M.J., et al., *Novel vectors for the expression of antibody molecules using variable regions generated by polymerase chain reaction.* J Immunol Methods, 1992. **152**(1): p. 89-104.
200. Keppler, A., et al., *Labeling of fusion proteins of O6-alkylguanine-DNA alkyltransferase with small molecules in vivo and in vitro.* Methods, 2004. **32**(4): p. 437-44.
201. Keppler, A., et al., *Labeling of fusion proteins with synthetic fluorophores in live cells.* Proc Natl Acad Sci U S A, 2004. **101**(27): p. 9955-9.
202. Danke, C., et al., *Adjusting transgene expression levels in lymphocytes with a set of inducible promoters.* J Gene Med, 2010. **12**(6): p. 501-15.

203. Roder, F., et al., *Rapid transfer of transmembrane proteins for single molecule dimerization assays in polymer-supported membranes.* ACS Chem Biol, 2014. **9**(11): p. 2479-84.

204. VandeVondele, S., J. Voros, and J.A. Hubbell, *RGD-grafted poly-L-lysine-graft-(polyethylene glycol) copolymers block non-specific protein adsorption while promoting cell adhesion.* Biotechnol Bioeng, 2003. **82**(7): p. 784-90.

205. Chen, C. and H. Okayama, *High-efficiency transformation of mammalian cells by plasmid DNA.* Mol Cell Biol, 1987. **7**(8): p. 2745-52.

206. Vogelsang, J., et al., *A reducing and oxidizing system minimizes photobleaching and blinking of fluorescent dyes.* Angew Chem Int Ed Engl, 2008. **47**(29): p. 5465-9.

207. Appelhans, T., et al., *Nanoscale organization of mitochondrial microcompartments revealed by combining tracking and localization microscopy.* Nano Lett, 2012. **12**(2): p. 610-6.

208. Sander, J.E., M.; Kriegel H.P.; Xu, X., *Density-Based Clustering in Spatial Databases: The Algorithm GDBSCAN and Its Applications.* Data Min Knowl Discov, 1998. **2**(2): p. 169–194.

209. Waichman, S., et al., *Diffusion and interaction dynamics of individual membrane protein complexes confined in micropatterned polymer-supported membranes.* Small, 2013. **9**(4): p. 570-7.

210. Schmedt, D., *Assemblierung, Effektoraktivierung und Endozytose des Interleukinrezeptorsystems IL-4Ra/IL-13Ra1*, Master thesis, FB5 - Department of Biology / Division of Biophysics. 2012, University of Osnabrueck.

211. Roder, F., et al., *Reconstitution of membrane proteins into polymer-supported membranes for probing diffusion and interactions by single molecule techniques.* Anal Chem, 2011. **83**(17): p. 6792-9.

212. Degrip, W.J., J. Vanoostrum, and P.H. Bovee-Geurts, *Selective detergent-extraction from mixed detergent/lipid/protein micelles, using cyclodextrin inclusion compounds: a novel generic approach for the preparation of proteoliposomes.* Biochem J, 1998. **330 (Pt 2)**: p. 667-74.

213. Tokunaga, M., N. Imamoto, and K. Sakata-Sogawa, *Highly inclined thin illumination enables clear single-molecule imaging in cells.* Nat Methods, 2008. **5**(2): p. 159-61.

214. Kitamura, T., et al., *Establishment and characterization of a unique human cell line that proliferates dependently on GM-CSF, IL-3, or erythropoietin.* J Cell Physiol, 1989. **140**(2): p. 323-34.

215. Codling, E.A., M.J. Plank, and S. Benhamou, *Random walk models in biology.* J R Soc Interface, 2008. **5**(25): p. 813-34.

216. Chotard-Ghodsnia, R.D., et al., *Static and Dynamic Interactions between Endothelium and Circulating Cells in Cancer. In: Cancer Modelling and simulation. Edited by Preziosi, L.* 2003, CRC Press: London. p. 243-267.

217. Pettersen, E.F., et al., *UCSF Chimera--a visualization system for exploratory research and analysis.* J Comput Chem, 2004. **25**(13): p. 1605-12.

218. Guex, N. and M.C. Peitsch, *SWISS-MODEL and the Swiss-PdbViewer: an environment for comparative protein modeling.* Electrophoresis, 1997. **18**(15): p. 2714-23.

219. Lata, S., M. Gavutis, and J. Piehler, *Monitoring the dynamics of ligand-receptor complexes on model membranes.* J Am Chem Soc, 2006. **128**(1): p. 6-7.

220. Spector, I., et al., *Latrunculins--novel marine macrolides that disrupt microfilament organization and affect cell growth: I. Comparison with cytochalasin D.* Cell Motil Cytoskeleton, 1989. **13**(3): p. 127-44.

221. Wilmes, S., et al., *Triple-color super-resolution imaging of live cells: resolving submicroscopic receptor organization in the plasma membrane.* Angew Chem Int Ed Engl, 2012. **51**(20): p. 4868-71.

222. Riedl, J., et al., *Lifeact: a versatile marker to visualize F-actin.* Nat Methods, 2008. **5**(7): p. 605-7.

223. Kusumi, A., et al., *Single-molecule tracking of membrane molecules: plasma membrane compartmentalization and dynamic assembly of raft-philic signaling molecules.* Semin Immunol, 2005. **17**(1): p. 3-21.

224. McKenzie, A.N., et al., *Interleukin 13, a T-cell-derived cytokine that regulates human monocyte and B-cell function.* Proc Natl Acad Sci U S A, 1993. **90**(8): p. 3735-9.

225. Kalie, E., et al., *The stability of the ternary interferon-receptor complex rather than the affinity to the individual subunits dictates differential biological activities.* J Biol Chem, 2008. **283**(47): p. 32925-36.

226. Shutes, A., et al., *Specificity and mechanism of action of EHT 1864, a novel small molecule inhibitor of Rac family small GTPases.* J Biol Chem, 2007. **282**(49): p. 35666-78.

227. Onesto, C., et al., *Characterization of EHT 1864, a novel small molecule inhibitor of Rac family small GTPases.* Methods Enzymol, 2008. **439**: p. 111-29.

228. Wiley, H.S., S.Y. Shvartsman, and D.A. Lauffenburger, *Computational modeling of the EGF-receptor system: a paradigm for systems biology.* Trends Cell Biol, 2003. **13**(1): p. 43-50.

229. Maruyama, I.N., *Activation of transmembrane cell-surface receptors via a common mechanism? The "rotation model".* Bioessays, 2015. **37**(9): p. 959-67.

230. Livnah, O., et al., *Crystallographic evidence for preformed dimers of erythropoietin receptor before ligand activation.* Science, 1999. **283**(5404): p. 987-90.

231. Chan, F.K., et al., *A domain in TNF receptors that mediates ligand-independent receptor assembly and signaling.* Science, 2000. **288**(5475): p. 2351-4.

232. Horan, T., et al., *Dimerization of the extracellular domain of granuloycte-colony stimulating factor receptor by ligand binding: a monovalent ligand induces 2:2 complexes.* Biochemistry, 1996. **35**(15): p. 4886-96.

233. Weidemann, T., et al., *Single cell analysis of ligand binding and complex formation of interleukin-4 receptor subunits.* Biophys J, 2011. **101**(10): p. 2360-9.

234. Hansen, G., et al., *The structure of the GM-CSF receptor complex reveals a distinct mode of cytokine receptor activation.* Cell, 2008. **134**(3): p. 496-507.

235. Oh, C.K., G.P. Geba, and N. Molfino, *Investigational therapeutics targeting the IL-4/IL-13/STAT-6 pathway for the treatment of asthma.* Eur Respir Rev, 2010. **19**(115): p. 46-54.

236. Gour, N. and M. Wills-Karp, *IL-4 and IL-13 signaling in allergic airway disease.* Cytokine, 2015. **75**(1): p. 68-78.

237. Li, Z., L. Chen, and Z. Qin, *Paradoxical roles of IL-4 in tumor immunity.* Cell Mol Immunol, 2009. **6**(6): p. 415-22.

238. Ritchie, K. and A. Kusumi, *Role of the membrane skeleton in creation of microdomains.* Subcell Biochem, 2004. **37**: p. 233-45.

239. Tamarit, B., et al., *Membrane microdomains and cytoskeleton organization shape and regulate the IL-7 receptor signalosome in human CD4 T-cells.* J Biol Chem, 2013. **288**(12): p. 8691-701.

240. Rose, T., et al., *Interleukin-7 compartmentalizes its receptor signaling complex to initiate CD4 T lymphocyte response.* J Biol Chem, 2010. **285**(20): p. 14898-908.

241. Kruse, N., et al., *Two distinct functional sites of human interleukin 4 are identified by variants impaired in either receptor binding or receptor activation.* EMBO J, 1993. **12**(13): p. 5121-9.

242. Lowenthal, J.W., et al., *Expression of high affinity receptors for murine interleukin 4 (BSF-1) on hemopoietic and nonhemopoietic cells.* J Immunol, 1988. **140**(2): p. 456-64.

243. Lingwood, D. and K. Simons, *Lipid rafts as a membrane-organizing principle.* Science, 2010. **327**(5961): p. 46-50.

244. Low-Nam, S.T., et al., *ErbB1 dimerization is promoted by domain co-confinement and stabilized by ligand binding.* Nat Struct Mol Biol, 2011. **18**(11): p. 1244-9.

245. Mattila, P.K., F.D. Batista, and B. Treanor, *Dynamics of the actin cytoskeleton mediates receptor cross talk: An emerging concept in tuning receptor signaling.* J Cell Biol, 2016. **212**(3): p. 267-80.

246. Kalie, E., et al., *An interferon alpha2 mutant optimized by phage display for IFNAR1 binding confers specifically enhanced antitumor activities.* J Biol Chem, 2007. **282**(15): p. 11602-11.

247. Pearce, K.H., Jr., et al., *Growth hormone binding affinity for its receptor surpasses the requirements for cellular activity.* Biochemistry, 1999. **38**(1): p. 81-9.

248. Selzer, T., S. Albeck, and G. Schreiber, *Rational design of faster associating and tighter binding protein complexes.* Nat Struct Biol, 2000. **7**(7): p. 537-41.

249. Francois-Newton, V., et al., *USP18-based negative feedback control is induced by type I and type III interferons and specifically inactivates interferon alpha response.* PLoS One, 2011. **6**(7): p. e22200.

250. Kossiakoff, A.A., *The structural basis for biological signaling, regulation, and specificity in the growth hormone-prolactin system of hormones and receptors.* Adv Protein Chem, 2004. **68**: p. 147-69.

251. Thomas, C., et al., *Structural linkage between ligand discrimination and receptor activation by type I interferons.* Cell, 2011. **146**(4): p. 621-32.

252. Sarkar, C.A., et al., *Parsing the effects of binding, signaling, and trafficking on the mitogenic potencies of granulocyte colony-stimulating factor analogues.* Biotechnol Prog, 2003. **19**(3): p. 955-64.

253. Lauffenburger, D.A., E.M. Fallon, and J.M. Haugh, *Scratching the (cell) surface: cytokine engineering for improved ligand/receptor trafficking dynamics.* Chem Biol, 1998. **5**(10): p. R257-63.

254. Ring, A.M., et al., *Mechanistic and structural insight into the functional dichotomy between IL-2 and IL-15.* Nat Immunol, 2012. **13**(12): p. 1187-95.

255. Schreiber, G. and J. Piehler, *The molecular basis for functional plasticity in type I interferon signaling.* Trends Immunol, 2015. **36**(3): p. 139-49.

256. Kennedy-Nasser, A.A., et al., *Ultra low-dose IL-2 for GVHD prophylaxis after allogeneic hematopoietic stem cell transplantation mediates expansion of regulatory T cells without diminishing antiviral and antileukemic activity.* Clin Cancer Res, 2014. **20**(8): p. 2215-25.

257. Posch, C., et al., *Low-dose inhalation of interleukin-2 bio-chemotherapy for the treatment of pulmonary metastases in melanoma patients.* Br J Cancer, 2014. **110**(6): p. 1427-32.

258. Yu, A., et al., *Selective IL-2 responsiveness of regulatory T cells through multiple intrinsic mechanisms supports the use of low-dose IL-2 therapy in type 1 diabetes.* Diabetes, 2015. **64**(6): p. 2172-83.

Acknowledgments

First and foremost I would like to thank my supervisor Prof. Dr. Jacob Piehler for providing me the opportunity to work on an exciting and highly topical research project, sharing his experience and ideas in numerous inspiring discussions, and improving my way of thinking and my abilities to formulate statements more precisely. But above all I cannot thank Jacob enough for always supporting me in many difficult times. I really appreciate his faith in me!

Many thanks go to Stephan “Teff” Wilmes for introducing me into the world of cytokine receptors and single molecules, for his exhaustless support in all matters and in particular for goofing around all the time. It is a great pity that Teff is going to leave Osnabrück, but I wish him and his family all the best and a wonderful time in Scotland.

I sincerely thank Oliver Beutel for being a limitless source of scientific knowledge and the most helpful person I know, for his excellent expertise in fluorescence microscopy and TIRFS/RIf, but most of all for being a friend. I really miss the time we spend together in the lab.

Special thanks go to Hauke Winkelmann, who helped me immensely by taking over a lot of the microscopy work and by providing valuable results. I always enjoyed working together with Hauke and I’m looking forward to our future projects.

I would also like thank Ignacio Moraga for the excellent cooperation and for replying to each of my requests instantaneously. At times it seemed that Ignacio’s response was already present in my email inbox before I was able to click the “send” button ☺.

Warm thanks go to Hella Kenneweg, who does an excellent job expressing and labeling proteins, and to Gabi Hikade, who is always of great help due to her expertise in molecular cloning. Besides, I totally enjoyed the numerous funny chats with Hella and the regular “lunch talks” with Gabi.

I am very grateful to Oliver Birkholz, who is an expert in the field of supported membranes and kindly put a lot of effort into the PSM experiments.

Moreover, gratitude is owed to Philipp Selenschik, who introduced me into PICCS and who always has a sympathetic ear for me. But most importantly, Philipp is a great friend and during the shared time in Osnabrück he was the best companion one could find.

My thanks also go to Richard Wagner, Christian Paolo Richter, Christoph Drees, Domenik Liße, Sara Löchte, Changjiang You, Katharina Hötte, Markus Staufenbiel, Rainer Kurre, Tim Wedeking, Julia Flesch, Friedrich Roder, Dirk Paterok, Elisabeth Olaru, Carmen Larberg and Ulrich Kunze, who each in his or her way supported me and contributed to the success of this project.

I sincerely thank my parents for always being there for me and for unconditionally supporting me on my way. I would never have managed all this without you.

Finally and above all I dearly thank my wife Daniela, who is the most wonderful and important person in my life: for her love, her patience and endurance, her neverending support and for always being by my side, although I’m sure this is frequently not easy ☺

Declaration

I hereby declare that the presented thesis ”Regulation of type II interleukin-4 receptor assembly and signaling by ligand binding kinetics and affinities” was prepared entirely on my own and I have not used outside sources without declaration in the text. Any concepts or quotations applicable to these sources are clearly attributed to them. I have not attempted a promotion before.

Ibbenbüren, March 27th 2017

(David Richter, geb. Schmedt)